

https://dspace.org/

Effect of deformation on the broad and fine structure of the Isovector Giant Dipole Resonance in 142-150 Nd and 152 Sm

Donaldson, Lindsay Michelle

2016

http://hdl.handle.net/10539/21288

Donaldson, Lindsay Michelle (2016) Effect of deformation on the broad and fine structure of the Isovector Giant Dipole Resonance in 142-150 Nd and 152 Sm, University of Witwatersrand, Johannesburg, <http://wiredspace.wits.ac.za/handle/10539/21288>

Downloaded from a DSpace repository. https://dspace.org/

Effect of deformation on the broad and fine structure of the Isovector Giant Dipole Resonance in $^{142-150}$Nd and ^{152}Sm

Lindsay Michelle Donaldson

A thesis submitted to the Faculty of Science,
University of the Witwatersrand, in fulfilment of
the requirements for the degree of
Doctor of Philosophy.

Johannesburg 2016

Declaration

I declare that this thesis is my own unaided work. It is being submitted for the Degree of Doctor of Philosophy to the University of the Witwatersrand, Johannesburg. It has not been submitted previously for any degree or examination to any other university.



2 June 2016

Lindsay Michelle Donaldson Date

Abstract

This study investigates the effect of nuclear deformation on both the broad and fine structure of the Isovector Giant Dipole Resonance (IVGDR) in the rare-earth region. The IVGDR is strongly excited at and close to zero degrees by virtual-photon Coulomb excitation. As such, the Zero-degree Facility of the K600 magnetic spectrometer of iThemba Laboratory for Accelerator Based Sciences (iThemba LABS) was used with an incident proton beam energy of 200 MeV to measure high energy-resolution (p,p′) scattering on a range of neodymium isotopes from spherical $^{142}_{60}\mathrm{Nd}_{82}$ to the permanently deformed $^{150}_{60}\mathrm{Nd}_{90}$ and the correspondingly deformed $^{152}_{62}\mathrm{Sm}_{90}$ in the region of the IVGDR. It is important to note that for nuclei with $88 \leq N \leq 92$, a detailed study of the IVGDR is of specific interest since it is here that a transition from spherical to permanently deformed nuclei occurs.

An extensive data analysis procedure was performed, which included cross section extraction and conversion to equivalent photo-absorption spectra for comparison with existing photo-absorption data and theoretical predictions. With respect to the evolution of the shape of the IVGDR with increasing deformation, generally good agreement is seen between the two datasets for the $^{142-148}$Nd isotopes. For the more deformed ^{150}Nd and ^{152}Sm nuclei, however, the data from this study lack the expected double-peaked structure resulting from the splitting of the IVGDR into $K = 0$ and $K = 1$ components, and display a significant reduction in the strength of the $K = 0$ component of the IVGDR in comparison to previously published photo-absorption spectra. This reduced strength near the neutron threshold agrees very well with recent photo-neutron experiments.

A fine structure analysis was performed on all of the measured isotopes, that is, ^{142,144,146,148,150}Nd and ^{152}Sm through the use of techniques associated with

the continuous wavelet transform. Characteristic energy scales for the present high energy-resolution data are extracted using the complex Morlet mother-wavelet and compared to those obtained for the theoretically predicted $B(E1)$ strength functions. Finally, conclusions regarding the suitability of the model predictions to the current data are drawn.

Acknowledgements

"There comes that mysterious meeting in life when someone acknowledges who we are and what we can be, igniting the circuits of our highest potential." – Rusty Berkus

For me, that someone is my principal supervisor and mentor, Professor John Carter, who believed in me even before I ventured down this path. Thank you, Prof-san, for your support, guidance, reassurance and patience, especially during my 'O ye of little faith' (or lack-of-lettuce-leaf induced) moments. You have made an immeasurable and indelible contribution to shaping who I am, both personally and professionally.

To my co-supervisor, Dr Iyabo Usman for being a role-model, not only as a young researcher but also as a woman in science. Thank you for understanding the delicate balance between life and a PhD and for your perspective with respect to integrating both my personal and professional commitments. Thank you for allowing me the freedom to make the decisions that facilitated the writing of this thesis and especially for supporting them. You have always been available to listen to me and to guide me through the intricacies of academia. Your constant support and encouragement have meant so much.

To my iThemba LABS supervisor, Dr Retief Neveling who has never been too busy to help me, regardless of the time of day, night or weekend. Thank you, Sir Co-Supervisor Sir, for the role you played throughout my PhD including things like handing me 'The Hitchhiker's Guide to the Galaxy' and telling me not to panic during a particularly traumatic beamtime experience. Thank you for your patience and for explaining concepts in a way that makes sense to me. Your knowledge and expertise with regards to the data extraction and analysis were, and continue to be, invaluable. Thank you for your encouragement and

insight as well as for your willingness to read countless versions of my thesis.

I would like to thank Professor Dr Peter von Neumann-Cosel for his contribution to both this thesis and my academic development. Thank you for the opportunities you provided that have allowed me to gain experience and to grow within the field, such as the invitation to participate in one of your experiments in Japan. Thank you for teaching me to trust my data and for always being willing and available to offer your insight and expertise.

The theoretical contribution to the results chapter of this thesis would not have been possible without the extensive SSRPA calculations performed by Valentin Nesterenko. In the midst of your own commitments, you always found the time to respond to my queries in a way that taught me rather than merely informing me. Thank you for the contribution you made to this thesis and for your readiness to read the relevant sections and provide insightful comments at critical stages.

Thank you to Vladimir Ponomarev for the additional calculations required for the analysis of my experimental results. Thank you for answering my questions whenever I had any and for being so willing to read and provide your thoughts on Chapter 2 of this thesis.

Thank you to the Wits Nuclear Structure Research Group (NSRG), in particular, to then members Oscar Kureba and Max Jingo who welcomed me so warmly into the group. Thank you for the advice and support along the way.

Special thanks go to the physicists and students of the iThemba LABS collaboration involved in the experiments and data collection for this thesis. Thank you for ensuring the integrity and usability of the data and for giving up personal and family time. In particular, to Dr Ricky Smit, thank you for your wisdom, technical know-how and also, for the nibbles.

I cannot not say thank you to Dr Philip Adsley for the regular doses of realism, but not really for the just as regular terror-inducing check-ins regarding the progress of my thesis. Thank you, too, for the numerous discussions around the possible interpretations of my experimental results. Your particular brand

of support was refreshing and greatly appreciated.

I would like to express my appreciation to Dr Zinhle Buthelezi for being somewhat of an iThemba LABS mom to me. Thank you for everything.

To Dr Lowry Conradie, Dr Dirk Fourie and the beam operators of iThemba LABS: thank you for your patience and dedication to ensuring the exceptional quality of the beam delivered to the spectrometer. The seemingly endless hours of tweaking and fine-tuning made all the difference to a high energy-resolution experiment of this nature.

To Ntombi Kheswa, the iThemba LABS target maker: thank you for the effort and time you put into preparing all five neodymium targets as well as the samarium targets required for this study.

I would like to thank the members of RCNP for providing me with such a fruitful learning experience during my time in Japan. In particular, my thanks go to Dr Hiro Fujita for introducing me to new methods regarding the data extraction in my study as well as to Professor Atsushi Tamii for his input regarding the comparisons to RCNP data and calibrations.

I would like to acknowledge the financial support that I received throughout the duration of the study, namely the iThemba LABS Top-Up Bursary as well as the Wits Post-graduate Merit Award.

I have been lucky enough to be surrounded by friends who have been with me at every step on this journey. You know who you are. Thank you for the walks to the Matrix whenever I needed to clear my head, for the pep talks and for all of the hugs. Your support got me through some difficult times. To my best friend, Bronwyn, thank you for understanding - always.

To my mom, for all the little things but especially for listening, understanding and for offering a different perspective. Being my mom can't be an easy task on the best of days but you have stuck with it (and with me) through this and I can't thank you enough.

To my dad who has always been a role model of logic, dedication and

commitment to finding a solution. Somehow you always have the right plan of action for any situation but you also know when I just need a dad-hug. Thank you for your guidance and for the unfailing support when it comes to what makes me happy.

To my sister, for your sense of humour and for the crisis management. You have always been the person I could call when I felt I couldn't manage and when I needed a sounding board. Thank you for the advice and most importantly, for the coffee.

And finally, to Trav, thank you for being my safe space.

Contents

Declaration i

Abstract ii

Acknowledgements iv

List of Figures xii

List of Tables xxii

1 Introduction 1

2 Theoretical considerations 11

2.1 Basic concepts of giant resonances 11

2.2 Isovector Giant Dipole Resonance 15

2.2.1 Overview 15

2.2.2 Techniques for IVGDR excitation 17

2.2.2.1 Gamma-absorption: real photons 18

2.2.2.2 Radiative capture 20

2.2.2.3 Coulomb excitation: absorption of virtual photons 21

2.2.3 Theoretical descriptions of Coulomb excitation 22

2.2.3.1 Semi-classical description of Coulomb excitation 22

2.2.3.2 Equivalent virtual photon method 25

2.2.3.3 Eikonal description of Coulomb excitation . . . 27

2.3 Model predictions of giant resonance behaviour 29

2.3.1 Macroscopic model predictions 29

2.3.1.1 Brief overview of the collective model 29

2.3.1.2 K-splitting and the shape of the IVGDR for deformed nuclei 32

2.3.2 Microscopic model predictions . . . 36
2.3.2.1 Random Phase Approximation (RPA) . . . 36
2.3.2.2 Self-consistent Separable Random Phase Approximation (SSRPA) . . . 36
2.4 Properties of the IVGDR . . . 41
2.4.1 Resonance excitation energy . . . 41
2.4.2 Resonance strength . . . 42
2.4.3 Resonance width . . . 42
2.4.4 Area ratio for deformed nuclei . . . 43
2.5 Damping of giant resonances . . . 43
2.6 Extraction of characteristic energy scales . . . 46
2.6.1 Wavelet analysis . . . 46
2.6.1.1 Wavelet analysis formalism . . . 47
2.6.1.2 Continuous Wavelet Transform (CWT) . . . 49
2.6.1.3 Discrete Wavelet Transform (DWT) . . . 50
2.6.1.4 Power spectrum . . . 51
2.6.2 Wavelet-based semblance analysis . . . 51

3 Experimental details and data extraction 53
3.1 Accelerator facility . . . 53
3.2 K600 magnetic spectrometer . . . 56
3.2.1 Focal plane detector package . . . 58
3.2.1.1 Plastic scintillator detectors . . . 59
3.2.1.2 Vertical drift chambers . . . 60
3.2.2 Zero-degree mode . . . 60
3.3 Data acquisition system . . . 61
3.4 Targets . . . 62
3.5 Experimental procedure . . . 63
3.5.1 Background contributions . . . 63
3.5.1.1 Beam-related background . . . 64
3.5.1.2 Target-related background . . . 65
3.5.2 Dispersion matching . . . 67
3.5.2.1 Kinematic correction . . . 70
3.5.2.2 Focus matching . . . 70
3.5.2.3 Lateral dispersion matching . . . 71
3.5.2.4 Angular dispersion matching . . . 71
3.5.2.5 Matched system . . . 72
3.5.2.6 Matching in practice . . . 73

3.5.3 Faint beam method 75
3.6 Data extraction 79
3.6.1 Particle identification 79
3.6.1.1 Time-of-flight selection 79
3.6.1.2 The $\Delta E - \Delta E$ technique 80
3.6.2 VDC data extraction 84
3.6.2.1 VDC operation and focal plane position determination 84
3.6.2.2 Position resolution 87
3.6.2.3 VDC efficiency 88
3.6.2.4 Angle calibration 89
3.7 Data optimisation 94
3.7.1 Background subtraction 94
3.7.2 Lineshape correction 95
3.7.3 Data offsets and chained data 97
3.7.4 Energy resolution 97
3.7.5 Energy calibration 98
3.7.5.1 Position to momentum calibration 98
3.7.5.2 Momentum to energy calibration 99
3.7.5.3 Excitation-energy spectra: ^{24}Mg and ^{26}Mg . . . 99
3.7.6 Double-differential cross sections 101

4 Results, analysis and discussion 115
4.1 Overview and description of measured (p,p′) data 115
4.2 Conversion to equivalent photo-absorption spectra and comparison with existing photo-absorption and photo-neutron data 119
4.2.1 Conversion of the measured (p,p′) spectra to (p,p$'_{\gamma\mathrm{corr}}$) spectra 119
4.2.1.1 Background subtraction in the region of the IVGDR 119
4.2.1.2 Virtual photon production 120
4.2.1.3 Application of the equivalent virtual photon method 121
4.2.2 A comparison of the (p,p$'_{\gamma\mathrm{corr}}$) and the (γ,abs) results . . 121
4.2.3 A comparison between the (p,p$'_{\gamma\mathrm{corr}}$) and the (γ,n) data near the neutron threshold 124

4.3 Fine structure of the IVGDR and comparison with theoretical predictions . . . 135
4.3.1 Results and Continuous Wavelet Transform analysis . . . 135
4.3.2 Isotones in the transitional region: ^{150}Nd and ^{152}Sm comparison . . . 146
4.4 General discussion of results . . . 149

5 Conclusions **152**

References **155**

Appendix A **163**

List of Figures

1.1 Distorted Wave Born Approximation (DWBA) calculation for the angular distribution of the various multipoles (all $T = 0$ except $L = 1$ multipole) for the reaction ^{208}Pb(p,p$'$) at $E_{\mathrm{p}} = 200$ MeV (taken from [Spe81]). It can be seen that the appropriate selection of the scattering angle determines the selection of the multipole. 2

1.2 Dependence of the GDR width and the modulus of the nuclear quadrupole deformation parameter on the number of neutrons in the nucleus. The experimentally measured GDR widths, Γ, are shown with circles. The β_2 values (left axis) are indicated with crosses. The curves are constructed for the purpose of better visualization: the solid line is the GDR width and the dashed line is the quadrupole deformation parameter. The neutron magic numbers, $N = 28, 50, 82, 126$ are shown with vertical lines [Ish11]. 4

1.3 Regions of deformed nuclei where the filled circles represent even-even nuclei, in which the ratio $E(4^+)/E(2^+) > 2.7$ where $E(4^+)$ and $E(2^+)$ are the energies of the first 4^+ state and first 2^+ state respectively. The line of β-stability is indicated by the thin long-dashed curve. The thin straight lines parallel to the x and y axes indicate the magic numbers of protons and neutrons, which are known in nuclei along the β-stability line [Ham12]. 5

1.4 A comparison of the variation of $E(4^+)/E(2^+)$ with respect to the neutron number N for the neodymium and samarium isotope chains where $E(4^+)$ and $E(2^+)$ are the energies of the first 4^+ state and first 2^+ state, respectively. Dashed lines with open symbols indicate transitions to unstable isotopes. 6

1.5 Total photo-absorption cross sections for the neodymium isotope chain where the Lorentzian line fits are shown (taken from [Mas06]). 7

1.6 Total photo-absorption cross sections for the doubly-even samarium isotopes, where the Lorentzian line fits are shown (taken from [Car74]). 8

2.1 A schematic representation of various giant resonance modes. . . 12

2.2 Schematic representation of electric multipole transitions between shell-model states of a hypothetical nucleus [Ber81]. . . 14

2.3 Systematics of the IVGDR excitation energy, width and sum rule depletion for many nuclei across the periodic table (taken from [Ber81]). 16

2.4 GDR width *versus* the modulus of the nuclear quadrupole deformation parameter, $|\beta_2|$, for medium and heavy nuclei (taken from [Ish11]). 17

2.5 Tools for exciting isovector non-spin-flip transitions. 19

2.6 A schematic representation of Coulomb excitation. 22

2.7 Virtual photon numbers per unit solid angle for $E1$ transitions in Coulomb excitation induced by 296 MeV protons on a ^{154}Sm target at $E_\gamma = 3$ MeV and 16 MeV where in blue: the semi-classical description and in red: the Eikonal description [Kru14]. 28

2.8 A vibrating nucleus with a spherical equilibrium shape [Kra88]. 30

2.9 The ratio $E(4^+)/E(2^+)$ for the lowest 2^+ and 4^+ states of even-even nuclei, where the lines connect sequences of isotopes [Kra88]. 31

2.10 Equilibrium shapes of nuclei with permanent deformations [Kra88]. 32

2.11 Standing waves in a spherical nucleus (a) and in a prolate deformed nucleus (b). 33

2.12 Theoretical representation of the dependence of the curve shape for the giant dipole resonance on the type of the nuclear shape [Mas06]. 34

2.13 A schematic representation of the contributions to the width of a nuclear giant resonance. 44

2.14 A schematic representation of the coupling to more and more complex states via the doorway mechanism [She05]. 45

2.15 The fine structure formation from a mixture of multiple scales of fluctuations [She05]. 45

2.16 A schematic representation of the most frequently used wavelet families. The real and complex parts of the complex Morlet wavelet are illustrated in solid and dashed lines, respectively [Jin14]. Further details regarding the Biorthogonal6.8 wavelet and its implementation can be found in [Kur14, Jin14]. 48

2.17 (a) The real part of the Complex Morlet wavelet and (b) the imaginary part of the Complex Morlet wavelet [Coo08]. 49

2.18 An overview of the principles involved in the wavelet analysis procedure [Ric05]. 51

3.1 A schematic overview of the cyclotron facility at iThemba LABS, where the enlarged section shows the position of the object slit 9X, the emittance slit 12X as well as the first clean up slit 1P. 55

3.2 A schematic overview of the K600 magnetic spectrometer. . . . 56

3.3 Pole-face current windings showing the dipole and quadrupole components of the K-coil as well as the dipole and hexapole components of the H-coil. 57

3.4 The K600 magnetic spectrometer focal plane detector package. . 59

3.5 A schematic overview of the K600 magnetic spectrometer in the zero-degree mode. 61

3.6 A comparison of the focal plane position spectrum acquired for the ^{27}Al(p,p$'$) reaction at $E_p = 200$ MeV using a 49 mm diameter collimator with an 11 mm thick brass lip (lower black line) to that of the position spectrum acquired without a collimator (upper red line). Note the large background peaks present in the spectrum without the collimator [Nev11a]. 66

3.7 The slight tapering of the 49 mm diameter, 11 mm thick entrance collimator. 66

3.8 An explanatory diagram illustrating the effect of the tapered lip. 67

3.9 A schematic representation of ion trajectories representing particles of different momenta under different matching conditions. The following scenarios are illustrated: (a) achromatic beam transportation where only focus matching is realised; (b) lateral dispersion matching is realised; and (c) both lateral and angular dispersion matching are realised [Fuj02]. 68

3.10 A schematic overview of a section of the iThemba LABS beamline where the red arrows indicate the locations of the beam attenuation meshes. 76

3.11 Left: The faint beam mesh which allows just 1/100th of the beam to pass through it and Right: the two beam meshes which collectively allow just 1/10000th of the beam to pass through them. 76

3.12 The x_{fp}-θ_{fp} image of the beam in the focal plane. The beam ellipses are shown for the cases where (a) focus matching, lateral dispersion matching and angular dispersion matching are realised; (b) only focus matching and lateral dispersion matching are realised; (c) only focus matching is realised and (d) none of the focus, lateral or angular dispersion matching conditions is realised [Fuj02]. 77

3.13 The faint beam image in the x_{fp}-θ_{fp} scatterplot for 200 MeV protons at iThemba LABS where (a) no dispersion matching techniques have been applied; (b) only focus matching has been achieved and (c) both focus and lateral dispersion matching have been achieved. 78

3.14 The pulse heights in paddle 1 plotted as a function of TOF values for the case where (top) a ^{144}Nd target was used and (bottom) no target was used. 81

3.15 The pulse heights in paddle 2 plotted as a function of TOF values for the case where (top) a ^{144}Nd target was used and (bottom) no target was used. 82

3.16 The energy loss in paddle 1 plotted as a function of the energy loss in paddle 2 for the case where (top) a ^{144}Nd target was used and (bottom) no target was used. Note that a TOF software gate has not been applied in either of these cases. 83

3.17 The two-dimensional resolution spectra indicating a need for LUT offsets in X1 and X2 (top) and the corrected spectra following the inclusion of LUT offsets (bottom). 85

3.18 A schematic representation of the trajectory associated with a charged particle intersecting the VDC resulting in an event. . . 86

3.19 A schematic representation of the effect of a look-up table offset. 86

3.20 The pepperpot collimator used during experiments at iThemba LABS. The first hole relative to the middle of the collimator on the x-axis/y-axis is centred at 0.819°, the second at 1.679° and the third at 2.251°. These holes span 0.41°. 90

3.21 A focal plane angle (θ_{fp}) pepperpot spectrum showing Gaussian fits to the observed peaks. 90

3.22 Graphs showing the conversion of focal plane angle (θ_{fp}) to scattering angle (θ_{scat}) for five pepperpot spectra with different focal plane positions. 91

3.23 Left: The slope as a function of focal plane position (x_{fp}). Right: The offset as a function of focal plane position (x_{fp}). 91

3.24 The ^{150}Nd double-differential cross section following angular calibration using U1 and U2 (top) and X1 and X2 (bottom). . . 93

3.25 The time-of-flight values for the detected particles plotted as a function of their focal plane position in the case where (top) a ^{144}Nd target was used and (bottom) no target was used. 104

3.26 Top: The y_{fp} projection of the focal plane events showing a total fit (in orange) as well as the fitted components, namely the events of interest (in blue), which sit on top of the background events (in red); Bottom: the two-dimensional x_{fp} *versus* y_{fp} scatterplot. 105

3.27 Top: The focal plane position spectrum showing the components involved in the background subtraction procedure, namely, the raw data (in black), the background components (in yellow and green) and the total background (in red). Bottom: A comparison of the raw data (in black) and the background subtracted data (in blue). 106

3.28 Top: A prominent excited state in a $\theta_{\rm scat}$-$x_{\rm fp}$ scatterplot with no lineshape correction applied; Bottom: a graph of the points used to reproduce the lineshape of the state shown in the upper panel with its associated fit and parameters. 107

3.29 The effect of lineshape correction. Top: $x_{\rm fp}$ *versus* $\theta_{\rm scat}$ with no lineshape correction applied; and Bottom: $x_{\rm fp}$ *versus* $\theta_{\rm scat}$, following a full lineshape correction. 108

3.30 The effect of lineshape correction. Top: The focal plane position spectrum with no lineshape correction applied; and Bottom: The focal plane position spectrum following a full lineshape correction. 109

3.31 The effect of position offsets on the resolution of the chained spectrum where (a) illustrates the case where the offsets have been neglected and (b) illustrates the effect of offset inclusion. . 110

3.32 The momentum calibration curves for each of the neodymium isotope groups as well as for the ^{152}Sm group. 111

3.33 An excitation-energy spectrum obtained for the ^{24}Mg(p,p$'$) reaction at iThemba LABS. 112

3.34 An excitation-energy spectrum obtained for the ^{26}Mg(p,p$'$) reaction at iThemba LABS. 113

3.35 A comparison between RCNP and iThemba LABS (iTL) data for the purposes of a broad structure comparison for the ^{24}Mg(p,p′) reaction (top) and for the ^{26}Mg(p,p′) reaction (bottom). 114

4.1 Experimentally obtained excitation energy spectra for ^{142,144,146,148,150}Nd(p,p′) and ^{152}Sm(p,p′) for $E_{\mathrm{p}} = 200$ MeV and $\theta_{\mathrm{Lab}} = 0^{\circ} - 1.91^{\circ}$. 117

4.2 Experimentally obtained double-differential cross sections for ^{142,144,146,148,150}Nd(p,p′) and ^{152}Sm(p,p′) for $E_{\mathrm{p}} = 200$ MeV and $\theta_{\mathrm{Lab}} = 0^{\circ} - 1.91^{\circ}$. 118

4.3 The IVGDR and ISGQR strengths as calculated for ^{142}Nd using standard DWBA [Pon15]. 125

4.4 An overview of the conversion process from ^{142}Nd(p,p′) to ^{142}Nd(p,p$'_{\gamma\mathrm{corr}}$). 126

4.5 An overview of the conversion process from ^{144}Nd(p,p′) to ^{144}Nd(p,p$'_{\gamma\mathrm{corr}}$). 126

4.6 An overview of the conversion process from ^{146}Nd(p,p′) to ^{146}Nd(p,p$'_{\gamma\mathrm{corr}}$). 127

4.7 An overview of the conversion process from ^{148}Nd(p,p′) to ^{148}Nd(p,p$'_{\gamma\mathrm{corr}}$). 127

4.8 An overview of the conversion process from ^{150}Nd(p,p′) to ^{150}Nd(p,p$'_{\gamma\mathrm{corr}}$). 128

4.9 An overview of the conversion process from ^{152}Sm(p,p′) to ^{152}Sm(p,p$'_{\gamma\mathrm{corr}}$). 128

4.10 An overview of virtual-gamma production functions for ^{142}Nd(p,p′) across the angular acceptance of the K600 Magnetic Spectrometer. 129

4.11 An overview of the average virtual-gamma production functions for Nd(p,p′) and ^{152}Sm(p,p′). 129

4.12 A direct comparison between the rebinned (and unnormalised) ^{142,144,146,148,150}Nd(p,p′$_{\gamma\mathrm{corr}}$) and ^{152}Sm(p,p′$_{\gamma\mathrm{corr}}$) spectra and the (γ, abs) data obtained by Carlos *et al.* [Car71, Car74]. 130

4.13 An overview of the comparison between the normalised ^{142,144,146,148,150}Nd(p,p′$_{\gamma\mathrm{corr}}$) and ^{152}Sm(p,p′$_{\gamma\mathrm{corr}}$) spectra and the (γ, abs) parametrisations [Cap09] (in orange). The $K = 0$ and $K = 1$ components (where applicable) have been plotted in green and blue, respectively. 132

4.14 An overview of the newly determined Lorentz parametrisations (in pink) that accurately describe the ^{142,144,146,148,150}Nd(p,p′$_{\gamma\mathrm{corr}}$) and ^{152}Sm(p,p′$_{\gamma\mathrm{corr}}$) spectra. The $K = 0$ and $K = 1$ components (where applicable) have been plotted in green and blue, respectively. 133

4.15 An overview of the comparison between the (p,p′$_{\gamma\mathrm{corr}}$) spectra and the (γ,n) data for the energy range near the neutron threshold for the ^{144,146,148}Nd and ^{152}Sm isotopes. 134

4.16 Overview of the cross sections obtained for ^{142,144,146,148,150}Nd(p,p′$_{\gamma\mathrm{corr}}$) and ^{152}Sm(p,p′$_{\gamma\mathrm{corr}}$) with $E_{\mathrm{p}} = 200$ MeV. 139

4.17 A complete overview of wavelet analysis and power spectra results for the experimental and SSRPA cases for ^{142}Nd. 140

4.18 A complete overview of wavelet analysis and power spectra results for the experimental and SSRPA cases for ^{144}Nd. 141

4.19 A complete overview of wavelet analysis and power spectra results for the experimental and SSRPA cases for ^{146}Nd. 142

4.20 A complete overview of wavelet analysis and power spectra results for the experimental and SSRPA cases for ^{148}Nd. 143

4.21 A complete overview of wavelet analysis and power spectra results for the experimental and SSRPA cases for ^{150}Nd. 144

4.22 A complete overview of wavelet analysis and power spectra results for the experimental and SSRPA cases for ^{152}Sm. 145

4.23 The result of the semblance analysis on the experimental ^{150}Nd(p,p$'_{\gamma\text{corr}}$) and ^{152}Sm(p,p$'_{\gamma\text{corr}}$) spectra. 147

4.24 The result of the semblance analysis on the theoretical ^{150}Nd and ^{152}Sm SSRPA predictions. 147

4.25 The result of the semblance analysis on the experimental ^{150}Nd(p,p$'_{\gamma\text{corr}}$) and the associated SSRPA prediction. 148

4.26 The result of the semblance analysis on the experimental ^{152}Sm(p,p$'_{\gamma\text{corr}}$) and the associated SSRPA prediction. 148

A.1 A schematic representation of the relationship between the incident particle ray 1 and the outgoing particle ray 2 relative to the central ray in the beamline and the spectrometer. 164

List of Tables

2.1 Multipole excitations as particle-hole excitations across major shells [Wou91, Har01]. 14

2.2 Summary of the main techniques used in the study of electric giant resonances [Spe81] where round brackets indicate weak excitation of the mode. 18

3.1 Technical specifications for the focal plane detector package . . . 58

3.2 A summary of the targets used in this study 63

3.3 A summary of the standard deviations (σ_{D}) and intrinsic FWHM position resolutions ($\mathrm{FWHM}_{\mathrm{pos}}$) of the X1, U1, X2 and U2 wireplanes, as calculated for a typical neodymium data file. 88

3.4 A comparison of the parameters obtained for the angular calibration by means of the X and U wireplanes. 92

3.5 A summary of the position (σ_{pos}) and energy (E_{res}) resolutions obtained for each of the ^{24}Mg (^{26}Mg) chains associated with the neodymium (samarium) isotopes. 98

3.6 A comparison of the position to momentum calibration parameters for the neodymium and samarium isotope groups. . 99

3.7 A comparison of the energy values for the excited states of ^{24}Mg obtained in this work and those provided by the NNDC [Fir07]. 100

3.8 A comparison of the energy values for the excited states of ^{26}Mg obtained in this work and those provided by the NNDC [End98]. 100

4.1 A comparison of the parametrisations for the present study's data and those provided in the literature for the neodymium data measured by Carlos et al. in 1971 [Car71], and those for the samarium data measured by Carlos et al. in 1974 [Car74]. Note that the superscript [a] indicates the parameters provided in [Car71], [b] indicates those provided in [Cap09] and [c] indicates those provided in [Car74]. A_T (where $A_T = 0.5\pi\sigma_1\Gamma_1$ for the spherical nuclei and $0.5\pi(\sigma_1\Gamma_1 + \sigma_2\Gamma_2)$ for the deformed nuclei) denotes the total area under the Lorentzian fits as calculated using the parameters given in the table for each isotope. 131

4.2 A comparison between the experimental and SSRPA Complex Morlet scales extracted for ^{142}Nd. Bold print indicates the presence of a clearly identifiable scale. 140

4.3 A comparison between the experimental and SSRPA Complex Morlet scales extracted for ^{144}Nd. Bold print indicates the presence of a clearly identifiable scale. 141

4.4 A comparison between the experimental and SSRPA Complex Morlet scales extracted for ^{146}Nd. Bold print indicates the presence of a clearly identifiable scale. 142

4.5 A comparison between the experimental and SSRPA Complex Morlet scales extracted for ^{148}Nd. Bold print indicates the presence of a clearly identifiable scale. 143

4.6 A comparison between the experimental and SSRPA Complex Morlet scales extracted for ^{150}Nd. Bold print indicates the presence of a clearly identifiable scale. 144

4.7 A comparison between the experimental and SSRPA Complex Morlet scales extracted for ^{152}Sm. Bold print indicates the presence of a clearly identifiable scale. 145

4.8 A comparison between the experimental complex Morlet scales extracted for ^{150}Nd(p,p$'_{\gamma\mathrm{corr}}$) and ^{152}Sm(p,p$'_{\gamma\mathrm{corr}}$). Bold font indicates the presence of a clearly identifiable scale. 149

4.9 A comparison between the complex Morlet scales extracted for ^{150}Nd and ^{152}Sm SSRPA predictions. Bold font indicates the presence of a clearly identifiable scale. 149

Chapter 1

Introduction

Collective excitations in quantum many-body systems such as atomic nuclei are a common occurrence. Typically, within this context, nuclear giant resonances are essentially a collective motion of many, if not all, particles in the nucleus [Har01]. In quantum-mechanical terms, they correspond to a transition between the ground state and the collective state, with strengths described by transition amplitudes. It is for this reason that nuclear giant resonances serve as a prime example of collective modes in the nucleus. A smooth mass-number dependence of the resonance parameters is characteristic of all nuclear giant resonances [Dro91] and, as such, a study into their properties yields information about the non-equilibrium dynamics and the bulk properties of the nucleus.

Bothe and Gentner [Bot37] first obtained evidence of a giant-resonance type of phenomenon in nuclei in 1937. Later, in 1944, the concept of a dipole oscillation was recognised by Migdal and eventually a systematic investigation of the giant resonance phenomenon was undertaken by Baldwin and Klaiber in 1947 [Har01]. The oldest and best known giant resonance is the Isovector Giant Dipole Resonance (IVGDR). This is owing to the high selectivity for IVGDR excitation by photo-absorption as well as the availability of appropriate Bremsstrahlung-producing electron accelerators in the 1950's [Har01]. The details of this resonance will be discussed in Chapter 2.

Although photo-absorption has been used most extensively to study the

IVGDR, direct nuclear reactions such as inelastic scattering are just as effective in the study of giant resonances in general provided that the appropriate scattering angle is selected [Spe81]. This concept is illustrated in Fig. 1.1 where it can be seen that the choice of scattering angle is sensitive to the multipole excited. An additional incentive for the use of inelastic scattering experiments such as (p,p′) stems from the observation that part of the continuum can be attributed to quasi-elastic scattering and, as such, the magnitude of the continuum relative to the resonance strength would be decreased [Spe81]. Later, in Chapter 2, the various techniques and probes used in the study of the IVGDR will be described in detail.

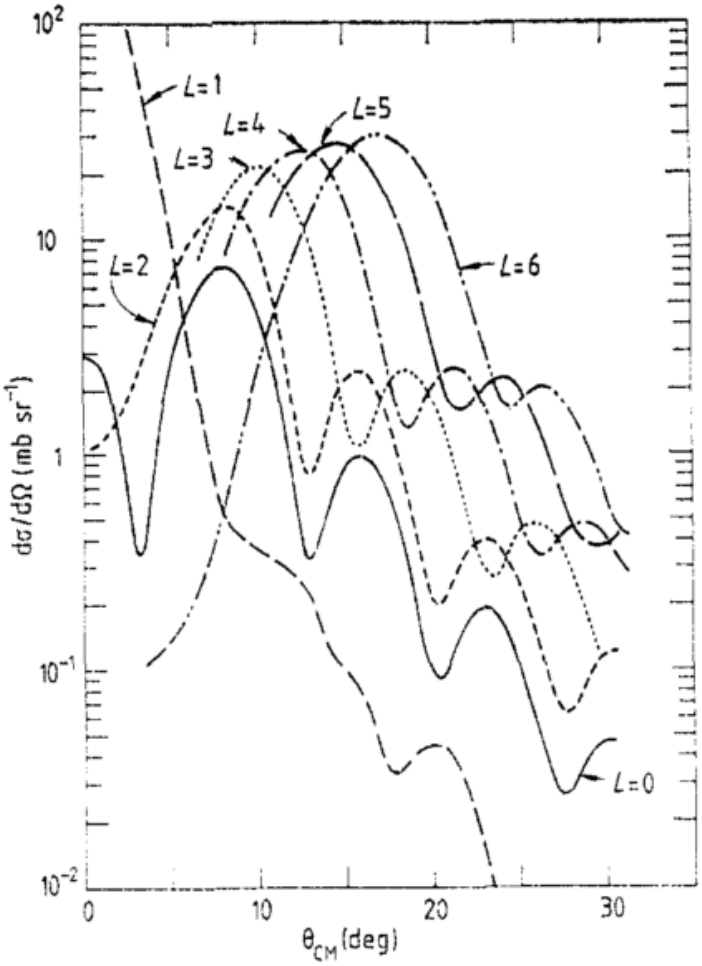


Figure 1.1: Distorted Wave Born Approximation (DWBA) calculation for the angular distribution of the various multipoles (all $T = 0$ except $L = 1$ multipole) for the reaction ^{208}Pb(p,p′) at $E_{\mathrm{p}} = 200$ MeV (taken from [Spe81]). It can be seen that the appropriate selection of the scattering angle determines the selection of the multipole.

An important feature of any giant resonance is its width, Γ, which arises from the combination of three major processes: the width of the direct decays of doorway one particle - one hole states, the width of the spread in energy of the doorway states, and the width of the decay of the doorway states into more complex two particle - two hole to n particle - n hole states [Kap15]. The width of the resonance is particularly noteworthy since it provides valuable information on the excitation and decay of the giant resonance. A number of open questions pertaining to the IVGDR in particular remain despite the fact that it is the most extensively studied case, both experimentally and theoretically [Har01]. One such question is that of the observed widths as a function of mass number showing strong fluctuations. It must be noted that the phenomenological collective models used in the study of giant resonances give a generally correct description of the $E1$ giant resonance. They are, however, not completely accurate since there are fundamental restrictions on them which are associated with neglecting the individual motion of the nucleons in a nucleus. Although the collective models allow for the processes owing to which the GDR arises to be clearly described and explained, and also provide an understanding of the coupling between dipole oscillations, nuclear surface vibrations and rotation, they do not, however, explain the nature of the change in the GDR width [Mas06]. Such shortcomings can be addressed in an analysis of the fine structure of the resonance thus providing new information about this problem and allowing for stringent model tests. It can, therefore, be concluded that the IVGDR provides the ideal test case in which the interplay of all of the major damping mechanisms can be investigated.

Related to the width of the resonance is the nuclear deformation parameter and, consequently, the shape of the giant resonance [Ish11]. Figure 1.2 displays the dependence of the GDR width Γ and the nuclear deformation parameter on the number of neutrons in the nucleus. As can be seen, for heavy spherical nuclei with $N = 82$, the GDR occurs in the form of a narrow, single peak. Since the GDR in this region is almost completely collectivised, no configurational splitting of the resonance occurs [Ish11]. Slight deformations with increasing N result merely in an increase in the GDR width, whereas the strong deformations result in the splitting of the GDR into two distinct components [Ish11].

In the early 1950's, the discovery was made that some nuclei are deformed in

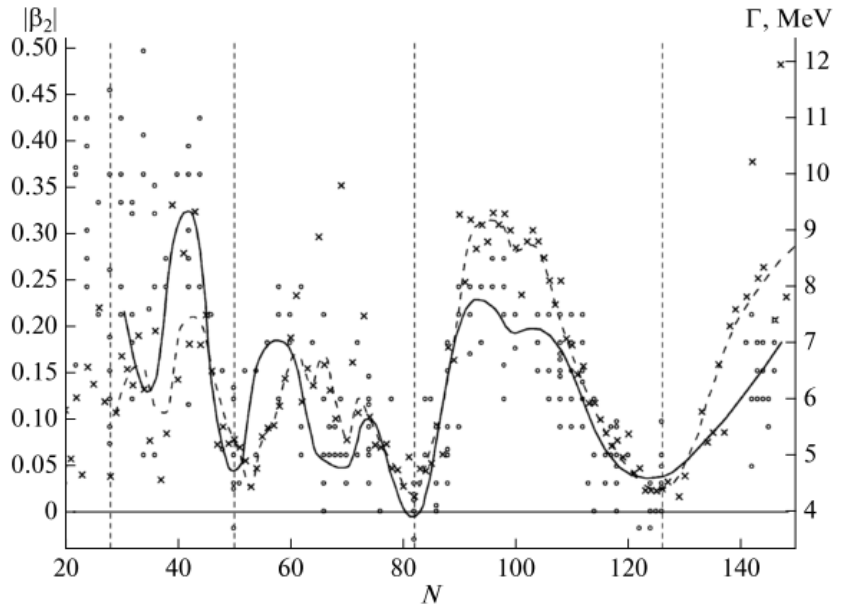


Figure 1.2: Dependence of the GDR width and the modulus of the nuclear quadrupole deformation parameter on the number of neutrons in the nucleus. The experimentally measured GDR widths, Γ, are shown with circles. The β_2 values (left axis) are indicated with crosses. The curves are constructed for the purpose of better visualization: the solid line is the GDR width and the dashed line is the quadrupole deformation parameter. The neutron magic numbers, $N = 28, 50, 82, 126$ are shown with vertical lines [Ish11].

their ground states. Research in this area has focussed primarily on the rare-earth (for which $82 < N < 120$) and actinide regions since a large number of deformed nuclei are located near or on the line of beta-stability in these regions, as can be seen in Fig. 1.3. These regions are, as a result, easily experimentally accessible [Ben84]. The increased permanent deformation of the ground state with increasing neutron number, N, is typified by the even-even neodymium and samarium isotope chains. This is shown by the ratio $E(4^+)/E(2^+)$ in Fig. 1.4. As will be explained in detail in Section 2.3.1.1 of Chapter 2, the ratio $E(4^+)/E(2^+)$ is a useful method for determining the extent of nuclear deformation in a nucleus. Figure 1.4 separates both of the neodymium and samarium isotope chains into three regions, namely, the quasi-spherical region, the transitional region and the deformed region. It is the transitional region that is of most interest as this region is comprised of nuclei that alter the properties of nuclear surfaces dramatically. In the range where the neutron number varies from 88 to 92 there is essentially a phase transition from a

spherical vibrator (or non-deformed spherical nucleus) to an axial rotator (or deformed nucleus) [Opr12].

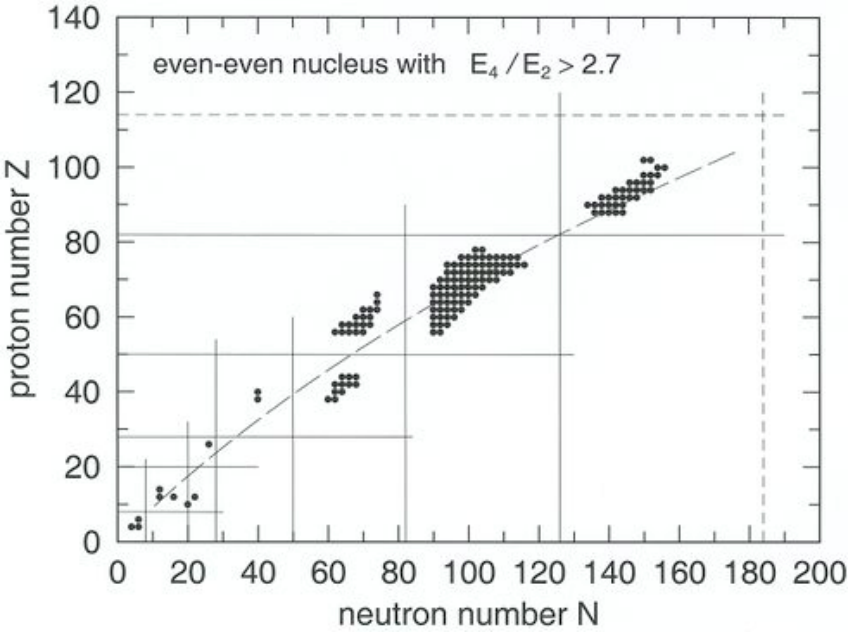


Figure 1.3: Regions of deformed nuclei where the filled circles represent even-even nuclei, in which the ratio $E(4^+)/E(2^+) > 2.7$ where $E(4^+)$ and $E(2^+)$ are the energies of the first 4^+ state and first 2^+ state respectively. The line of β-stability is indicated by the thin long-dashed curve. The thin straight lines parallel to the x and y axes indicate the magic numbers of protons and neutrons, which are known in nuclei along the β-stability line [Ham12].

The evolution of the IVGDR shape is clearly illustrated in Fig. 1.5, which displays the results of the photo-absorption experiments performed by Carlos *et al.* [Car71] on the neodymium isotope chain. The nucleus ^{142}Nd is almost spherical and, as such, has an IVGDR that is relatively narrow and single-peaked. Noting that the deformation parameter increases as mass number increases from ^{142}Nd to ^{150}Nd, the IVGDR gets progressively broader and for the ^{150}Nd isotope (a permanently-deformed nucleus), a double-peaked shape is observed. The anisotropic properties exhibited by deformed nuclei, that is, the dependence of their electric characteristics on the orientation of a nucleus with respect to an external field, have been proven experimentally.

The even-even samarium isotope chain was studied by Carlos *et al.* [Car74] in 1974, illustrating the evolution of the IVGDR shape in the transition from quasi-spherical to permanently deformed nuclei. The total photo-absorption

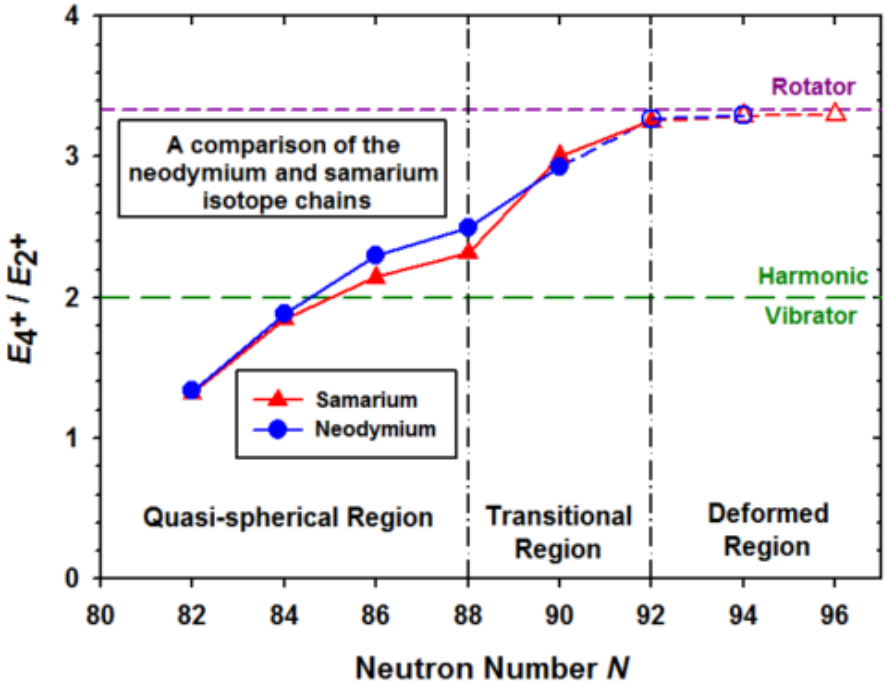


Figure 1.4: A comparison of the variation of $E(4^+)/E(2^+)$ with respect to the neutron number N for the neodymium and samarium isotope chains where $E(4^+)$ and $E(2^+)$ are the energies of the first 4^+ state and first 2^+ state, respectively. Dashed lines with open symbols indicate transitions to unstable isotopes.

cross sections measured by Carlos *et al.* [Car74] for the ^{144,148,150,152,154}Sm chain are provided in Fig. 1.6. As expected, the resonances for the quasi-spherical nuclei, namely ^{144}Sm, ^{148}Sm and ^{150}Sm are single-peaked whereas there is observed splitting in the ^{152}Sm and ^{154}Sm resonances, which is indicative of a prolate deformed nucleus [Car74]. The two components of the split resonances correspond to the vibrations along the shorter a-axis of the prolate deformed nucleus and the longer b-axis of symmetry perpendicular to it. The vibrations along the longer b-axis of the prolate ellipsoid are characterised by lower frequencies than those along the shorter a-axis resulting in the splitting of the GDR into two distinct components [Ish11]. The splitting of the giant dipole resonance in deformed nuclei and the reasons therefor as well as the effect on the GDR shape will be discussed in detail in Section 2.3.1.2 of Chapter 2.

It is important to note that the energy-resolution for both the neodymium and samarium photo-absorption data is low. It was reported by Carlos *et*

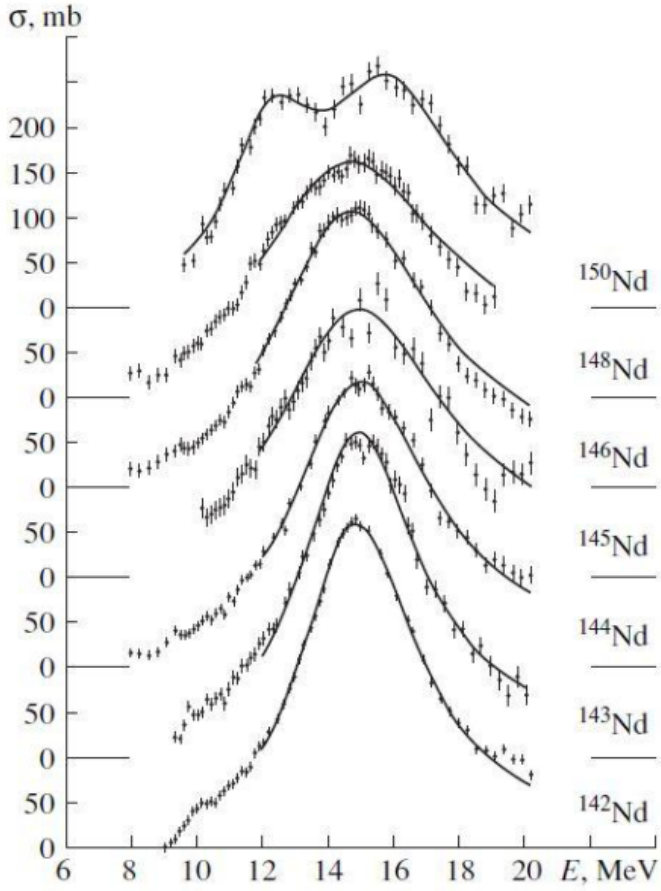


Figure 1.5: Total photo-absorption cross sections for the neodymium isotope chain where the Lorentzian line fits are shown (taken from [Mas06]).

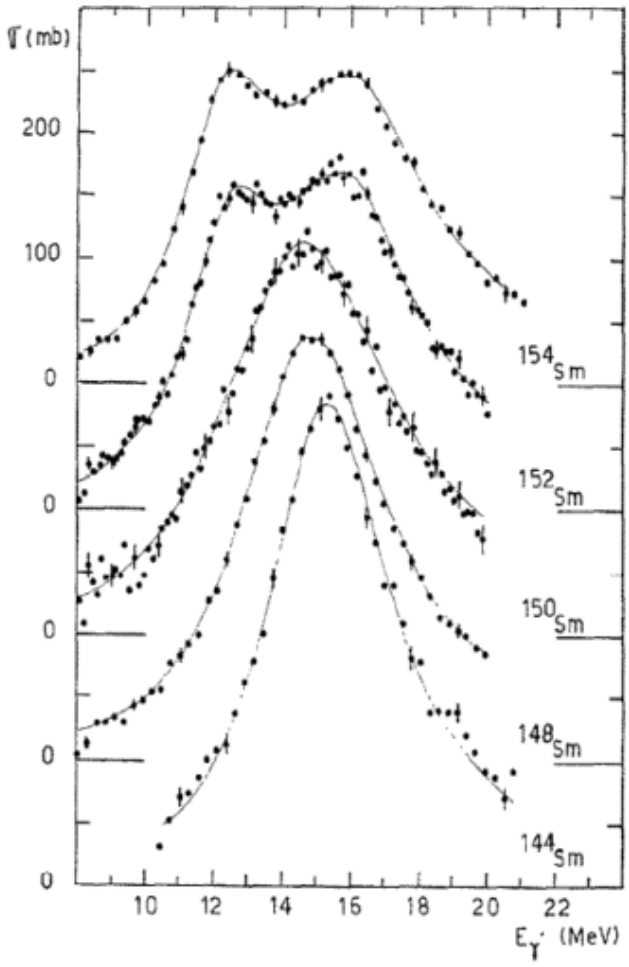


Figure 1.6: Total photo-absorption cross sections for the doubly-even samarium isotopes, where the Lorentzian line fits are shown (taken from [Car74]).

al. [Car71, Car74] that the width of the quasi-monochromatic γ-ray beam, which was obtained from the annihilation in flight of monochromatic positons was approximately 300 keV. Not only did the present study seek to investigate the shape evolution of the IVGDR from spherical to deformed nuclei in the rare-earth region and investigate the reproducibility of the photo-absorption results, but it also aimed to study the fine structure of the IVGDR. Previous high energy-resolution studies [She04, She09, Usm11a, Usm11b, Jin14] for medium-mass through to heavy-mass nuclei have established the global existence of fine structure in giant resonances and have succeeded in the interpretation of the resonance width, Γ. In order to facilitate the fine structure investigations, high energy-resolution inelastic proton scattering experiments using the Zero-degree Facility of the K600 Magnetic Spectrometer of iThemba Laboratory for Accelerator Based Sciences (iThemba LABS) were selected for the present study. In particular, the even-even ^{142,144,146,148,150}Nd chain as well as one samarium isotope, ^{152}Sm, were chosen. The study included ^{152}Sm since a comparison can easily be made between ^{150}Nd and ^{152}Sm, which are isotones of comparable deformation in the transitional region, as can be seen in Fig. 1.4. This was motivated in order to provide further insight into the nature of the transition region itself and could allow for an investigation into the change in characteristic energy scales in the region where the onset of deformation is seen. Studying the ^{152}Sm isotope in conjunction with the neodymium isotope chain could also allow for the influence of the proton number, Z, on the fine structure of the IVGDR as a function of nuclear deformation to be investigated.

The layout of this thesis is as follows:

Chapter 2 provides a detailed overview of the necessary theoretical considerations in the study of nuclear giant resonances with a focus on the Isovector Giant Dipole Resonance (IVGDR). The tools used in the excitation of the IVGDR as well as the properties of the IVGDR are discussed. A detailed account of Coulomb excitation, which includes both the semi-classical and Eikonal descriptions is provided. Also presented, are the theoretical models which are applicable in the study of the transition from spherical to deformed nuclei. In addition, the methods used in the extraction of characteristic energy scales are discussed with emphasis on the continuous

wavelet transform analysis technique.

Chapter 3 contains experimental details such as the equipment used for the beam delivery and data acquisition. Specific focus is placed on dispersion matching as well as on the offline data-extraction procedure.

Chapter 4 provides an overview of the experimental data as well as the theoretically predicted results and details their analyses, comparisons and associated discussions.

Chapter 5 presents the conclusions that can be drawn from the present study.

Chapter 2

Theoretical considerations

This chapter outlines the relevant theoretical considerations for this study. A general description of nuclear giant resonances is provided with specific focus on the Isovector Giant Dipole Resonance (IVGDR) and its properties. Also contained in this chapter are the theoretical descriptions of Coulomb excitation as well as details regarding the model predictions of giant resonance behaviour.

2.1 Basic concepts of giant resonances

Giant resonances have a collective nature since an appreciable fraction of nucleons in the nucleus participate simultaneously in the vibration [Eji99]. The extent of the collective motion is such that the modes of excitation may be likened to the oscillation of a liquid drop if it is studied in hydrodynamic terms [Har01]. Figure 2.1 shows a schematic representation of various giant resonance modes where each mode is identified by the angular momentum transfer L, the spin excitation ΔS and the isospin excitation ΔT. The monopole mode, for which $L = 0\hbar$, is a spherically symmetric oscillation (or compression) of the nucleus whereas the $L = 1\hbar$ or dipole mode is a motion during which the nucleons oscillate en masse against one another. An oscillation of the spherical nucleus to an oblate shape and then to a prolate shape characterises the quadrupole mode with $L = 2\hbar$. Isoscalar modes (denoted by $\Delta T = 0$) are those modes in which the protons and neutrons

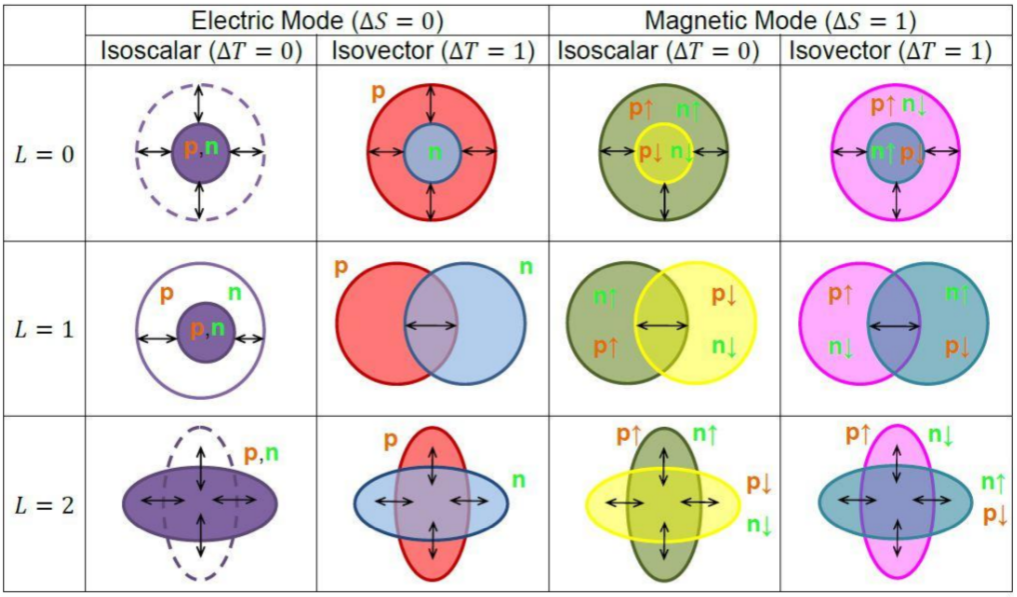


Figure 2.1: A schematic representation of various giant resonance modes.

oscillate in phase, i.e. they are modes without isospin excitation. Isovector modes (denoted by $\Delta T = 1$) are those modes in which the protons and neutrons oscillate out of phase with one another, i.e. they are the modes associated with isospin excitation [Eji99]. The isovector oscillations will be at higher excitation energies than those of the isoscalar modes for the same multiplicity. This is as a result of the additional energy that is required to separate the proton and neutron distributions [Wou91]. The electric $\Delta S = 0$ modes are the modes in which the spin-up and spin-down nucleons oscillate in phase [Har01]. The magnetic isoscalar mode, for which $\Delta S = 1$ and $\Delta T = 0$, is characterised by the oscillation of the nucleons with spin-up against those with spin-down. In the case of the isovector mode, for which $\Delta T = 1$, the neutrons with spin-up oscillate against the protons with spin-down and *vice-versa* [Wou91]. The magnetic modes are thus those modes associated with spin excitation [Eji99]. It should be noted that the $\Delta T = 0$, $L = 1\hbar$ mode has been included in Fig. 2.1 for completeness but it is not considered an intrinsic excitation of the nucleus since it is essentially an oscillation of the entire nucleus as a whole [Wou91]. Also included is the $\Delta T = 0$, $L = 0\hbar$ mode, which is referred to as the breathing mode. It involves the radial expansion and contraction of the nucleus such that its form is maintained but its volume changes [Ber09].

Sum rules provide an estimate of the total photo-absorption cross section that can be expected for a mode with particular L, T and S values [Ber09]. This total transition strength is the sum over all transitions from the initial state. The Energy-Weighted Sum Rule (EWSR) is particularly useful to describe giant resonance strength since it is nearly model independent. To be considered collective, a transition must have a transition rate that is appreciably (≥ 10 times) higher than the single particle value and should exhaust a substantial fraction of the EWSR for the mode under investigation [Ber81].

Giant resonances can be described microscopically as the coherent superposition of particle-hole excitations following the action of an electromagnetic operator on the ground state [Wou91]. This can be expressed mathematically as [Har01]:

$$|\Psi_{\mathrm{GR}}^{\lambda,\sigma,\tau}\rangle = O^{\lambda,\sigma,\tau}|\Psi_{\mathrm{g.s.}}\rangle \ , \tag{2.1}$$

where λ, σ and τ refer to the multipolarity, spin and isospin of the resonance, respectively.

An example of one such operator is given for the electric isoscalar transitions as:

$$O_{\mu}^{\lambda,0,0} = \sum_{i=1}^{\mathrm{A}} r_i^{\lambda} Y_{\lambda\mu}\left(\Omega_i\right) \quad \lambda \geq 2 \ , \tag{2.2}$$

where the summation runs over all nucleons i. Figure 2.2 illustrates the shell-model picture that must be considered in order to understand the qualitative features of giant resonances [Har01]. In this model, the major shells, which are denoted by $N, N+1, N+2...$, are separated by an energy $\Delta E + \Delta N \times 1\hbar\omega$ or $\Delta N \times 41A^{-1/3}$ MeV and the parity of the single particle wave function in subsequent shells is alternating. The only transitions that can be induced by the operator $O_{\mu}^{\lambda,0,0}$ are those with $\Delta N \leq \lambda$. Owing to parity conservation, odd transitions require $\Delta N = 1, 3, \ldots$ whereas $\Delta N = 0, 2, 4, \ldots$ is required for even transitions [Wou91]. In this way, the scheme displayed in Table 2.1 is obtained.

Table 2.1: Multipole excitations as particle-hole excitations across major shells [Wou91, Har01].

Monopole	$\lambda = 0$			$2\hbar\omega$		
Dipole	$\lambda = 1$		$1\hbar\omega$			
Quadrupole	$\lambda = 2$	$0\hbar\omega$		$2\hbar\omega$		
Octupole	$\lambda = 3$		$1\hbar\omega$		$3\hbar\omega$	
Hexadecapole	$\lambda = 4$	$0\hbar\omega$		$2\hbar\omega$		$4\hbar\omega$

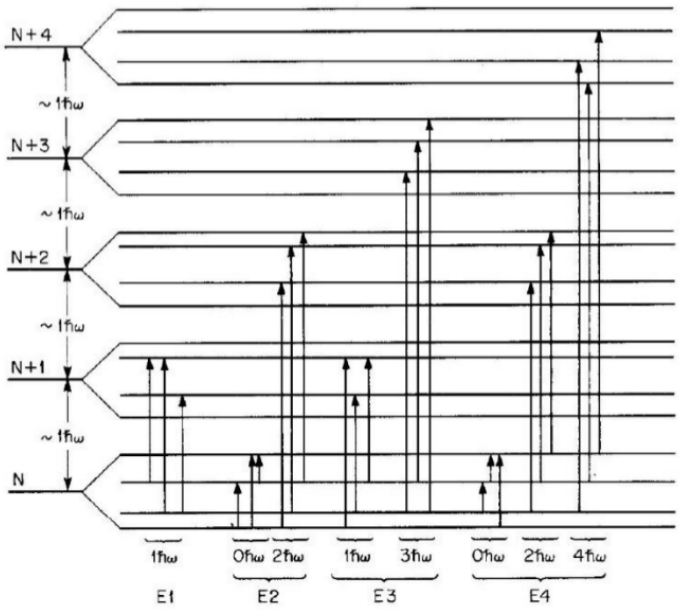


Figure 2.2: Schematic representation of electric multipole transitions between shell-model states of a hypothetical nucleus [Ber81].

A residual particle-hole interaction results in the formation of a collective state, which is simply a coherent superposition of all possible particle-hole states of a given multipolarity and parity. All of the transition strengths are absorbed by this collective state [Har01]. In other words, the collective state exhausts the sum rule. The residual particle-hole interaction is repulsive for isovector excitations so, in the case of the IVGDR, the resonance will be found above the corresponding unperturbed energies $\Delta N \times 41A^{-1/3}$ MeV. The isoscalar resonances, however, will be found below these unperturbed energies.

2.2 Isovector Giant Dipole Resonance

2.2.1 Overview

The Isovector Giant Dipole Resonance (IVGDR) is excited by means of a transmission of 1 unit of angular momentum to the nucleus, hence $\Delta L = 1$. In an even-even nucleus, this will result in a $J^\pi = 1^-$ excited state following the excitation of a $J^\pi = 0^+$ ground state. In this particular interaction, the isospin is also altered by 1 unit ($\Delta T = 1$) and hence it is termed an isovector resonance [Ber09]. Since giant resonances can be considered as a result of transitions of nucleons from one major shell to another, it is important to note that a nucleon can be excited by at most $L\,\hbar\omega$ in the interaction for inelastic scattering [Ber81]. The IVGDR is thus built up of $E1$ transitions spanning $1\,\hbar\omega$. As was discussed in [Ber81], one might expect the IVGDR to be located at an excitation energy of $\approx 41A^{-1/3}$ MeV. It has been found, however, that it is located at $\approx 77A^{-1/3}$ MeV. The discrepancy is as a result of the nucleon-nucleon interaction being dependent on spin and isospin, which ensures that the $\Delta S = \Delta T = 0$ collective states move down in energy and that $\Delta S = 1$ or $\Delta T = 1$ states move up from the expected energy [Ber81].

Photo-nuclear measurements have been used to study the GDR in many nuclei across the periodic table [Ber81]. The measured photo-absorption cross section has been found to exhibit a substantial bump structure with its centroid between $10 - 20$ MeV excitation energy depending on the mass number of the target [Eji99]. Figure 2.3 shows the systematics of the IVGDR excitation energy (E_x) plotted as $E_\mathrm{x}A^{1/3}$ MeV, width and sum rule depletion for many nuclei spanning the periodic table. As can be seen, the width of the IVGDR is narrowest near the doubly-magic nuclei shell closures ($A = 90, 144, 208$) and widest for light and deformed nuclei (e.g. rare-earth nuclei). A few characteristics of giant resonances have been established from these systematics and are summarised as follows:

- giant resonances are general properties of nuclei,
- over most of the nuclear mass range, the excitation energy of a giant resonance varies smoothly with mass,
- giant resonances exhaust an appreciable fraction of an appropriate sum

rule and

- giant resonance strength is generally localised in excitation energy.

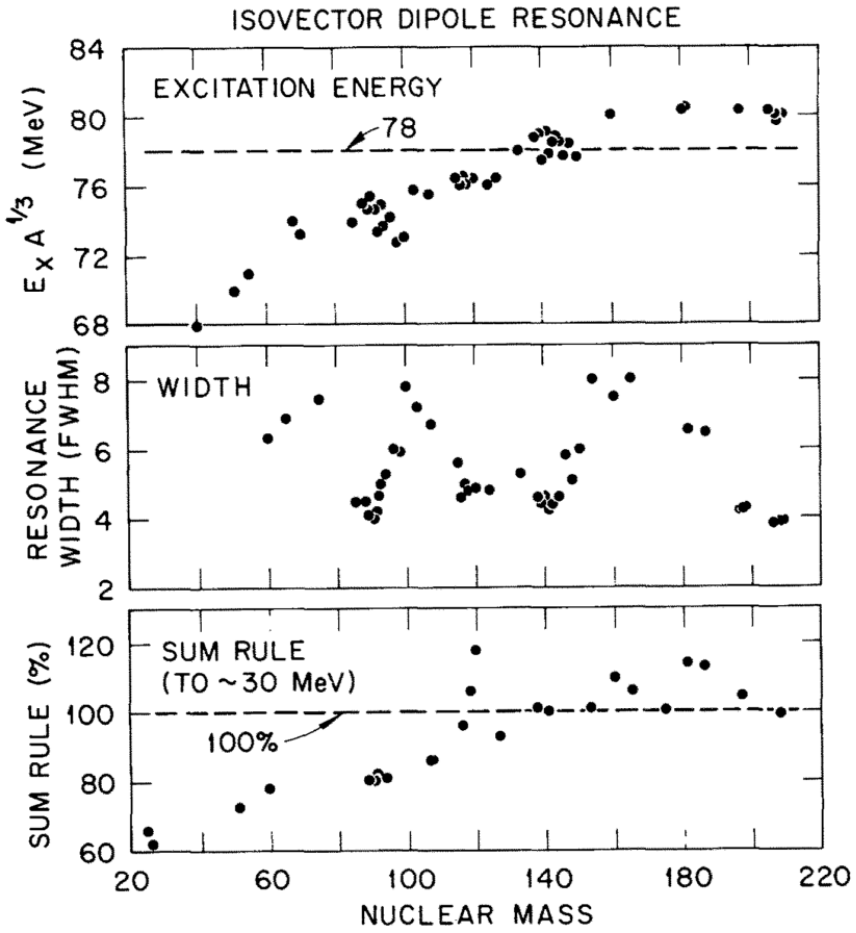


Figure 2.3: Systematics of the IVGDR excitation energy, width and sum rule depletion for many nuclei across the periodic table (taken from [Ber81]).

It has also been shown that there is a correlation between the width, Γ, of the IVGDR and the value of the nuclear deformation parameter as can be seen in Fig. 2.4. For low values of the deformation parameter ($\beta_2 < 0.1$), the width of the GDR is at a minimum ($\Gamma \approx 4\,\text{MeV}$). The width increases to values over 7 MeV as the deformation parameter increases. The effect of the nuclear deformation on the shape of the IVGDR is discussed in Section 2.3.1.2.

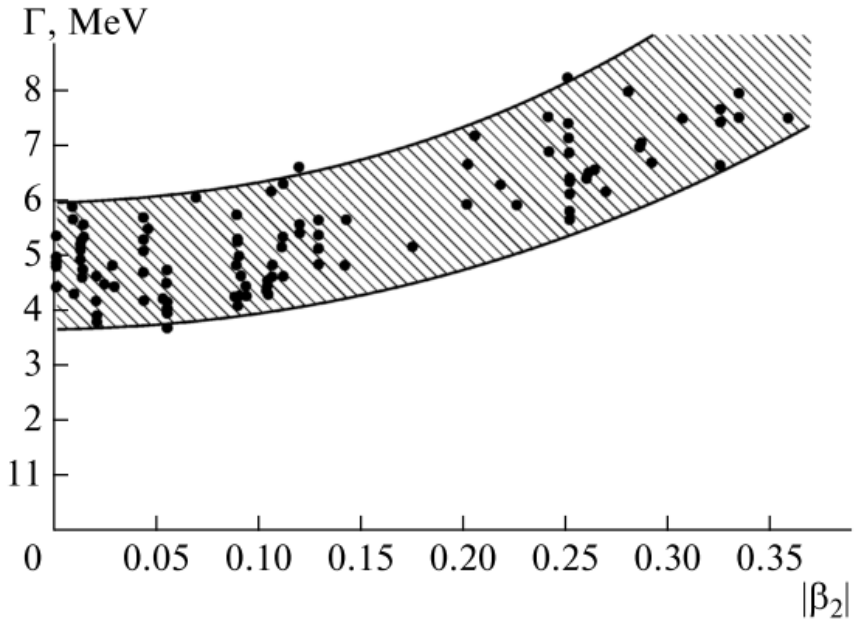


Figure 2.4: GDR width *versus* the modulus of the nuclear quadrupole deformation parameter, $|\beta_2|$, for medium and heavy nuclei (taken from [Ish11]).

2.2.2 Techniques for IVGDR excitation

Giant resonances of different multipolarities are often not energetically well-separated [Goe82]. The $2\hbar\omega$ isoscalar giant quadrupole resonance, for example, with $\Delta L = 2$ and $\Delta T = \Delta S = 0$ is located at nearly the same excitation energy as the $1\hbar\omega$ isovector giant dipole resonance, which has $\Delta L = \Delta T = 1$ and $\Delta S = 0$. This presents a distinct challenge in the study of giant resonances and in the analysis of the experimentally obtained data. In order to disentangle these resonances, specific probes that excite only one type of resonance should be considered. An example of this is the use of photo-absorption reactions [Har01] or of direct reactions such as inelastic scattering [Ber81] to excite the IVGDR specifically.

Table 2.2 provides a summary of the main techniques used in the study of giant resonances. All of these techniques are used to examine the properties of giant resonances that are built on nuclear ground states. That is, all of the excitation energy which is transferred to the nucleus contributes directly to the giant resonance [Sno86]. Both the strong (nuclear) and the

electromagnetic interactions are effective in giant resonance excitation but the weak interaction, although possible, has never been used owing to the small cross sections involved [Har01]. The study of the isovector resonances in particular necessitates a probe which has the ability to discriminate between the protons and the neutrons in the nucleus [Wou91]. An overview of the techniques used for the excitation of isovector non-spin-flip transitions is provided in Fig. 2.5. These techniques will be discussed in more detail in the subsequent sections.

Table 2.2: Summary of the main techniques used in the study of electric giant resonances [Spe81] where round brackets indicate weak excitation of the mode.

		$E0$		$E1$	$\geq E2$	
		$T=0$	$T=1$	$T=1$	$T=0$	$T=1$
Electromagnetic interaction	γ-absorption (γ,n), (γ,f), ...			+	(+)	(+)
	Radiative capture (p,γ)			+		+
	(α,γ)			+	+	
	Inelastic electron scattering (e,e′)	+	+	+	+	+
Strong interaction	Inelastic hadron scattering (p,p′)	+	(+)	(+)	+	(+)
	(d,d′)	+			+	
	(^{3}He,^{3}He′)	+	((+))	((+))	+	((+))
	(^{4}He,^{4}He′)	+			+	
	(heavy ion)				+	
	Decay experiments (α,α'c)	+			+	

2.2.2.1 Gamma-absorption: real photons

Gamma-absorption excites $\Delta T = \Delta L = 1$ excitations almost exclusively for $(kR)^2 \ll 1$ where the wave number $k \approx E_\gamma$ (MeV)(200 fm^{-1}). The IVGDR

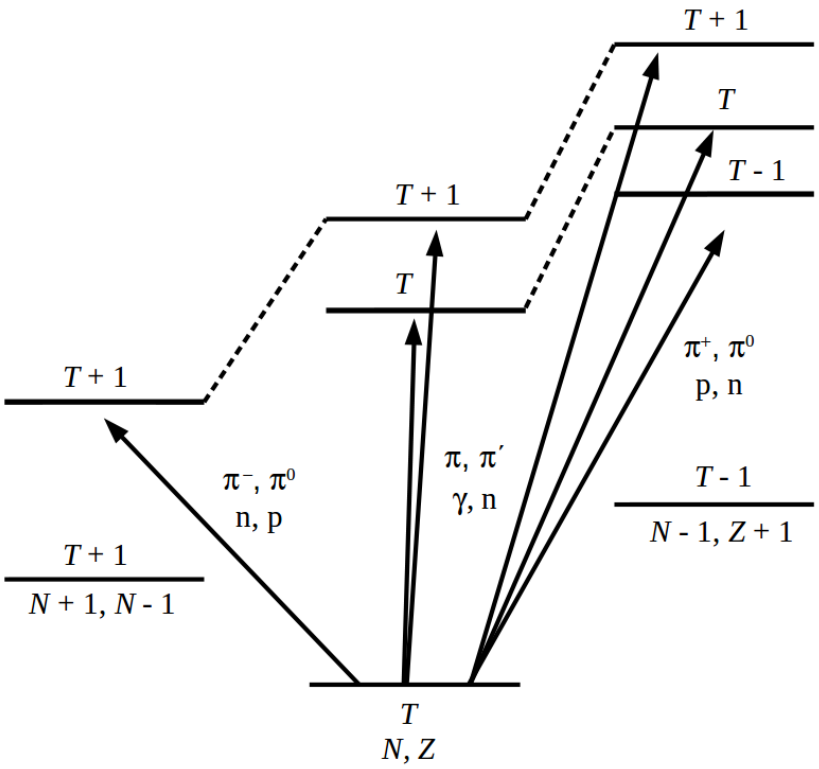


Figure 2.5: Tools for exciting isovector non-spin-flip transitions.

has $E_\gamma = 15$ MeV [Har01], which makes γ-absorption the ideal tool for IVGDR investigations [Wou91].

Beams of γ-rays, however, exist only as secondary beams and their production is thus an experimental challenge. When a high-intensity electron beam strikes a target of high-Z it decelerates in the nuclear electric field and the resultant loss in energy manifests as a γ-quantum [Har01]. The photon spectrum that results has an approximate dE_γ/E_γ dependence with the photon energy E_γ. This is the bremsstrahlung process which is used for the production of the γ-ray beams.

Originally, a step by step increase of the beam energy allowed for the shape of the resonance to be determined [Har01]. A more modern approach involves the use of tagged photons. Here, the γ-quantum energy is found through the measurement of the residual energy of the electron (which gave rise to the production of the γ-quantum through the above-described bremsstrahlung process) in coincidence with the γ-quantum itself [Wou91]. The photon-flux is low in these experiments but this can be compensated for through the use of

thick targets (several gcm^{-2}) [Har01].

Annihilation in flight is another technique used in the production of monochromatic γ-ray beams. In this method, a beam of fast positrons impinges on a thin, low-Z target with the result being the production of a monoenergetic beam of annihilation photons in the forward direction [Ber75].

The total photo-absorption cross section is obtained through the measurement of all of the important partial cross sections:

$$\sigma(\gamma) = \sigma(\gamma, \gamma') + \sigma(\gamma, \mathrm{n}) + \sigma(\gamma, 2\mathrm{n}) + \sigma(\gamma, \mathrm{p}) + \dots \ . \tag{2.3}$$

This is necessary in order for the nuclear processes to be distinguished from the atomic interactions [Wou91]. The IVGDR is located well above the particle emission threshold for all nuclei and, as a result, particle emission is far more likely than γ-emission. The $\sigma(\gamma, \gamma')$ contribution to $\sigma(\gamma)$ is thus low. Additionally, any significant charged-particle decay in medium- and heavy-mass nuclei is prevented by the Coulomb barrier [Spe81]. The $\sigma(\gamma, \mathrm{p})$ contribution is, thus, also small for heavy nuclei. In experiments on medium- and heavy-mass nuclei, therefore, $\sigma(\gamma)$ can be obtained by measuring the neutron yield as a function of γ-energy. That is, the (γ, n) contribution. In the cases where $E_\gamma > E_{2\mathrm{n}}$ (the two-neutron emission threshold), the $(\gamma, 2\mathrm{n})$ contribution must be included [Spe81]. In the same way, for actinide nuclei, the fission contribution $\sigma(\gamma, \mathrm{f})$ must be considered. Note that in the case of light nuclei, $\sigma(\gamma, \mathrm{p})$ contributes more significantly and cannot be ignored [Har01].

2.2.2.2 Radiative capture

Radiative capture reactions (n, γ), (p, γ) or (α, γ) are, by detailed balance, the inverses of the associated photo-nuclear reactions. That is, in the γ-induced interaction $(\gamma + \mathrm{A} \rightarrow x + \mathrm{B})$ the particle x populates final states in nucleus B whereas in the radiative capture reactions $(x + \mathrm{B} \rightarrow \gamma + \mathrm{A})$, the final states in nucleus A are populated [Har01]. The advantage of this technique is that

precise excitation functions are measurable but the disadvantage is that only a part of $\sigma(\gamma)$ is measured [Spe81].

2.2.2.3 Coulomb excitation: absorption of virtual photons

Coulomb excitation is the term used when describing inelastic Coulomb scattering. Here, the interaction of the target nucleus with the projectile leaves the target nucleus in an excited state. This is followed by rapid decay to the ground state via γ-ray emission, which is why Coulomb excitation can be conceptualised as the emission and absorption of virtual photons. The possibility exists that the projectile may also be left in an excited state but this is not usual [Kra88]. Since Coulomb excitation can occur at energies much lower than those required to overcome the Coulomb barrier, the projectile and target remain far enough apart such that the finite-range nuclear interaction is excluded [Cli86]. This remains the case for inelastic scattering at and close to zero-degrees for all incident projectile energies, including well above the Coulomb barrier.

Inelastic scattering is effective in the strong excitation of low-lying collective states and so, it is not unreasonable to assume that it would excite high-lying collective states of similar modes. In the specific case of the GDR, inelastic electron scattering has been used [Ber81]. This particular reaction mechanism is well known but the selectivity of the reaction is fairly low. A solution to this is the use of hadrons (such as protons, for example) as projectiles as it provides greater variety for the reactions and as a result, greater selectivity. The reason for this is that the interaction between a nucleon in the projectile and a nucleon in the target is both spin and isospin dependent [Ber81]. Various hadronic probes produce different strengths of the four components of an interaction. As can be seen in Table 2.2, the (p,p′) reaction can excite all four terms but will excite the $\Delta T = \Delta S = 0$ term particularly strongly whereas inelastic α-particle scattering will only excite the $\Delta T = \Delta S = 0$ term [Usm07].

The probability of giant resonance excitation through the Coulomb interaction has been calculated in the semi-classical approximation [Ber88, Win79] as well as in the Eikonal approximation [Ber93]. These approaches will be discussed in detail in Sections 2.2.3.1 and 2.2.3.3, respectively.

2.2.3 Theoretical descriptions of Coulomb excitation

Classically, as can be seen in Fig. 2.6, the projectile approaches the target nucleus along a straight line that would pass a distance b from the nucleus in the case of no repulsive force being present. This distance b is the impact parameter. Coulomb excitation dominates for $b \geq r_c = R_P + R_T$ where R_P and R_T are the projectile radius and target radius, respectively. For a value of r_c selected in this way, the nuclear interaction is negligible [Har01]. Assuming a hyperbolic path is followed by the projectile in the Coulomb field of the target, and with a simple calculation of the scattering angle, θ, the Rutherford differential cross section can be obtained as:

$$\frac{d\sigma_{\mathrm{Ru}}}{d\Omega} = \left(\frac{Z_P Z_T e^2}{4\pi\epsilon_0 E}\right) \mathrm{cosec}^4\left(\frac{\theta}{2}\right) \quad . \tag{2.4}$$

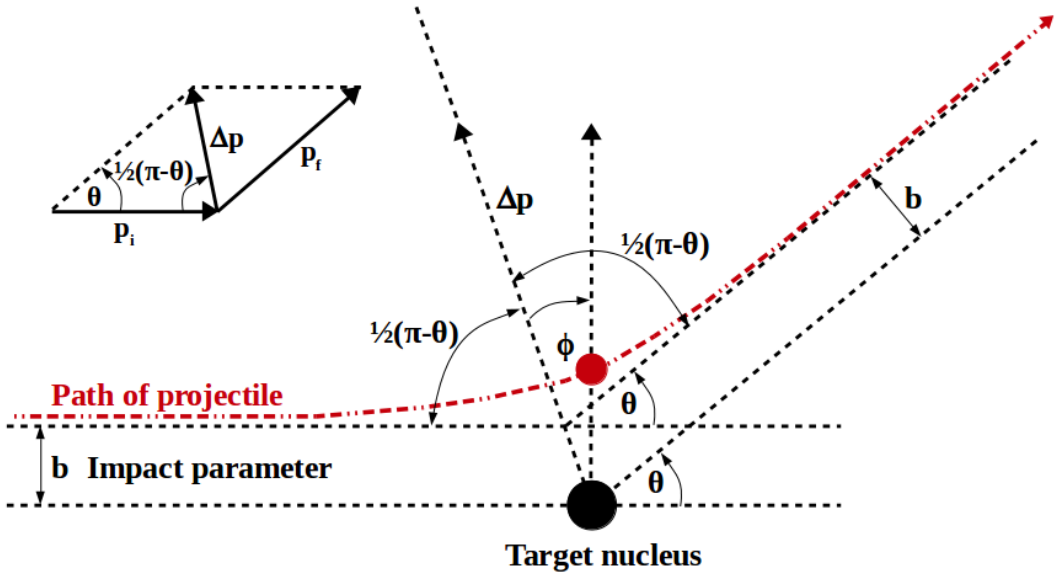


Figure 2.6: A schematic representation of Coulomb excitation.

2.2.3.1 Semi-classical description of Coulomb excitation

In the semi-classical description of Coulomb excitation, the classical Rutherford trajectory is considered a very good approximation of the relative motion that occurs in the interaction [Win79]. The differential cross section

in this case, however, is a slightly modified version of the Rutherford case and is given by:

$$\frac{d\sigma}{d\Omega} = \frac{d\sigma_{\mathrm{Ru}}}{d\Omega} P_{i\to f} \ , \tag{2.5}$$

where $P_{i\to f}$ is the probability of exciting an initial state $|i\rangle$ to a final state $|f\rangle$.

The target nucleus is excited by the time-dependent electromagnetic field, $V(r)$, created by the projectile. If the excitation is weak then pertubation theory can be used to evaluate $P_{i\to f}$ such that

$$P_{i\to f} = |a_{i\to f}|^2 \ , \tag{2.6}$$

where

$$a_{i\to f} = \frac{1}{i\hbar}\int_{-\infty}^{\infty} e^{i\omega t}\langle f|V(r(t))|i\rangle dt \tag{2.7}$$

and

$$\omega = \frac{(E_f - E_i)}{\hbar} \ . \tag{2.8}$$

Expansion of the field $V(r)$ in multipole components allows for the excitation amplitude to be expressed in terms of the matrix elements of the electric and magnetic multipole moments $\mathcal{M}(\mathrm{E}\lambda\mu)$ and $\mathcal{M}(\mathrm{M}\lambda\mu)$, respectively, as follows:

$$a_{i\to f} = i\sum_{\lambda} \chi_{i\to f}^{\pi(\lambda)} f_\lambda(\xi) \ , \tag{2.9}$$

where

$$\chi_{i\to f}^{\pi(\lambda)} \simeq \frac{Z_{\mathrm{P}} e\langle f|\mathcal{M}\left(\left\{\begin{smallmatrix}\mathrm{E}\\ \mathrm{M}\end{smallmatrix}\right\}\lambda\mu\right)|i\rangle}{\hbar\left\{\begin{smallmatrix}\nu\\ c\end{smallmatrix}\right\} b^\lambda} \ . \tag{2.10}$$

Here, Z_{P} is the charge of the projectile and ν is its velocity. The degree of

adiabaticity is given by the parameter ξ:

$$\xi(b) = \omega\tau = \omega\frac{b}{\nu\gamma} \ , \tag{2.11}$$

where τ is the collision time. The function $f_\lambda(\xi)$ is thus indicative of the dependence of the cross section on ξ.

The Coulomb excitation cross section of a final state $|f\rangle$ is given by:

$$\sigma_\lambda = 2\pi \int_{r_\mathrm{c}}^{b_\mathrm{a}} b|\chi^{(\pi\lambda)}(b)|^2 db \ , \tag{2.12}$$

where the nuclear radius r_c is the distance above which nuclear interaction is negligible and $b_\mathrm{a} = \nu\gamma/\omega$ is the impact parameter for $\xi = 1$. At this point, adiabatic cut-off will occur. Substituting Eq. (2.10) into Eq. (2.12) and considering a 0^+ ground state, which is the case for even-even nuclei, the cross section becomes:

$$\sigma_{\pi\lambda} \approx \left(\frac{Z_\mathrm{P} e^2}{\hbar c}\right)^2 \frac{B(\pi\lambda; 0 \to \lambda)}{e^2 {r_\mathrm{c}}^{2\lambda}} \pi {r_\mathrm{c}}^2 \begin{cases} (\lambda - 1)^{-1} & \text{for} \quad \lambda \geq 2 \\ 2\ln\left(b_\mathrm{a}/r_\mathrm{c}\right) & \text{for} \quad \lambda = 1 \end{cases} \ . \tag{2.13}$$

In the case of the IVGDR transitions (for which $\lambda = 1$), Eq. (2.13) becomes

$$\sigma_{E1} = \left(\frac{Z_\mathrm{P} e^2}{\hbar c}\right)^2 \frac{2\pi \ln\left(b_\mathrm{a}/r_\mathrm{c}\right)}{e^2} B(E1; 0 \to 1) \ , \tag{2.14}$$

where $B(E1; 0 \to 1)$ is the electric dipole strength function.

2.2.3.2 Equivalent virtual photon method

The equivalent virtual photon method describes the excitation of a target nucleus as the absorption of equivalent photons whose spectrum is determined by the Fourier transform of the projectile's time-dependent electromagnetic field [Ber88]. In depth theoretical descriptions of the equivalent virtual photon method can be found in the literature [Ber88, Ber09]. For the purpose of this study, only a brief summary of the key results is necessary.

The probability of an electromagnetic process occurring in a relativistic nuclear collision is given by:

$$P(b) = \int \frac{1}{E_\gamma} n_{\pi\lambda}(E_\gamma, b)\sigma_\gamma^{\pi\lambda}(E_\gamma)dE_\gamma \ , \tag{2.15}$$

where $\sigma_\gamma^{\pi\lambda}(E_\gamma)$ is the photo-nuclear absorption cross section for given multipolarity $\pi\lambda$ and $n_{\pi\lambda}(E_\gamma, b)$ is the number of equivalent virtual photons of energy $E_\gamma = \hbar\omega$ incident on the target per unit area in a collision with impact parameter b.

Since the cross section is obtained following the integration of the probability of a collision from $b_{\min} = R_c$ to $b = \infty$, Eq. (2.12) can also be expressed as

$$\begin{aligned} \sigma_{\pi\lambda} &= \int_{R_c}^{\infty} 2\pi b P(b) db \\ &= \int \frac{1}{E_\gamma} N_{\pi\lambda}(E_\gamma)\sigma_\gamma^{\pi\lambda}(E_\gamma)dE_\gamma \ , \end{aligned} \tag{2.16}$$

where $N_{\pi\lambda}(E_\gamma)$ is the total number of virtual photons given by:

$$N_{\pi\lambda}(E_\gamma) = 2\pi \int_{R_c}^{\infty} b n_{\pi\lambda}(E_\gamma, b) db \ . \tag{2.17}$$

Note that R_c is called the low-cutoff impact parameter for virtual photon

production and is given by:

$$R_{\mathrm{c}} = r_0 \left[{A_{\mathrm{P}}}^{\frac{1}{3}} + {A_{\mathrm{T}}}^{\frac{1}{3}} \right] + R_{\mathrm{sep}} \ , \tag{2.18}$$

where R_{sep} represents the separation distance between the projectile and target surfaces.

In the case of $E1$ transitions, the total number of virtual photons is given by:

$$N_{E1}(E_\gamma) = \frac{2{Z_{\mathrm{P}}}^2\alpha}{\pi} \left(\frac{c}{\nu}\right)^2 \left[\xi K_0 K_1 - \frac{2{Z_{\mathrm{P}}}^2\alpha}{2c^2}({K_1}^2 - {K_0}^2) \right] \ , \tag{2.19}$$

where Z_{P} is the charge number of the projectile, α is the fine structure constant given by $e^2/\hbar c$, ν is the velocity of the projectile and $K_{0,1}$ are the modified Bessel functions. The double-differential cross section is thus obtained in the following way:

$$\frac{d^2\sigma}{d\Omega dE_\gamma} = \frac{1}{E_\gamma}\frac{dN_{E1}}{d\Omega}\sigma_\gamma^{\pi\lambda}(E_\gamma) \tag{2.20}$$

with

$$\frac{dN_{E1}}{d\Omega} = \frac{{Z_{\mathrm{P}}}^2\alpha}{4\pi^2}\zeta^2\varepsilon^4\frac{c}{\gamma\nu}^2 \left[{K_1}^2(x) + \frac{1}{\gamma^2}{K_0}^2(x) \right] \ , \tag{2.21}$$

where

$$\zeta = \frac{\omega a}{\nu} = \frac{\omega}{\nu}\left(\frac{Z_{\mathrm{P}} Z_{\mathrm{T}} e^2}{m_0 \nu^2}\right) \tag{2.22}$$

is the adiabaticity parameter for half the distance of closest approach with reduced mass m_0, the eccentricity parameter $\varepsilon = (\sin(\theta/2))^{-1}$ and $x = \omega b/\gamma\nu$.

2.2.3.3 Eikonal description of Coulomb excitation

The semi-classical approach to the calculation of the virtual photon number breaks down at very small scattering angles and also produces a pole at 0° [Kru14]. The Eikonal description was developed by Bertulani and Nathan [Ber93] in an attempt to compensate for this and include the effects of strong absorption, relativity and retardation. Here, the number of virtual photons is given by:

$$N_{\pi\gamma}(E_\gamma) = {Z_\mathrm{P}}^2 \alpha \frac{\lambda[(2\lambda+1)!!]^2}{(2\pi)^3(\lambda+1)} \sum_m |G\pi\lambda m|^2 g_m(\omega) \tag{2.23}$$

with

$$g_m(\omega) = 2\pi \left(\frac{\omega}{\gamma\nu}\right)^2 \int b {K_m}^2 \left(\frac{\omega b}{\gamma\nu}\right) \exp\{-2\chi_\mathrm{I}(b)\} db \ , \tag{2.24}$$

where $\chi_\mathrm{I}(b)$ is the imaginary part of $\chi(b)$, which is given by

$$\chi(b) = -\frac{1}{\hbar\nu} \int_0^\infty U_\mathrm{N}^\mathrm{opt}(z', b) dz' + \psi_c(b) \ . \tag{2.25}$$

Here, $U_\mathrm{N}^\mathrm{opt}$ is the nuclear optical potential which is found from fits to existing elastic-scattering data at intermediate energies. The Coulomb phase is given by:

$$\psi_\mathrm{c}(b) = 2\frac{Z_\mathrm{P} Z_\mathrm{T} e^2}{\hbar\nu} \left\{ \ln(kb) + \frac{1}{2} E_1 \left(\frac{b^2}{R_\mathrm{G}^2}\right) \right\} \tag{2.26}$$

with

$$E_1(x) = \int_x^\infty \frac{e^{-t}}{t} dt \ , \tag{2.27}$$

where R_G is related to the Gaussian radii of the nuclei. Further details can be found in the literature [Ber93].

The equivalent photon number in this approximation is given by:

$$\frac{dN_{\pi\lambda}}{d\Omega} = {Z_P}^2\alpha\left(\frac{\omega k}{\gamma\nu}\right)^2 \frac{\lambda[(2\lambda+1)!!]^2}{(2\pi)^3(\lambda+1)}\sum_m |G\pi\lambda m|^2|\Omega_m(q)|^2 \ , \tag{2.28}$$

where

$$\Omega_m(q) = \int_0^\infty bJ_m(qb)K_m\left(\frac{\omega b}{\gamma\nu}\right)\exp\{i\chi(b)\} \tag{2.29}$$

with the momentum transfer given by $q = 2k\sin(\theta/2)$ and the polar scattering angle given by θ.

Figure 2.7 is taken from the doctoral thesis by A. Krugmann [Kru14] and illustrates the differences between the semi-classical description (blue lines) and the Eikonal description (red lines). As can be seen, the results obtained from the two methods differ at $\theta = 0°$ and the discrepancies increase further with increasing energy E_γ.

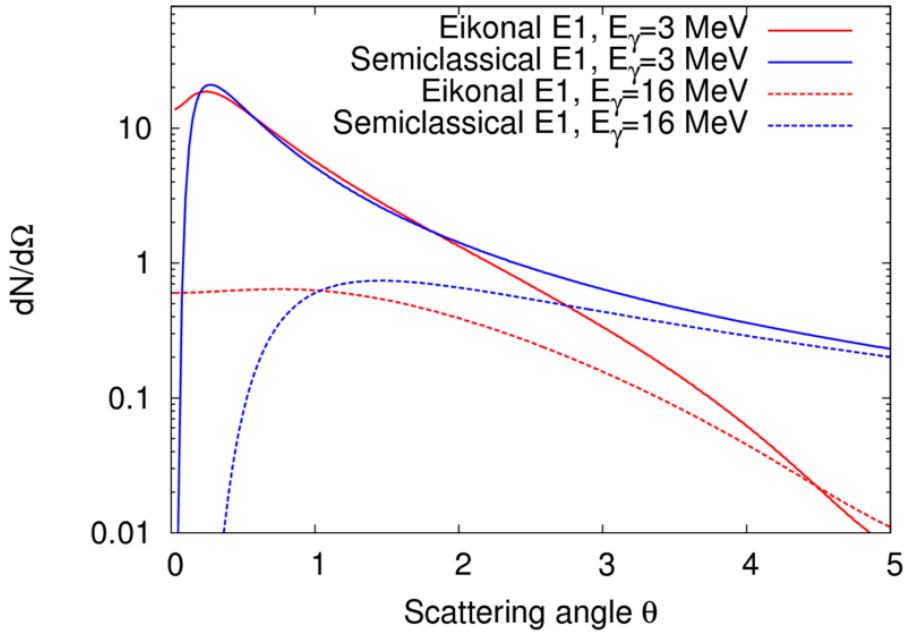


Figure 2.7: Virtual photon numbers per unit solid angle for $E1$ transitions in Coulomb excitation induced by 296 MeV protons on a ^{154}Sm target at $E_\gamma = 3$ MeV and 16 MeV where in blue: the semi-classical description and in red: the Eikonal description [Kru14].

2.3 Model predictions of giant resonance behaviour

The giant dipole resonance is a particularly important and extensively studied mode of nuclear excitation and, as such, has prompted many theoretical investigations into nuclear collective motion [Kle08]. The resulting theoretical descriptions were initially purely collective but have gradually come to link to microscopic models in the framework of the Random Phase Approximation (RPA).

2.3.1 Macroscopic model predictions

The fundamental versions of the shell model treat the nuclear potential as spherically symmetric and stationary and do not make allowances for the deformation of the nucleus into spheroidal or nonaxial shape [Mar70]. The collective model, however, takes this deformation into consideration and was originally developed by Bohr and Mottelson to meet the requirement of an effective interpretation of levels in heavy nuclei. It is in essence a compromise between the extreme single-particle theory and the earlier liquid-drop model [Liv66], and is best illustrated by considering even-even nuclei [Bli91].

2.3.1.1 Brief overview of the collective model

The two major types of collective nuclear motion that should be considered are vibrations and rotations. A model based on vibrations about a spherical equilibrium shape, which is illustrated in Fig. 2.8, is used for nuclei with $A < 150$, whereas nuclei in the range $150 < A < 190$ exhibit structures associated with rotations of a nonspherical system [Kra88].

A quantum of vibrational energy is called a phonon. The production of mechanical vibrations is essentially equivalent to the production of vibrational phonons, and so a single unit of $\lambda = 2$ (quadrupole) nuclear

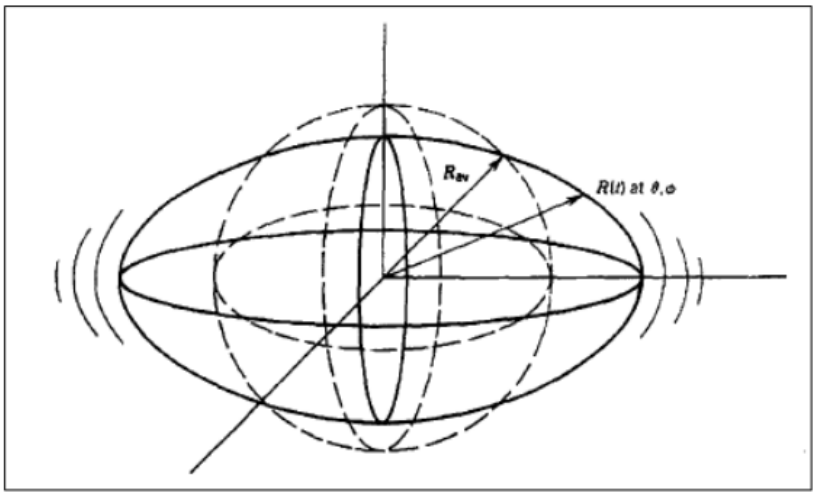


Figure 2.8: A vibrating nucleus with a spherical equilibrium shape [Kra88].

vibration is thus a quadrupole phonon [Kra88]. The ground state spin and parity of an even-even nucleus is always 0^+. Adding a quadrupole phonon (or one unit of vibrational energy), which carries two units of angular momentum and even parity results in a 2^+ state. This is exactly what has been observed for the first excited states of spherical even-even nuclei. Detailed calculations show that by adding a second quadrupole phonon, one would expect a 4^+ state, which is at twice the excitation energy of the first 2^+ state. This is because two identical phonons carry twice as much energy as one. A common feature of vibrational nuclei is thus a triplet of states with spins 0^+, 2^+, 4^+ [Kra88].

It is important to note that the ratio $E\left(4^+\right)/E\left(2^+\right)$ gives an indication as to the extent of the nuclear deformation. The vibrational model predicts that if the 2^+ state in the ratio is the first excited state and the 4^+ state is a member of the two-phonon triplet then the expected ratio is 2.0. In the range where $A < 150$, Fig. 2.9 shows sufficient agreement with this prediction [Kra88].

Rotational motion is only observable in nuclei whose equilibrium shapes are nonspherical as is illustrated in Fig. 2.10. These nuclei are often called deformed nuclei and are found in the mass ranges $150 < A < 190$ and $A > 220$ [Kra88], that is, the rare-earths and actinides, respectively.

When considering rotational nuclei, the term 'rotational band' is used to

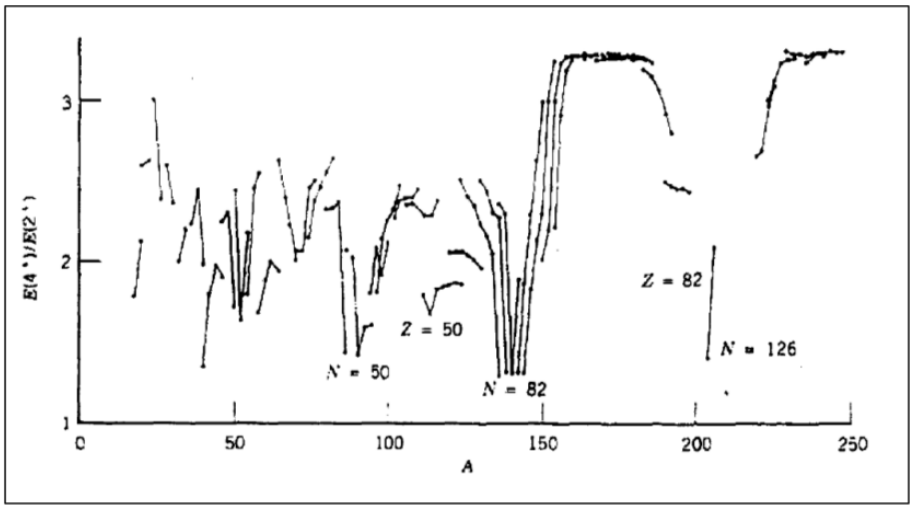


Figure 2.9: The ratio $E\left(4^{+}\right)/E\left(2^{+}\right)$ for the lowest 2^{+} and 4^{+} states of even-even nuclei, where the lines connect sequences of isotopes [Kra88].

refer to the sequence formed by the nuclear excited states [Kra88]. As was mentioned previously, the ground state of an even-even nucleus is always a 0^{+} state. The sequence of rotational states is also restricted by the mirror symmetry of the nucleus to even values of the angular momentum quantum number, I, for which

$$E = \frac{\hbar^2}{2J} I\left(I+1\right) \quad , \tag{2.30}$$

where J is the effective moment of inertia about a minor axis [Liv66].

The following sequence of states is thus expected:

$$E\left(0^{+}\right) = 0 \tag{2.31}$$

$$E\left(2^{+}\right) = 6\left(\hbar^2/2J\right) \tag{2.32}$$

$$E\left(4^{+}\right) = 20\left(\hbar^2/2J\right) \tag{2.33}$$

and so on. This gives a predicted value of 3.33 for the ratio $E\left(4^{+}\right)/E\left(2^{+}\right)$, which is in agreement with the systematics of the nuclear levels shown in Fig. 2.9 for $150 < A < 190$ and $A > 220$ [Kra88].

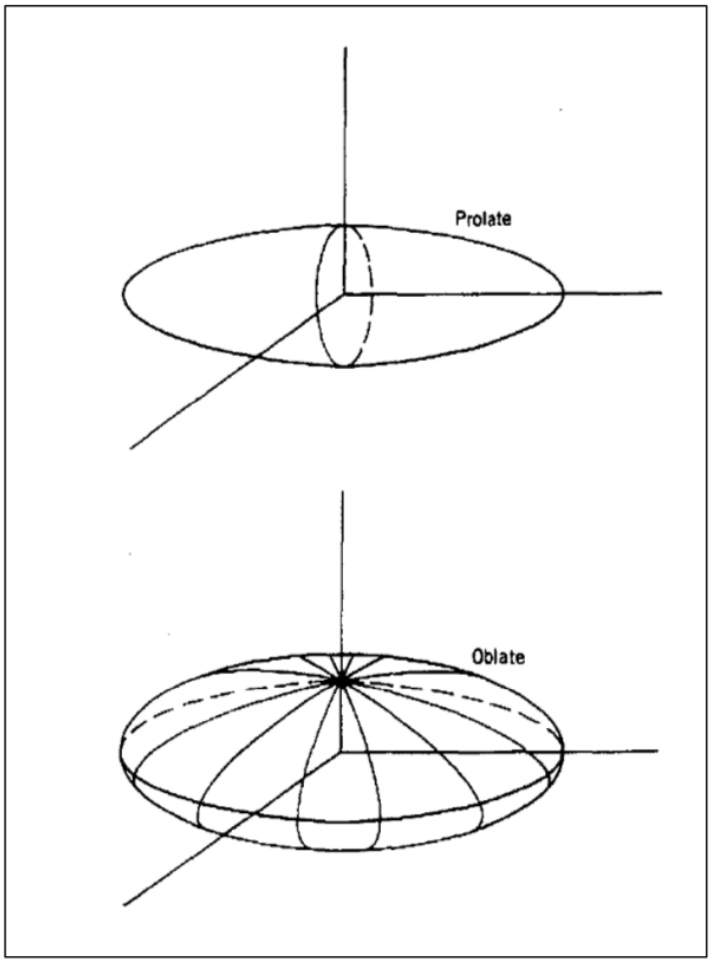


Figure 2.10: Equilibrium shapes of nuclei with permanent deformations [Kra88].

2.3.1.2 *K*-splitting and the shape of the IVGDR for deformed nuclei

One of the properties of the IVGDR in statically deformed nuclei is that it splits into two components. This splitting has been observed experimentally many times using both bremsstrahlung and quasi-monochromatic photon beams [Mas06] and can be understood in the framework of the collective model. As can be seen in Fig. 2.11(b), the shape of a deformed nucleus is often represented by an ellipsoid of revolution with two principal axes, a and b.

These principal axes can be associated with two standing waves with

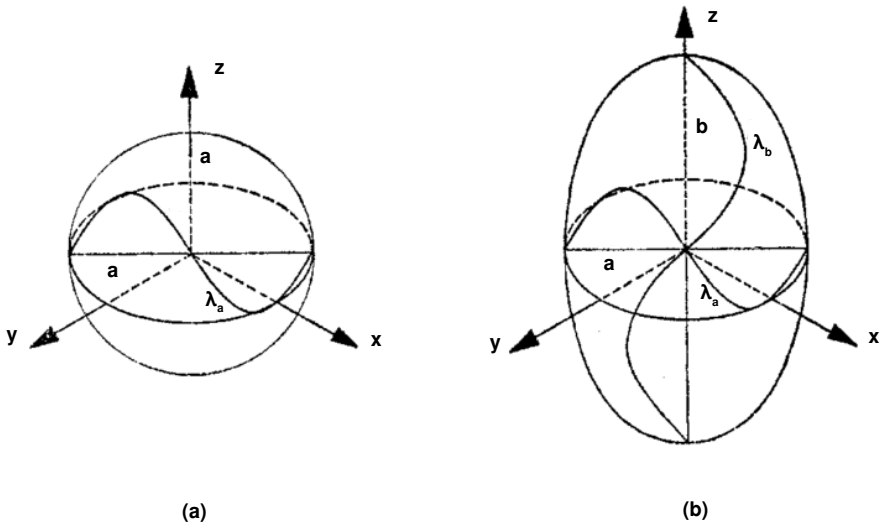


Figure 2.11: Standing waves in a spherical nucleus (a) and in a prolate deformed nucleus (b).

wavelengths $\lambda_a \sim R_a$ and $\lambda_b \sim R_b$ [Spe81]. The relative energy difference is proportional to the nuclear deformation β_2 of the corresponding nucleus:

$$\frac{E_b - E_a}{E_b} \propto \frac{R_a - R_b}{R_a} \propto \beta_2 \ . \tag{2.34}$$

In the case of the axially-symmetric prolate nuclei, the high-energy state $|\Psi(K=1)\rangle$ with an energy E_a and a width $\Gamma(E_a)$ represents the vibrations along the minor (transverse) axes, x and y, of the deformed nucleus. The low-energy state $|\Psi(K=0)\rangle$ with energy E_b and width $\Gamma(E_b)$ represent the vibrations along the major axis of symmetry, z, of the ellipsoid. Note that K is the projection of the nuclear momentum, I, to the axis of symmetry. In the formation of the GDR, the dipole transitions are related to either $K = 0$ or $K = 1$.

Figure 2.12 shows a theoretical representation of the dependence of the curve shape on the type of nuclear shape [Mas06]. The modelling types of the nuclear shapes are given in Fig. 2.12a, namely, a sphere, a prolate axially-symmetric ellipsoid and an oblate ellipsoid. The vibration energy value along the corresponding axes and the dipole-transition intensity, F, are

given in Fig. 2.12b where it can be seen that for spherical nuclei, vibrations along the three axes degenerate and their energies coincide. For the axially-symmetric prolate and oblate shapes, the vibrations along the equivalent shorter or longer axes remain degenerated [Mas06].

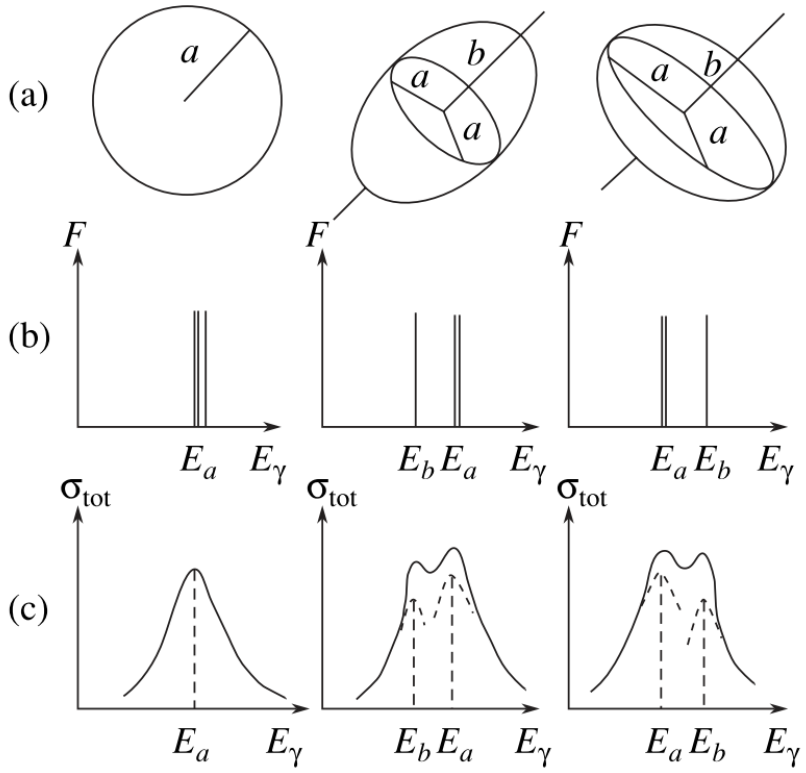


Figure 2.12: Theoretical representation of the dependence of the curve shape for the giant dipole resonance on the type of the nuclear shape [Mas06].

It is important to note that in axially-symmetric nuclei, the dipole oscillations along the x- and y-axes have the same frequency:

$$\omega_x = \omega_y = \omega(K = 1) \ . \tag{2.35}$$

The $K = 1$ component peak is, therefore, the combination of both the x- and y-oscillations and so, its cross section is larger than that of the $K = 0$ peak, which embraces only the z-oscillations [Nes15]. In prolate axially-symmetric deformed nuclei, $R_{x,y} < R_z$ and so, $\omega(K = 1) > \omega(K = 0)$. The smaller $K = 0$ peak precedes the large $K = 1$ peak as can be seen in Fig. 2.12. The opposite

is true for the case of an oblate ellipsoid.

The instantaneous coordinate of a point on an ellipsoid of revolution is given by [Kra88]:

$$R(\Theta,\phi) = R_{\text{av}}\left[1 + \beta \text{Y}_{20}(\Theta,\phi)\right] \ , \tag{2.36}$$

where R_{av} is the average radius, which is $r_0 A^{1/3}$, β is the deformation parameter and Y_{20} is the spherical harmonic given by:

$$\text{Y}_{20}(\Theta) = \left(\frac{5}{16\pi}\right)^{\frac{1}{2}} (3\cos^2\Theta - 1) \ . \tag{2.37}$$

The value for the radius of the minor axis of symmetry is found when $\Theta = 0$, that is,

$$\begin{aligned} \text{Y}_{20}(0) &= 2\left(\frac{5}{16\pi}\right)^{\frac{1}{2}} && (2.38)\\ \Rightarrow \quad a = R(0,\phi) &= r_0 A^{\frac{1}{3}}\left(1 + 2\beta\left(\frac{5}{16\pi}\right)^{\frac{1}{2}}\right) && (2.39)\\ &= R_{\text{av}}\left(1 + 0.63\beta\right) \ . && (2.40) \end{aligned}$$

The radius of the major axis of symmetry is found when $\Theta = \frac{\pi}{2}$:

$$\begin{aligned} \text{Y}_{20}\left(\frac{\pi}{2}\right) &= -\left(\frac{5}{16\pi}\right)^{\frac{1}{2}} && (2.41)\\ \Rightarrow \quad b = R\left(\frac{\pi}{2},\phi\right) &= r_0 A^{\frac{1}{3}}\left(1 - \beta\left(\frac{5}{16\pi}\right)^{\frac{1}{2}}\right) && (2.42)\\ &= R_{\text{av}}\left(1 - 0.32\beta\right) \ . && (2.43) \end{aligned}$$

2.3.2 Microscopic model predictions

A well-established property of giant resonances is the exhaustion of an appreciable fraction of the energy-weighted sum rule. Sum rules allow for the integral of the strength distribution of the excited states over all energies to be related to simple and experimentally observable ground state properties. For this reason, the only applicable microscopic theoretical descriptions of giant resonance behaviour are those whose model states satisfy the sum rules in the same way as the exact states [Goe82]. The Random Phase Approximation (RPA) is the simplest many-body theory that satisfies this criterion, thus making it the basic microscopic theory for the description of giant resonances.

2.3.2.1 Random Phase Approximation (RPA)

In the framework of the RPA, giant resonances are described as a coherent superposition of one particle-one hole ($1p - 1h$) excitations that are built on the corresponding ground state. The RPA has been proven effective in the description of mean energies and total transition strengths. In deformed nuclei, this method even allows for the estimation of the widths of giant resonances [Nes16]. Modern nuclear models exploit the self-consistent RPA methods based on energy-density functionals [Ben03]. One such model is the self-consistent Separable Random Phase Approximation (SRPA), which was formulated by Nesterenko *et al.,* [Nes02]. Specific application of this model has been made (with the specification of Skyrme forces with pairing) to describe giant resonances in axially-symmetric deformed nuclei [Nes06].

2.3.2.2 Self-consistent Separable Random Phase Approximation (SSRPA)

Self-consistent mean-field models with effective energy-density functionals such as the Skyrme-Hartree-Fock (SHF) model have been proven reliable in the description of nuclear structure and dynamics. Their applications to nuclear dynamics are, however, still somewhat limited even in the linear

regime, which is usually considered within the RPA. This is because the RPA requires the diagonalisation of large matrices where the rank is determined by the size of the one particle-hole ($1ph$) space. In the case of deformed nuclei, this space is huge owing to the lack of symmetry present [Nes02]. Although standard RPA calculations are possible for deformed nuclei, the time required to perform them renders the calculations impractical for systematic investigations [Kle08]. Alternate, still accurate but less computationally demanding RPA techniques have thus been developed. One such technique is the self-consistent Separable Random Phase Approximation based on the Skyrme functional [Kle08]. Usually denoted as the SRPA, the self-consistent Separable Random Phase Approximation is not to be confused with the Second Random Phase Approximation and, as such, will be referred to as the SSRPA throughout the remainder of this thesis. The most noteworthy features of the SSRPA are [Nes16]:

(i) Unlike the Quasiparticle-Phonon Nuclear Model (QPNM), the SSRPA is fully self-consistent, that is, the mean field and the residual interaction are derived from the same initial functional. The advantage of this feature is that there are no fitting parameters required in addition to those in the initial functional, thus ensuring the high predictive potential of the model.

(ii) Owing to the self-consistent factorisation of the residual interaction, the SSRPA requires a modest computational effort, even in calculations for heavy, deformed nuclei which are characterised by a very large two-quasiparticle configuration space. Systematic investigations of nuclear giant resonances in both spherical and deformed nuclei are, therefore, more easily performed in the framework of the SSRPA.

(iii) Despite the separable ansatz, the SSRPA has a high accuracy when compared with that of exact (without the separable ansatz) RPA methods.

Exhaustive descriptions of the SSRPA and its applications can be found in the literature [Nes02, Nes06, Kle08] and, as such, only the main points are summarised here.

In the framework of the SSRPA, the factorisation of the residual interaction of the Skyrme RPA is given in the most general form as:

$$\hat{V}_{\text{res}} \rightarrow \hat{V}_{\text{res}}^{\text{sep}} = -\frac{1}{2}\sum_{ss'}\sum_{k,k'=1}^{K}\left\{\kappa_{sk,s'k'}\hat{X}_{sk}\hat{X}_{s'k'} + \eta_{sk,s'k'}\hat{Y}_{sk}\hat{Y}_{s'k'}\right\} \ , \tag{2.44}$$

where the indices s and s' label neutrons and protons, $\hat{X}_{sk}$ and $\hat{Y}_{sk}$ are the time-even and time-odd hermitian one-body operators, respectively, and $\kappa_{sk,s'k'}$ and $\eta_{sk,s'k'}$ are the strength matrices [Nes06]. Both $\hat{X}_{sk}$ and $\hat{Y}_{sk}$ are necessary since the applicable Skyrme functionals involve both time-even (nucleon ρ, kinetic τ and spin-orbital $\mathcal{J}$) and time-odd (current $\vec{j}$, spin σ and spin kinetic $\vec{T}$) densities. More details on this can be found in [Ben03].

The Skyrme functional is denoted as $E\left[J_s^{\alpha}(\vec{r},t)\right]$, where J_s^{α} represents a set of local densities sorted by α [Kle08]. From this functional, the separable operators and strength matrices can be derived using the scaling transformation for the perturbed wave-function of the system, which is given by:

$$|\Psi(t)\rangle_s = \prod_{k=1}^{K}\exp[-iq_{sk}(t)\hat{P}_{sk}]\exp[-ip_{sk}(t)\hat{Q}_{sk}]|\rangle_s \ , \tag{2.45}$$

where $|\Psi(t)\rangle_s$ and the ground state $|\rangle_s$ are Slater determinants. $\hat{Q}_{sk}(\vec{r})$ and $\hat{P}_{sk}(\vec{r}) = i[\hat{H},\hat{Q}_{sk}]$ are the generalised coordinate (time-even) and momentum (time-odd) Hermitian operators where $\hat{H}$ represents the full Hamiltonian. The corresponding collective variables $q_{sk}(t)$ and $p_{sk}(t)$ are given by:

$$q_{sk}(t) = \bar{q}_{sk}\cos(\omega t) \tag{2.46}$$

and

$$p_{sk}(t) = \bar{p}_{sk}\sin(\omega t) \ . \tag{2.47}$$

The number of separable terms in $\hat{V}_{\rm res}^{\rm sep}$ is determined by the number of input operators, K, in Eq. (2.45). For $K \to \infty$, the treatment converges to the exact RPA but a good approximation can be found for $K = 2 - 5$ provided that $\hat{Q}_{sk}$ and $\hat{P}_{sk}$ are adequately selected [Kle08]. It should be noted that $\hat{Q}_{sk}$ must be selected such that good convergence of Eq. (2.44) to the true Skyrme residual interaction is achieved with the minimal number of operators. In addition, it is important to note that the SSRPA does not provide an exact method to obtain $\hat{Q}_{sk}$ but a value can be selected following intuitive physical arguments [Nes06].

The resulting SSRPA operators and inverse strength matrices in Eq. (2.44) are given by [Kle08]:

$$\hat{X}_{sk} = \sum_{s'} \hat{X}_{sk}^{s'} = i \sum_{\alpha' \alpha s'} \frac{\delta^2 E}{\delta J_{s'}^{\alpha'} \delta J_{s}^{\alpha}} \langle [\hat{P}_{sk}, \hat{J}_{s}^{\alpha}] \rangle \hat{J}_{s'}^{\alpha'} \tag{2.48}$$

$$\hat{Y}_{sk} = \sum_{s'} \hat{Y}_{sk}^{s'} = i \sum_{\alpha' \alpha s'} \frac{\delta^2 E}{\delta J_{s'}^{\alpha'} \delta J_{s}^{\alpha}} \langle [\hat{Q}_{sk}, \hat{J}_{s}^{\alpha}] \rangle \hat{J}_{s'}^{\alpha'} \tag{2.49}$$

$$\kappa^{-1}_{s'k',sk} = \sum_{\alpha' \alpha s'} \frac{\delta^2 E}{\delta J_{s'}^{\alpha'} \delta J_{s}^{\alpha}} \langle [\hat{P}_{sk}, \hat{J}_{s}^{\alpha}] \rangle \langle [\hat{P}_{s'k'}, \hat{J}_{s'}^{\alpha'}] \rangle \tag{2.50}$$

$$\eta^{-1}_{s'k',sk} = \sum_{\alpha' \alpha s'} \frac{\delta^2 E}{\delta J_{s'}^{\alpha'} \delta J_{s}^{\alpha}} \langle [\hat{Q}_{sk}, \hat{J}_{s}^{\alpha}] \rangle \langle [\hat{Q}_{s'k'}, \hat{J}_{s'}^{\alpha'}] \rangle \ , \tag{2.51}$$

where $\hat{J}_{s}^{\alpha}$ are the operators associated with the densities J_{s}^{α}.

Note that the final RPA equations are given by:

$$\sum_{sk} \left\{ \bar{q}_{sk}^{\nu} [F^{(XX)}_{s'k',sk} - \kappa^{-1}_{s'k',sk}] + \bar{p}_{sk}^{\nu} F^{(XY)}_{s'k',sk} \right\} = 0 \tag{2.52}$$

and

$$\sum_{sk} \left\{ \bar{q}_{sk}^{\nu} F^{(YX)}_{s'k',sk} + \bar{p}_{sk}^{\nu} [F^{(YY)}_{s'k',sk} - \eta^{-1}_{s'k',sk}] \right\} = 0 \ , \tag{2.53}$$

where

$$F^{(AB)}_{s'k',sk} = 2 \sum_{s'',ph\in s''} \alpha_{AB} \frac{\langle ph|\hat{A}^{s''}_{sk}|\rangle^* \langle ph|\hat{B}^{s''}_{sk}|\rangle}{\varepsilon^2_{ph} - \omega^2_\nu} \tag{2.54}$$

and

$$\alpha_{AB} = \begin{cases} \varepsilon_{ph} & \text{for} \quad \hat{A} = \hat{B} \\ -i\omega_\nu & \text{for} \quad \hat{A} = \hat{Y}; \hat{B} = \hat{X} \\ i\omega_\nu & \text{for} \quad \hat{A} = \hat{X}; \hat{B} = \hat{Y} \end{cases} . \tag{2.55}$$

The matrix element for the two-quasiparticle state $|ph\rangle$ is given by $ph|\hat{A}^{s''}_{sk}|\rangle$ with energy ε_{ph}. The energy of the RPA state $|\nu\rangle$ is given by ω_ν. The RPA phonon operator is:

$$\hat{C}^\dagger_\nu = \sum_s \sum_{ph\in s} (c^{\nu-}_{ph} \hat{A}^\dagger_{ph} - c^{\nu+}_{ph} \hat{A}_{ph}) \ , \tag{2.56}$$

where $\hat{A}^\dagger_{ph}$ and $\hat{A}_{ph}$ are the creation and annihilation operators of two-quasiparticle states. The amplitudes of the RPA operator are given by

$$c^{\nu\pm}_{ph\in s} = -\sum_{s'k'} \frac{\bar{q}^\nu_{s'k'} \langle ph|\hat{X}^s_{s'k'}\rangle \mp i\bar{p}^\nu_{s'k'} \langle ph|\hat{Y}^s_{s'k'}\rangle}{2(\varepsilon_{ph} \pm \omega_\nu)} \tag{2.57}$$

and are determined via the solutions of Eq. (2.52) and Eq. (2.53). The number of input parameters in Eq. (2.45) determines the rank of the RPA matrix (Eqs. (2.52) and (2.53)). As previously mentioned, for an SSRPA calculation, K is usually assigned a value between 2 and 5, which results in a small rank value. This in turn reduces the RPA computational cost significantly.

The SSRPA equations are derived for arbitrary Skyrme functionals $E\left[J^\alpha_s(\vec{r},t)\right]$. The self-consistency of the SSRPA lies in the fact that both the static mean field

$$\hat{h}_0 = \sum_{\alpha s} \frac{\delta E}{\delta J^\alpha_s} \hat{J}^\alpha_s \tag{2.58}$$

and the residual interaction of Eqs. (2.48), (2.49), (2.50) and (2.51) are all derived from the same functional [Kle08].

2.4 Properties of the IVGDR

The IVGDR has been extensively studied in past experiments and as such, its main features have been well established and documented. A brief overview of these features is provided as follows.

The total absorption cross section for non-deformed nuclei with $A > 50$ can be fitted by a non-standard Lorentzian of the form [Car71, Car74]:

$$\sigma(E) = \frac{\sigma_{\mathrm{R}}}{1 + [(E^2 - {E_{\mathrm{R}}}^2)^2 / E^2\Gamma^2]} \ , \tag{2.59}$$

where R refers to the the resonance peak cross section. For axially-symmetric deformed nuclei, a split in the resonance is expected and as such, the cross section can be modelled by a sum of two non-standard Lorentzians:

$$\sigma(E) = \sum_{i=1}^{2} \frac{\sigma_{\mathrm{R}i}}{1 + [(E^2 - {E_{\mathrm{R}i}}^2)^2 / E^2{\Gamma_i}^2]} \ . \tag{2.60}$$

2.4.1 Resonance excitation energy

The resonance excitation energy, E_{R}, can be calculated from [Har01]:

$$E_{\mathrm{R}} = 31.2A^{-\frac{1}{3}} + 20.6A^{-\frac{1}{6}} \quad \mathrm{MeV} \ . \tag{2.61}$$

This formula results from the combination of both the Goldhaber-Teller and the Steinwedel-Jenson models. Another version of this combination, which gives slightly different results, is derived in [Mye77] and is given by:

$$E_{\mathrm{R}} = 112 \times \left[A^{\frac{2}{3}} + (A_0 A)^{\frac{1}{3}} \right]^{-\frac{1}{2}} \quad \mathrm{MeV} \ , \tag{2.62}$$

where $A_0 \approx 274$. These equations simply convey the idea that the restoring force is not dominated by either the density gradient effect (the $A^{-1/3}$ term) or the nuclear surface effect (the $A^{-1/6}$ term) [Wou91].

For a prolate deformed nucleus, E_{R} is given by [Ber75]:

$$E_{\mathrm{R}} = \frac{(E_{\mathrm{R1}} + 2E_{\mathrm{R2}})}{3} \quad \mathrm{MeV} \ . \tag{2.63}$$

2.4.2 Resonance strength

The IVGDR strength can be expressed in terms of the Thomas-Reiche-Kuhn (TRK) sum rule, which is given by:

$$\int_{E_{\mathrm{min}}}^{E_{\mathrm{max}}} \sigma_{\gamma}^{\mathrm{abs}}(E) = \frac{60NZ}{A}(1+\kappa) \quad \mathrm{MeV\,mb} \ , \tag{2.64}$$

where the factor κ is owing to meson exchange contributions, which are characteristic of all isovector resonances. For an E_{min} value equal to the neutron separation energy and an $E_{\mathrm{max}} = 25$ MeV, $\kappa \sim 0.1$ to 0.2 for nuclei with $A > 100$.

2.4.3 Resonance width

The resonance width of the IVGDR varies from ~ 4 to 8 MeV [Sno86] and is the result of damping processes in the resonance. This concept is explained in detail in Section 2.5.

2.4.4 Area ratio for deformed nuclei

The area under a Lorentzian curve is given by [Ber75]:

$$\int_0^\infty \sigma(E)dE = \frac{\pi}{2}\sigma_{\mathrm{R}}\Gamma \tag{2.65}$$

and so, for a deformed nucleus with two Lorentzian components, the summed area is given by

$$\int_0^\infty \sigma(E)dE = \left(\frac{\pi}{2}\right)\left(\sigma_{\mathrm{R1}}\Gamma_1 + \sigma_{\mathrm{R2}}\Gamma_2\right) \ . \tag{2.66}$$

It was predicted in the hydrodynamic model by Okamoto and Danos that the strengths of the two Lorentzian components should have a $1:2$ ratio, which corresponds to the number of degrees of freedom for these vibrations [Ber75]. That is,

$$R_{\mathrm{A}} = \frac{\sigma_{\mathrm{R1}}\Gamma_1}{\sigma_{\mathrm{R2}}\Gamma_2} = \frac{1}{2} \tag{2.67}$$

for a prolate axially-symmetric deformed nucleus. The values of R_{A} for the deformed rare-earth nuclei provide an important test of the hydrodynamic model.

2.5 Damping of giant resonances

The damping of resonances in many-body systems can involve many different processes and so, appears to be more complex. As can be seen in Fig. 2.13, the observed width of a nuclear giant resonance given by $\Gamma = \Delta\Gamma + \Gamma\uparrow + \Gamma\downarrow$ [Goe82], is most often explained to result from the following processes: Landau damping (represented by $\Delta\Gamma$), in which the initial one particle-one hole (1p-1h) excitations fragment; direct particle

emission from the (1p-1h) excitations, which give rise to an escape width $\Gamma\uparrow$, and coupling to more complex two particle-two hole (2p-2h) states through the residual two-body interaction [Dro91] and finally to (np-nh) states. The coupling to more and more complex states results in a spreading width $\Gamma\downarrow$ and ultimately terminates in the chaos of compound nucleus states. This particular coupling mechanism is referred to as the doorway states mechanism and is illustrated in Fig. 2.14. Fine structure in the response of the nucleus may be induced by this chaos of nuclear states mentioned above [Lac99]. Figure 2.15 shows a schematic representation of the fine structure formation from a mixture of multiple scales of fluctuation where the escape width is given by δE_1 and the spreading width is given by δE_2 [She05].

Insight into the dominant damping mechanisms of nuclear giant resonances is provided in the properties of the fine structure, which, in the case of the IVGDR, is understood to be the result of the characteristic energy scales or energies of the coupling steps. The theoretical overview of this process is given in Section 2.6.

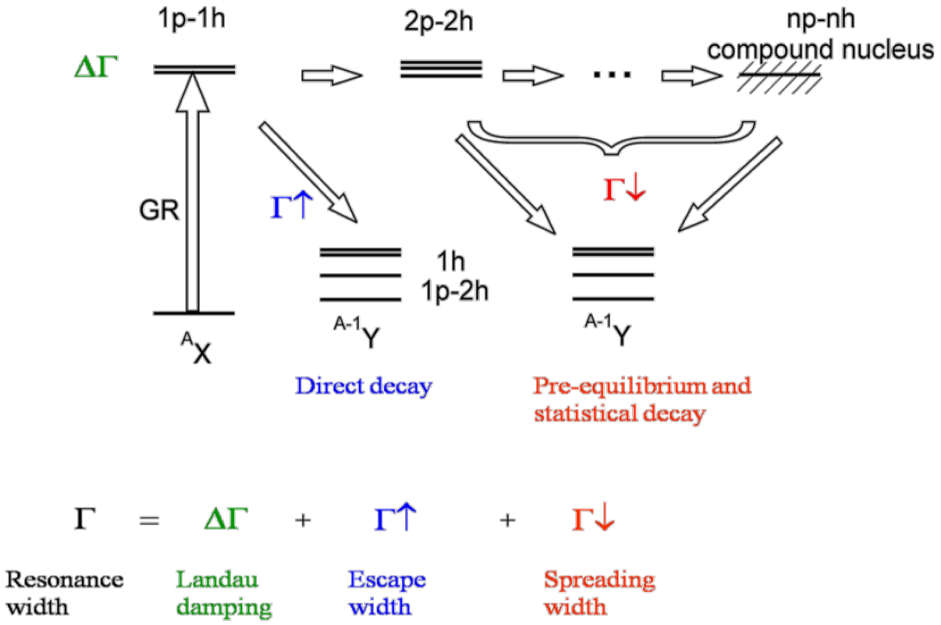


Figure 2.13: A schematic representation of the contributions to the width of a nuclear giant resonance.

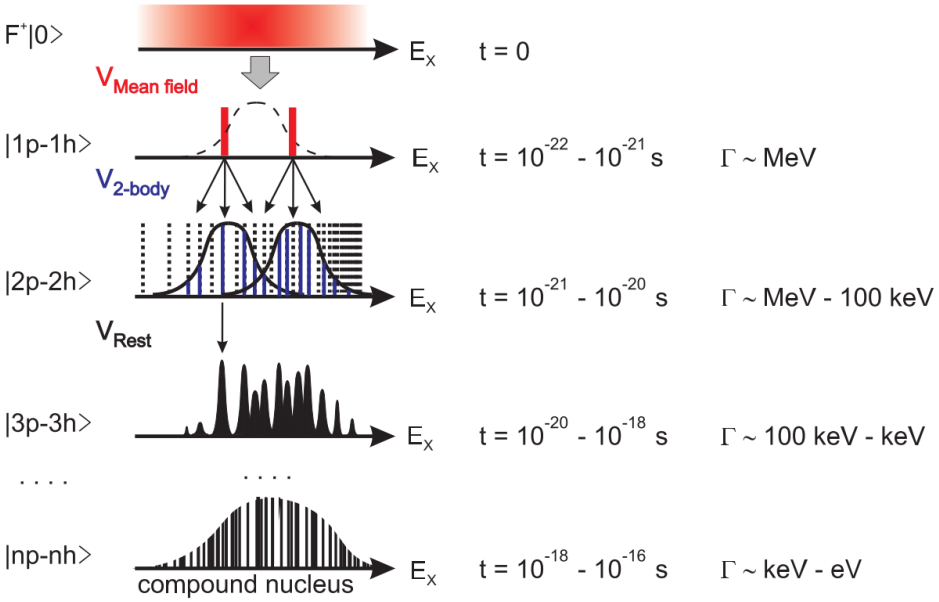


Figure 2.14: A schematic representation of the coupling to more and more complex states via the doorway mechanism [She05].

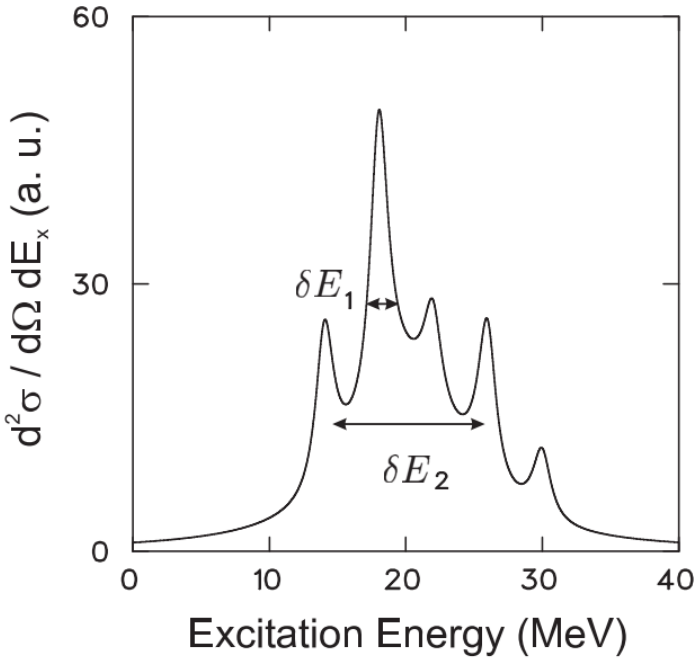


Figure 2.15: The fine structure formation from a mixture of multiple scales of fluctuations [She05].

2.6 Extraction of characteristic energy scales

An entropy index method [Lac99, Lac00] and a multifractal analysis [Aib99, Aib03] of the fluctuating strength function are two of the earlier proposed methods used to obtain information on the characteristic energy scales of the fine structure. A recent method, which is based on a continuous wavelet transform has been investigated and has shown to be promising [She04, Kal06]. The variety of methods available is critically discussed in [She08]. For the purposes of this study, only the wavelet analysis approach will be discussed.

2.6.1 Wavelet analysis

The fundamental concept behind the use of wavelets in data analysis and interpretation is that the analysis is performed according to scale. Wavelets are functions that satisfy a set of predetermined mathematical requirements and are useful in the representation of data or other functions. This concept is not unique to wavelet analysis since the same idea is used in Fourier analysis, where functions are represented by a superposition of sine and cosine functions [Gra95]. Wavelet algorithms process data at different scales or resolutions and what distinguishes wavelet analysis from other approaches is the special role that these scales play in the interpretation of the data. If a signal or function is observed through a large window, one would notice the gross features and, similarly, for a small window, the small features. Wavelet analysis, therefore, by analogy, allows for the forest as well as the trees to be seen [Gra95].

In the case of Fourier analysis, the sine and cosine functions that are used to represent the data are non-local and expand to infinity. The disadvantage of this is that any sharp spikes in the data are badly approximated. The function that form the basis of wavelet analysis, however, are approximating functions that are contained in finite domains, making them ideal for the analysis of data with sharp discontinuities. In light of this, wavelet analysis is well-suited to the fine structure analysis of giant resonances.

The wavelet analysis procedure involves the selection of a wavelet prototype, which is referred to as a mother-wavelet [Gra95]. The time-based analysis is conducted with a contracted, high-frequency version of this mother-wavelet. In contrast, the frequency analysis is performed using a dilated, low-frequency version. The selection of a particular wavelet as the mother-wavelet depends on its adherence to the set of predefined mathematical criteria [She05] outlined in the formalism below.

2.6.1.1 Wavelet analysis formalism

A real or complex function $\Psi(x)$, may only be used as a mother-wavelet if:

$$\int_{-\infty}^{\infty} \Psi^*(x)dx = 0 \tag{2.68}$$

and

$$K_\Psi = \int_{-\infty}^{\infty} |\Psi^2(x)|dx < \infty \ , \tag{2.69}$$

where $\Psi^*(x)$ is the complex conjugate of $\Psi(x)$ and K_Ψ is the wavelet norm or rather, the admissibility constant. This varies depending on the wavelet under consideration.

The first condition imposes the requirement of an oscillating function for which the mean value should be zero in the absence of an imaginary component [She05]. The second condition requires the restriction of the function to a finite domain, hence the naming convention, wave*let*. Since wavelets are localised both in time and in frequency, they are unaffected by the properties of the data far away from the region of interest and as such, are ideal for the description of the local behaviour. Some examples of the most frequently used functions in wavelet analysis are provided in Fig. 2.16.

The analytical form of the real Morlet wavelet is given by:

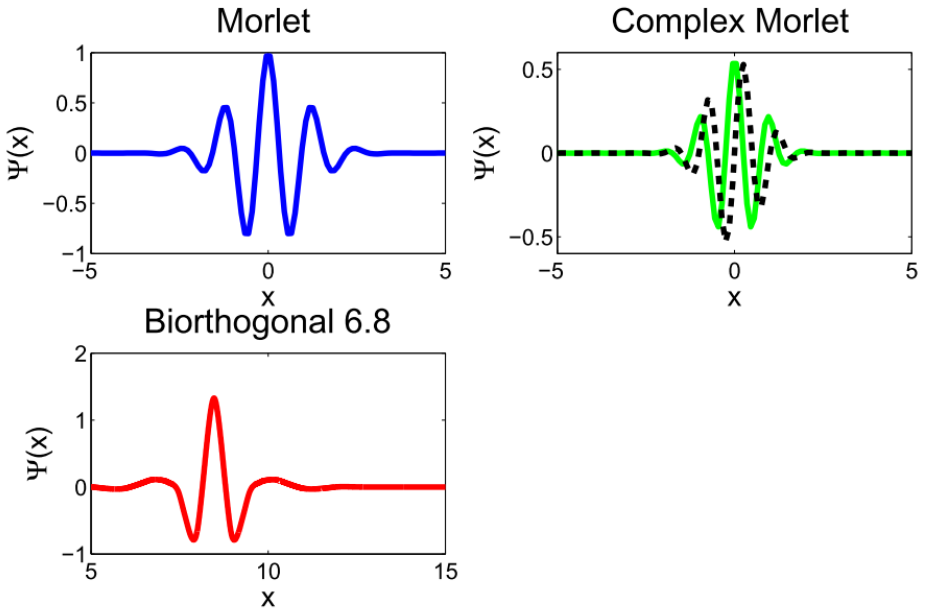


Figure 2.16: A schematic representation of the most frequently used wavelet families. The real and complex parts of the complex Morlet wavelet are illustrated in solid and dashed lines, respectively [Jin14]. Further details regarding the Biorthogonal6.8 wavelet and its implementation can be found in [Kur14, Jin14].

$$\Psi(x) = \frac{1}{\pi^{\frac{1}{4}}} \cos(ikx) \exp\left(-\frac{x^2}{2}\right) \quad , \tag{2.70}$$

where k is a measure of the resolution in scales *versus* the resolution in localisation [Usm09]. Here, the admissibility condition is satisfied for $k \leq 5$.

The Complex Morlet wavelet is given by:

$$\Psi(x) = \frac{1}{\pi^{\frac{1}{2}} f_b} \exp(2\pi i f_c) \exp\left(-\frac{x^2}{f_b}\right) \quad , \tag{2.71}$$

where f_b controls the wavelet bandwidth and f_c is the centre frequency of the wavelet [Usm09]. The real and imaginary parts of the Complex Morlet wavelet are illustrated in Fig. 2.17.

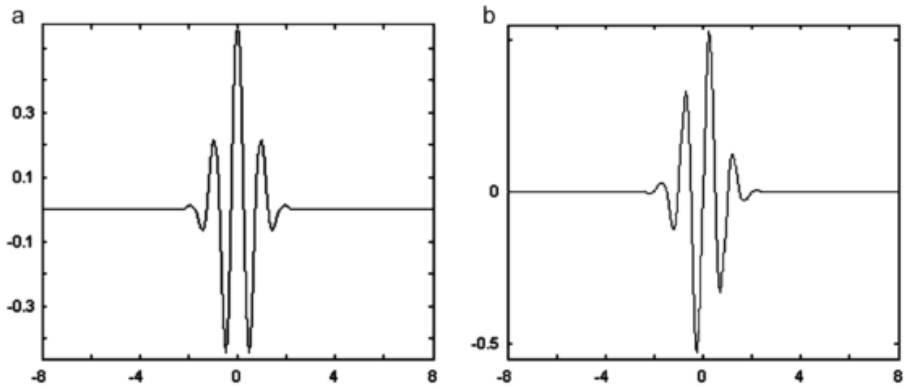


Figure 2.17: (a) The real part of the Complex Morlet wavelet and (b) the imaginary part of the Complex Morlet wavelet [Coo08].

There are two classes of wavelet transforms available when performing a wavelet analysis, namely the Continuous Wavelet Transform (CWT) and the Discrete Wavelet Transform (DWT).

2.6.1.2 Continuous Wavelet Transform (CWT)

The coefficients of the wavelet transform of some data sample or spectrum, $\sigma(E)$, following its convolution with the (generally complex-conjugated) wavelet function are given by:

$$C(\delta E, E_{\mathrm{x}}) = \frac{1}{\sqrt{\delta E}} \int \sigma(E) \Psi^{*} \left(\frac{E_{\mathrm{x}} - E}{\delta E} \right) dE \ , \tag{2.72}$$

where δE is the bin size and is responsible for the scaling of the function. Here, E_{x} shifts the position of the wavelet in excitation energy and thus, provides access to the scale localisation information.

Should the form of a scaled and shifted wavelet, $\Psi(x)$, be remarkably similar to the original spectrum, $\sigma(E)$, the values of $C(\delta E, E_{\mathrm{x}})$ will be large. Similarly, if the form differs greatly, the coefficients obtained will be small. The study of the two-dimensional distribution of the wavelet coefficients allows for, not only the extraction of the characteristic scales, but also for their locations. This is particularly useful for non-stationary processes.

The original spectrum can be reconstructed from the wavelet coefficients through the use of the inverse wavelet transform:

$$\sigma(E) = \frac{1}{K_\Psi} \int_{-\infty}^{\infty} \int_{0}^{\infty} C(\delta E, E_\mathrm{x}) \frac{1}{(\delta E)^{\frac{5}{2}}} \Psi \left(\frac{E_\mathrm{x} - E}{\delta E} \right) d(\delta E) dE_\mathrm{x} \ . \tag{2.73}$$

In the CWT, the scale and location parameters δE and E_x are varied continuously. This is what distinguishes the CWT from the DWT.

2.6.1.3 Discrete Wavelet Transform (DWT)

The DWT is characterised by its configuration in powers of 2. That is,

$$\delta E = 2^k \Delta \tag{2.74}$$

with

$$E_{xk} = k \cdot \delta E_k, \quad k = 1, 2, \dots \ , \tag{2.75}$$

where Δ is the bin size of the data and k is the specification of the number of significant sinusoidal oscillations with a Gaussian window.

The DWT is more suitable for applications such as compression and filtering than the CWT since the DWT represents data more efficiently [Usm09]. One drawback of the DWT is its lack of shift-invariance. The DWT of one function and a shifted version of the same function are thus, not shifted versions of each other.

An overview and summary of the wavelet analysis procedure is provided in Fig. 2.18.

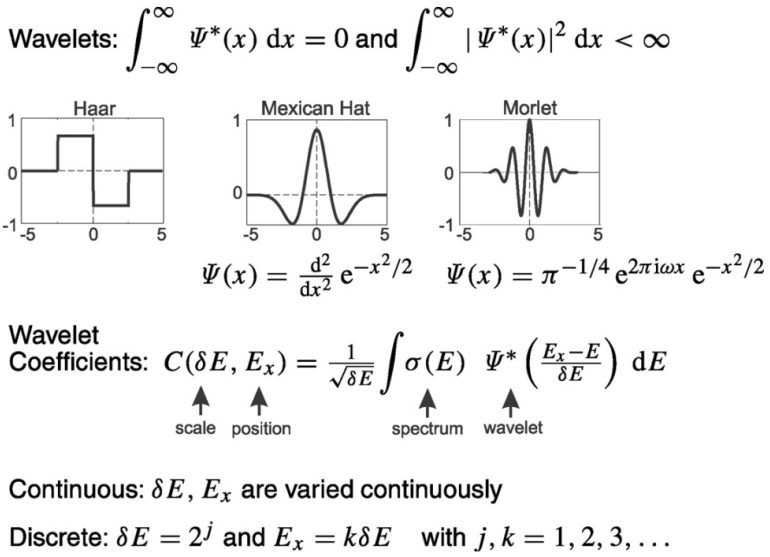


Figure 2.18: An overview of the principles involved in the wavelet analysis procedure [Ric05].

2.6.1.4 Power spectrum

A Fourier transform of the form $\hat{f}(k)$ on a function $f(x)$ can be related to the corresponding Fourier power spectrum $P_f(k)$ as [Jin14]:

$$P_f(k) = |\hat{f}(k)\hat{f}^*(k)| \ , \tag{2.76}$$

up to a normalisation of the spectrum. P, which is the power, is given by the absolute value of the complex vector. In analogy to this, the power spectrum for a CWT case is given by the square root of the sum of the squares of the complex coefficients determined using the complex Morlet wavelet, which yields an equivalent Fourier scale.

2.6.2 Wavelet-based semblance analysis

Semblance analysis compares two datasets on the basis of their phase as a function of frequency [Coo08]. The use of the continuous wavelet transform in the semblance calculation allows for the local phase relationships between the

two datasets as a function of both wavelet (scale) and time to be investigated. The selection of a complex mother-wavelet such as the complex Morlet wavelet given by Eq. (2.71) results in the CWT being complex. This means that the CWT has a phase at each time (or position) and scale [Coo08].

The cross-wavelet transform [Tor98] is one method through which two time series can be compared using wavelets. It is defined as:

$$\mathrm{CWT}_{1,2} = \mathrm{CWT}_1 \times \mathrm{CWT}_2^* \tag{2.77}$$

and is a complex quality with amplitude

$$A = |\mathrm{CWT}_{1,2}| \tag{2.78}$$

and local phase, θ, which ranges from $-\pi$ to $+\pi$ and is given by:

$$\theta = \tan^{-1}(\mathfrak{I}(\mathrm{CWT}_{1,2})/\mathfrak{R}(\mathrm{CWT}_{1,2})) \ , \tag{2.79}$$

where $\mathfrak{I}$ and $\mathfrak{R}$ represent the imaginary and real parts of the transform, respectively.

The use of θ as a measure of phase correlation between two datasets has been found to be ineffective [Coo08] and as such, the concept of semblance was devised and defined as:

$$S = \cos^n \theta \ , \tag{2.80}$$

where n is an odd integer greater than zero. When using S (as opposed to θ), the values range from -1 (inversely correlated) through zero (uncorrelated) to $+1$ (correlated). The semblance analysis technique and its applications are detailed in [Coo08].

Chapter 3

Experimental details and data extraction

The experiments for the investigation into the influence of the proton core on the fine structure of the Isovector Giant Dipole Resonance (IVGDR) across the neodymium isotope chain and a correspondingly highly deformed samarium isotope were performed at the iThemba Laboratory for Accelerator Based Sciences (iThemba LABS), situated near Somerset West in the Western Cape, South Africa. The recently commissioned Zero-degree Facility of the K600 magnetic spectrometer was used in conjunction with a dispersion-matched proton beam, which was delivered from the Separated Sector Cyclotron (SSC) of iThemba LABS.

This chapter will provide an overview of the experimental equipment and techniques used during these experiments. In particular, being one of the first projects to use the Zero-degree Facility, extensive detail is provided in the sections critical to set-up and successful running of the experiment.

3.1 Accelerator facility

A schematic overview of iThemba LABS with specific reference to the facilities used during these experiments is given in Fig. 3.1. Clearly indicated in this figure is the Separated Sector Cyclotron (SSC), which is in essence the heart of

iThemba LABS. The SSC is fundamental to all processes undertaken by the lab as it delivers beams to the hospital wing for proton and neutron therapy, beams required for radioactive isotope production as well as beams ranging from light to heavy ions (including polarised light-ion beams) for nuclear physics research. The experimental facilities used for this nuclear physics research can be divided into a number of groups, namely: the K600 magnetic spectrometer, which will be discussed in detail in Section 3.2, the A-line nuclear reaction scattering chamber, and the gamma detector array AFRODITE.

As can be seen in Fig. 3.1, there are two injector cyclotrons, both with a K-value of 8: Solid Pole injector Cyclotron 1 (SPC1), which has an internal ion source, namely the Penning Ionisation Gauge (PIG); and Solid Pole injector Cyclotron 2 (SPC2), which can be used in conjunction with two external ion sources. These external ion sources are the polarised proton ion source and the Electron Cyclotron Resonance (ECR) ion source, which is the ion source used for this set of experiments.

Beginning at the ECR ion source, proton beams are produced through the dissociation of hydrogen gas into hydrogen atoms within a Radio Frequency (RF) field. The required proton beam is injected from the ECR ion source into SPC2. The beam then moves through to the $K = 200$ SSC via the K and J beamlines at which point it is accelerated to the specified energy of 200 MeV. The accelerated protons are transferred to the $K = 600$ magnetic spectrometer by means of a high-resolution double monochromator system consisting of the X, P1, P2 and S beamlines which are indicated in Fig. 3.1. This system makes use of quadrupole magnets, dipole magnets and slits for optimisation.

In order to achieve dispersion matching at 0°, the faint beam technique must be implemented. In order to do this, three beam meshes are positioned between the ECR ion source and SPC2. As a result, it is possible to reduce the number of protons in the beam significantly without changing the ion-optical characteristics of the beam or the beam profile itself. The process of dispersion matching as well as the faint beam technique will be covered in more detail in Sections 3.5.2 and 3.5.3, respectively.

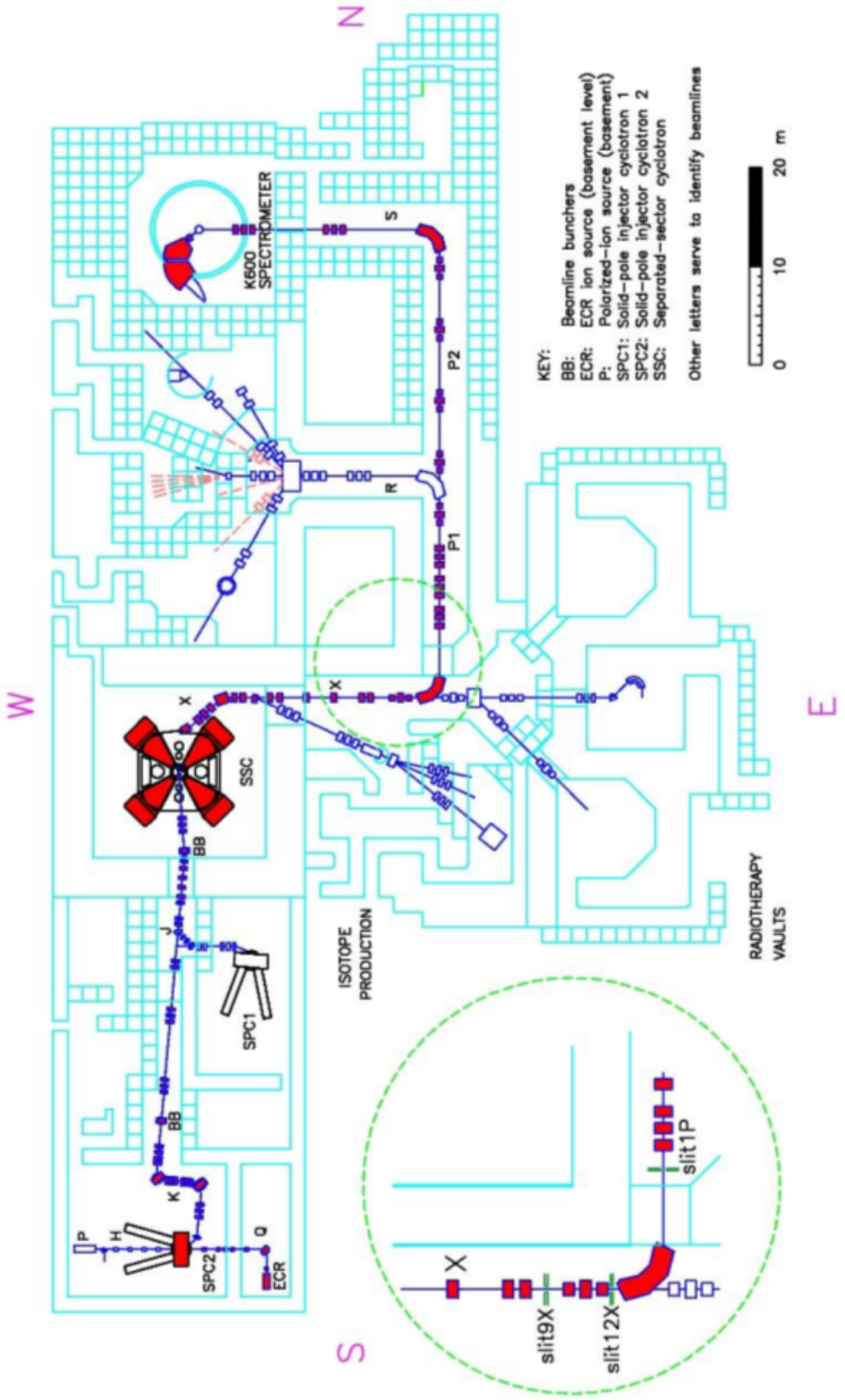


Figure 3.1: A schematic overview of the cyclotron facility at iThemba LABS, where the enlarged section shows the position of the object slit 9X, the emittance slit 12X as well as the first clean up slit 1P.

3.2 K600 magnetic spectrometer

A quadrupole magnet, two dipole magnets (D1 and D2) and two trim coils (K and H) represent the five active elements of the K600 QDD magnetic spectrometer. The layout of these elements is shown in Fig. 3.2. Varying the ratio of the fields of D1 and D2 allows for the momentum dispersion along the focal plane to be varied between the nominal values of 6.2 cm/% and 10.9 cm/%. The result of this variation is three distinct possible focal planes, namely the low-, medium- and high-dispersion focal planes, which are indicated in Fig. 3.2. A quadrupole magnet at the entrance of the spectrometer is used for the purposes of vertical focusing at the focal plane. The final horizontal focussing at the focal plane is achieved through the use of the K and H trim coils, which are pole-face current windings inside the dipoles. Because of its shape, the K-coil has both a dipole and a quadrupole component and is used to compensate for first-order kinematic variations of momentum with θ_{scat} (the horizontal scattering angle), as described by the ion-optical variable $(x|\theta)$. The shape of the H-coil, however, results in a dipole as well as a hexapole component, and is used to correct for $(x|\theta^2)$ aberrations. The different field components can be obtained from the

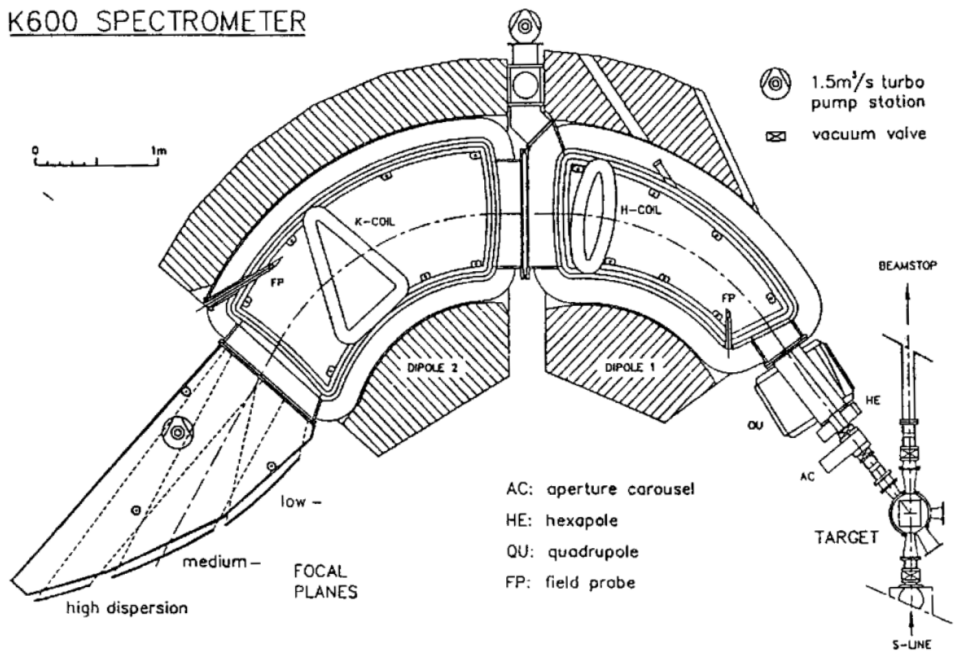


Figure 3.2: A schematic overview of the K600 magnetic spectrometer.

integration of the field along the path of the projectile across the K- and H-coils. This is illustrated schematically in Fig. 3.3.

The collimator carousel, which contains six collimators, is located in front of the quadrupole. At the turning axis of the spectrometer is a scattering chamber, which contains a turntable on which detectors or an internal beamstop can be mounted as well as a target ladder with six target positions. The focal plane detector package, for which details are provided in Section 3.2.1, is located behind the second dipole.

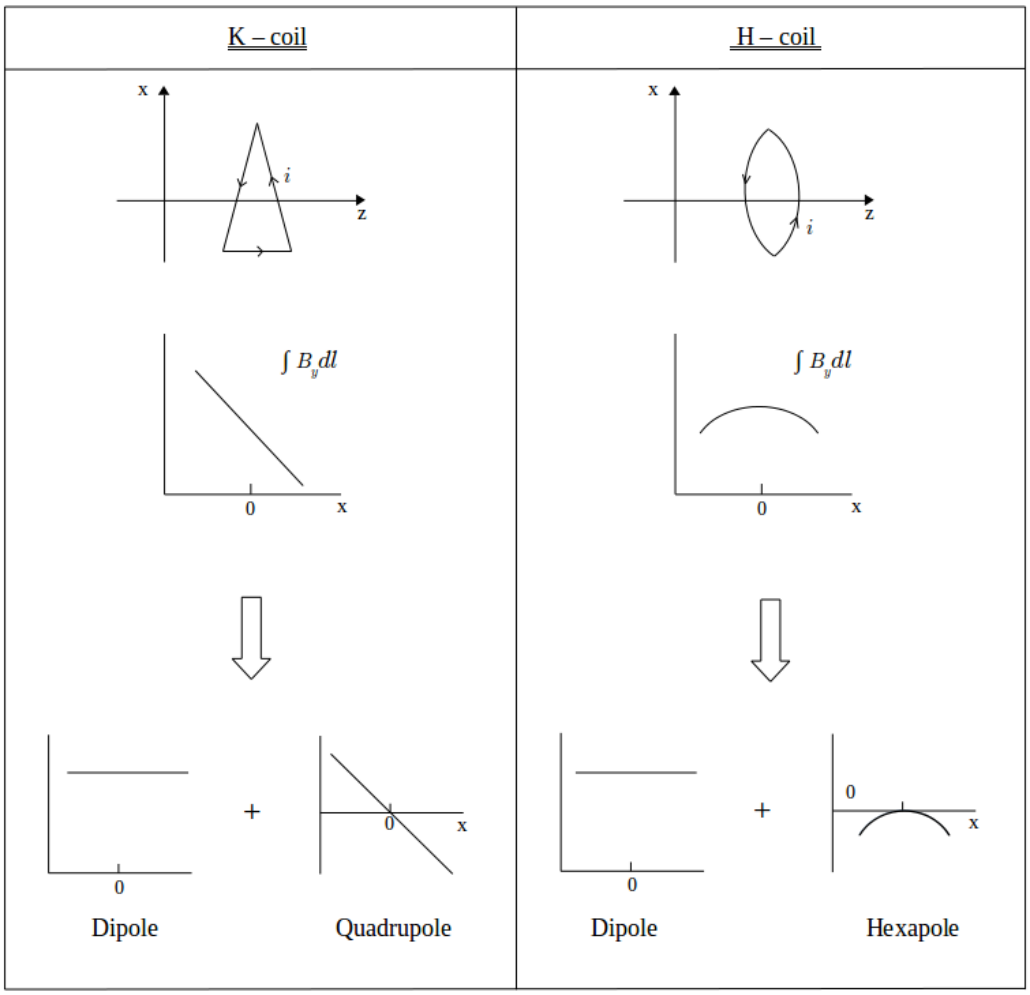


Figure 3.3: Pole-face current windings showing the dipole and quadrupole components of the K-coil as well as the dipole and hexapole components of the H-coil.

3.2.1 Focal plane detector package

The focal plane detector package is composed of two plastic scintillator detectors and two vertical drift chambers (VDCs). Summarised in Table 3.1 are the technical specifications for these detectors.

Table 3.1: Technical specifications for the focal plane detector package

X & U Vertical Drift Chambers	Specification
Wire configuration	vertical (X) and 50° (U)
Horizontal VDC acceptance	78 cm
Vertical VDC acceptance	10 cm
Signal wire	20 μm gold plated tungsten
Guard wire	50 μm gold plated tungsten
Cathode planes	20 μm Al foil
Number of signal wires	198 (X) and 143 (U)
Number of guard wires	199 (X) and 144 (U)
Cathode-anode spacing	8 mm
Signal wire spacing	4 mm
Guard wire spacing	4 mm
Gas mixture	90% Ar and 10% CO_2
Entrance and exit windows	25 μm mylar
Pre-amplifier	Technoland (13 units (X) and 9 units (U))
Typical guard wire voltage	$\sim$ -500 V
Typical cathode plane voltage	$\sim$ -3800 V
Scintillators	**Specification**
Scintillating material	Bicron BC-408
Scintillator dimensions	$48 \times 4 \times 0.5$ (or 0.25) inch^3
	$= 1219.2 \times 101.6 \times 12.7$ (or 6.4) mm^3
Lightguide	Saint Gobain Crystals 90°
	adiabatic twisted pair
Photomultiplier tube (PMT)	Hamamatsu R329-02 PMT tube
	with a Hamamatsu E934 base
Typical PMT voltage	$\sim$ -1700 V for 0.5 inch
for 200 MeV protons	$\sim$ -1900 V for 0.25 inch
Maximum PMT voltage	2700 V

The components of the focal plane detector package are discussed in detail in [Kur14, Jin14] and as such, only a brief description is provided below.

3.2.1.1 Plastic scintillator detectors

The plastic scintillators, which are also referred to as paddle detectors owing to their geometry, are shown in Fig. 3.4. As can be seen, the plastic scintillators, each with dimensions 122 cm $\times$ 10.2 cm, are positioned just downstream from the drift chambers and are very close to the focal plane. The detectors are $1/4''$ and $1/2''$ thick and are wrapped in sheets of aluminised mylar to ensure that they are light tight. Photomultiplier tubes are connected vertically via 90° twisted pair adiabatic lightguides to both ends of each of the scintillators. This configuration allows for the scintillators to be placed close to the beampipe. Used primarily for the provision of event trigger signals, the scintillator detectors are also helpful in particle identification through $\Delta E - \Delta E$ particle identification spectra.

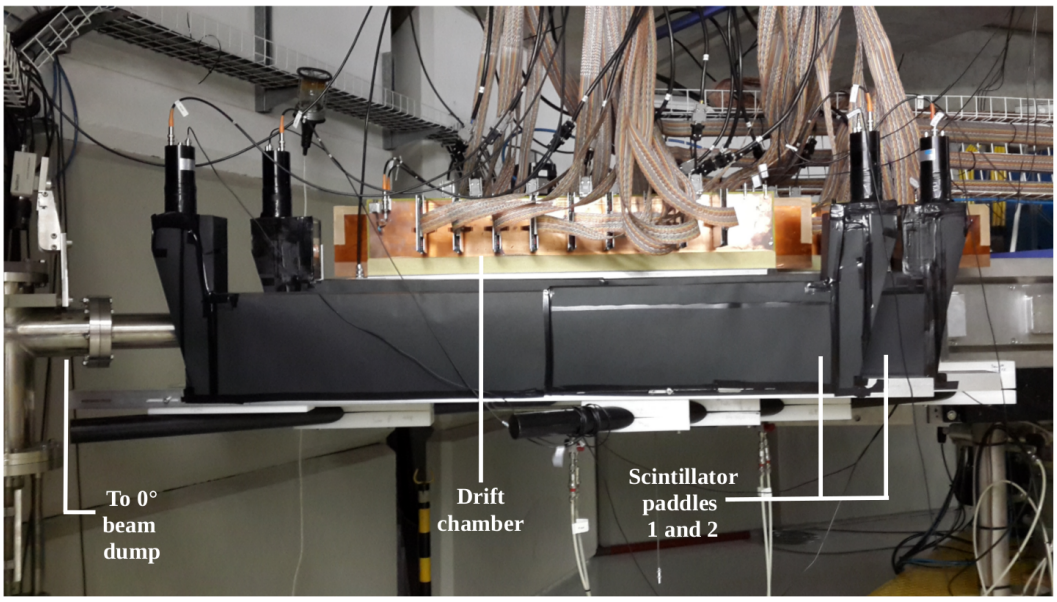


Figure 3.4: The K600 magnetic spectrometer focal plane detector package.

3.2.1.2 Vertical drift chambers

The Vertical Drift Chambers (VDCs) are the means by which the accurate determination of both the horizontal and vertical components of the particle tracks in the focal plane is achieved. This is important in order to determine the particle rigidity and the scattering angle accurately. Each of the VDCs has two wire-planes in an XU configuration. The X-wires are perpendicular with respect to the scattering plane whereas the U-wires are angled at 50°. The interior of the drift chambers is isolated from atmosphere by two 25 μm thick mylar planes, which contain a mixture of 90% Ar and 10% CO_2 gas between them. The position accuracy of the VDCs, denoted σ_x [Ber77], has been found to be ~ 80.9 μm. This factor contributes to the overall position resolution that can be achieved using the spectrometer and also determines the angle accuracy that can be achieved with the VDCs.

3.2.2 Zero-degree mode

The nuclear interaction is by nature complex and results in many contributions to the experimental spectra. Reactions at 0°, however, have the advantage of being highly selective to excitations with low angular momentum transfer. States with low spin and parity are favoured, which results in a simplified analysis of the resultant spectra. iThemba LABS is one of only a few facilities worldwide at which high energy-resolution experiments of this nature can be performed [Nev11b]. This is because a magnetic spectrometer (such as the K600 at iThemba LABS) provides a means by which the primary beam can be separated from the inelastically scattered particles or reaction products.

The zero-degree (p,p′) experiment is unique in that the primary proton beam as well as the inelastically scattered particles pass through the K600 magnetic spectrometer. In the zero-degree mode, the beam passes just 10 cm from the focal plane detectors, which is one of the reasons for the requirement of very little halo. The focal plane detectors are positioned in the high-dispersion focal plane. Of the three focal planes mentioned in Section 3.2, the high-dispersion plane was selected since good separation of the beam from the lowest measurable excitation energy requires high

dispersion [Nev11a]. Once through the spectrometer, the beam moves through the zero-degree beamline to the zero-degree beamdump (a Faraday cup embedded in the concrete wall of the spectrometer vault). In order to assist in the optimisation of the transport through the spectrometer, the zero-degree beamline is equipped with a scintillating viewer, which is just downstream from the last focal plane detector. Figure 3.5 illustrates the positioning of the detectors in the high-dispersion focal plane as well as the zero-degree beamline to the (p,p′) zero-degree beamdump.

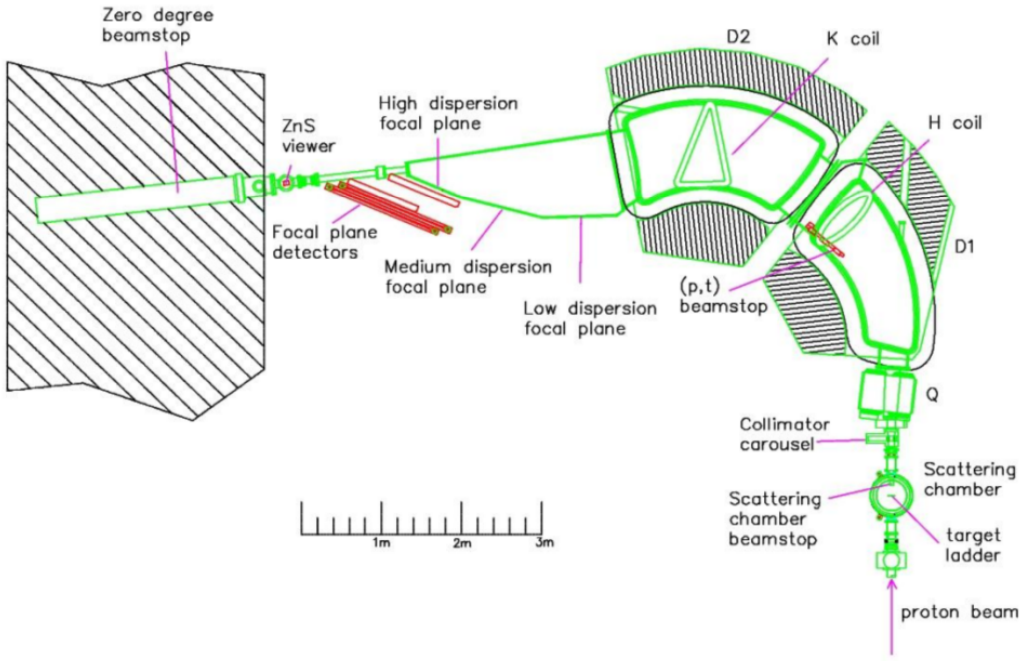


Figure 3.5: A schematic overview of the K600 magnetic spectrometer in the zero-degree mode.

3.3 Data acquisition system

The K600 data acquisition (DAQ) system is comprised of hardware modules which adhere to Versa Module Europa (VME) standards. Signals from the wireplanes are pre-amplified and discriminated by 16-channel electronic cards, which are located on the VDC PC board. The signals are transported to the CAEN V1190A Time-to-Digital Converters (TDCs), which are capable of 100 ps resolution, via 16-channel twisted-pair ribbon cables. As described

in Section 3.2.1, a pair of plastic scintillator detectors is positioned behind the VDCs. The signals from the photomultiplier tubes attached to these scintillators are digitised by a 12 bit current integrating CAEN V792 charge-to-digital converter (QDC). The coincidence of the two scintillator detectors, which are assumed to have 100 % efficiency for the detection of heavy charged particles, forms the trigger signals for the Maximum Integrated Data Acquisition System (MIDAS). MIDAS is widely used in physics experiments and was developed by S. Ritt and P. A. Amaudruz [Rit97].

3.4 Targets

All of the targets summarised in Table 3.2 were prepared in the iThemba LABS target laboratory. The neodymium targets were used in the PhD project by C. O. Kureba and as such, a brief summary of the target preparation is provided here. A more in depth description can be found in [Kur14].

The material for three of the five neodymium targets, namely ^{142}Nd, ^{144}Nd and ^{150}Nd, was supplied by Medical Isotopes as pure metal lumps, which were rolled under argon atmosphere to the desired thicknesses. The Nd_2O_3 material for the preparation of the the remaining ^{146}Nd and ^{148}Nd targets was supplied by Isoflex and these targets were prepared using a vacuum reduction-distillation process.

The material used in the preparation of the ^{152}Sm target was supplied as a pure metal lump by Oakridge National Laboratory and was rolled under inert atmosphere to the desired thickness, as was done with the ^{142}Nd, ^{144}Nd and ^{150}Nd. All thicknesses were measured using a technique called X-ray fluorescence spectrometry (XRF) [Khe11, Khe15].

Table 3.2: A summary of the targets used in this study

Target	Z	N	Areal Density(mg/cm^2)	Isotopic Enrichment (%)
^{142}Nd	60	82	2.51 ± 0.01	98.26
^{144}Nd	60	84	1.92 ± 0.02	97.30
^{146}Nd	60	86	1.99 ± 0.02	97.40
^{148}Nd	60	88	2.62 ± 0.04	90.10
^{150}Nd	60	90	1.82 ± 0.02	96.11
^{152}Sm	62	90	2.32 ± 0.03	98.27

3.5 Experimental procedure

In the case of high energy-resolution experiments at and close to 0°, stringent requirements with regard to beam delivery must be adhered to. The beam must have a small energy spread, a small emittance and very little halo. The stability of these conditions over long periods of time is also of utmost importance in order to ensure the practicality of the measurements. The procedures that must be followed when pursuing a good beam setup are discussed in detail in the subsequent sections.

3.5.1 Background contributions

The susceptibility of a measurement to any beam fluctuations and ensuing background fluctuations is enhanced at zero degrees. This is as a result of the small rigidity difference between the projectiles and the scattered particles [Nev11a]. For these reasons, the minimisation of the background contribution to the observed spectrum in the focal plane is of utmost importance.

The undesirable background, which contributes to the position spectrum in the focal plane, has both beam-related and target-related components. The beam-related component (or beam halo as it is referred to colloquially) is comprised of the beam particles whose coordinates in phase space differ from those of the core beam. The target-related component arises as a result of particles being

elastically scattered off the target itself and subsequently re-scattered off any exposed hardware in the spectrometer [Nev11b].

3.5.1.1 Beam-related background

In the case of 200 MeV protons, the SSC transmission efficiency is subject to limitations of the beam emittance of the accelerator complex. As such, only $50 - 60$ % of the total beam injected into the SSC is extracted from it. The energy spread of the beam as well as its divergence are then defined using slits downstream of the object point (defined by slit 9X), namely slits 12X and 1P, respectively. The result of this is a mere 8 % of the beam extracted from the SSC (that is, 8 % of the already reduced $50 - 60$ %) reaching the target [Nev11b]. The creation of beam halo is an unfortunate consequence of the interaction between the beam and beamline elements such as slits.

A thin-lipped slit at the object point (to minimise background created through small-angle slit-scattering) in conjunction with two 90° bending magnets and four sets of horizontal and vertical clean-up slits ensure that low beam halo conditions can be achieved [Nev11b]. In addition, in an attempt to further minimise beam-related background in a zero-degree experiment, the potential sites at which the beam halo could interact with the beamline material in the last section of the beamline were minimised. The diameter of the S-line beam-pipe was increased from 75 mm to 100 mm. This resulted in the use of quadrupole magnets of larger diameter. The sliding seals of the scattering chamber were modied such that the entrance and exit flanges were increased from round apertures, 40 mm in diameter to 64×64 mm^2 square apertures. The low momentum side of the target frame was also removed, leaving an L-shaped frame in an effort to minimise the number of particles scattered off the frame itself [Nev11a].

In practice, once the cyclotron beam operators have delivered the beam to the K600 experimental area, proper beam alignment has been achieved and the beam spot on the target verified as properly positioned, the background is characterised through a measurement on an empty target while the VDCs are off. The operators minimise the detected count rate by optimising the slit positions and opening sizes. All slits, including 9X and 12X, may be optimised

at the outset of the experiment but thereafter, 9X and 12X values should remain fixed. Once the count rate is at acceptable levels, the background is further characterised using a position spectrum taken with a target.

3.5.1.2 Target-related background

The target-related background is slightly more problematic than the beam halo in that the constituent particles are detected in the focal plane with energies and coordinates that are not significantly different from those of the inelastically scattered particles of interest [Nev11b].

Sensitivity of the target-related background to the geometry of the collimator which defines the spectrometer acceptance has been established. While the minimisation of the material that can induce small-angle scattering is important, there are additional contributions that must be considered, as can be seen in Fig. 3.6. The red spectrum, which represents the case of no collimator, shows substantial background in the form of two distinct bumps in the focal plane position spectrum when compared to data acquired with a 49 mm collimator with an 11 mm thick lip [Nev11a]. This can be explained by the resultant increase in the angular spread of elastically scattered particles following collimator removal. New scattering sources internal to the spectrometer are thus introduced such as the aperture edges of the vacuum valves on either side of the collimator carousel. Another example is the reintroduction of the downstream exit flange of D2 as a scattering source.

Background conditions are optimal when a 49 mm diameter entrance collimator with an 11 mm thick lip, tapered to the angular acceptance is used. This corresponds to a horizontal and vertical acceptance of $\pm$ 1.91°. The background associated with the use of this collimator is relatively featureless, with only a slight increase towards the region of low excitation energy [Nev11a]. Without the brass lip, the number of slit-scattered protons from the inner walls of the collimator increases dramatically. This is owing to the very high elastic scattering cross sections at small scattering angles. The brass lip and in particular the tapered character (shown in Fig. 3.7) provides a compromise between creating additional potential surfaces for slit-scattering and degrading the slit-scattered protons out of the focal plane

energy acceptance region. This is illustrated in Fig. 3.8.

Once low and stable background conditions have been achieved, the conditions for dispersion matching can be realised with the faint beam method.

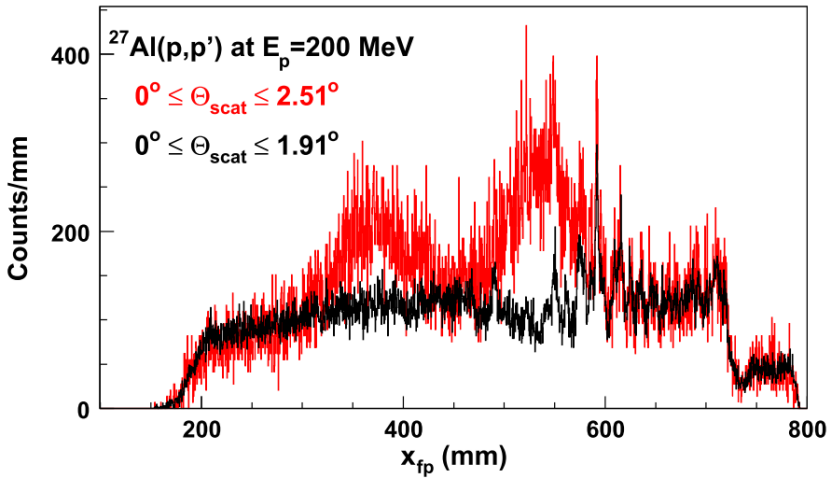


Figure 3.6: A comparison of the focal plane position spectrum acquired for the ^{27}Al(p,p′) reaction at $E_p = 200$ MeV using a 49 mm diameter collimator with an 11 mm thick brass lip (lower black line) to that of the position spectrum acquired without a collimator (upper red line). Note the large background peaks present in the spectrum without the collimator [Nev11a].

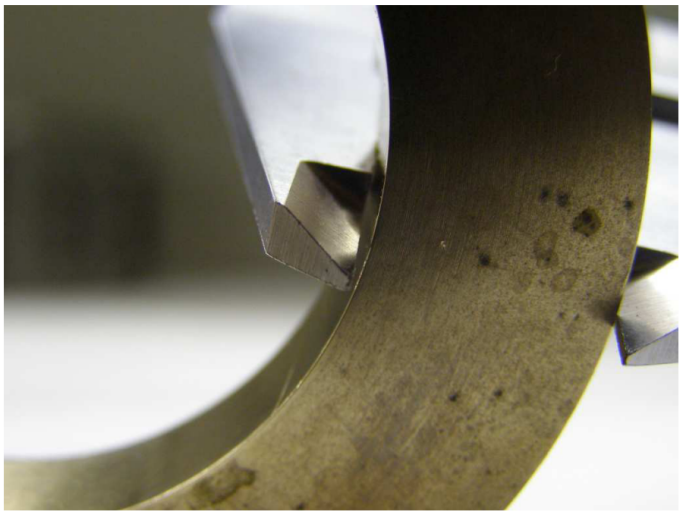


Figure 3.7: The slight tapering of the 49 mm diameter, 11 mm thick entrance collimator.

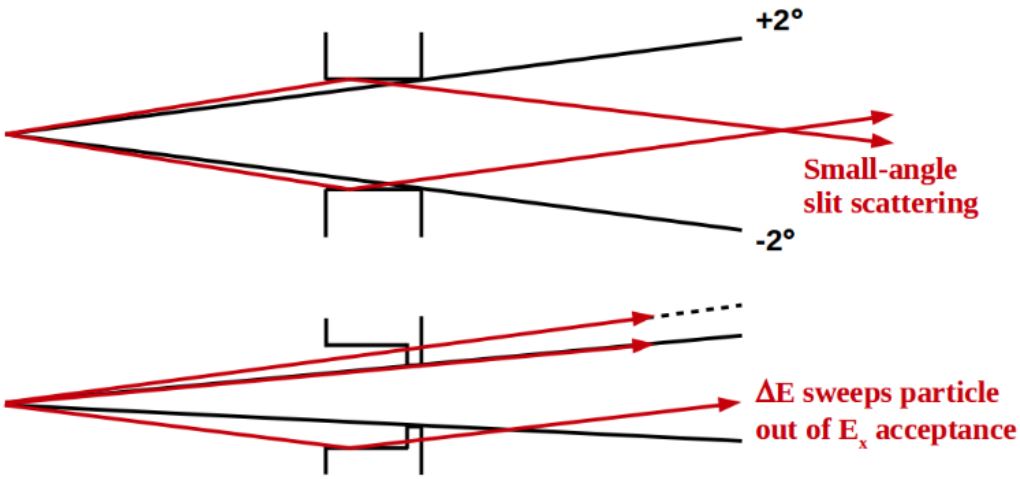


Figure 3.8: An explanatory diagram illustrating the effect of the tapered lip.

3.5.2 Dispersion matching

The purpose of matching the ion optical characteristics of the beamline to the spectrometer is to achieve the best possible spatial definition in the focal plane of the K600 magnetic spectrometer as well as scattering angle definition. Cohen [Coh59] first proposed the concept of dispersion matching, and illustrated that the spectral resolution can exceed the beam energy resolution up to the limit of the resolving power of the spectrometer, provided that the beamline and the spectrometer are properly matched. Blosser *et al.* [Blo71] later demonstrated this concept. Detailed experimental procedures have been developed to achieve the required matching conditions. These procedures include kinematic correction, focus matching, lateral dispersion matching and angular dispersion matching. The successful implementation of these procedures ensures that the full capability of the magnetic spectrometer is achieved [Fuj97].

For a non-dispersion matched beam, it is standard procedure to set up the beam for double-achromatic transport. This means that the beam is set up in such a way that both the position and the angle of the protons on the target are independent of the momentum of the incident proton. Put succinctly, $(x \mid \frac{\delta p}{p}) = 0$ and $(\theta \mid \frac{\delta p}{p}) = 0$ [Eng81] and in TRANSPORT [Bro83] notation, $b_{16} = 0$ and $b_{26} = 0$ [Fuj97, Fuj02, Wak02]. These matrix elements are defined and explained in detail in Appendix A. A consequence of this particular

beamline setup is that the energy resolution in the K600 focal plane is limited by the inherent momentum distribution of the proton beam.

To compensate for this, the protons are spatially separated according to momentum such that the protons with lower momentum will travel shorter distances through the spectrometer than those with higher momentum. For such a dispersion matched beam, an effective achromatic focus in the focal plane is achieved [Fuj02]. A high energy-resolution excitation-energy spectrum but not a high energy-resolution absolute energy spectrum is thus obtained. This assumes that the energy spread of the beam is small enough such that the sensitivity of the nuclear reaction to the different beam energies is negligible.

Figure 3.9 provides a schematic overview of the result of the successful application of the matching procedures discussed above.

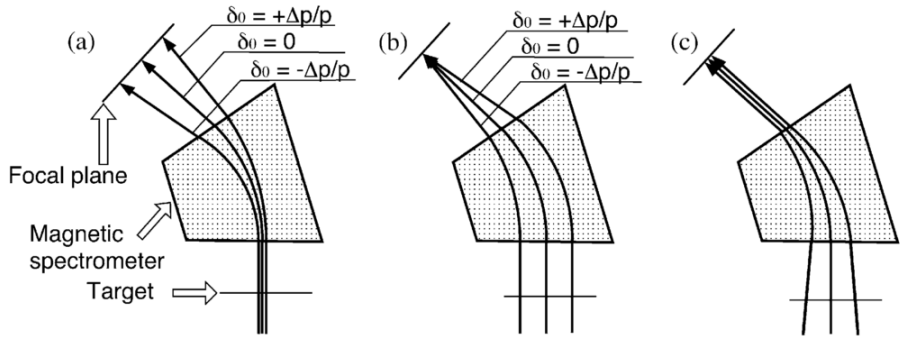


Figure 3.9: A schematic representation of ion trajectories representing particles of different momenta under different matching conditions. The following scenarios are illustrated: (a) achromatic beam transportation where only focus matching is realised; (b) lateral dispersion matching is realised; and (c) both lateral and angular dispersion matching are realised [Fuj02].

As detailed in Appendix A, the position and angle in the focal plane of the spectrometer are given by the following set of equations:

$$
\begin{aligned}
x_{\mathrm{fp}} = \quad & x_0 \quad (s_{11} b_{11} T + s_{12} b_{21}) \\
& + \quad \theta_0 \, (s_{11} b_{12} T + s_{12} b_{22}) \\
& + \quad \delta_0 \, (s_{11} b_{16} T + s_{12} b_{26} + s_{16} C) \\
& + \quad \Theta \, (s_{12} + s_{16} K) \qquad (3.1)
\end{aligned}
$$

$$
\begin{aligned}
\theta_{\mathrm{fp}} = \quad & x_0 \quad (s_{21} b_{11} T + s_{22} b_{21}) \\
& + \quad \theta_0 \, (s_{21} b_{12} T + s_{22} b_{22}) \\
& + \quad \delta_0 \, (s_{21} b_{16} T + s_{22} b_{26} + s_{26} C) \\
& + \quad \Theta \, (s_{22} + s_{26} K) \quad , \qquad (3.2)
\end{aligned}
$$

where the horizontal coordinates $(x_0, \theta_0, \delta_0)$ represent the deviations of the particle trajectory from the central trajectory with respect to the position, angle and fractional momentum at the source point. The elements of the 3×3 beam transfer matrix are given by $(b_{\mu\nu})$ and those of the spectrometer transfer matrix are given by $(s_{\mu\nu})$ where $\mu, \nu = 1, 2, 6$. The subscripts 1, 2 and 6 represent the coordinates of position, angle and fractional momentum, respectively.

The uncertainties in x_{fp} and θ_{fp} are reduced by minimising the beam parameters x_0, θ_0 and δ_0 at the source point. Thereafter, the aim of the subsequent matching procedures is to minimise the corresponding coefficients as far as possible. This addresses the first three terms in Eqs. (3.1) and (3.2) since these terms are dependent on the beam parameters and also on the transfer matrix elements $(b_{\mu\nu})$ and $(s_{\mu\nu})$.

The fourth term of Eq. (3.1), however, depends only on the matrix elements s_{12} and s_{16}. These elements can be eliminated using a procedure called kinematic correction [Fuj02], which is discussed below.

3.5.2.1 Kinematic correction

Kinematic correction is the first step towards high energy-resolution and is achieved by ensuring that

$$s_{12} + s_{16}K = 0 \ . \tag{3.3}$$

In order to achieve this, the magnetic spectrometer field is adjusted such that any particular nuclear state appears upright in the two-dimensional x_{fp} versus θ_{fp} spectrum. That is, when particles with different θ_{fp} from the same state converge at the same position x_{fp}. This is achieved by making changes to the K-coil i.e. adjusting $(x|\theta)$ and thus s_{12} for first order focussing and changing the H-coil for the correction of the $(x|\theta^2)$ aberrations. It is important to note that the ion optical properties of the spectrometer are altered by the kinematic correction procedure which means that it should be achieved before adjusting the coefficients of δ_0 and θ_0.

Following kinematic correction, x_{fp} must be made independent of the momentum spread and angle at the source point. With the coefficients of θ_0 and δ_0 adjusted to zero (focus matching and lateral and angular dispersion matching respectively), then the smallest possible focal plane image and as a result, resolution, is dictated by the only remaining term $x_0\left(s_{11}b_{11}T + s_{12}b_{21}\right)$ [Fuj02].

3.5.2.2 Focus matching

As mentioned above, focus matching involves the zeroing of the coefficient of θ_0 in Eq. (3.1). This can be achieved by relocating the focus on the target further downstream from the target [Nev11a]. In the case of a zero-degree experiment, the coefficient of θ_0 is zeroed as a direct result of ensuring that $b_{12} = 0$ if the kinematic correction is realised [Fuj02]. This is because at 0°, $K = 0$ and $s_{12} = 0$ (as a result of Eq. (3.3)) and so, if $b_{12} \neq 0$ then the coefficient of θ_0 is not zero.

3.5.2.3 Lateral dispersion matching

Lateral dispersion matching or simply dispersion matching as it is often called, requires the following condition:

$$b_{16} = -\frac{s_{16}}{s_{11}} \left(1 + s_{11}s_{26}K - s_{21}s_{16}K\right) \frac{C}{T} \tag{3.4}$$

and results in the elimination of the coefficients of the δ_0 term in Eq. (3.1) [Fuj97].

As can be seen in Fig. 3.9(b), rays with different δ_0 are positioned at different positions on the target, which effectively results in a dispersive monochromatic focus of the beam on the target. The dispersion of the spectrometer compensates for the dispersion of the beam at the target and so, an achromatic focus in the focal plane of the spectrometer is achieved [Fuj02].

Prevention of the sensitivity of x_{fp} to the ranges of both θ_0 and δ_0 at the source point, in conjunction with the range of the scattering angles at the target will, in turn, result in the lowering of the ranges for x_{fp} and θ_{fp}. This ultimately means better spatial and angular definition, which is the goal of dispersion matching.

3.5.2.4 Angular dispersion matching

An unfortunate side-effect of the realisation of lateral dispersion matching is the introduction of additional ambiguity in the scattering angle as can be seen in Fig. 3.9(b). The accuracy of the angle definition can be improved by adjusting the angular dispersion, that is, choosing appropriate incident angles for beam rays with different δ_0 at the target [Fuj02]. This can be seen in Fig. 3.9(c). Angular dispersion matching requires the following condition:

$$b_{26} = \left(s_{21}s_{16} - s_{11}s_{26}\right) C \ . \tag{3.5}$$

Equations (3.4) and (3.5) illustrate the contrast between the focus settings for lateral and angular dispersion matching and those for achromatic focus where $b_{16} = b_{26} = 0$.

Angular dispersion matching is particularly important if information about the scattering angle is crucial as is the case with zero-degree experiments. For precise determination of the scattering angle, measurements of both the horizontal and the vertical angle components are necessary. In order to measure the vertical angle component, however, the system must be run in an off-focus mode in the vertical direction [Fuj01]. In this mode, particles with different vertical angles from the target are transported to different vertical positions in the focal plane. It is, therefore, possible to obtain ϕ information from y_{fp} measurements. Unfortunately, it is impossible to run in off-focus mode for 200 MeV (p, p') measurements at iThemba LABS. This procedure did not, therefore, form part of the method used in this experiment, but it has been discussed for completeness.

3.5.2.5 Matched system

The successful implementation of the above-described matching procedures results in the matched system having a resolving power which is given by:

$$R = \left(\frac{1}{2x_0}\right)\left(\frac{s_{16}}{M_{\mathrm{ov}}}\right) \ , \tag{3.6}$$

where M_{ov} is referred to as an overall magnification and is the coefficient of the x_0 term in Eq. (3.1), i.e. $(s_{11}b_{11}T + s_{12}b_{21})$ [Fuj97]. With matching conditions fulfilled, M_{ov} is given by:

$$M_{\mathrm{ov}} = s_{11}b_{11}T - s_{16}b_{21}K \ . \tag{3.7}$$

3.5.2.6 Matching in practice

The iThemba LABS accelerator and beam transport system shown in Fig. 3.1 can be divided into two distinct sections. The first section is comprised of all the components up to the object point (slit 9X), that is, the ion source, SPC2, the SSC and the transfer beamlines. The beam transport system from the object point to the target makes up the second section. With reference to Eq. (A.2) in Appendix A, it is important to note that the vector, $\vec{x_0}$, describes the conditions at slit 9X and the transport matrix, **B**, refers to the beam transport from slit 9X to the target.

Accelerator systems such as the cyclotron facility at the Research Center for Nuclear Physics (RCNP) in Osaka, Japan have the advantage of emittance limiting mechanisms, such as flat-topping for both the injector and main cyclotrons. This allows for the beam object point to be defined without using hardware slits such as 9X as is the case at iThemba LABS [Nev11b]. This also results in a beam energy spread that is small enough so that no beam intensity is lost in the beam transmission to the target [Nev15]. In practice, at RCNP the beam energy spread is optimised by using the width of an elastic scattering peak measured with Grand Raiden as an observable. This is performed with with an achromatic beam tune and with the spectrometer at a finite angle [Tam09].

At iThemba LABS, however, it is necessary to define the size of the beam at the object point by means of a slit. This results in the creation of beam halo. Furthermore the beam energy spread is defined after the first bending magnet downstream from slit 9X. The method of beam optimization followed at RCNP is, therefore, not applicable at iThemba LABS since good resolution for an achromatic beam depends not on the inherent quality of the beam but mainly on the size of the opening of energy selection slit 1P [Nev14]. For this reason, at the start of the experiment, the X, P and S beamlines are set up in the double-dispersive mode [Hin74] and not in the achromatic mode as performed at RCNP.

To provide an indication of the inherent beam quality, the emittance of the beam is measured in the S-line using three harps. As the beam moves through the transport system to the target, the emittance will be conserved

regardless of the magnet focussing or bending operations performed. The emittance is in essence the area of an ellipse in position and momentum phase space. In general, if the emittance of the horizontal and vertical components of the beam are $\sim 5\,\pi\,\mathrm{mm\,mrad}$ and $\sim 1.5\,\pi\,\mathrm{mm\,mrad}$, respectively, then there should be a reasonable chance of success in the endeavour to achieve dispersion matching.

Any kinematic corrections must be made in the next stage of the matching procedure. A calibration target (such as ^{12}C or ^{24}Mg) is placed in beam and the excited states are used to ascertain if any changes to the values of the K- and H-coils are necessary. In most cases, previously applied values for these coils are sufficient and little change is required. Minimal time is spent on this stage since any further corrections can be applied offline during the data analysis procedure. Once the K- and H-coil values are set, they may not be changed at any stage later in the experiment as this will affect the spectrometer matrix elements and thus alter the matching conditions between the spectrometer and the beamline.

The realisation of the final stages of the dispersion matching procedure involves the implementation of the faint beam method which is described in Section 3.5.3. In essence, it must be ensured that the beamline dispersion at the target is matched to the dispersion of the K600 magnetic spectrometer. The beam at this stage is, under normal conditions, well set up and as such, only fine adjustments to the beam dispersion on target are usually required. These adjustments are made by altering the current values of specific quadrupoles in the S- and P-lines by 3 % or less. The dispersion is mainly tuned with Q6S, which also influences the vertical size of the beam spot. The changes in the vertical beam spot size can be corrected for by optimising Q5S. In cases where changes to Q6S are insufficient to achieve adequate resolution, then changes to other quadrupoles such as Q18P and Q21P in the second part of the P-line must be considered. These quadrupoles influence the position of the focal point in front of the second bending magnet (B3P), which can influence the dispersion achieved in the S-line.

3.5.3 Faint beam method

During a finite angle measurement, the ground state of a calibration target (usually ^{197}Au) would be used to achieve dispersion matching. This is, however, not the case for a 0° measurement since the detected excitation energy of the particles, E_x, begins at $E_x \approx 8$ MeV, rendering the ground state unobservable. The faint beam method was thus specifically developed as a means of achieving both lateral and angular dispersion matching in a short time frame for zero-degree experiments [Fuj02].

If a beam going directly into the spectrometer at 0° is used, the matching conditions of the system can be analysed from the beam properties in the focal plane. The only problem with this, however, is that the focal plane detector system cannot handle and will be damaged by normal beam intensities even if the beam current is as low as 1 nA. As a result of this, a beam with far lower intensity of approximately 10^3 particles per second is used [Fuj02]. In the case of iThemba LABS, this faint beam is obtained following the insertion of three beam attenuation meshes between the ECR ion source and SPC2 as can be seen in Fig. 3.10 and Fig. 3.11. These meshes have reduction factors of 10, 100 and 1000, respectively and are configured in such a way that the mesh with factor 100 stands alone to form the first aperture and the two remaining meshes with factors 10 and 1000 are grouped together to form the second aperture.

Listed as APP1 and APP2 in the iThemba LABS accelerator control system, these meshes reduce the number of protons by a factor of 10^2 and 10^4, respectively, while leaving the beam profile and ion-optical characteristics of the beam unchanged [Nev11a]. The meshes are made of special perforated copper plates and can be seen in Fig. 3.11. Additionally, all five of the magnetic elements in the spectrometer are scaled such that the faint beam passes through to the focal plane detectors.

Assuming that the focus condition for zero-degree scattering is achieved, that is, $K = 0$ ($s_{12} = 0$) then the focus, lateral and angular dispersion matching conditions are easily verified by observing the beam image in the x_{fp}-θ_{fp} scatterplot [Fuj02]. The satisfaction of the different matching conditions affects the beam image as is shown in Fig. 3.12.

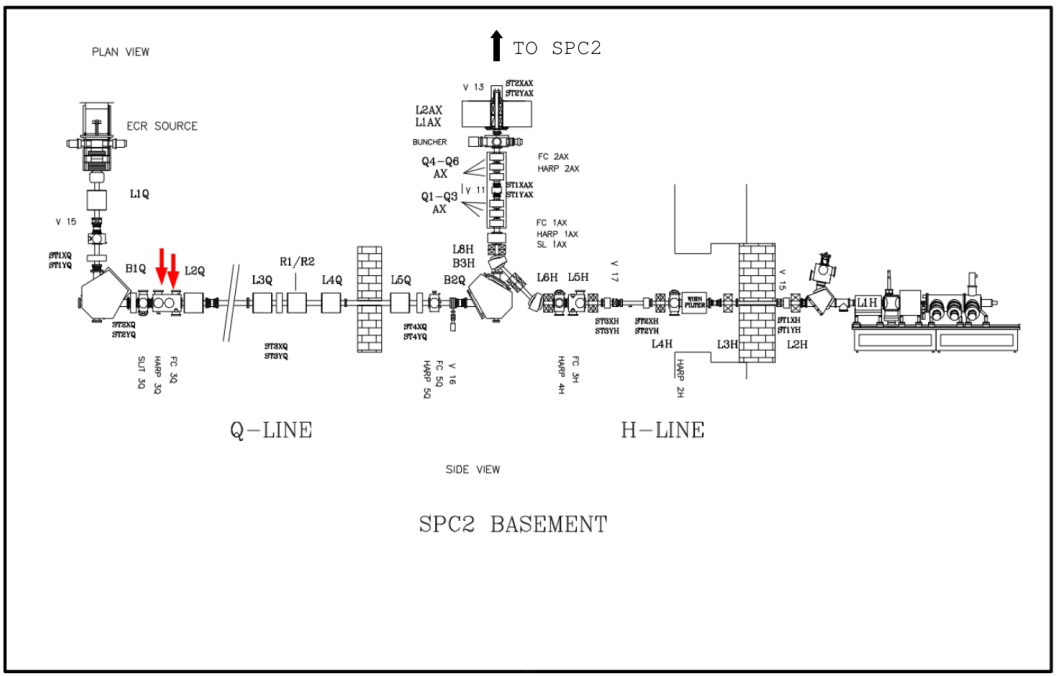


Figure 3.10: A schematic overview of a section of the iThemba LABS beamline where the red arrows indicate the locations of the beam attenuation meshes.

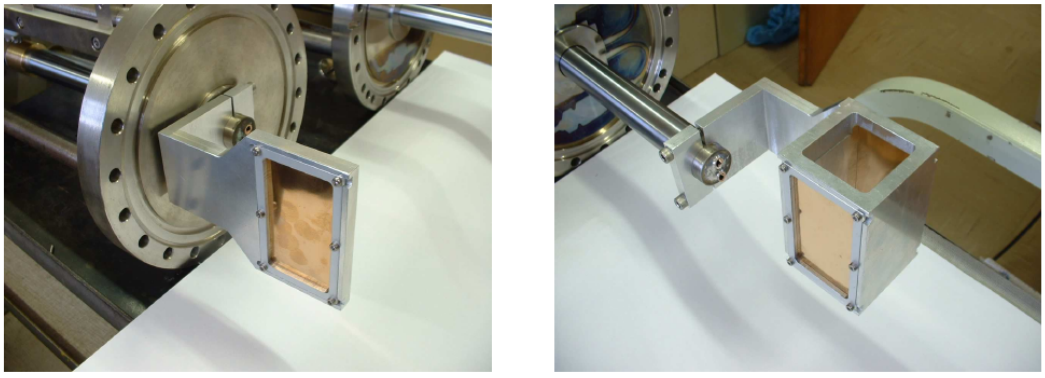


Figure 3.11: Left: The faint beam mesh which allows just 1/100th of the beam to pass through it and Right: the two beam meshes which collectively allow just 1/10000th of the beam to pass through them.

The realisation of all three matching conditions is illustrated in Fig. 3.12(a) where it can be seen that the position and angle spread of the beam have been minimised. In the absence of angular dispersion matching, i.e. when only focus and lateral dispersion matching have been achieved, the width of θ_{fp} increases in the x_{fp}-θ_{fp} image, and is detected as an elongated ellipse in θ_{fp}. This case is

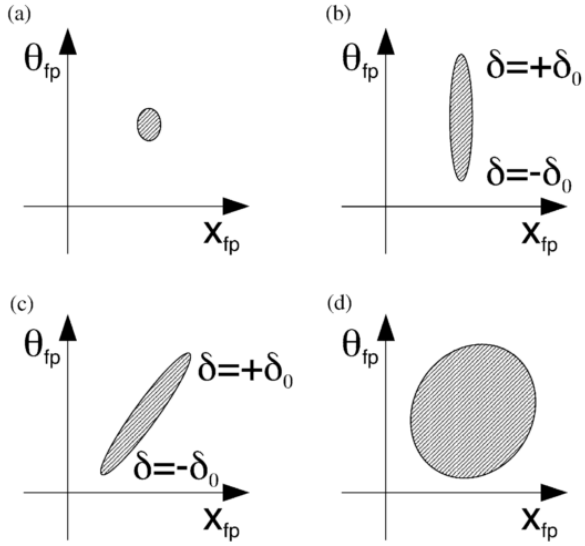


Figure 3.12: The x_{fp}-θ_{fp} image of the beam in the focal plane. The beam ellipses are shown for the cases where (a) focus matching, lateral dispersion matching and angular dispersion matching are realised; (b) only focus matching and lateral dispersion matching are realised; (c) only focus matching is realised and (d) none of the focus, lateral or angular dispersion matching conditions is realised [Fuj02].

shown in Fig. 3.12(b). As was illustrated in Fig. 3.9(a), in the case where only focus matching is achieved, particles with different δ_0 are detected at different positions on the focal plane [Fuj02]. Particles with $\delta_0 = +\Delta p/p$ form one end of the ellipse and particles with $\delta_0 = -\Delta p/p$ form the other end. The ellipse tilts in the x_{fp}-θ_{fp} plane as is shown in Fig. 3.12(c). In the case where none of the three matching conditions is realised, the beam image will be wide in both the x_{fp} and θ_{fp} directions. The minimisation of the faint beam image in the x_{fp}-θ_{fp} plane is thus the ultimate goal of the faint beam technique [Fuj02].

As has been mentioned, it is impossible to operate in off-focus mode for a 200 MeV (p,p′) experiment and thus, to obtain good vertical angle resolution at iThemba LABS. Under dispersion matched conditions for the K600 magnetic spectrometer, therefore, the beam image will more closely resemble the case shown in Fig. 3.12(b) as opposed to Fig. 3.12(a), which is obtained at facilities such as RCNP. Figure 3.13 provides a similar overview to that provided in Fig. 3.12 but now for the K600 magnetic spectrometer and this experiment in particular. The final dispersion matched scatterplot is shown

in Fig. 3.13(c) and closely resembles Fig. 3.12(b), as predicted. Focus matching and lateral dispersion matching are achieved by optimising elements in the P and S beamlines and the size of the beam image in the x_{fp}-θ_{fp} scatterplot is minimised. Faint beam resolutions of $\sim$ 20 keV (FWHM) for 200 MeV protons were obtained in this experiment following this procedure. It is important to note that in the case of the K600 magnetic spectrometer, the beam dispersion required at the target position is much smaller than that of other laboratories. A smaller beamspot on target ($\sim$ 6 mm wide) is thus obtained, which results in an angular dispersion mismatch that is less severe. Since a faint beam measurement is similar to pure zero-degree scattering, a horizontal angular resolution of 0.5° (FWHM) can be estimated from faint beam measurements under dispersion matched conditions [Nev11a].

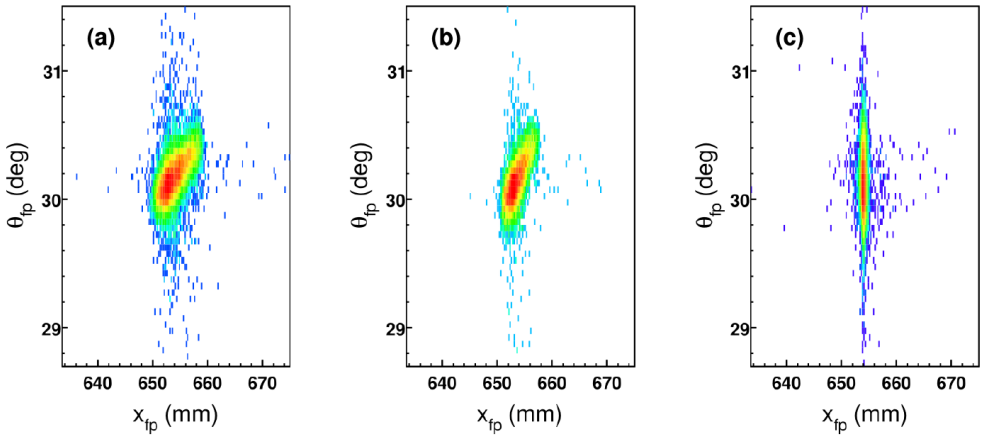


Figure 3.13: The faint beam image in the x_{fp}-θ_{fp} scatterplot for 200 MeV protons at iThemba LABS where (a) no dispersion matching techniques have been applied; (b) only focus matching has been achieved and (c) both focus and lateral dispersion matching have been achieved.

The sensitivity of a zero-degree experiment to any fluctuations in the beam setup is high and as such, additional care must be taken in order to ensure and maintain beam stability [Nev11a]. It is not uncommon for the magnetic fields of the SSC to drift during the initial stages of the experimental period. These drifts may jeopardise the initial dispersion matching conditions and so, small adjustments to the cyclotron acceleration (D-voltage) and the phase of the radio-frequency of the SSC may be made to ensure that the spectrometer remains properly dispersion matched to the beamline. The main coil current

of the SSC may also need adjustment during the first 24 hours to keep the magnetic field isochronised.

3.6 Data extraction

The MIDAS data files that were created during the data acquisition period were analysed offline using ROOT software and specialised scripts created by users at iThemba LABS in C and C++ programming languages. A number of procedures (detailed below) had to be followed in order to extract the important information from the experimentally obtained data files.

3.6.1 Particle identification

As a particle travels through the focal plane detector system, characteristic information is left behind. Particle identification, therefore, is the successful interpretation of this information in order to identify and group the detected particles. The two methods employed in the particle identification procedure are Time-Of-Flight (TOF) selection and a $\Delta E - \Delta E$ technique, that is, the use of information pertaining to the energy loss of the particles through the scintillation detectors.

3.6.1.1 Time-of-flight selection

For TOF selection, it is important to note that the magnetic field setting of the spectrometer only provides information regarding the magnetic rigidity, R, and thus, the momentum, p, of a particle with known charge, q, passing through it. It does not provide information regarding the mass, energy or charge of the detected particle. The radius of curvature, r, and hence the length of the path travelled by the particle through the spectrometer, is related to momentum in the following way:

$$R = rB = \frac{p}{q} \ , \tag{3.8}$$

where B is the magnetic field.

The TOF of a particle is essentially the time it takes the particle to move from its interaction with the target to the point where it is detected in the focal plane. TOF selection is particularly useful because even though different types of particles may have similar rigidities, their different momenta will associate them with different TOFs and thus allow for successful particle identification. Figure 3.14 displays the scintillator pulse height *versus* the TOF spectrum for Paddle 1 for the case where a ^{144}Nd target was used as well as for the case where no target was used. Similar spectra are shown for Paddle 2 in Fig. 3.15. The application of software gates such as those indicated in Figs. 3.14 and 3.15 allowed for the isolation of the inelastically scattered protons of interest.

3.6.1.2 The $\Delta E - \Delta E$ technique

The type of particle and its associated kinetic energy will determine its loss of energy through the scintillation detectors. For this reason, a $\Delta E - \Delta E$ spectrum is valuable when performing particle identification. Ordinarily, the scintillator pulse height would be dependent on the position of the detected particle along the length of the scintillation detector. This dependence was removed, however, by taking the geometrical average of the signals from the two photomultiplier tubes that are placed on the ends of each scintillation detector. Figure 3.16 shows the $\Delta E - \Delta E$ spectrum for the ^{144}Nd case and again, for the case where no target was used. The region containing the protons of interest has been indicated in both spectra. It is important to note that in addition to the particle identification techniques that were applied, the spectrum requires further background subtraction since background events are still present in the region of interest as can be seen in the lower panel of Fig. 3.16.

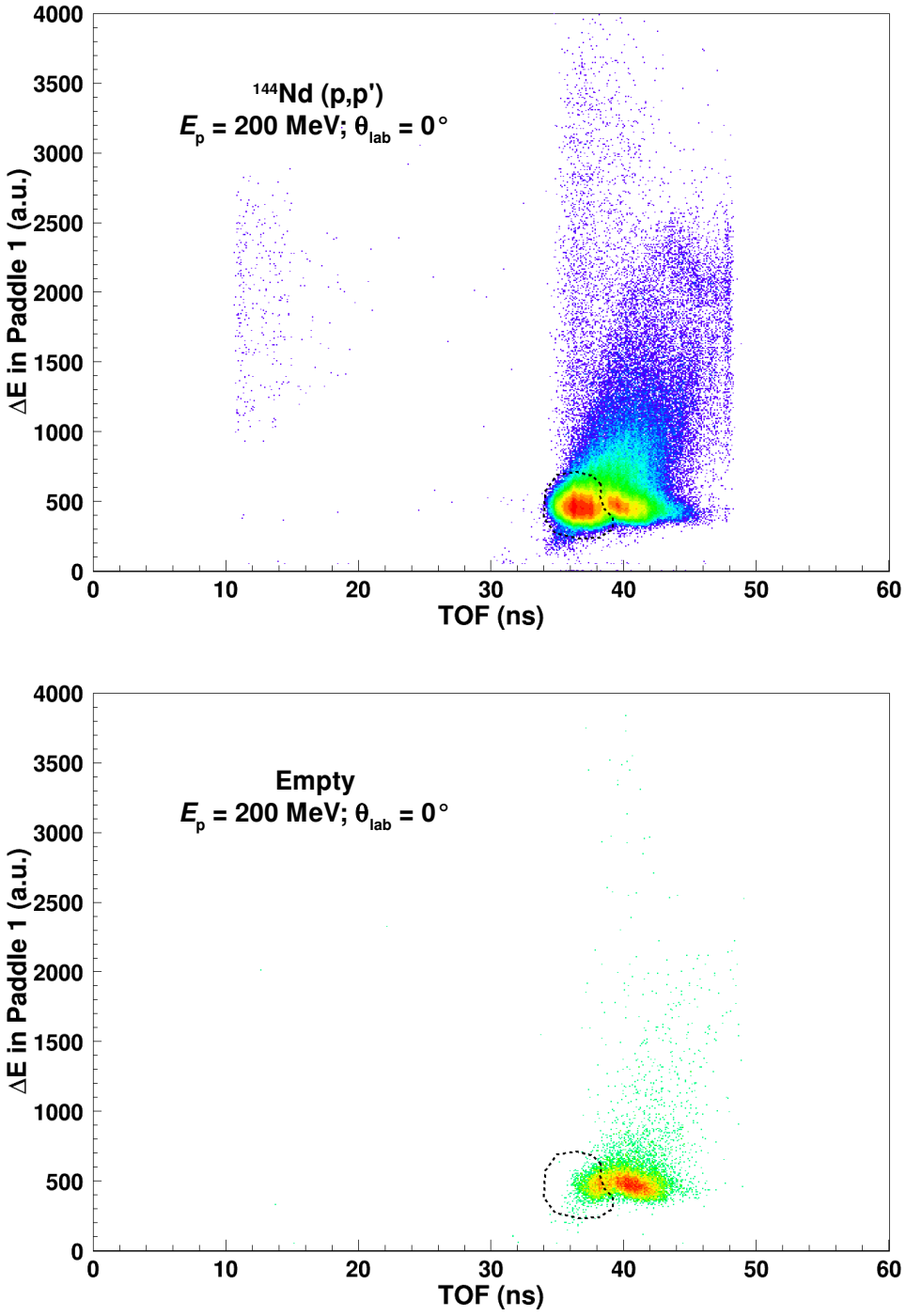


Figure 3.14: The pulse heights in paddle 1 plotted as a function of TOF values for the case where (top) a ^{144}Nd target was used and (bottom) no target was used.

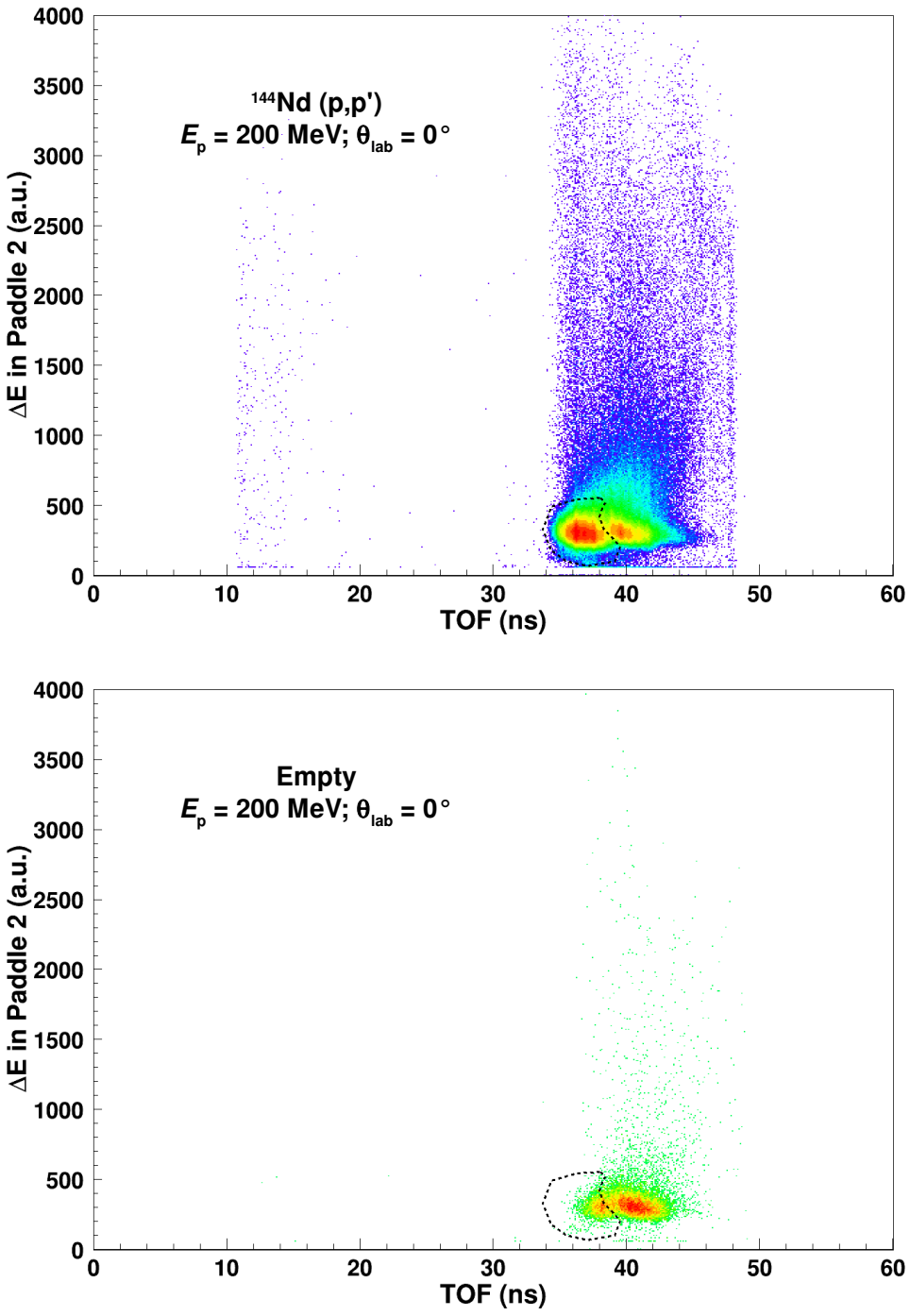


Figure 3.15: The pulse heights in paddle 2 plotted as a function of TOF values for the case where (top) a ^{144}Nd target was used and (bottom) no target was used.

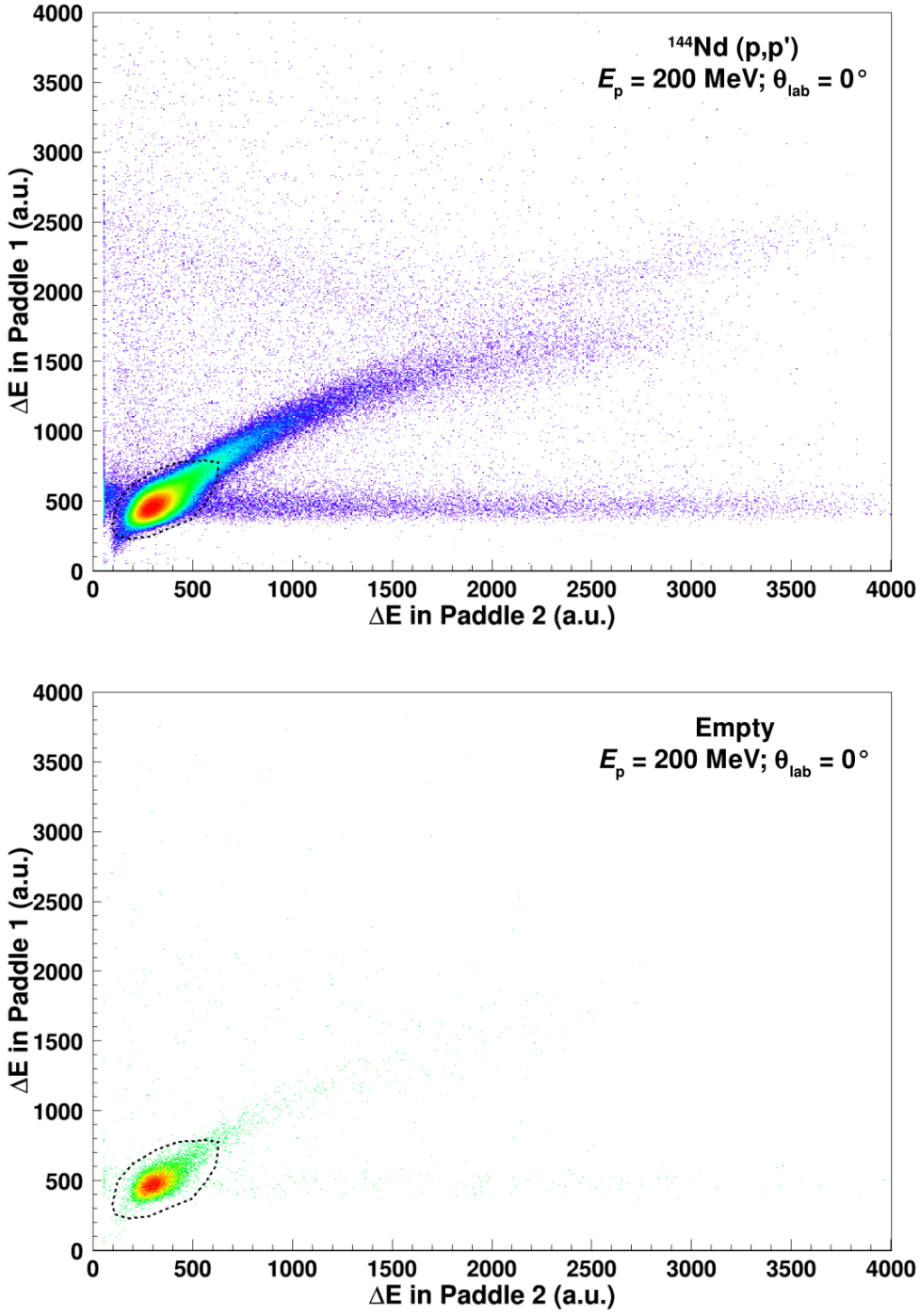


Figure 3.16: The energy loss in paddle 1 plotted as a function of the energy loss in paddle 2 for the case where (top) a ^{144}Nd target was used and (bottom) no target was used. Note that a TOF software gate has not been applied in either of these cases.

3.6.2 VDC data extraction

The procedures that must be implemented to obtain accurate focal plane position information and spatial resolution are detailed extensively in [Nev01], [Kur14] and [Jin14] and as such, are only outlined briefly for completeness.

3.6.2.1 VDC operation and focal plane position determination

Focal plane coordinates are determined by means of a ray-tracing algorithm where drift times in the drift cells of the VDCs are measured and translated to drift distances. Variations in measured drift times owing to variations in ribbon cable lengths (pre-amplifier to TDC) must be corrected for in order to ensure the accuracy of the drift times and ultimately, the accuracy of the excitation-energy spectra. The bulk of the cable length correction procedure described in [Kur14] has since been automated through the use of a C++ script, written by J. J. van Zyl. As such, only minor adjustments are required to correct for any observed variations in the cable lengths. The drift times are then mapped to their associated drift distances by means of a Look-Up Table (LUT). In some instances, these LUTs require offsets. An indication of whether an offset adjustment is required is provided from a two-dimensional resolution (Res2D) spectrum such as those shown in Fig. 3.17.

With reference to Fig. 3.18, the Res2D spectrum displays the relative position in the drift cell where the track crosses the wireplane (referred to in the analysis code as Res0) *versus* the slope difference (Res1), which is given by:

$$\text{Res1} = \frac{d_{\text{first}} - d_{\text{min}}}{w_{\text{first}} - w_{\text{min}}} + \frac{d_{\text{last}} - d_{\text{min}}}{w_{\text{min}} - w_{\text{last}}} \ . \tag{3.9}$$

The effect of a LUT offset is illustrated in Fig. 3.19. The sensitivity of the mapping between drift times and drift distances is highest for shorter distances as can be seen in region C of Fig. 3.19. As such, Res1 is highly sensitive to any LUT offsets for distances at and close to d_{min}. The upper panel of Fig. 3.17 provides an example of the Res2D spectra for the case in which LUT offsets

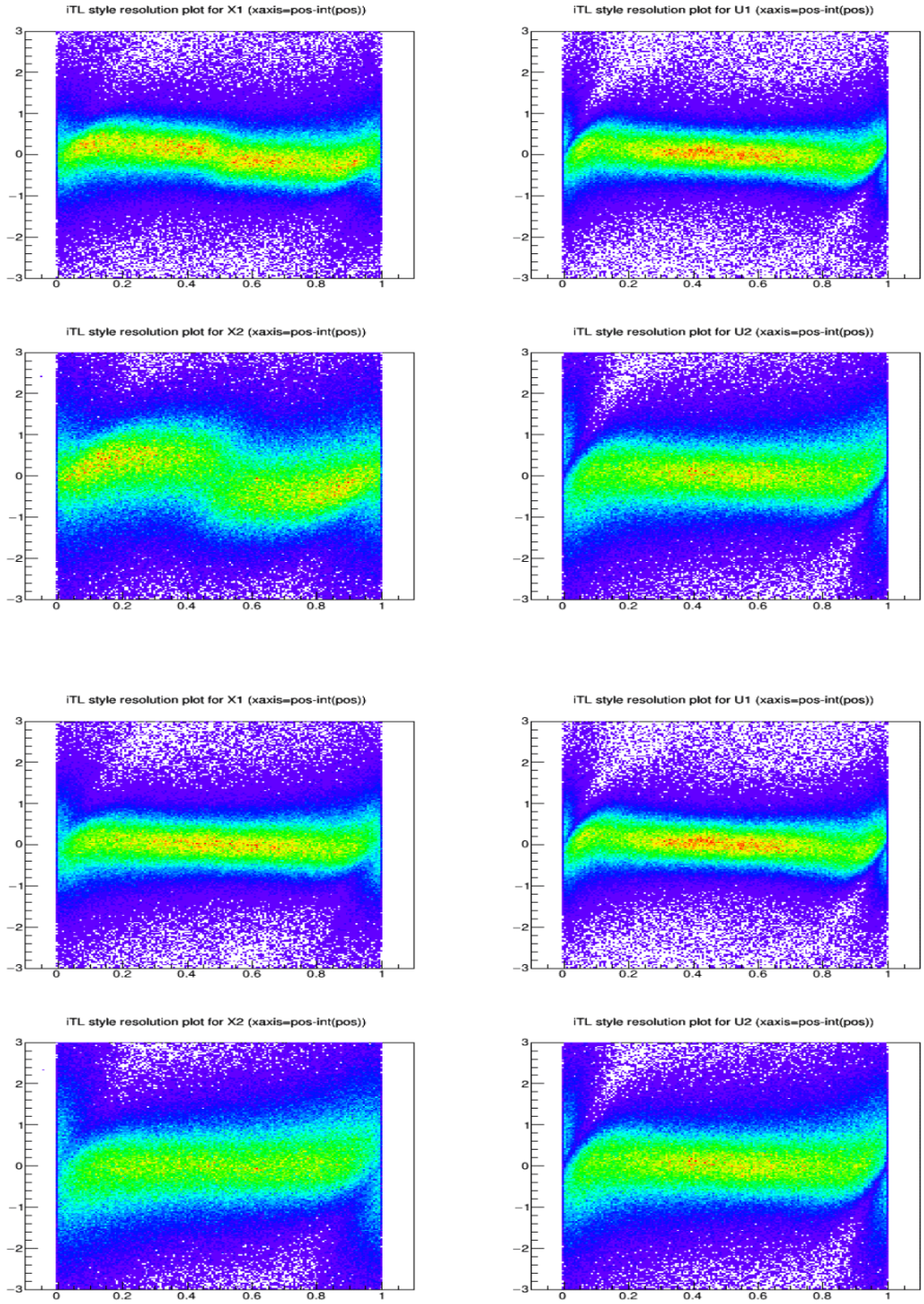


Figure 3.17: The two-dimensional resolution spectra indicating a need for LUT offsets in X1 and X2 (top) and the corrected spectra following the inclusion of LUT offsets (bottom).

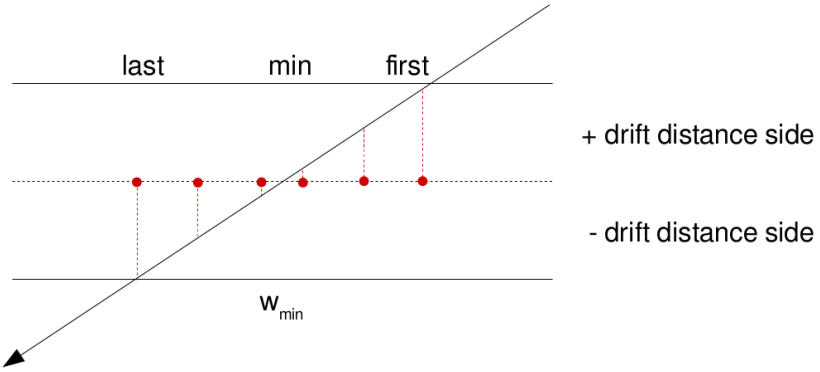


Figure 3.18: A schematic representation of the trajectory associated with a charged particle intersecting the VDC resulting in an event.

are required. The need for the offsets is identified from the misaligned central regions of the spectra. Including a LUT offset allows for the alignment of the central regions and thus for the correct mapping from drift times to drift distances. The corrected two-dimensional spectra following the inclusion of the LUT offsets can be seen in the lower panel of Fig. 3.17.

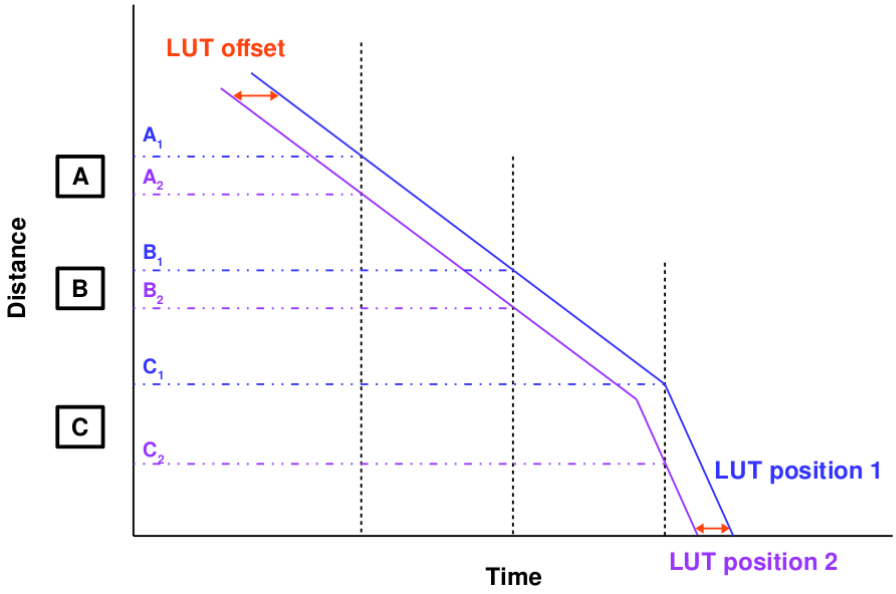


Figure 3.19: A schematic representation of the effect of a look-up table offset.

3.6.2.2 Position resolution

For any n-wire VDC event, the track angle on both sides of the wireplane should be more or less constant. This means that the difference in slopes, given by:

$$D = \frac{d_{t(1)} - d_{t(2)}}{\textit{wire separation}} - \frac{d_{t(n-1)} - d_{t(n)}}{\textit{wire separation}} \tag{3.10}$$

should ideally be equal to zero, where $d_{t(i)}$ is the drift distance as calculated from the drift time t of wire i. Owing to statistical fluctuations, however, a distribution of values around zero is obtained from a number of events.

The formula for the accuracy in the position of the drift chamber is derived in [Ber77] and is given by:

$$\sigma_{\mathrm{x}} = \frac{\sigma_{\mathrm{c}}}{\sqrt{n}} = \frac{\sigma_{\mathrm{D}}}{2\sqrt{n}} \ , \tag{3.11}$$

where σ_{c} is the intrinsic cell accuracy, σ_{D} is the standard deviation of the difference in slopes given in Eq. (3.10), and n is the number of wires used to determine the position. The intrinsic Full Width at Half Maximum (FWHM) position resolution of the drift chamber is, therefore, given by:

$$\mathrm{FWHM_{pos}} = 2.35 \times \sigma_{\mathrm{x}} = 2.35 \times \frac{\sigma_{\mathrm{c}}}{\sqrt{n}} = 2.35 \times \frac{\sigma_{\mathrm{D}}}{2\sqrt{n}} \ . \tag{3.12}$$

By way of example, the typical intrinsic FWHM position resolutions for the four wireplanes were calculated for a neodymium data file and are summarised in Table 3.3.

Table 3.3: A summary of the standard deviations (σ_D) and intrinsic FWHM position resolutions ($FWHM_{pos}$) of the X1, U1, X2 and U2 wireplanes, as calculated for a typical neodymium data file.

Wireplane	σ_D (mm)	$FWHM_{pos}$ (mm)
X1	0.48	0.282
U1	0.45	0.264
X2	0.77	0.452
U2	0.67	0.394

3.6.2.3 VDC efficiency

An indication of how well a VDC is able to detect charged particles in the focal plane is provided by its efficiency, ε, where:

$$\varepsilon = \varepsilon_g \cdot \varepsilon_i \ . \tag{3.13}$$

The geometric efficiency, ε_g, is assumed to be 100%. In the vertically focussed ion-optical mode in which the experiment runs, the particles of a chosen rigidity have been measured to be well-focussed in the vertical direction in the focal plane position and, therefore, the assumption for the geometric efficiency is acceptable. The intrinsic efficiency, ε_i, is given by

$$\varepsilon_i = \frac{N_{accepted}}{N_{total}} \ , \tag{3.14}$$

where N_{total} is the total number of recorded events of a chosen rigidity in the focal plane and $N_{accepted}$ is the number of those recorded events that are considered to be valid. The validity of the events is assessed according to the following criteria:

- TOF and scintillator signals should fall within gated regions,
- the number of hit wires should be between 3 and 6,
- the reduced chi-squared should be less than 1 and

- the drift times should fall within gated regions.

3.6.2.4 Angle calibration

Although angular dispersion matching was not attempted as part of the experimental procedure for this study, the horizontal scattering angle resolution was sufficient to perform a horizontal angle calibration. This angle calibration provides useful information for the lineshape correction procedure, which is explained in Section 3.7.2. The horizontal angle calibration procedure is detailed below.

A series of measurements taken at a finite angle of 7° using a multi-hole (or pepperpot) collimator (shown in Fig. 3.20) was required for the reconstruction of the horizontal scattering angle, θ_{scat}, from the measured focal plane angle, θ_{fp}. The use of the multi-hole collimator results in a series of peaks being observed in the θ_{fp} spectrum. The parameters from Gaussian fits to these peaks as well as the values for their associated focal plane positions were used to determine the θ_{fp} to θ_{scat} conversion equation. The general form of this equation is given by:

$$\theta_{\text{scat}} = (a_1 x_{\text{fp}} + a_0)\,\theta_{\text{fp}} + (b_1 x_{\text{fp}} + b_0) \quad . \tag{3.15}$$

The aim of the calibration procedure, therefore, was to determine parameters a_1, a_0, b_1 and b_0.

Figure 3.21 shows the observed peaks in θ_{fp} as well as the associated Gaussian fits for one of the pepperpot measurements. Shown in Fig. 3.22 is the series of θ_{fp} to θ_{scat} conversions for five different focal plane positions. The values of the slopes from each of these five graphs were plotted as a function of x_{fp} as shown in Fig. 3.23 (a). Parameters a_1 and a_0 were found from the slope and offset of this graph, respectively. Similarly, the parameters b_1 and b_0 were obtained as a result of plotting the offsets from the five graphs in Fig. 3.22 as a function of x_{fp}, as can be seen in Fig. 3.23 (b).

It is important to note that the focal plane angle can be determined using



Figure 3.20: The pepperpot collimator used during experiments at iThemba LABS. The first hole relative to the middle of the collimator on the x-axis/y-axis is centred at 0.819°, the second at 1.679° and the third at 2.251°. These holes span 0.41°.

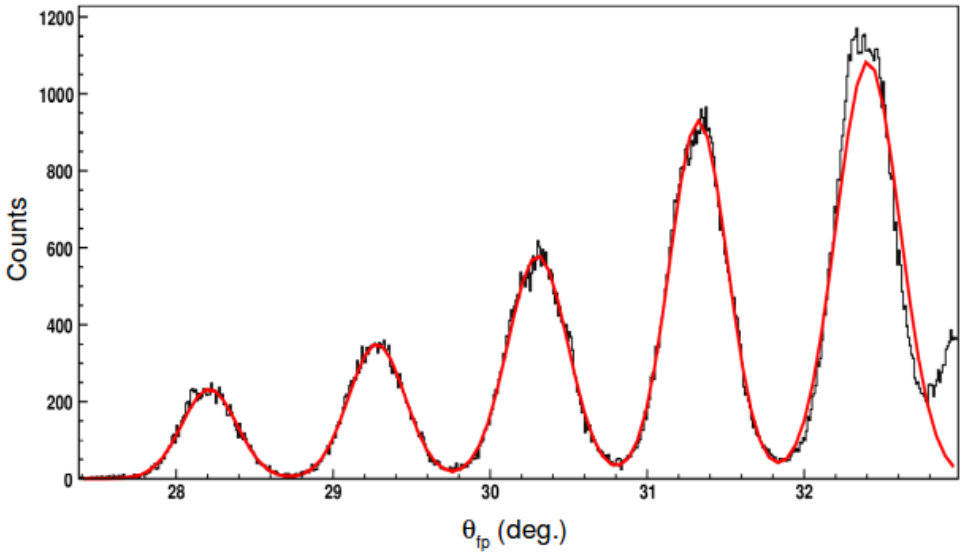


Figure 3.21: A focal plane angle (θ_{fp}) pepperpot spectrum showing Gaussian fits to the observed peaks.

the positions as determined in either the U1 and U2 wireplanes or the X1 and X2 wireplanes. The above-described procedure was performed using the focal plane angle as determined from U1 and U2. In order to investigate the effect of using U1 and U2 as opposed to X1 and X2 on the overall structure of the analysed data, the calibration was also performed using the focal plane angle from X1 and X2. The parameters of this second calibration are summarised in Table 3.4 along with those obtained using U1 and U2. The parameters from the

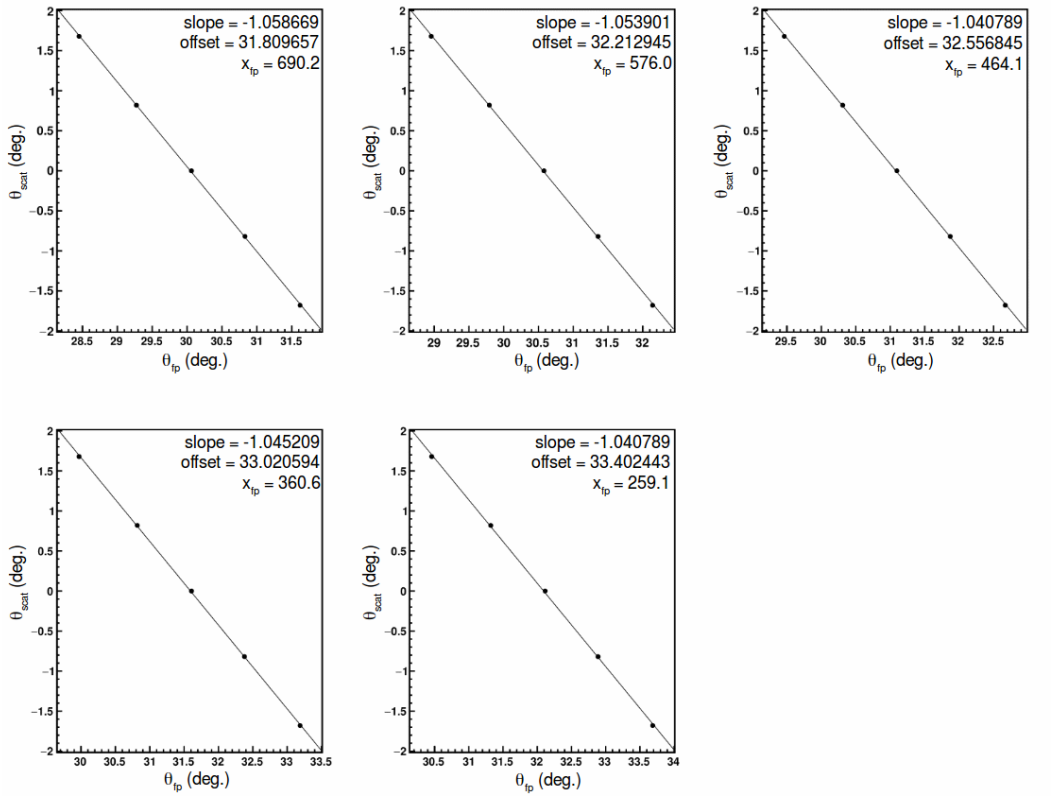


Figure 3.22: Graphs showing the conversion of focal plane angle (θ_{fp}) to scattering angle (θ_{scat}) for five pepperpot spectra with different focal plane positions.

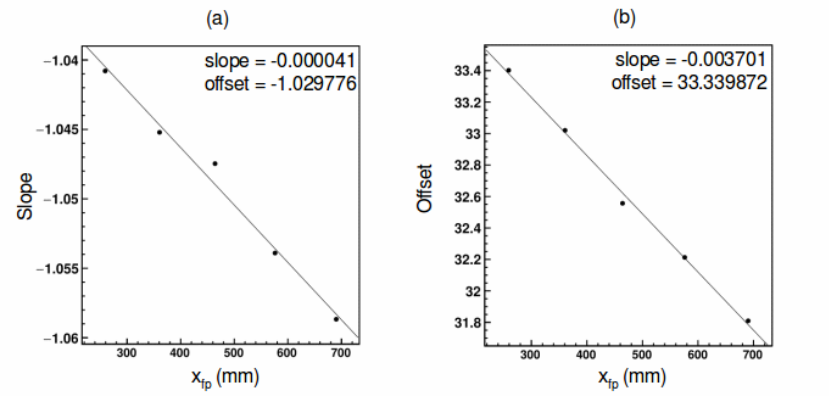


Figure 3.23: Left: The slope as a function of focal plane position (x_{fp}). Right: The offset as a function of focal plane position (x_{fp}).

two methods differ owing to the fact that U and X position reference frames differ. It was concluded, however, that there are no structural differences observed between the two sets of data, as can be seen in Fig. 3.24. Ultimately, since the efficiency in X2 was found to be low during measurements (this

could also be a reason for the slightly lower statistics seen in the X1X2 case in Fig. 3.24), the U1U2 angle calibration was selected.

Table 3.4: A comparison of the parameters obtained for the angular calibration by means of the X and U wireplanes.

Parameter	U1U2	X1X2
a_0	-1.02978	-0.73817
a_1	-4.13417×10^{-5}	-9.20152×10^{-5}
b_0	34.3399	25.6650
b_1	-0.0037008	-0.00198897

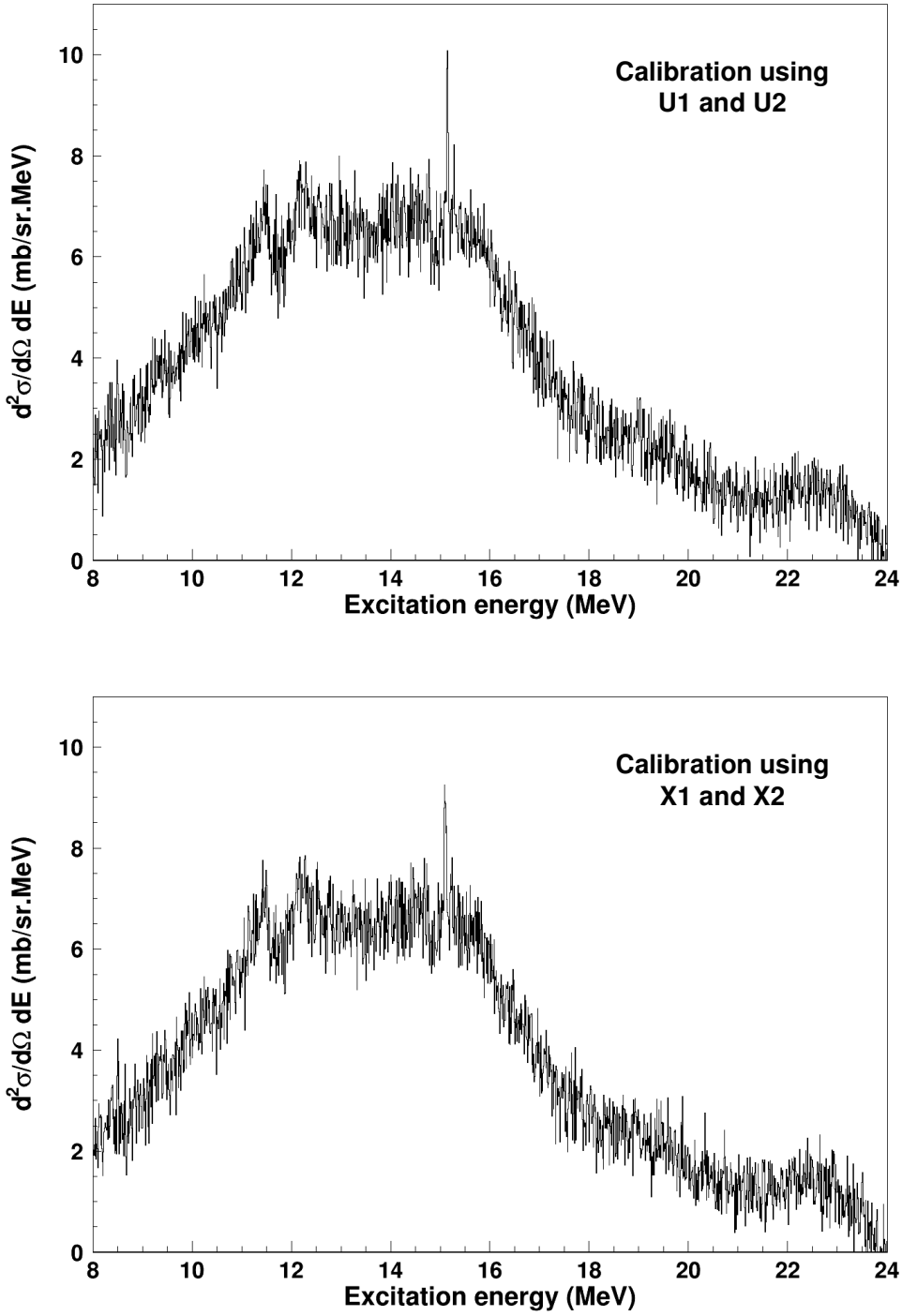


Figure 3.24: The ^{150}Nd double-differential cross section following angular calibration using U1 and U2 (top) and X1 and X2 (bottom).

3.7 Data optimisation

Figure 3.25 displays the two-dimensional spectrum of the TOF values for the detected particles *versus* their focal plane positions for the case where a ^{144}Nd target was used as well as for the case where no target was used. The application of a software gate such as the one indicated in Fig. 3.25 in addition to the gates required for TOF selection in the particle identification procedure allowed for further and more precise proton identification. Following the implementation of the TOF focal-plane position gates, the background subtraction procedure followed. It should be noted that for ease of continuity and comparison, all figures are placed at the end of this section.

3.7.1 Background subtraction

In an attempt to minimise target-related background, the spectrometer was operated in vertical focus mode. This means, in general, that the events of interest are focused around $y_{\mathrm{fp}} = 0$ and that the target and beam related background are evenly distributed in the vertical direction. In this particular experiment, however, centering the spectrum around $y_{\mathrm{fp}} = 0$ resulted in an undesirable amount of beam halo events and as such, the spectrum was shifted slightly by changing the vertical beam position on the target. The result of this is an unequal distribution of the background events above and below the area of interest. The method for background subtraction as described in [Jin14] relies on the x_{fp} *versus* y_{fp} spectrum having two equal background regions. Consequently, the method had to be adjusted for this case.

Figure 3.26 shows the x_{fp} *versus* y_{fp} as well as the y_{fp} projection. The total area of the projection is comprised of the events of interest and the background events. These components were fitted with a Gaussian peak (in blue) and a quadratic background (in red), respectively. The total fit, which is the addition of these components is shown in orange. Fitting the spectrum in this way allowed for the total number of background events directly underneath the area of interest to be determined. An area from the background sections, which contained the same number of background events was then identified

and subtracted in two equal portions as indicated by the green and yellow components in Fig. 3.26 and the upper panel of Fig. 3.27. This ensured that just the right amount of background was subtracted without inducing structure into the region of interest. The result of this procedure is illustrated in Fig. 3.27 for the ^{144}Nd isotope since the component breakdown is more clearly visible than that of the ^{24}Mg case.

3.7.2 Lineshape correction

Lineshape correction is imperative in order to obtain the best possible energy resolution. It corrects the remaining angular dependence of the focal plane position for any nuclear state that was not corrected during the kinematic correction procedure of the experiment. The poor overall resolution, which results from leaving this dependence uncorrected is indicated by a wide excited state such as the one shown in the upper panel of Fig. 3.28. Although the use of the K- and H-coils during the experimental procedure itself provides a reasonable starting point, additional offline adjustments to ensure an upright and well-resolved state are inevitable. To obtain some indication of the extent to which the lineshape of a state must be corrected, point markers were placed at regular intervals along the state in an attempt to reproduce the overall shape of the line. These points were then plotted separately and a polynomial of fifth order, given by:

$$f(x) = f_0 + f_1\theta_{\text{scat}} + f_2{\theta_{\text{scat}}}^2 + f_3{\theta_{\text{scat}}}^3 + f_4{\theta_{\text{scat}}}^4 + f_5{\theta_{\text{scat}}}^5 \tag{3.16}$$

was applied to them. This fit, which reproduces the lineshape of the state shown in the upper panel of Fig. 3.28, as well as the resulting fit parameters are shown in the lower panel of the same figure. The initial lineshape correction equation at this stage is thus:

$$X_{\text{C}_i} = x_{\text{fp}} - \left(f_1\theta_{\text{scat}} + f_2{\theta_{\text{scat}}}^2 + f_3{\theta_{\text{scat}}}^3 + f_4{\theta_{\text{scat}}}^4 + f_5{\theta_{\text{scat}}}^5\right) \tag{3.17}$$

and its application improves the resolution substantially. In order to fine-tune

the resolution even further, a dependence on $y_{\rm fp}$ had to be included. This is because, as stated in Section 3.7.1, the data were not centred around zero and as such, this offset had to be taken into account. By doing this, and thus centering the events around zero, any $y_{\rm fp}$ dependence of $x_{\rm fp}$ does not change the $x_{\rm fp}$ position but simply rotates it around the vertical center of gravity of the lineshape. In almost all cases, a lineshape correction of this form will produce well-resolved states. In a few cases, however, what is seen is that the prominent state (with focal plane position x_0) in the spectrum appears vertically straight and well-corrected but the states around it still have some structure. To correct for this, a dependence of the $\theta_{\rm scat}$ correction factors on $x_{\rm fp}$ must be built in. The general form of the overall lineshape correction equation is, therefore, given by:

$$\begin{aligned} X_{\rm C} = x_{\rm fp} - [&f_1\theta_{\rm scat} + f_2{\theta_{\rm scat}}^2 + f_3{\theta_{\rm scat}}^3 + f_4{\theta_{\rm scat}}^4 + f_5{\theta_{\rm scat}}^5 \\ &+ g_0(y_{\rm fp} + y_{\rm offset}) + g_1(y_{\rm fp} + y_{\rm offset})^2 + h_2(x_{\rm fp} - x_0){\theta_{\rm scat}}^2] \ . \end{aligned} \tag{3.18}$$

An example of the overall effect of the lineshape correction is given in Fig. 3.29 where the upper panel displays $x_{\rm fp}$ *versus* $\theta_{\rm scat}$ for the case where no lineshape correction has been applied and the lower panel displays the resultant spectrum following a full lineshape correction of the form given in Eq. (3.18). The effect of the lineshape correction on the focal plane position spectrum is displayed in Fig. 3.30.

It is important to note that the kinematic differences between the Mg(p,p′) and Nd(p,p′) reactions are very small at and close to 0°. To confirm this, relativistic kinematic calculations were performed to establish the energy of the detected particle in the focal plane for the ^{24}Mg(p,p′) and ^{150}Nd(p,p′) reactions at 0° with $E_p = 200$ MeV. By way of example, the values obtained for an excitation energy of 10 MeV were 189.993 MeV and 189.999 MeV, respectively. At an angle of 1.91°, these values were found to be 189.983 MeV and 189.997 MeV, respectively. The kinetic energy difference between 0° and 1.91° were thus calculated to be 10 keV and 2 keV for the ^{24}Mg(p,p′) and ^{150}Nd(p,p′) reactions, respectively. Small kinematic differences were observed not only at the excitation energy used in the above calculation but over a

wide range of excitation-energy values as well. In the case of the neodymium (and samarium) isotopes, there are no strong states on which to perform a lineshape correction. As a result, the correction had to be made using the information obtained from the correction on the magnesium spectrum. With reference to the values provided in the above calculation, there is an 8 keV difference between the ^{24}Mg(p,p$'$) and ^{150}Nd(p,p$'$) reactions for the $0^\circ - 1.91^\circ$ angle range. The experimental resolution for the neodymium, therefore, is merely the value obtained for the magnesium with the addition of 8 keV.

3.7.3 Data offsets and chained data

Shifts in the focal plane positions of the detected particles occur as a result of the field drifts (owing to day/night temperature changes) and RF changes (owing to optimisations performed by the operators), which affect the beam energy slightly. The particles pass through the K600 magnetic spectrometer just once, but pass through the SSC multiple times during the acceleration process and are thus affected by any modifications to the beam setup. In order to chain the data, that is, combine all relevant data files of a particular isotope, these shifts in the focal plane position had to be taken into account. Figure 3.31 shows the effect of including the position offsets in the chaining procedure as opposed to neglecting them. As can be seen, the position resolution of the chained spectrum is noticeably affected.

3.7.4 Energy resolution

Each of the neodymium (samarium) isotopes is associated with a ^{24}Mg (^{26}Mg) calibration chain. Following the lineshape correction procedure and the inclusion of the data offsets, the energy resolutions could be calculated from the position resolutions for each calibration chain. These resolutions are summarised in Table 3.5.

Table 3.5: A summary of the position (σ_{pos}) and energy (E_{res}) resolutions obtained for each of the ^{24}Mg (^{26}Mg) chains associated with the neodymium (samarium) isotopes.

Calibration Target	Association	σ_{pos} (mm)	E_{res} (keV)
^{24}Mg	^{142}Nd	0.58	42
^{24}Mg	^{144}Nd	0.46	34
^{24}Mg	^{146}Nd	0.52	38
^{24}Mg	^{148}Nd	0.48	35
^{24}Mg	^{150}Nd	0.51	37
^{26}Mg	^{152}Sm	0.46	34

3.7.5 Energy calibration

The excitation-energy calibration is comprised of two subroutines, namely a position to momentum calibration and a momentum to energy calibration. An energy calibration was done for each of the six isotope groups and is detailed below. It is important to note that each target has its own calibration as a result of slight beam energy changes during the different data collection periods.

3.7.5.1 Position to momentum calibration

Following a full background subtraction, lineshape correction and inclusion of position offsets, the predicted excited states were identified in the position spectrum and the respective focal plane positions were paired with the corresponding known values for the excitation energies of those states. The focal plane proton energies of the identified states were then calculated using a relativistic kinematics code and were subsequently converted to momentum (p) values. The focal plane positions were plotted against these calculated momenta. Figure 3.32 shows the calibration graph of the focal plane position *versus* momentum for each of the ^{24}Mg chains associated with the neodymium isotope groups as well as for the ^{26}Mg chain associated with the ^{152}Sm group. A second order polynomial was identified as the best fit in each case and thus, the x_{fp} to p calibration took the form:

$$p = c_1 {x_{\mathrm{fp}}}^2 + c_2 x_{\mathrm{fp}} + c_3 \ . \tag{3.19}$$

The resulting calibration parameters, c_1, c_2 and c_3 are listed for each case in Table 3.6.

Table 3.6: A comparison of the position to momentum calibration parameters for the neodymium and samarium isotope groups.

Parameter	^{142}Nd	^{144}Nd	^{146}Nd	^{148}Nd	^{150}Nd	^{152}Sm
$c_1(\times 10^{-6})$	-4.76716	-5.602811	-5.093214	-5.279774	-4.999880	-4.867092
$c_2(\times 10^{-2})$	6.152266	6.302112	6.214649	6.273241	6.226985	6.160983
c_3	586.7505	586.1297	586.4821	586.1721	586.3582	587.4982

3.7.5.2 Momentum to energy calibration

The equation used for the conversion of momentum to excitation energy is derived from two-body kinematics [Whe14] and is given by:

$$E_x = E_0 + m_1 + \sqrt{{p_2}^2 - {m_2}^2} - \left({p_0}^2 + {p_2}^2 - 2p_0 p_2 \cos(\theta) + {m_3}^2\right)^{\frac{1}{2}} \ , \tag{3.20}$$

where the subscripts 0, 1, 2 and 3 represent the projectile, target, ejectile and recoil nuclei, respectively. The value for p_2 is found as a result of the position to momentum calibration detailed above. The components of Eq. (3.20) were calculated for the calibration nuclei, each of the neodymium nuclei as well as for the ^{152}Sm nucleus and the conversion from excitation-energy calibration was implemented across all of the datasets.

3.7.5.3 Excitation-energy spectra: ^{24}Mg and ^{26}Mg

The calibrated ^{24}Mg and ^{26}Mg excitation-energy spectra can be seen in Fig. 3.33 and Fig. 3.34, respectively. A magnification of the region containing

the identified states used in the calibration is also included in both cases. A comparison of the energy values for the excited states of ^{24}Mg obtained in this work and those given by the National Nuclear Data Center (NNDC) can be found in Table 3.7. The same can be found in Table 3.8 for the ^{26}Mg excited states.

Table 3.7: A comparison of the energy values for the excited states of ^{24}Mg obtained in this work and those provided by the NNDC [Fir07].

J^{π}	NNDC (MeV)	iThemba LABS (MeV)	Difference (MeV)
0^+	9.30539	9.30712	0.00173
1^+	9.82811	9.82872	0.00061
1^+	9.96719	9.96602	0.00117
1^+	10.7117	10.7105	0.00124
0^+	11.7281	11.7255	0.00260
1^+,2^+	12.5265	12.5257	0.00080
1^+,2^+	12.8159	12.8175	0.00160
1^+,2^+	12.9549	12.9579	0.00300
Not assigned	13.8790	13.8757	0.00330

Table 3.8: A comparison of the energy values for the excited states of ^{26}Mg obtained in this work and those provided by the NNDC [End98].

J^{π}	NNDC (MeV)	iThemba LABS (MeV)	Difference (MeV)
1^+	9.23870	9.23851	0.00019
1^+	9.56000	9.56432	0.00432
1^+	9.77900	9.77161	0.00739
1^+	10.1480	10.1485	0.00050
1^+	10.3190	10.3195	0.00050
1^+	10.6460	10.6483	0.00230
Not assigned	10.8240	10.8171	0.00690
Not assigned	11.1532	11.1570	0.00380
Not assigned	11.4639	11.4707	0.00680
Not assigned	11.5408	11.5431	0.00230
6^-	12.8650	12.8620	0.00300

The ^{24}Mg and ^{26}Mg excitation-energy spectra obtained in this work were compared to those obtained at RCNP [Tam15]. These comparisons were

made with two outcomes in mind, the first being the verification of the peak identification and rough calibration. The second outcome was the verification of any broad structures observed in the spectra as a means of assessing whether any additional structure had been induced as a result of problems with the experimental setup. Figure 3.35 displays the comparison for both the ^{24}Mg and ^{26}Mg cases.

3.7.6 Double-differential cross sections

The experimental double-differential cross section for the inelastic proton scattering reaction, which has units of mb sr^{-1} MeV^{-1}, is given by:

$$\frac{d^2\sigma}{d\Omega dE} = \frac{10^{27}\cdot N_{\mathrm{c}}}{N_0\cdot\rho\cdot D\cdot\Delta\Omega\cdot\Delta E\cdot\varepsilon_{\mathrm{tot}}} \ , \tag{3.21}$$

where

N_{c}	is the corrected number of counts in a bin,
N_0	is the total number of incident protons on the target,
ρ	is the number of target nuclei per unit area (in mb^{-1}),
D	is the electronic dead time correction factor, which ranges from 0.994 to 0.997 for this set of experiments,
$\Delta\Omega$	is the solid angle of the K600 magnetic spectrometer in sr and has a value of 3.41 sr,
ΔE	is the energy bin size (in MeV) and
$\varepsilon_{\mathrm{tot}}$	is the total VDC efficiency of the K600, which ranges from 0.65 to 0.71 for this set of experiments.

The number of incident protons, N_0, is calculated by:

$$N_0 = \frac{CI\cdot R\cdot 10^{-12}}{e} \ , \tag{3.22}$$

where

CI	is the scalar read-out of the current integrator,
R	is the selected range (in nA) of the current integrator, which represents 1000 counts per second for a full scale current read-out and
e	is the proton electric charge (in coulombs).

The number of target nuclei per unit area, ρ, is given by:

$$\rho = \frac{\lambda \cdot N_A}{A} \ , \tag{3.23}$$

where

λ	is the target thickness (in gcm^{-2}),
N_A	is Avogadro's number and
A	is the mass number of the nucleus in question.

The calculation of the total VDC efficiency, $\varepsilon_{\rm tot}$, depends on which wireplanes were used for the angle calibration (described in Section 3.6.2.4). In this study, the U1 and U2 wireplanes were used and so, the total VDC efficiency is calculated as follows:

$$\varepsilon_{\rm tot} = \varepsilon_{\rm X1} \times \varepsilon_{\rm U1} \times \varepsilon_{\rm X2} \times \varepsilon_{\rm U2} \ , \tag{3.24}$$

where $\varepsilon_{\rm X1}$, $\varepsilon_{\rm U1}$, $\varepsilon_{\rm X2}$, and $\varepsilon_{\rm U2}$ are the efficiencies for the X1, U1, X2 and U2 wireplanes, respectively.

If the X1 and X2 wireplanes had been used for the angle calibration then $\varepsilon_{\rm tot}$ would have been given by:

$$\varepsilon_{\rm tot} = \varepsilon_{\rm X1} \times \varepsilon_{\rm X2} \times \varepsilon_{\rm U2}. \tag{3.25}$$

The double-differential cross sections were extracted for the ^{142,144,146,148,150}Nd nuclei, as well as for the ^{152}Sm nucleus. The associated statistical errors were deduced using the following:

$$\Delta \frac{d^2\sigma}{d\Omega dE} = \frac{1}{\sqrt{N_{\text{counts}}}} \frac{d^2\sigma}{d\Omega dE} \ , \tag{3.26}$$

where N_{counts} is the number of counts per energy bin.

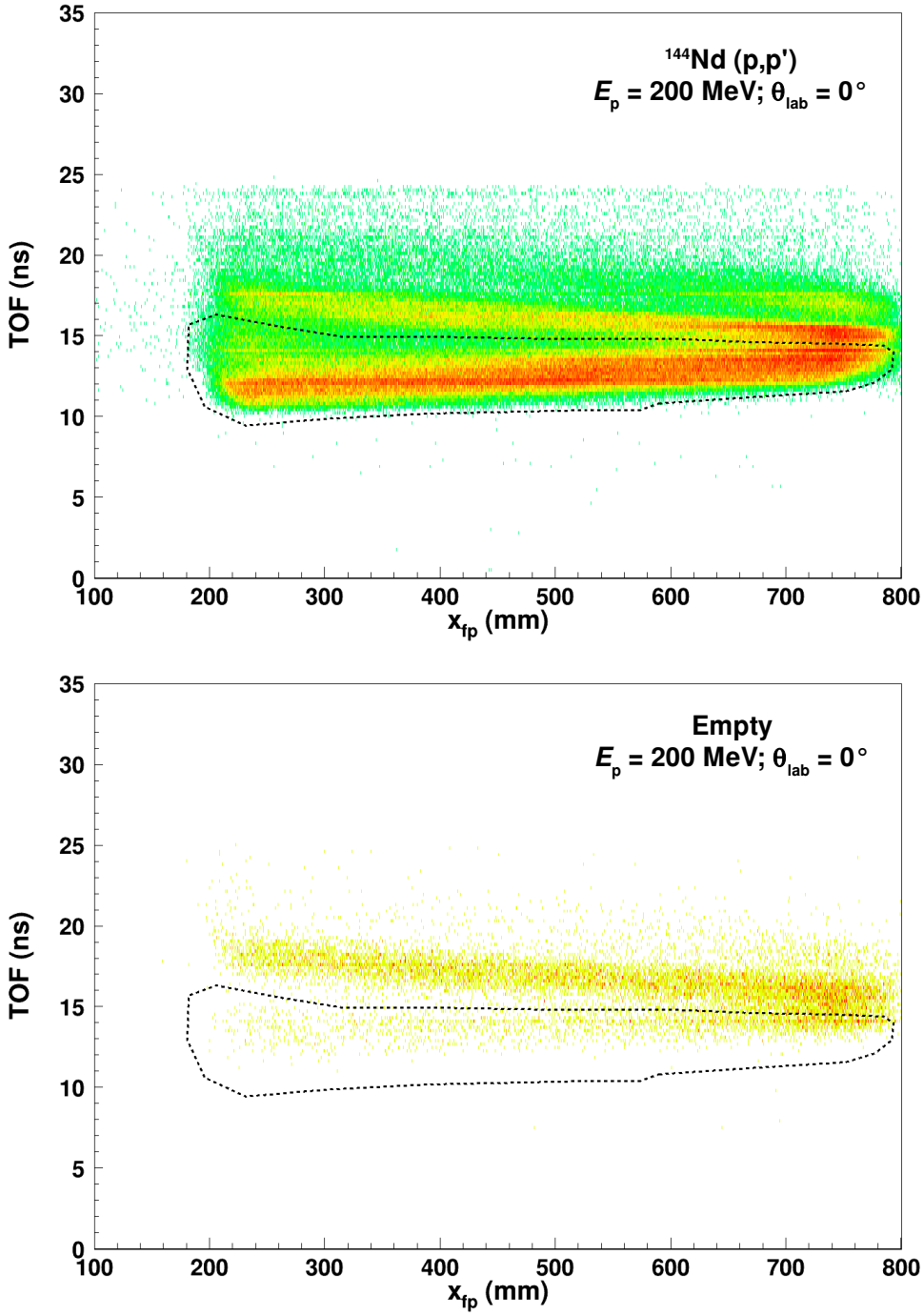


Figure 3.25: The time-of-flight values for the detected particles plotted as a function of their focal plane position in the case where (top) a ^{144}Nd target was used and (bottom) no target was used.

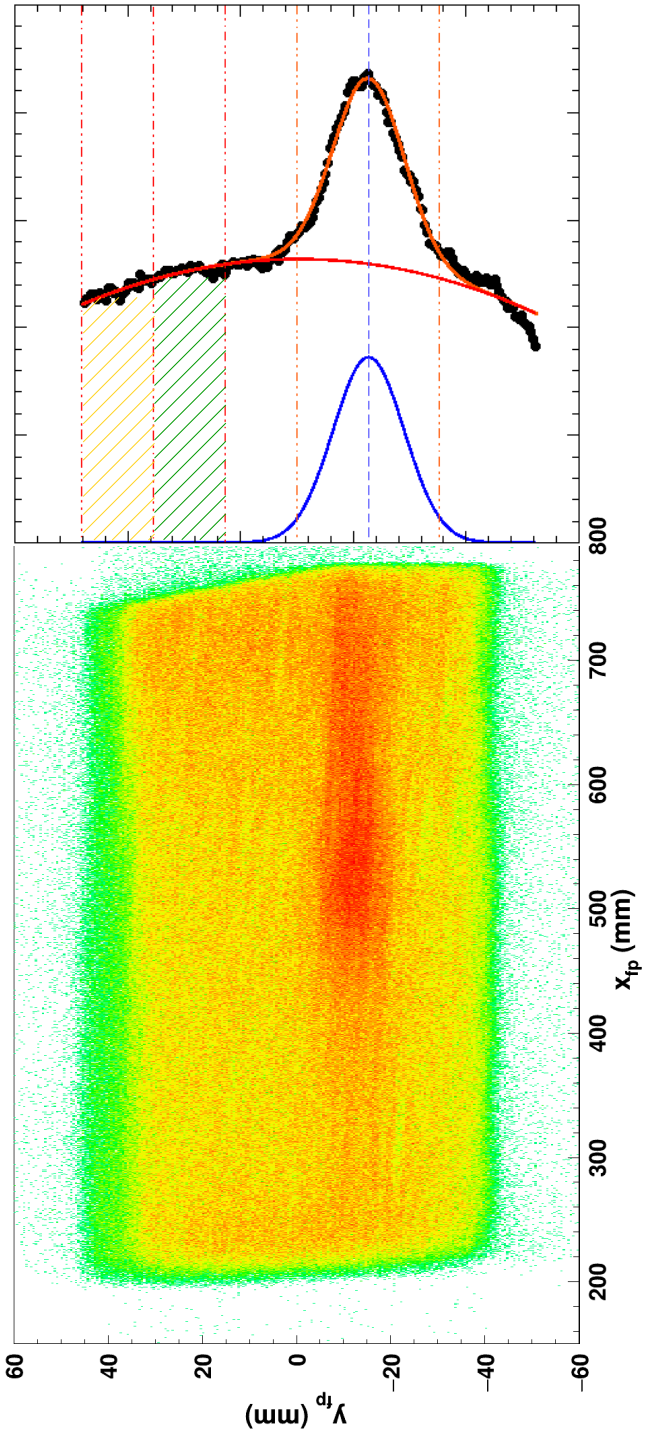


Figure 3.26: Top: The y_{fp} projection of the focal plane events showing a total fit (in orange) as well as the fitted components, namely the events of interest (in blue), which sit on top of the background events (in red); Bottom: the two-dimensional x_{fp} *versus* y_{fp} scatterplot.

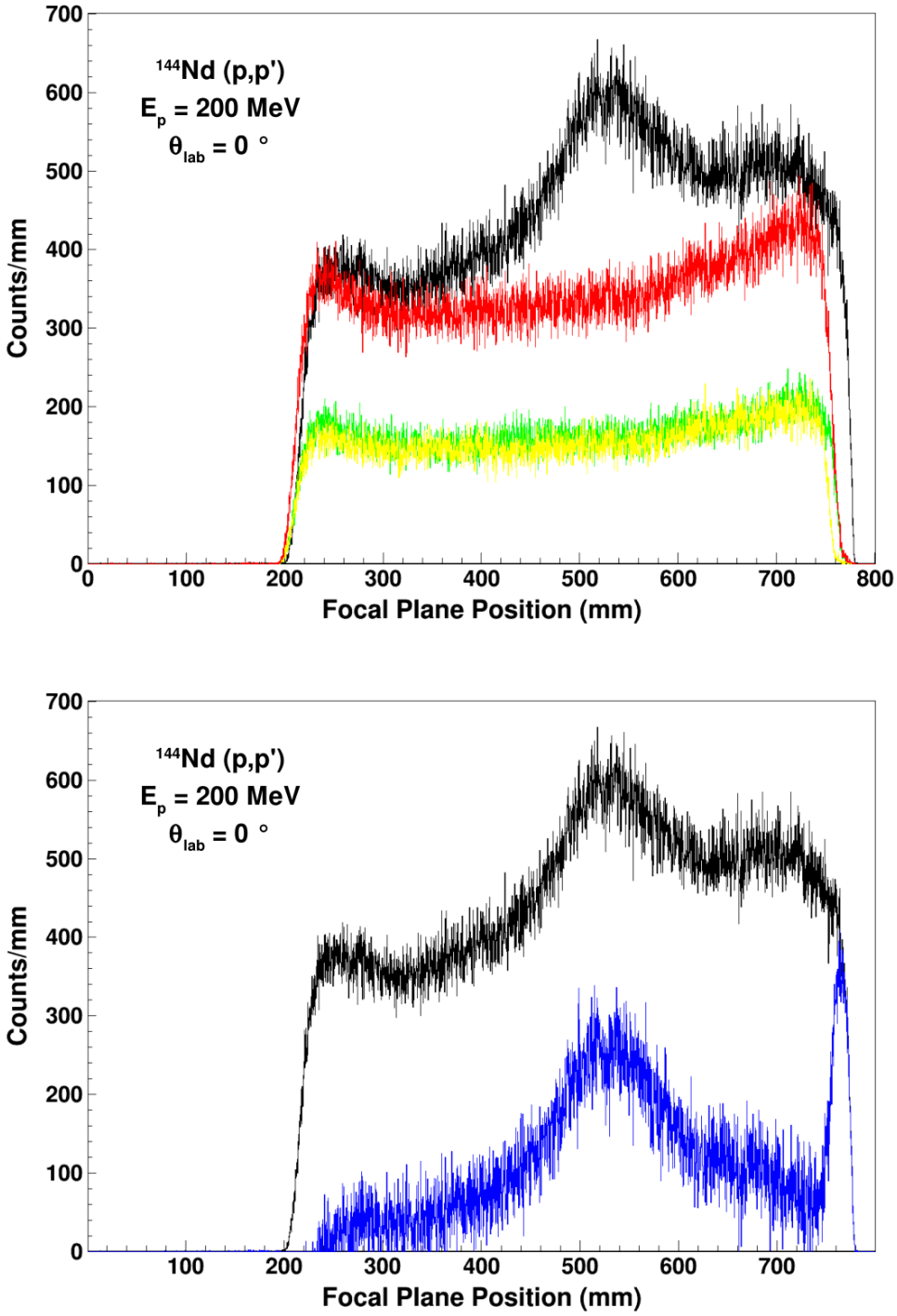


Figure 3.27: Top: The focal plane position spectrum showing the components involved in the background subtraction procedure, namely, the raw data (in black), the background components (in yellow and green) and the total background (in red). Bottom: A comparison of the raw data (in black) and the background subtracted data (in blue).

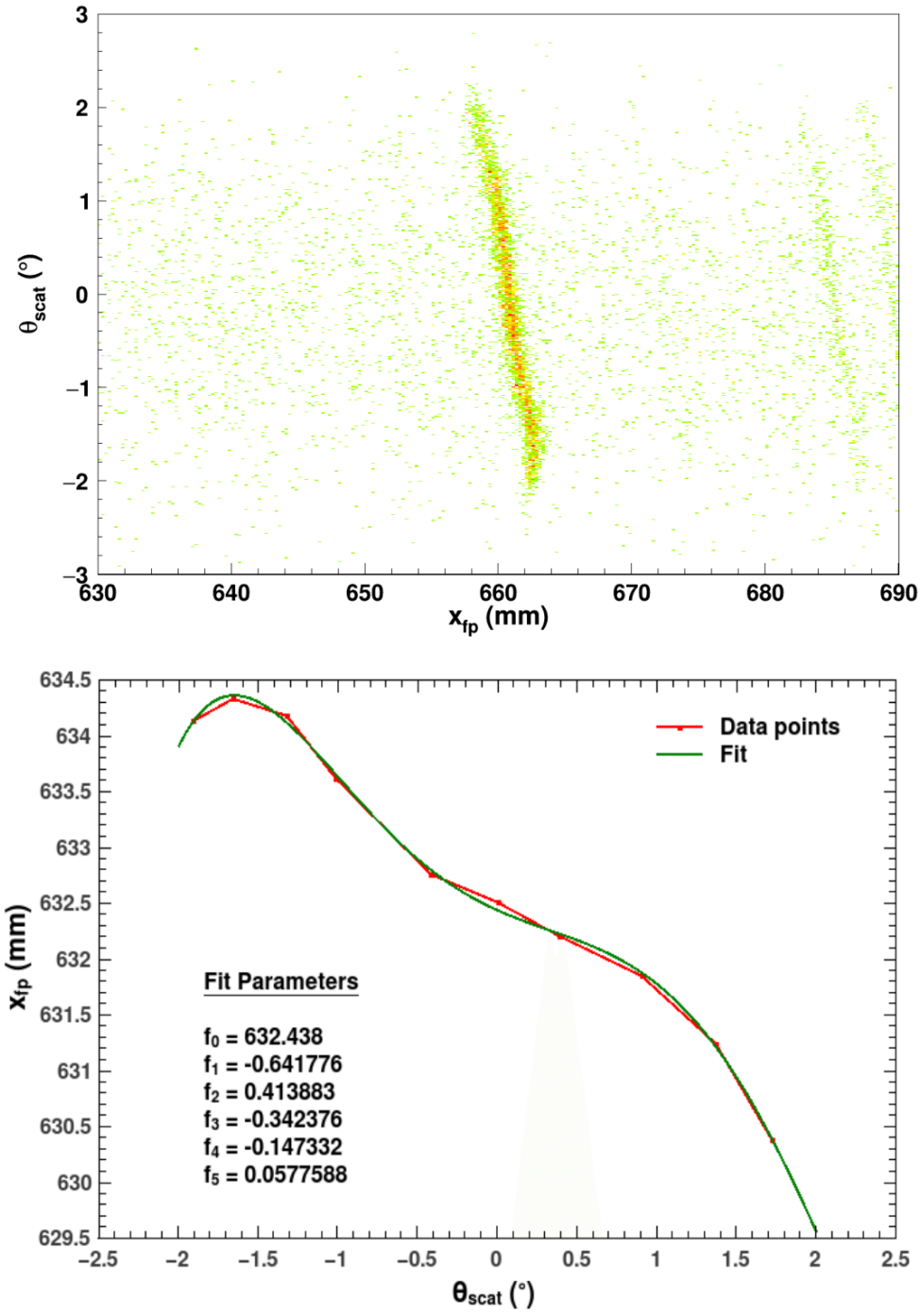


Figure 3.28: Top: A prominent excited state in a θ_{scat}-x_{fp} scatterplot with no lineshape correction applied; Bottom: a graph of the points used to reproduce the lineshape of the state shown in the upper panel with its associated fit and parameters.

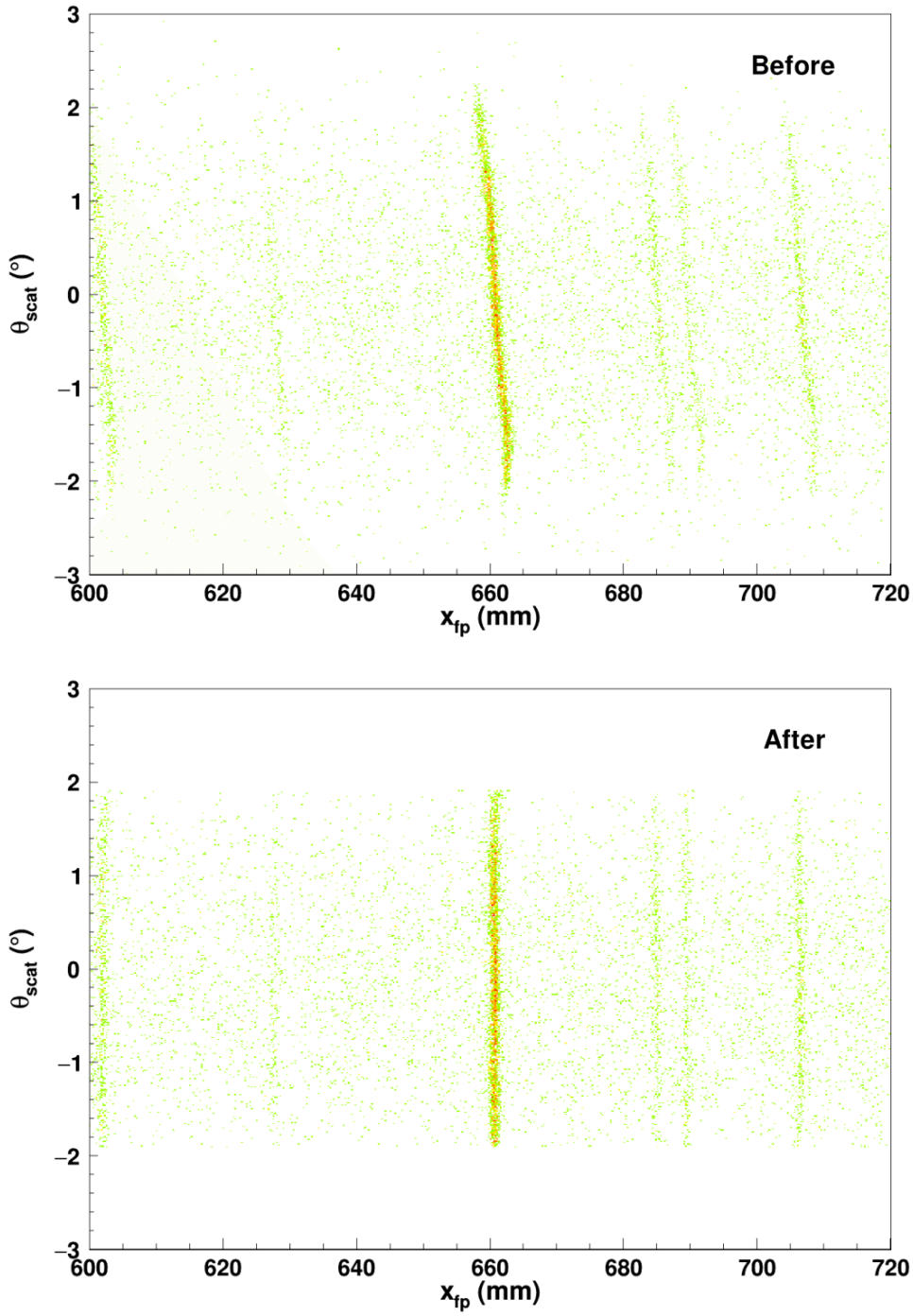


Figure 3.29: The effect of lineshape correction. Top: x_{fp} *versus* θ_{scat} with no lineshape correction applied; and Bottom: x_{fp} *versus* θ_{scat}, following a full lineshape correction.

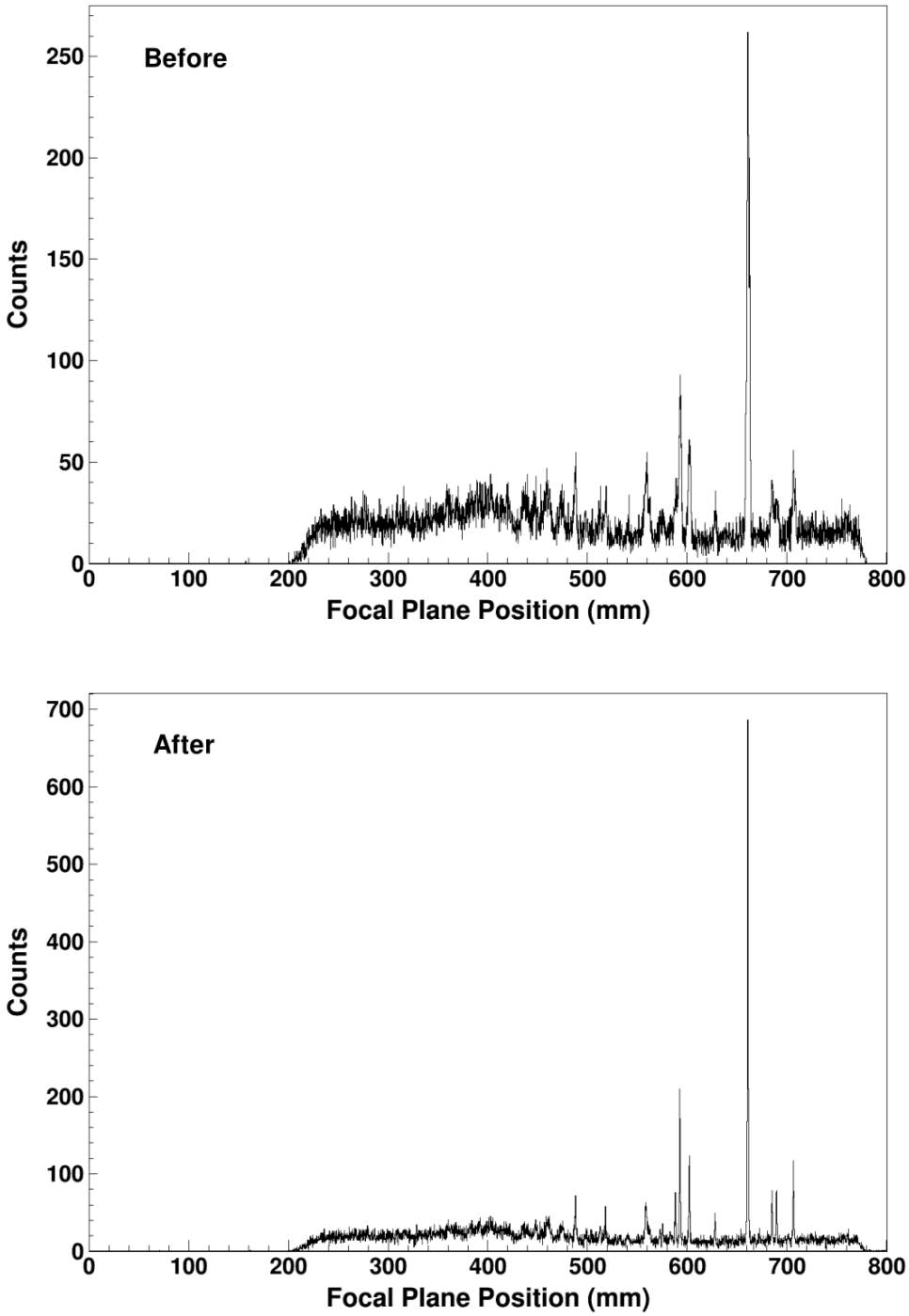


Figure 3.30: The effect of lineshape correction. Top: The focal plane position spectrum with no lineshape correction applied; and Bottom: The focal plane position spectrum following a full lineshape correction.

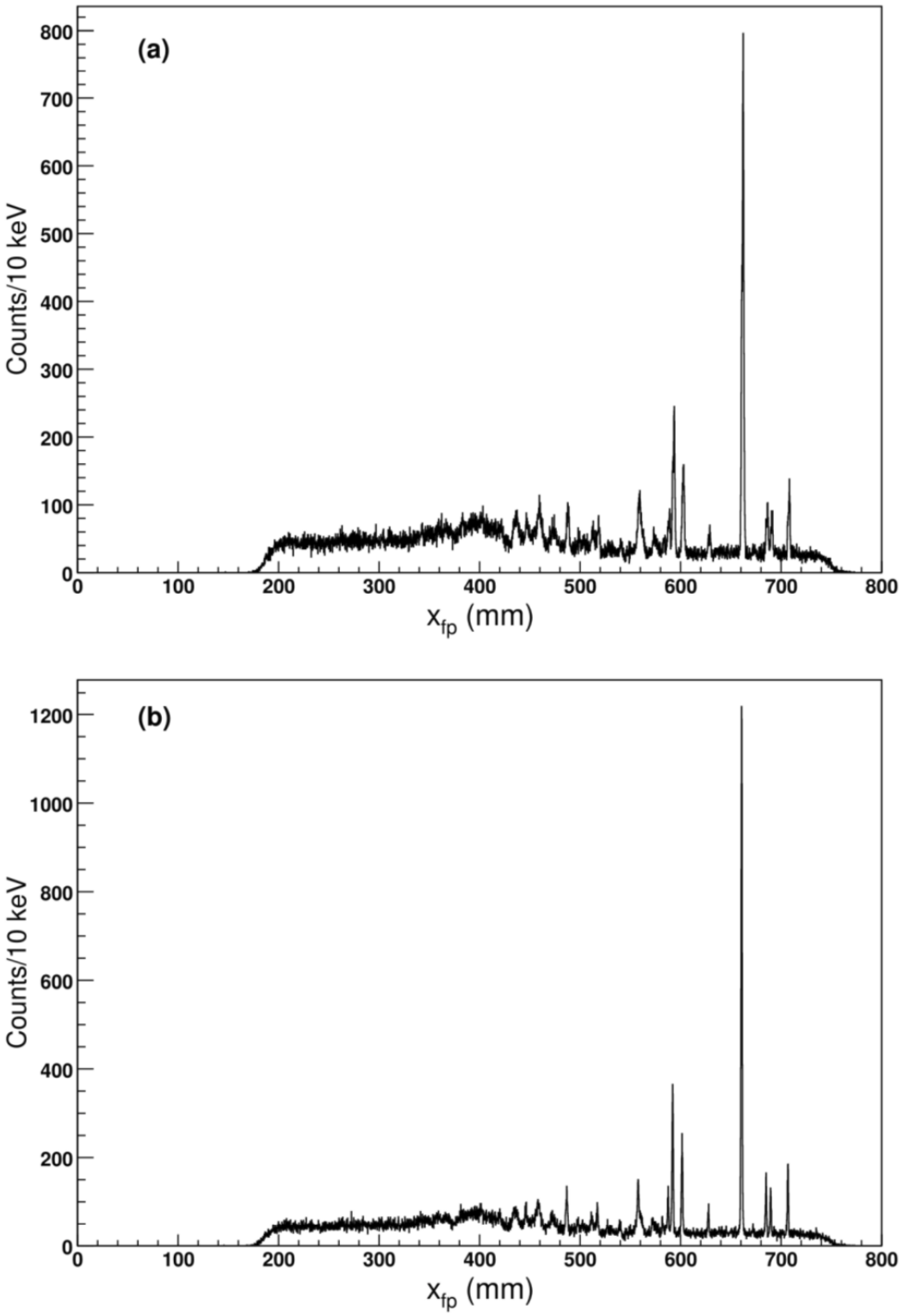


Figure 3.31: The effect of position offsets on the resolution of the chained spectrum where (a) illustrates the case where the offsets have been neglected and (b) illustrates the effect of offset inclusion.

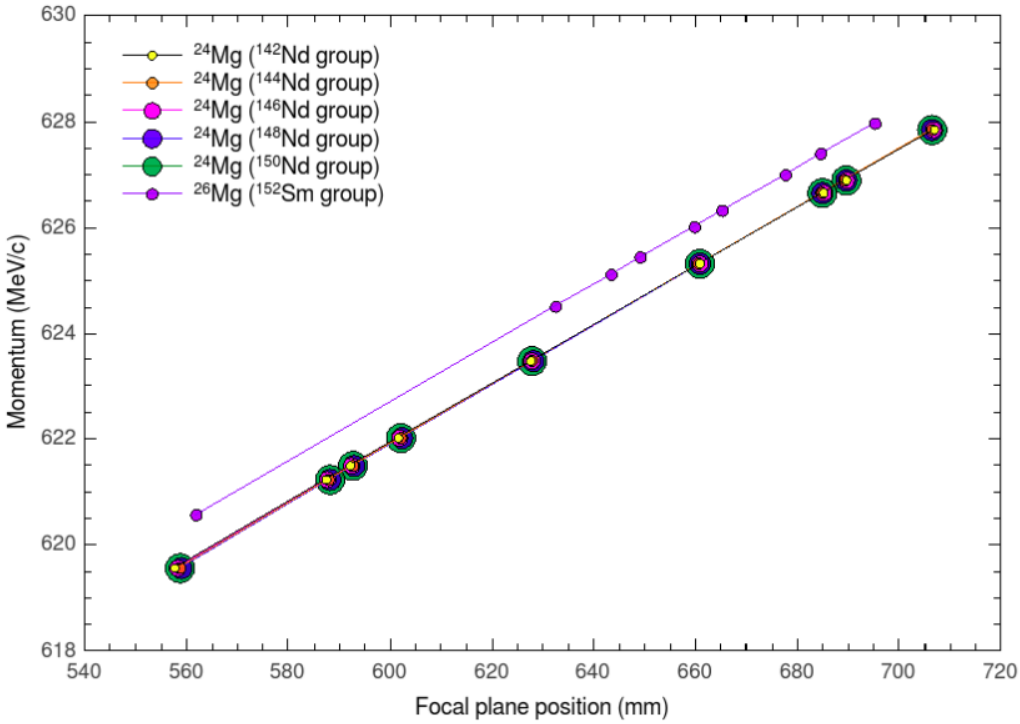


Figure 3.32: The momentum calibration curves for each of the neodymium isotope groups as well as for the ^{152}Sm group.

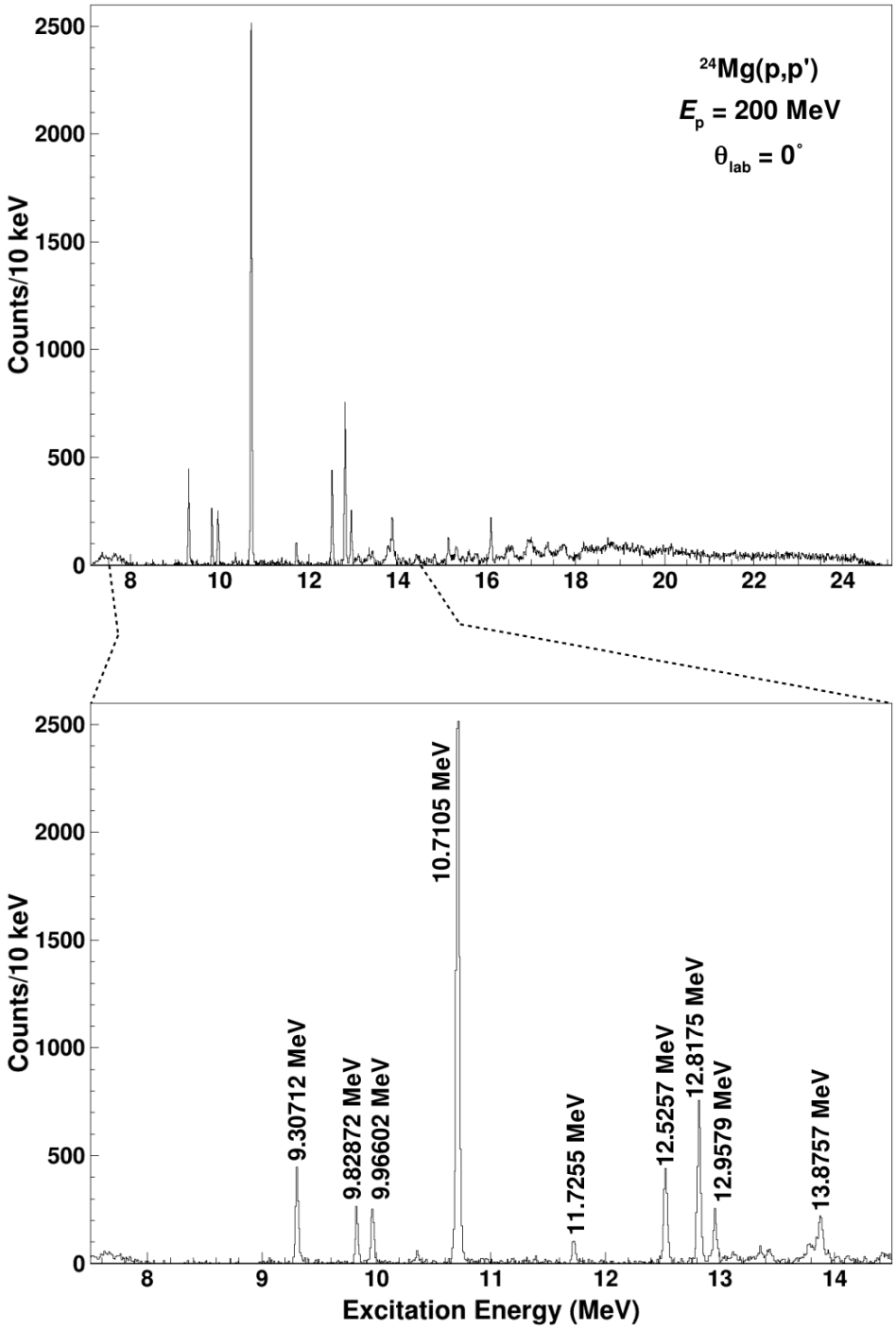


Figure 3.33: An excitation-energy spectrum obtained for the ^{24}Mg(p,p′) reaction at iThemba LABS.

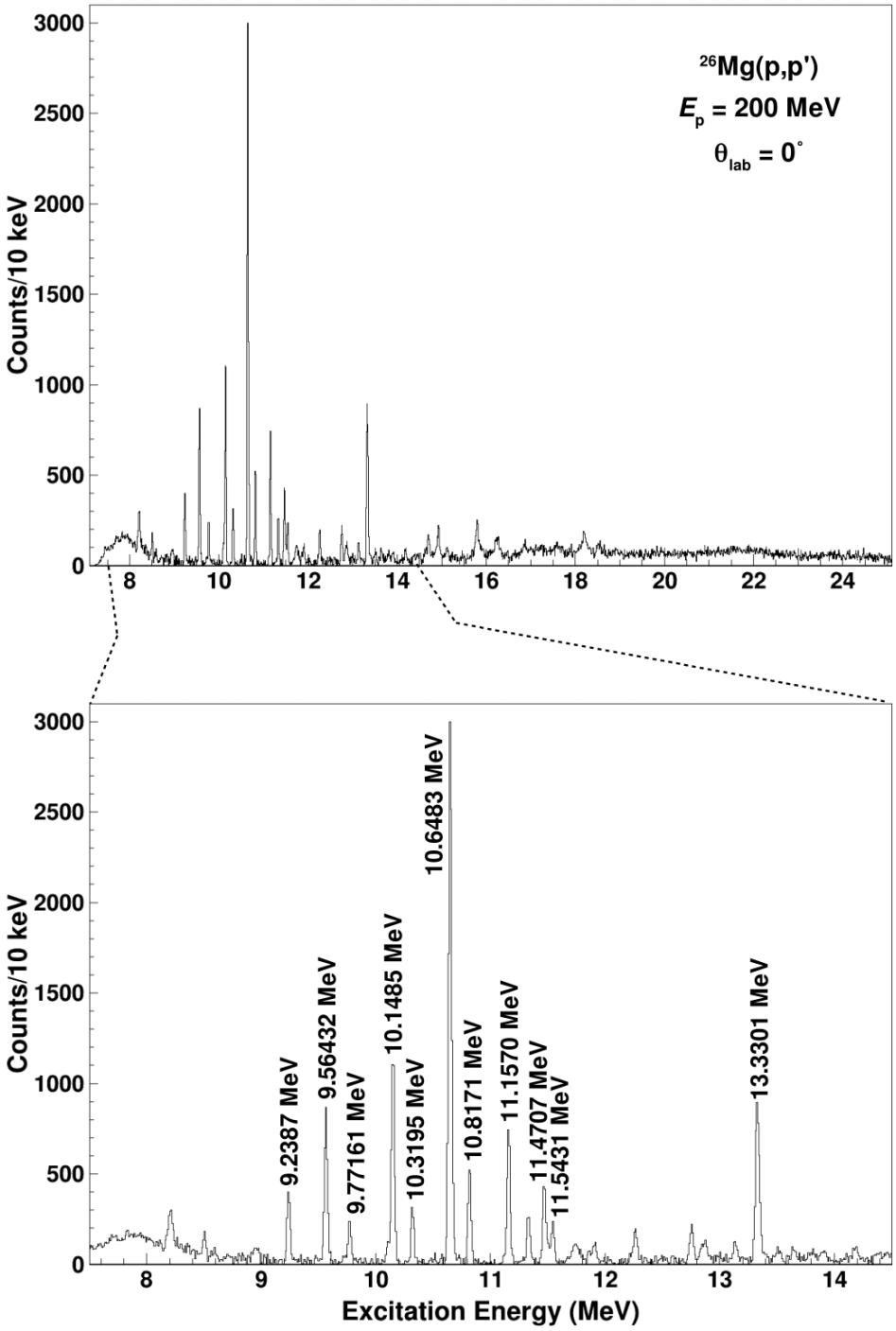


Figure 3.34: An excitation-energy spectrum obtained for the ^{26}Mg(p,p′) reaction at iThemba LABS.

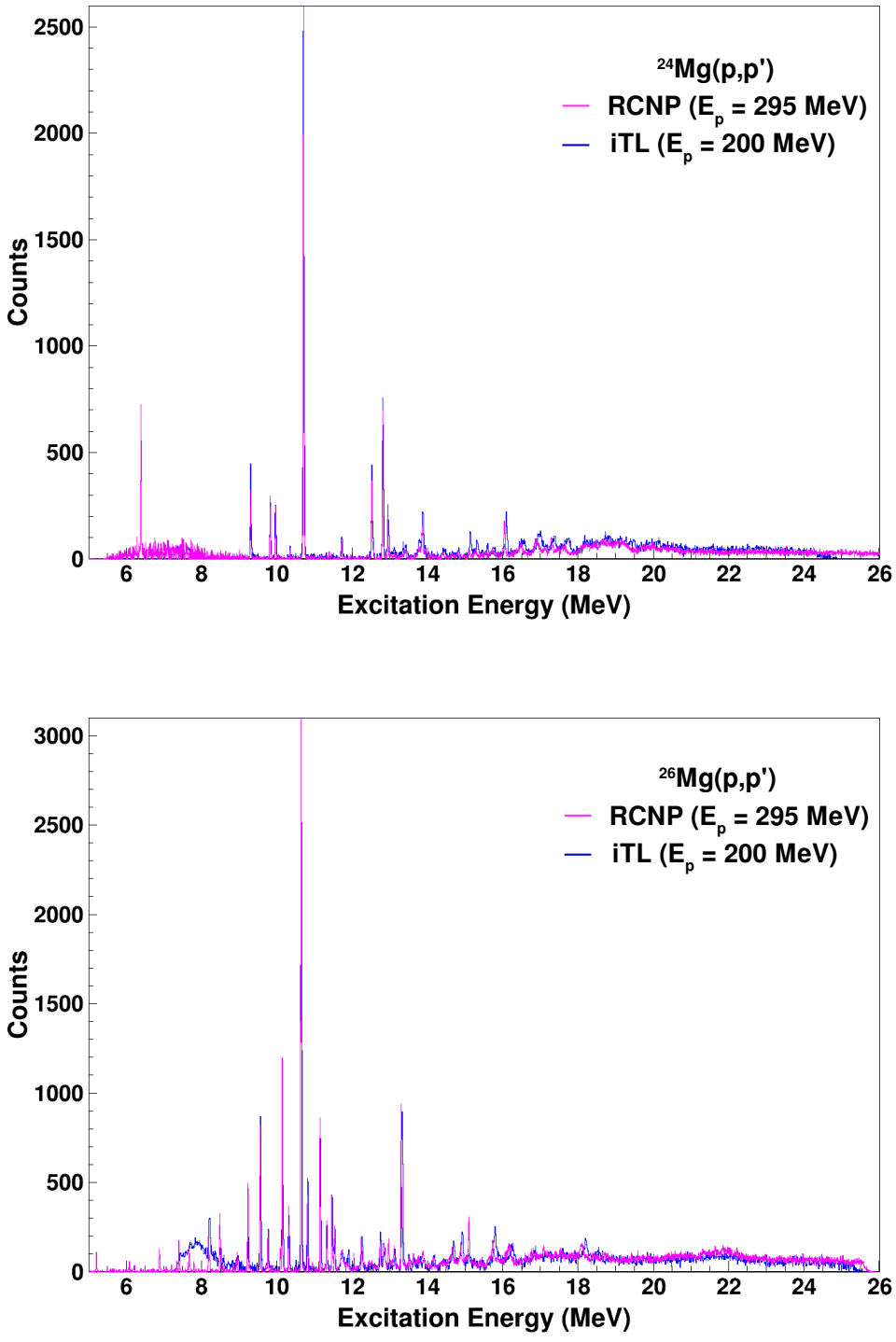


Figure 3.35: A comparison between RCNP and iThemba LABS (iTL) data for the purposes of a broad structure comparison for the ^{24}Mg(p,p′) reaction (top) and for the ^{26}Mg(p,p′) reaction (bottom).

Chapter 4

Results, analysis and discussion

This chapter provides details regarding the analysis and conversion of the extracted (p,p′) excitation energy spectra to equivalent photo-absorption cross sections for comparison with pre-existing photo-absorption and photo-neutron results. Also provided is a fine structure analysis of the experimentally obtained high energy-resolution data as well as a comparison of the experimental results to the theoretical predictions which are discussed in Chapter 2.

4.1 Overview and description of measured (p,p′) data

The experimentally measured (p,p′) excitation energy spectra which were obtained following the data extraction procedure detailed in Chapter 3 are displayed in Fig. 4.1. Through the use of Eq. (3.21), these excitation energy spectra were converted to double-differential cross sections, which are displayed in Fig. 4.2. It is important to note that as a result of the changing vertical acceptance in the lower excitation-energy region, the background subtraction procedure (detailed in Section 3.7.1 of Chapter 3) induces an artificial structure below $\sim$ 9.5 MeV. This structure is seen clearly in the blue focal plane position spectrum shown in the bottom panel of Fig. 3.27 and is associated with the gradual loss of efficiency at the end of the detectors. For this reason, the lower cut-off on the excitation-energy axis is

set at ~ 9.5 MeV for all spectra in both Figs. 4.1 and 4.2. The dashed-line in Figs. 4.1 and 4.2 indicates the upper cut-off on the excitation-energy axis, which takes into account the loss of efficiency on the other side of the detectors. The experimental energy-resolutions for the ^{142,144,146,148,150}Nd and ^{152}Sm are 50 keV, 42 keV, 46 keV, 43 keV, 45 keV and 42 keV (FWHMs), respectively.

From these overviews, it is immediately clear that the width of the IVGDR increases steadily from about 3 MeV (FWHM) for the nearly spherical ^{142}Nd nucleus through the transition region to about 7 MeV (FWHM) for the deformed ^{150}Nd and ^{152}Sm nuclei. This expected increase in width as deformation increases is discussed in Section 2.2 of Chapter 2. What is also already apparent at this stage of the analysis is the close comparison between the ^{150}Nd and ^{152}Sm, which are isotones in the transitional region. This comparison will be further investigated in Section 4.3.2 of this chapter.

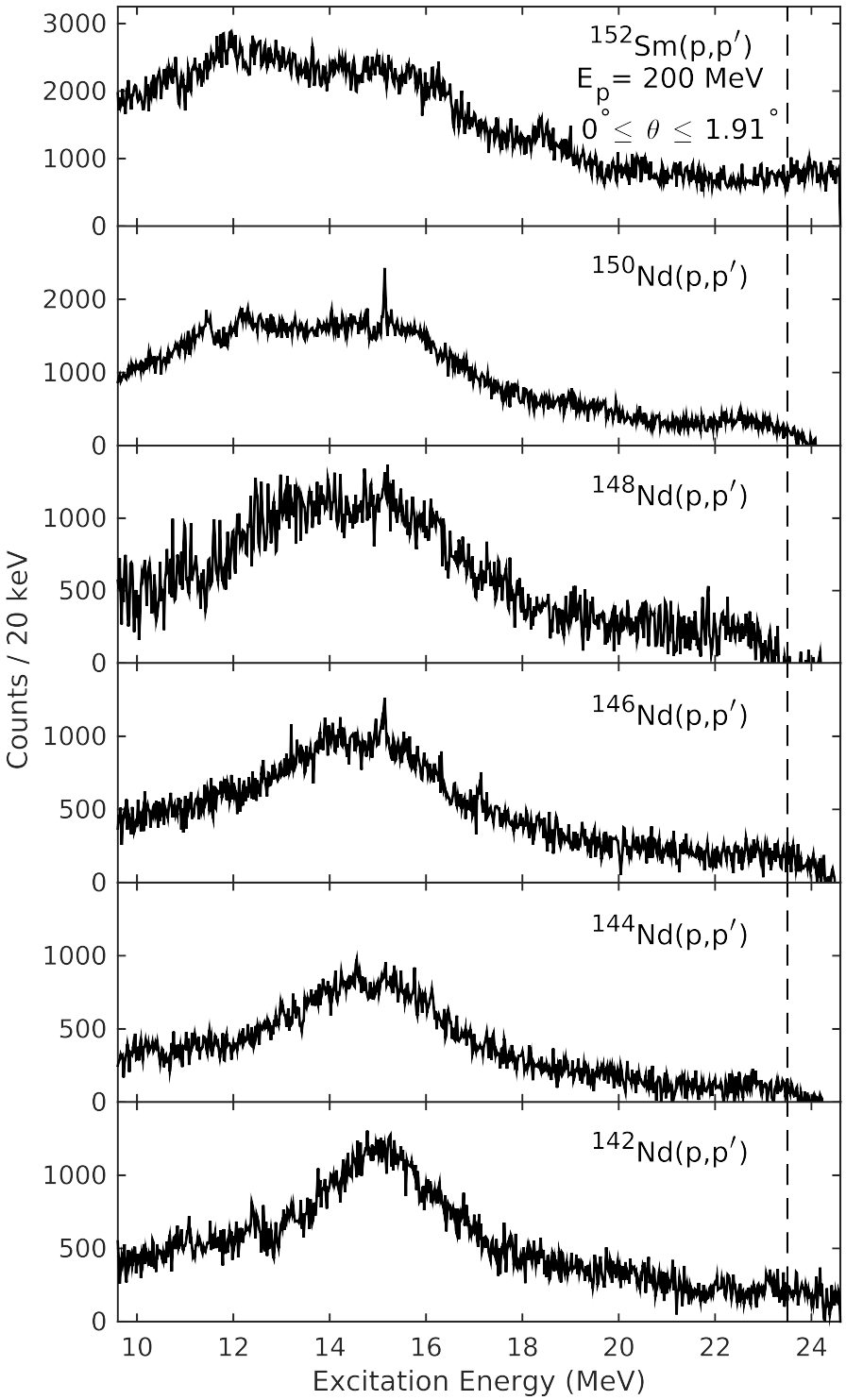


Figure 4.1: Experimentally obtained excitation energy spectra for ^{142,144,146,148,150}Nd(p,p′) and ^{152}Sm(p,p′) for $E_\mathrm{p} = 200$ MeV and $\theta_\mathrm{Lab} = 0° - 1.91°$.

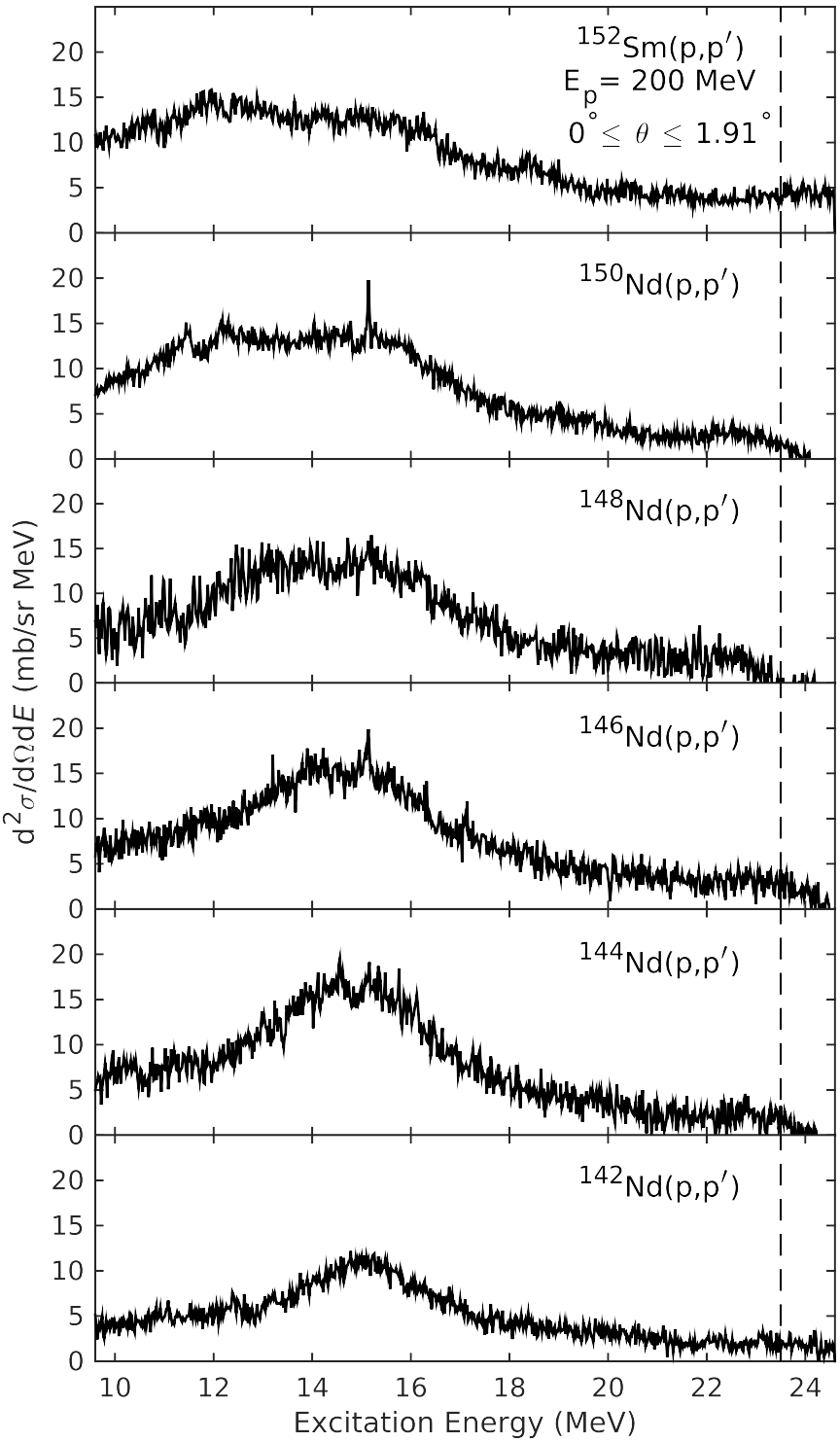


Figure 4.2: Experimentally obtained double-differential cross sections for ^{142,144,146,148,150}Nd(p,p′) and ^{152}Sm(p,p′) for $E_\mathrm{p} = 200$ MeV and $\theta_\mathrm{Lab} = 0° - 1.91°$.

4.2 Conversion to equivalent photo-absorption spectra and comparison with existing photo-absorption and photo-neutron data

In order to appreciate the change in shape of the IVGDR as deformation increases, it is necessary to convert the measured (p,p′) spectra to equivalent photo-absorption cross sections. These conversions allow for comparisons to pre-existing photo-absorption data to be made. An additional advantage of the conversions is that they allow for comparison to be made to the $B(E1)$ strength functions, which were calculated using the SSRPA with the SLy6 Skyrme interaction [Nes15]. These calculations were originally optimised for comparison with photo-absorption data [Nes07]. The equivalent photo-absorption cross sections will be denoted (p,p$'_{\gamma\mathrm{corr}}$) and will also be compared to the most recent photo-neutron data in the lower excitation energy region for the ^{144}Nd, ^{146}Nd, ^{148}Nd and ^{152}Sm isotopes [Fil14, Nyh15]. For the sake of continuity and ease of comparison, all figures and tables have been placed at the end of this section.

4.2.1 Conversion of the measured (p,p′) spectra to (p,p$'_{\gamma\mathrm{corr}}$) spectra

The conversion of the measured (p,p′) spectra to (p,p$'_{\gamma\mathrm{corr}}$) spectra is a multi-step process that can be divided into three distinct stages, namely, background subtraction in the region of the IVGDR, the calculation of the virtual-photon production, and the implementation of the equivalent virtual photon method. These processes will be detailed in the subsequent sections.

4.2.1.1 Background subtraction in the region of the IVGDR

Although inelastic proton scattering was selected for this study since it predominantly excites the IVGDR at zero degrees, other resonances of different multipolarities are also excited as is shown in Table 2.2 of

Chapter 2. In order to isolate the IVGDR reliably, these contributions to the obtained (p,p′) spectra must be taken into consideration and subtracted before a conversion to (p,p$'_{\gamma\mathrm{corr}}$) can be made.

Among these contributions is the Isoscalar Giant Quadrupole Resonance (ISGQR). A study of the ISGQR across the even-even neodymium isotope chain was performed by C. O. Kureba [Kur14] and as such the positions of these contributions are well-known. The relative strength of the ISGQR contributions compared to the IVGDR strength was established from Distorted Wave Born Approximation (DWBA) calculations using the code DWBA07 [Pon15]. These predictions are displayed in Fig. 4.3. It is clear from the lower panel of Fig. 4.3 that the interference between the Coulomb and nuclear components of the ISGQR is destructive at small scattering angles as expected.

The phenomenological background [Pol11], which describes the behaviour of the double-differential cross section at higher excitation energies must also be identified and subtracted. This component incorporates all unknown multipolarity contributions, the Isovector Giant Quadrupole Resonance (IVGQR) as well as quasi-free scattering. The phenomenological background is approximated by finding the maximum of the cross section between 20 MeV and 23 MeV and selecting an appropriate width. In this higher excitation-energy region, the Coulomb contribution to the cross section is negligible and, as such, all strength can be regarded as background [Neu15]. The double-differential cross sections as well as the decompositions of background contributions are displayed for the ^{142,144,146,148,150}Nd and ^{152}Sm isotopes in Figs. 4.4(a), 4.5(a), 4.6(a), 4.7(a), 4.8(a) and 4.9(a), respectively.

4.2.1.2 Virtual photon production

The virtual $E1$ γ-production rate was calculated for each of the neodymium and samarium isotopes using the Eikonal approximation as described in Section 2.2.3.3 of Chapter 2. The calculations were done at regular angle intervals within the angular acceptance of the K600 Magnetic Spectrometer, that is, $0^\circ < \theta_{\mathrm{lab}} < 1.91^\circ$. By way of example, the virtual $E1$ γ-production

functions for ^{142}Nd(p,p′) between 0° and 1.91° are displayed in Fig. 4.10. As can be seen, for angles towards the higher end of the angular acceptance, the virtual-γ production functions vary more substantially from one another at lower excitation energies than at higher excitation energies. To compensate for this, a weighted average of the virtual-γ production functions across the angular acceptance was calculated for each isotope. These average virtual-γ production functions are displayed for the ^{142,144,146,148,150}Nd(p,p′) and ^{152}Sm(p,p′) reactions in Figs. 4.4(b), 4.5(b), 4.6(b), 4.7(b), 4.8(b) and 4.9(b), respectively. A combined overview is displayed in Fig. 4.11. It should be noted that the average virtual-γ production functions for all of the neodymium isotopes coincide and, as such, the functions are represented by one curve in Fig. 4.11.

4.2.1.3 Application of the equivalent virtual photon method

The conversion of the (p,p′) spectra to equivalent photo-absorption cross sections was done using Eq. (2.20) as discussed in Section 2.2.3.2 of Chapter 2, being

$$\frac{d^2\sigma}{d\Omega dE_\gamma} = \frac{1}{E_\gamma}\frac{dN_{E1}}{d\Omega}\sigma_\gamma^{\pi\lambda}(E_\gamma).$$

Each (p,p′) spectrum for the neodymium and samarium isotopes was divided by the respective virtual-γ production function for that isotope. The results of this division for the ^{142,144,146,148,150}Nd and ^{152}Sm isotopes are displayed in Figs. 4.4(c), 4.5(c), 4.6(c), 4.7(c), 4.8(c) and 4.9(c), respectively.

4.2.2 A comparison of the (p,p′$_{\gamma\mathrm{corr}}$) and the (γ,abs) results

Through the simultaneous measurement of the partial photo-nuclear cross sections $\sigma(\gamma, \mathrm{n}) + \sigma(\gamma, \mathrm{pn})$ and $\sigma(\gamma, 2\mathrm{n})$ using a monochromatic photon beam, the giant dipole resonances of ^{142}Nd, ^{144}Nd, ^{146}Nd, ^{148}Nd and ^{150}Nd were

studied in 1971 by Carlos *et al.* [Car71]. Subsequently in 1974, using the same method, Carlos *et al.* [Car74] measured the giant dipole resonance of ^{152}Sm. It is important to note that the (p,p$'_{\gamma\mathrm{corr}}$) results displayed in Fig. 4.4(c) - Fig. 4.9(c) are for 20 keV bins. In order to make a direct comparison to the lower resolution (γ,abs) results and to focus on the broad structure (as opposed to the fine structure, which will be discussed in Section 4.3), the (p,p$'_{\gamma\mathrm{corr}}$) spectra were rebinned to 200 keV. These rebinned spectra are displayed in Figs. 4.4(d), 4.5(d), 4.6(d), 4.7(d), 4.8(d) and 4.9(d) for the ^{142,144,146,148,150}Nd(p,p$'_{\gamma\mathrm{corr}}$) and ^{152}Sm(p,p$'_{\gamma\mathrm{corr}}$) cases, respectively. A direct comparison of the data obtained by Carlos *et al.* [Car71, Car74] and those obtained in the current study is shown in Fig. 4.12. From this figure, it is clear that in order to facilitate a shape comparison between the two sets of data, a normalisation factor is required for all of the isotopes.

As discussed in Section 2.4 of Chapter 2, the total absorption cross section for a non-deformed nucleus can be fitted by a single Lorentzian given by Eq. (2.59), whereas the cross section for an axially symmetric deformed nucleus can be fitted by the sum of two Lorentzians as given by Eq. (2.60). A summary of the Lorentzian fit parameters to the (γ,abs) data as provided by Carlos *et al.* [Car71, Car74] can be found in Table 4.1. Also summarised are the fit parameters to the same (γ,abs) data as given by the Reference Input Parameter Library (RIPL-3) [Cap09], which aims to provide the most accurate parameters for theoretical model input. These parameters were established through the use of the Standard Lorentzian Model. An overview of the comparison between the rebinned and now normalised (p,p$'_{\gamma\mathrm{corr}}$) data and the parametrisations of the (γ,abs) data is provided in Fig. 4.13. The following normalisation factors were used to scale the (p,p$'_{\gamma\mathrm{corr}}$) spectra to the corresponding total photo-absorption cross sections: 1.24 (^{142}Nd), 0.75 (^{144}Nd), 0.79 (^{146}Nd), 0.78 (^{148}Nd), 0.82 (^{150}Nd) and 0.78 (^{152}Sm) and, with the exception of ^{142}Nd, the scaling factor averages at 0.78 $\pm$ 0.04.

As can be seen from the parametrisations (in orange) in Fig. 4.13, Carlos *et al.* [Car71, Car74] confirmed the spreading of the IVGDR as the nuclei became softer followed by the splitting of the IVGDR into two distinct dipole modes for the ^{150}Nd isotope. The same splitting was also seen for the ^{152}Sm isotope. This transition pattern for the even-even neodymium isotope chain as well as for the even-even ^{152}Sm isotope can be attributed to a change in the energy ratio of the

first 4^+ and 2^+ energy levels, which was explained in Section 2.3.1.1. Although the equivalent photo-absorption cross sections display a similar trend, that is, a general broadening of the IVGDR with increasing deformation, the predicted split of the resonance into two distinct components is not seen for either the ^{150}Nd or the ^{152}Sm isotopes. This is a particularly surprising result.

The obvious discrepancies (in both the $K = 0$ and $K = 1$ regions) between the (γ,abs) results and the (p,p$'_{\gamma\mathrm{corr}}$) spectra prompted an investigation into the parametrisations that would accurately describe the results obtained in the present study. The (p,p$'_{\gamma\mathrm{corr}}$) spectra were thus fitted using the same definition for the Lorentzian fits as provided by Carlos *et al.* [Car71, Car74], that is, using Eq. (2.59) for the spherical cases and Eq. (2.60) for the deformed cases. The "goodness of fit" was found to be close to unity for all of the parametrisations. These fits to the (p,p$'_{\gamma\mathrm{corr}}$) spectra are displayed in Fig. 4.14 and a summary of the fit parameters for all isotopes is provided in Table 4.1.

From the comparison between the (p,p$'_{\gamma\mathrm{corr}}$) data, the (p,p$'_{\gamma\mathrm{corr}}$) parametrisations and the Carlos *et al.* [Car71, Car74] (γ,abs) parametrisations, it is clear that the most obvious discrepancies are found in the lower E_x, $K = 0$ region at and just above the neutron threshold. The strengths of the equivalent photo-absorption cross sections are substantially lower (approximately 20 % lower for ^{150}Nd and ^{152}Sm) in this region than those reported by Carlos *et al.* [Car71, Car74]. Recent (γ,n) studies [Nyh15, Fil14] corroborate this reduced strength in the $K = 0$ region and ultimately report that the observed photo-neutron cross sections are approximately $20 - 37$ % lower relative to the Carlos *et al.* [Car71, Car74] data. A comparison between the most recent (γ,n) and the (p,p$'_{\gamma\mathrm{corr}}$) data and the discussion thereof is provided in Section 4.2.3. It is also interesting to note that along with the reduced $K = 0$ strength, the (p,p$'_{\gamma\mathrm{corr}}$) spectra display a $20 - 30$ % increase in the cross section strengths in the region containing the peak of the $K = 1$ contribution when compared with those obtained by Carlos *et al.* [Car71, Car74].

4.2.3 A comparison between the (p,p$'_{\gamma corr}$) and the (γ,n) data near the neutron threshold

Photo-neutron cross sections were measured for five stable neodymium isotopes (^{143,144,145,146,148}Nd) by Nyhus *et al.* [Nyh15] and for seven stable samarium isotopes (^{144,147,148,149,150,152,154}Sm) by Filipescu *et al.* [Fil14]. These measurements were performed near the neutron threshold using highly monochromatic and quasi-monochromatic laser-Compton scattering γ-rays, respectively. As mentioned previously, both (γ,n) studies reported significant discrepancies between the obtained photo-neutron cross sections and the Carlos *et al.* [Car71, Car74] photo-data measured in Saclay, which were concluded to be overestimated in this region. Similar reports were given for previous comparisons to Saclay photo-data such as those for ^{142}Nd [Ang12], which required a renormalisation factor of 0.86, for ^{144}Nd which required a factor of 0.80 [Nai10] and for ^{nat}Rb, ^{nat}Sr, ^{89}Y, ^{90}Zr, ^{93}Nb, ^{127}I, ^{197}Au and ^{208}Pb which required factors of 0.80-0.93 [Ber87].

The applicable data from the recent photo-neutron experiments [Uts15] are compared directly with the (p,p$'_{\gamma corr}$) spectra in Fig. 4.15. No normalisation factors were required to facilitate the comparison and as can be seen, there is reasonable agreement between the two sets of data near the neutron threshold. An additional comparison to the photo-neutron data obtained by Hara *et al.* [Har07] has been made for the ^{152}Sm isotope. There is good agreement between the equivalent photo-absorption cross section and both sets of photo-neutron data in the region corresponding to the peak of the $K = 0$ strength.

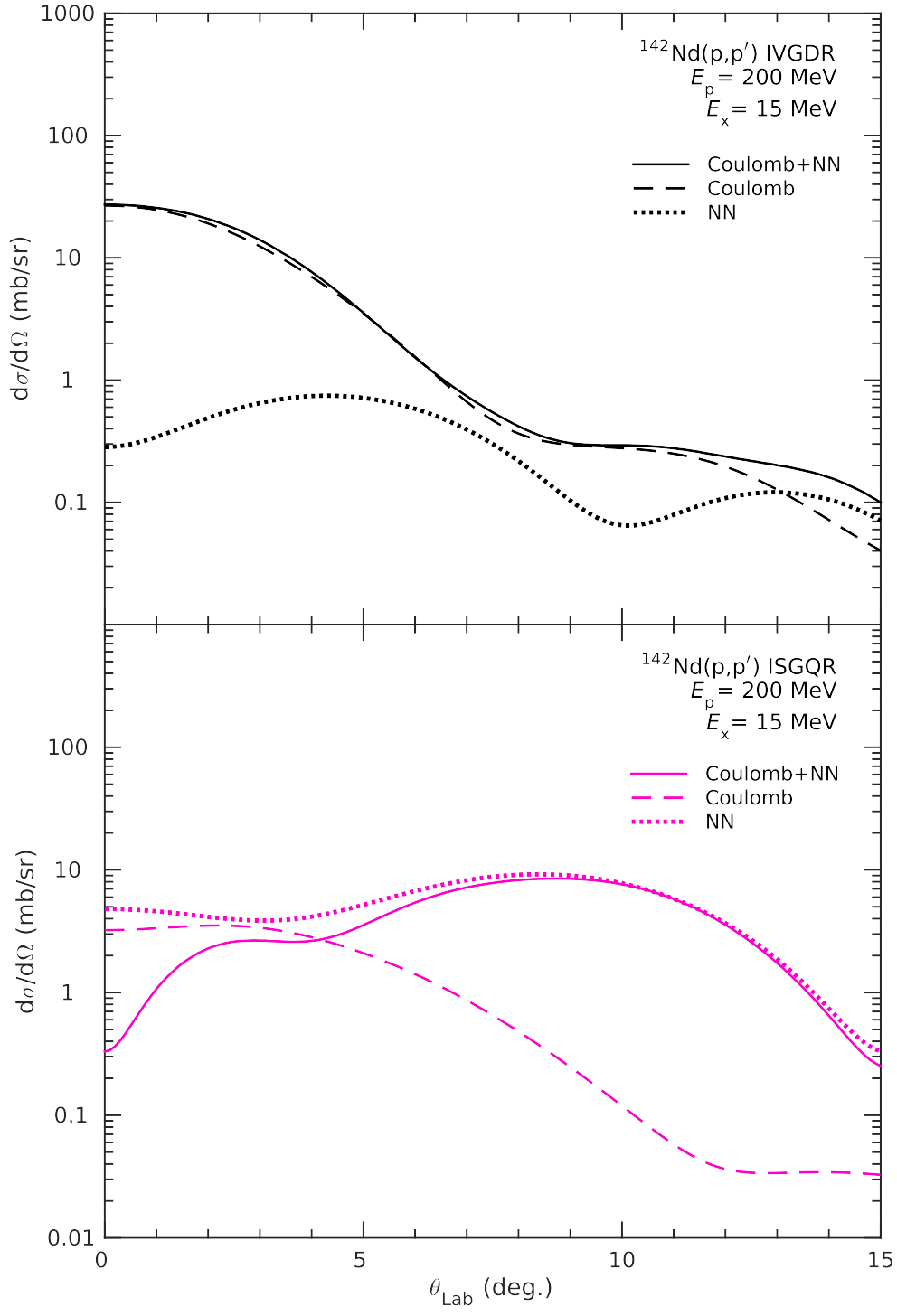


Figure 4.3: The IVGDR and ISGQR strengths as calculated for ^{142}Nd using standard DWBA [Pon15].

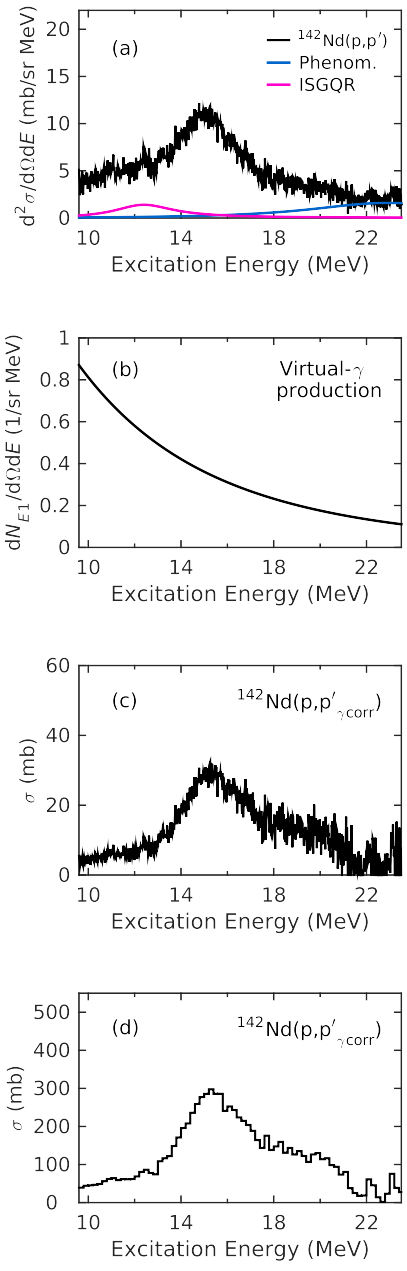


Figure 4.4: An overview of the conversion process from ^{142}Nd(p,p′) to ^{142}Nd(p,p′$_{\gamma corr}$).

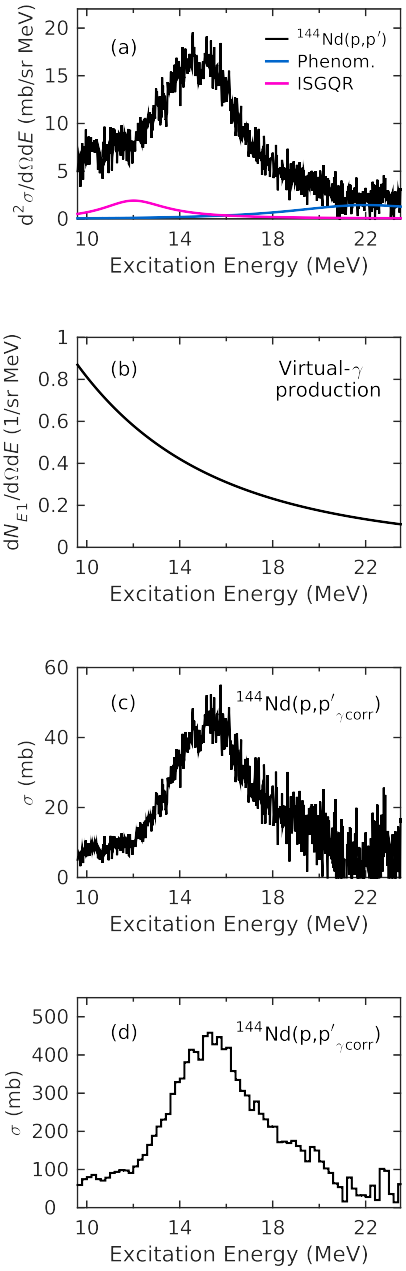


Figure 4.5: An overview of the conversion process from ^{144}Nd(p,p′) to ^{144}Nd(p,p′$_{\gamma corr}$).

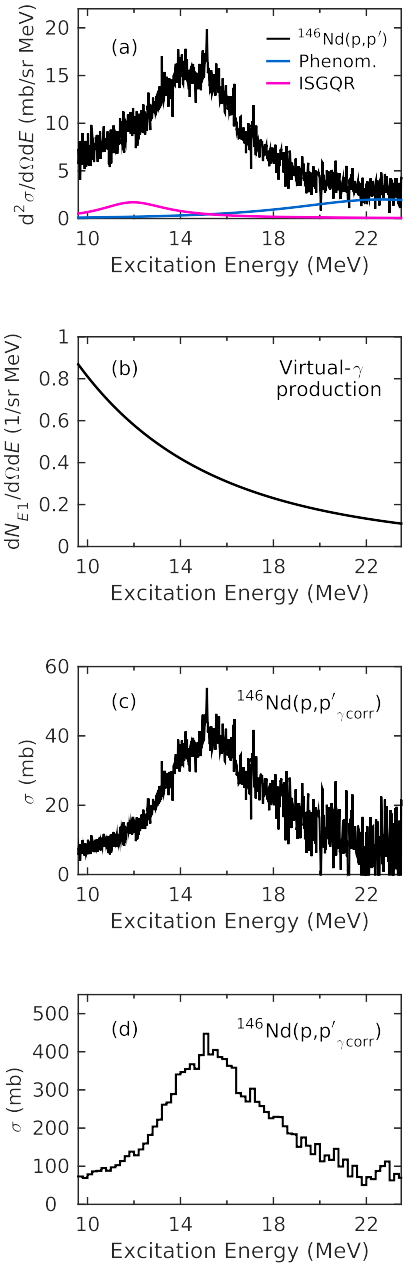


Figure 4.6: An overview of the conversion process from ^{146}Nd(p,p′) to ^{146}Nd(p,p′$_{\gamma corr}$).

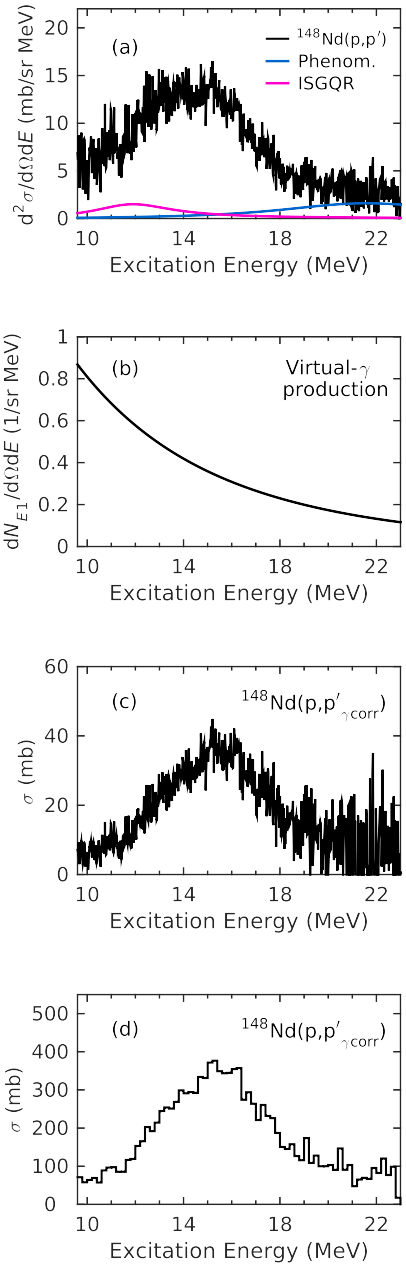


Figure 4.7: An overview of the conversion process from ^{148}Nd(p,p′) to ^{148}Nd(p,p′$_{\gamma corr}$).

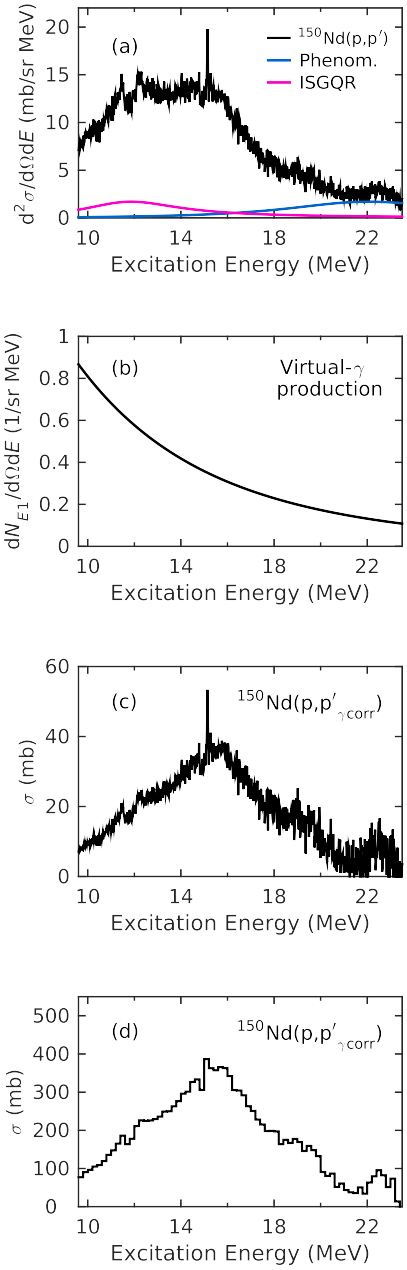


Figure 4.8: An overview of the conversion process from ^{150}Nd(p,p′) to ^{150}Nd(p,p′$_{\gamma corr}$).

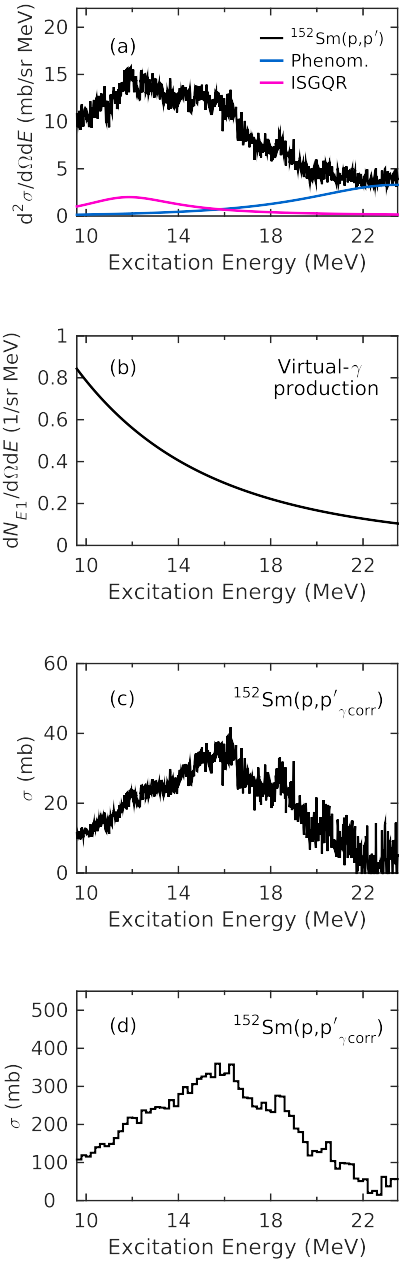


Figure 4.9: An overview of the conversion process from ^{152}Sm(p,p′) to ^{152}Sm(p,p′$_{\gamma corr}$).

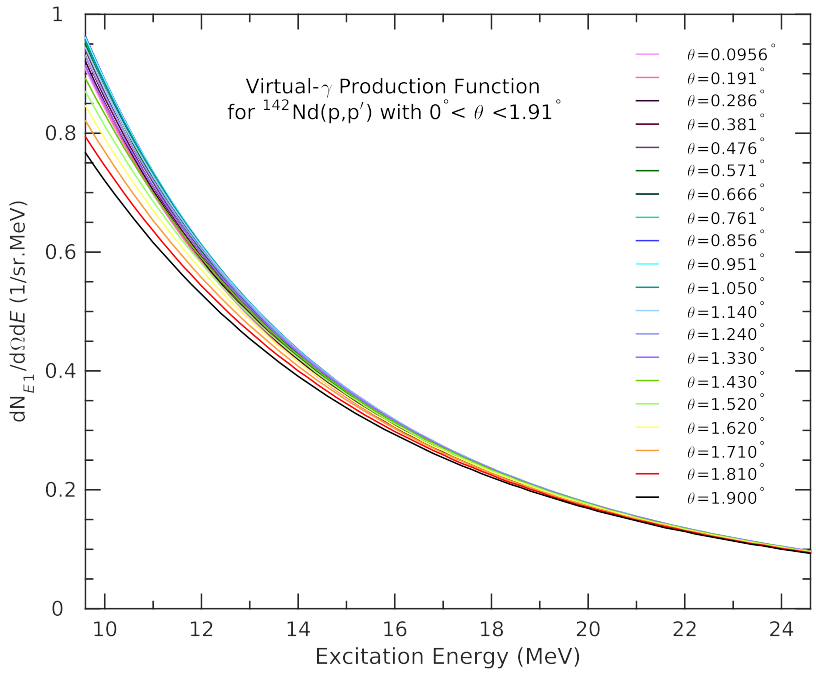


Figure 4.10: An overview of virtual-gamma production functions for ^{142}Nd(p,p′) across the angular acceptance of the K600 Magnetic Spectrometer.

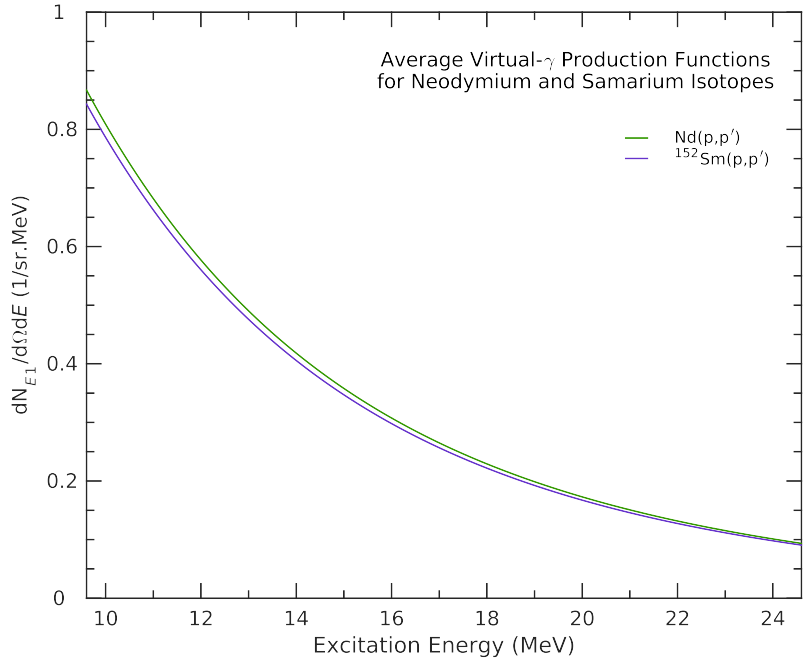


Figure 4.11: An overview of the average virtual-gamma production functions for Nd(p,p′) and ^{152}Sm(p,p′).

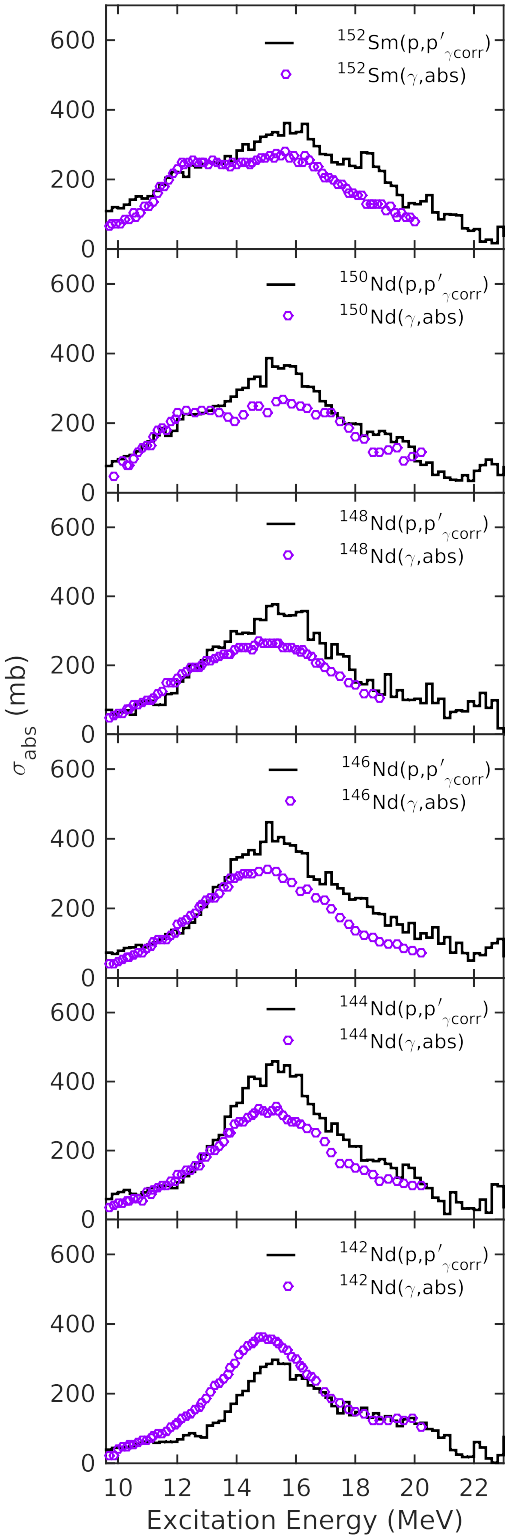


Figure 4.12: A direct comparison between the rebinned (and unnormalised) ^{142,144,146,148,150}Nd(p,p$'_{\gamma corr}$) and ^{152}Sm(p,p$'_{\gamma corr}$) spectra and the (γ, abs) data obtained by Carlos *et al.* [Car71, Car74].

Table 4.1: A comparison of the parametrisations for the present study's data and those provided in the literature for the neodymium data measured by Carlos et al. in 1971 [Car71], and those for the samarium data measured by Carlos et al. in 1974 [Car74]. Note that the superscript [a] indicates the parameters provided in [Car71], [b] indicates those provided in [Cap09] and [c] indicates those provided in [Car74]. A_T (where $A_T = 0.5\pi\sigma_1\Gamma_1$ for the spherical nuclei and $0.5\pi(\sigma_1\Gamma_1 + \sigma_2\Gamma_2)$ for the deformed nuclei) denotes the total area under the Lorentzian fits as calculated using the parameters given in the table for each isotope.

Isotope	E_1 (MeV)	σ_1 (mb)	Γ_1 (MeV)	E_2 (MeV)	σ_2 (mb)	Γ_2 (MeV)	$\frac{A_T}{0.06NZA^{-1}}$	$R_A = \frac{\sigma_1\Gamma_1}{\sigma_2\Gamma_2}$
	$14.95 \pm 0.10^{[a]}$	$359.0 \pm 15^{[a]}$	$4.43 \pm 0.20^{[a]}$				$1.20 \pm 0.10^{[a]}$	
^{142}Nd	$14.94^{[b]}$	$358.3^{[b]}$	$4.41^{[b]}$				1.19	
	15.38 ± 0.02	294.7 ± 2.4	3.92 ± 0.05				0.87	
	$15.05 \pm 0.10^{[a]}$	$317.0 \pm 15^{[a]}$	$5.30 \pm 0.25^{[a]}$				$1.25 \pm 0.10^{[a]}$	
^{144}Nd	$15.04^{[b]}$	$315.5^{[b]}$	$5.25^{[b]}$				1.24	
	15.14 ± 0.01	454.7 ± 3.1	4.21 ± 0.04				1.43	
	$14.80 \pm 0.10^{[a]}$	$308.0 \pm 16^{[a]}$	$6.00 \pm 0.30^{[a]}$				$1.35 \pm 0.10^{[a]}$	
^{146}Nd	$14.72^{[b]}$	$308.9^{[b]}$	$5.75^{[b]}$				1.32	
	15.20 ± 0.02	392.9 ± 2.7	5.70 ± 0.07				1.66	
	$14.70 \pm 0.15^{[a]}$	$263.0 \pm 15^{[a]}$	$7.20 \pm 0.30^{[a]}$				$1.40 \pm 0.10^{[a]}$	
^{148}Nd	$12.78^{[b]}$	$110.3^{[b]}$	$4.03^{[b]}$	$15.49^{[b]}$	$216.0^{[b]}$	$5.21^{[b]}$	1.15	0.395
	12.78 ± 0.13	58.5 ± 10.0	2.27 ± 0.48	15.31 ± 0.08	343.0 ± 8.6	5.19 ± 0.12	1.40	0.07
	$12.30 \pm 0.15^{[a]}$	$174.0 \pm 20^{[a]}$	$3.30 \pm 0.10^{[a]}$	$16.0 \pm 0.15^{[a]}$	$223.0 \pm 20^{[a]}$	$5.20 \pm 0.15^{[a]}$	$1.27 \pm 0.15^{[a]}$	0.495
^{150}Nd	$12.30^{[b]}$	$175.4^{[b]}$	$3.38^{[b]}$	$16.03^{[b]}$	$220.5^{[b]}$	$5.12^{[b]}$	1.25	0.525
	12.16 ± 0.15	138.4 ± 7.5	4.31 ± 0.53	15.59 ± 0.06	317.4 ± 12.39	4.34 ± 0.17	1.44	0.43
	$12.45 \pm 0.10^{[c]}$	$183.0 \pm 10^{[c]}$	$3.20 \pm 0.15^{[c]}$	$15.85 \pm 0.10^{[c]}$	$226.0 \pm 10^{[c]}$	$5.10 \pm 0.20^{[c]}$	$1.24^{[c]}$	0.508
^{152}Sm	$12.39^{[b]}$	$176.8^{[b]}$	$2.99^{[b]}$	$15.73^{[b]}$	$232.0^{[b]}$	$5.15^{[b]}$	1.23	0.442
	12.16 ± 0.22	145.8 ± 11.1	5.27 ± 0.86	16.05 ± 0.10	282.8 ± 18.99	5.52 ± 0.26	1.66	0.49

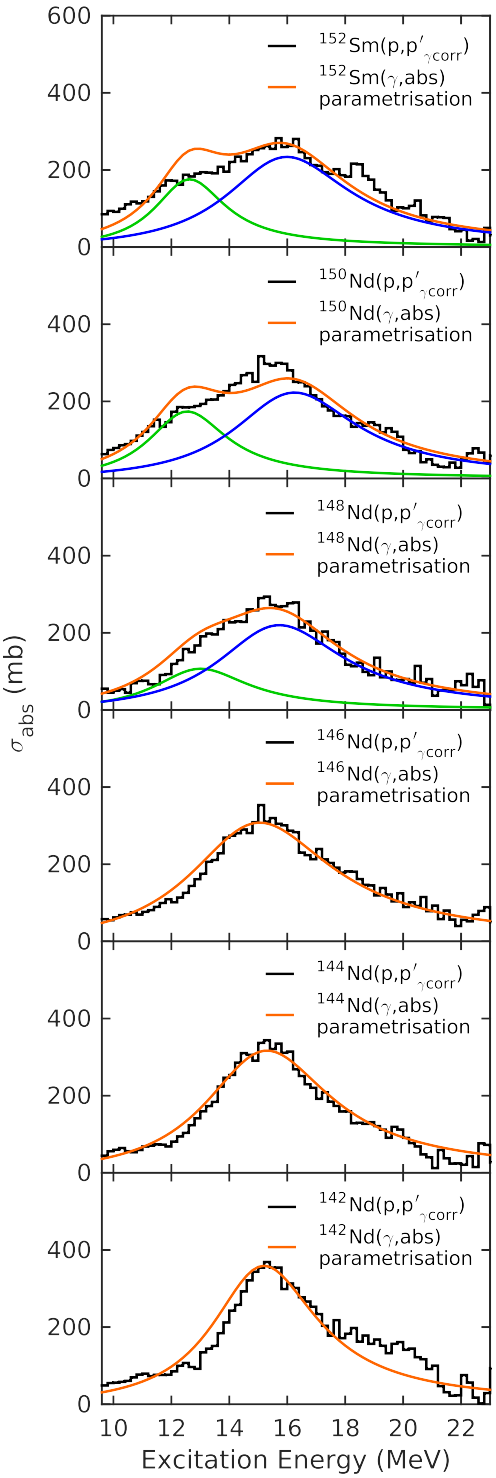


Figure 4.13: An overview of the comparison between the normalised ^{142,144,146,148,150}Nd(p,p$'_{\gamma corr}$) and ^{152}Sm(p,p$'_{\gamma corr}$) spectra and the (γ, abs) parametrisations [Cap09] (in orange). The $K = 0$ and $K = 1$ components (where applicable) have been plotted in green and blue, respectively.

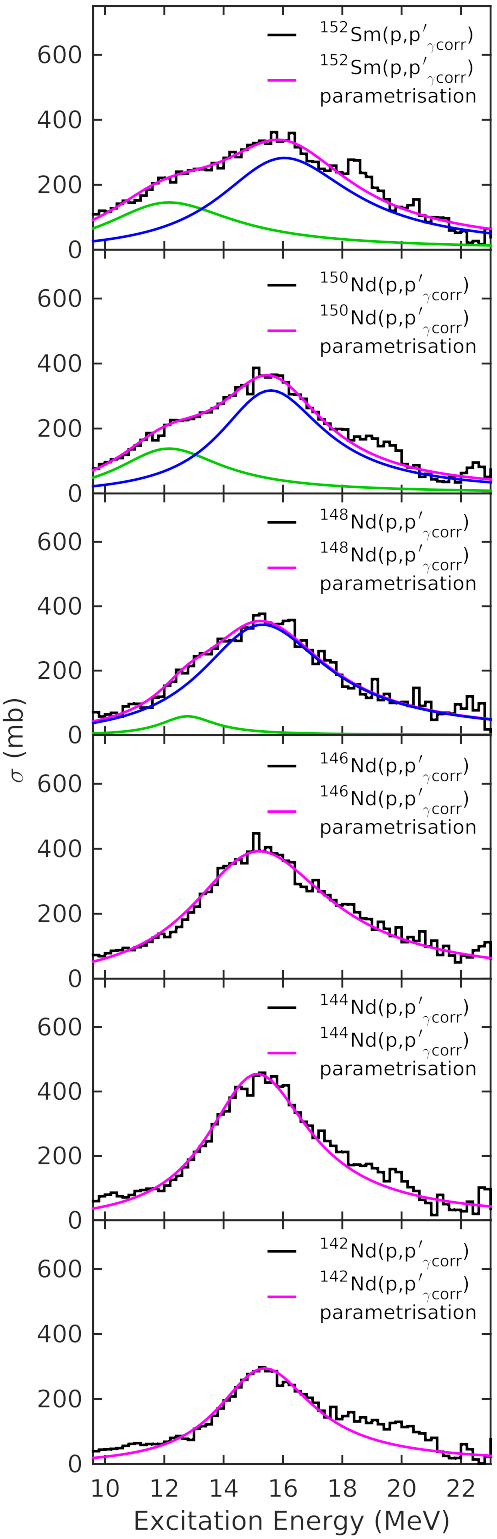


Figure 4.14: An overview of the newly determined Lorentz parametrisations (in pink) that accurately describe the ^{142,144,146,148,150}Nd(p,p$'_{\gamma corr}$) and ^{152}Sm(p,p$'_{\gamma corr}$) spectra. The $K = 0$ and $K = 1$ components (where applicable) have been plotted in green and blue, respectively.

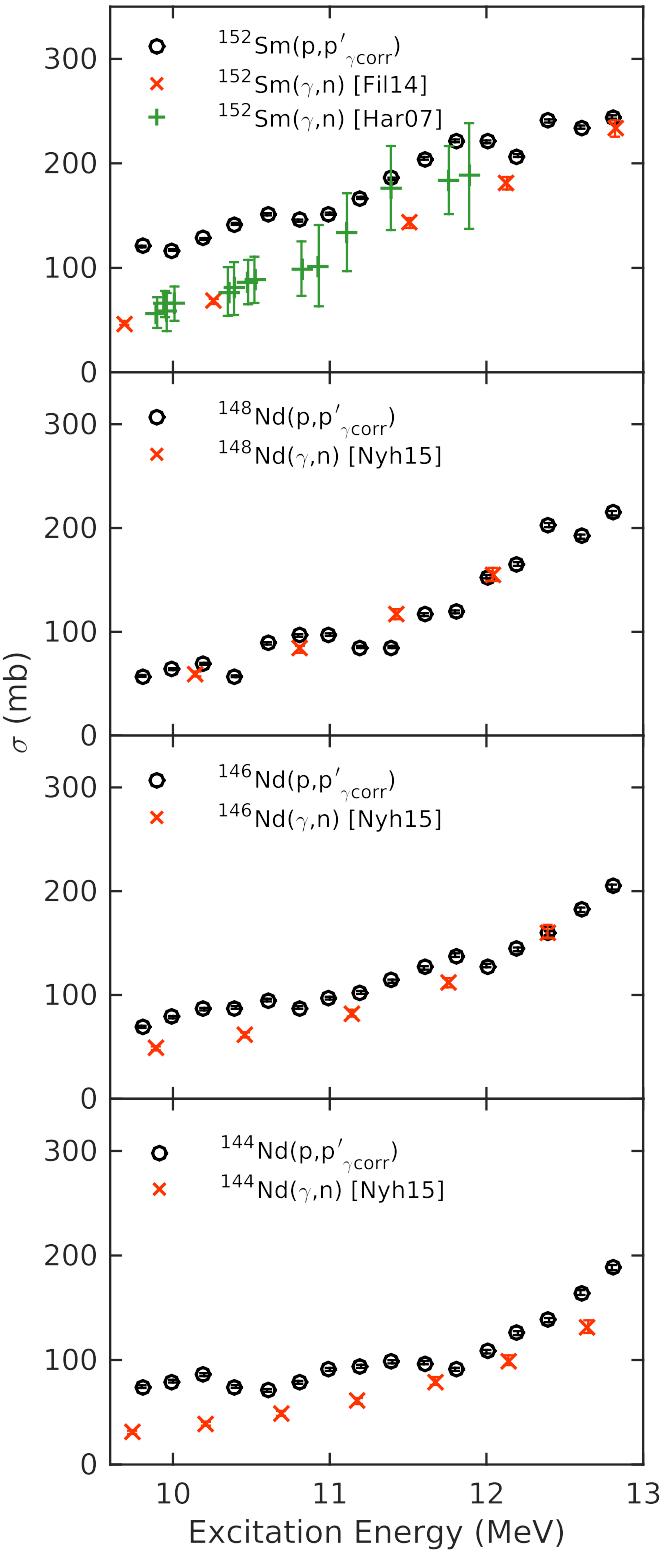


Figure 4.15: An overview of the comparison between the (p,p$'_{\gamma corr}$) spectra and the (γ,n) data for the energy range near the neutron threshold for the ^{144,146,148}Nd and ^{152}Sm isotopes.

4.3 Fine structure of the IVGDR and comparison with theoretical predictions

An overview of the equivalent photo-absorption cross sections for the even-even neodymium isotope chain and the doubly-even ^{152}Sm isotope is provided in Fig. 4.16. These cross sections were binned to 20 keV in order to facilitate a fine structure analysis. The increasing width of the IVGDR from the spherical ^{142}Nd through to the deformed ^{150}Nd and ^{152}Sm can be attributed to the increased splitting of the $K = 0$ and $K = 1$ components. The evolution of the width of the IVGDR with increasing deformation is clearly visible in this overview as is the presence of fine structure throughout the obtained (p,p$'_{\gamma\mathrm{corr}}$) spectra.

4.3.1 Results and Continuous Wavelet Transform analysis

Following the techniques outlined in Section 2.6.1, the energy-scales for each of the (p,p$'_{\gamma\mathrm{corr}}$) spectra were extracted using the complex Morlet mother-wavelet (see Section 2.6), which is given by Eq. (2.71). The results of these CWT analyses are displayed in Figs. 4.17 to 4.22. Note that for the sake of continuity and ease of comparison, all figures and associated tables have been placed at the end of this section.

By way of detailed example for the case of a spherical nucleus, Fig. 4.17 displays the CWT results for the experimentally obtained ^{142}Nd(p,p$'_{\gamma\mathrm{corr}}$) cross section in the top left panel. Correspondingly, for the theoretical case, the bottom left panel displays the CWT results for the SSRPA calculation, the details of which were outlined in Section 2.3.2.2 of Chapter 2. In the lower parts of the top left and bottom left panels, the wavelet coefficients as defined in Section 2.6.1.2 are plotted below the analysed spectrum. It should be noted that the displayed SSRPA cross sections are the SSRPA-calculated $B(E1)$ strength functions multiplied binwise by the excitation energy. Also displayed are the individual spectra for the $K = 0$ and $K = 1$ contributions plotted in green and blue, respectively. As can be seen, these contributions

are overlapping as would be expected in the case of an almost spherical nucleus. It is important to note that the CWT analysis was conducted on the sum of the $K = 0$ and $K = 1$ contributions, namely $K =$ sum, which is plotted in red.

In order to facilitate a broad structure comparison between the experimental results and the theoretical predictions, the SSRPA results for the $K = 0$, $K = 1$ and $K =$ sum components were smoothed to a large Γ. The smoothed $K = 0$, $K = 1$ and $K =$ sum components are displayed in green, blue and red, respectively, along with the experimental cross section in the top left panel of Fig. 4.17. As can be seen from the comparison, there is very good agreement between the two sets of results.

The top right and bottom right panels display the extracted power spectra (see Section 2.6.1.4) for the experimental and theoretical cases, respectively. For the SSRPA predictions, the power spectra for the $K = 0$ and $K = 1$ components, which were normalised to the $K =$ sum result are provided along with the $K =$ sum power spectrum. In reference to the experimental power spectra, a windowing technique has been used in an attempt to isolate the experimental scales that correspond to the theoretical scales for the individual $K = 0$, $K = 1$ and $K =$ sum components. In the case of the spherical ^{142}Nd nucleus, the $K = 0$ and $K = 1$ regions overlap, which is why the corresponding experimental power spectra are almost exactly alike.

By way of detailed example for the case of a deformed nucleus, Fig. 4.21 displays the CWT analysis and power spectra results for the ^{150}Nd(p,p$'_{\gamma\mathrm{corr}}$) cross section and corresponding SSRPA predictions. As for the case of the ^{142}Nd results, the SSRPA predictions for the $K = 0$, $K = 1$ and $K =$ sum components are displayed in the bottom left panel. As would be expected for a deformed nucleus, a clear splitting of the $B(E1)$ strength into $K = 0$ and $K = 1$ contributions is seen. It is important to note that ordinarily, it is traditional to leave the deformation parameter, β, free to vary for the SSRPA calculations. In this particular case (and that of the ^{152}Sm), however, β was set to a value comparable with the experimentally measured charge deformation for ^{150}Nd (^{152}Sm). Based on the numerous studies which indicate the overestimation of the $K = 0$ component in the experiments by Carlos *et al.* [Car71, Car74] and since the SSRPA SLy6 calculations were

developed to model those experimental results specifically, the decision to fix the deformation parameter in this case is, thus, justifiable. As can be seen in the top left panel of Fig. 4.21, there is excellent agreement with respect to the broad structure of the IVGDR between the experimental data and the SSRPA predictions, which were smoothed to a large Γ.

As would be expected, the results for the isotopes between the two extremes, that is, between the spherical ^{142}Nd and deformed ^{150}Nd, display a distinct increase in the splitting of the $K = 0$ and $K = 1$ components as deformation increases. This evolution can be seen through the comparison of Fig. 4.18, Fig. 4.19 and Fig. 4.20.

In the case of the ^{152}Sm, a deformed nucleus, the results are fairly similar to those of the ^{150}Nd isotope. The SSRPA predictions display a distinct splitting of the $K = 0$ and $K = 1$ components. As with the ^{150}Nd isotope, there is excellent agreement between the broad structure of the experimental data and the smoothed SSRPA predictions. A direct and more detailed comparison between the ^{150}Nd and ^{152}Sm results is provided in Section 4.3.2.

The energy scales corresponding to the experimental and theoretical power spectra have been extracted for each isotope and are displayed in Tables 4.2 to 4.7, where clearly identifiable scales are indicated in bold. Following a similar procedure to Refs. [She05, She04, Usm09], the scales are separated into three classes based on energy range. Class I contains all scales below 300 keV, which are a reflection of the fine structure present in the nucleus [Kur14]. Class II contains the intermediate scales, that is, those between 300 keV and 1000 keV. These scales vary strongly from nucleus to nucleus [Usm09]. Class III contains the scales between 1000 keV and 4000 keV, which provide information related to the gross structure of the resonance.

Both the (p,p$'_{\gamma\mathrm{corr}}$) and SSRPA results display characteristic scales in the region of the IVGDR as can be seen in Figs. 4.17 to 4.22 and Tables 4.2 to 4.7, respectively. It is important to note that only scales above 100 keV and below 4000 keV have been considered. Any scales visible below 100 keV are trivial as they stem from the experimental energy-resolution [Kur14]. The scales above 4000 keV have been excluded since they essentially account for the overall width of the IVGDR and as such, are not critical in a discussion of a fine

structure scales analysis.

From the inter-comparison between the characteristic energy scales extracted for the experimental data, it can be seen from Tables 4.2 to 4.7 that Class I dominant scales in the order of $\Delta E = 120 - 140$ keV have been identified for all neodymium isotopes as well as for the ^{152}Sm isotope. Smaller Class I scales in the order of $\Delta E = 60 - 80$ keV are present for the ^{142}Nd, ^{144}Nd and ^{146}Nd isotopes but are absent for the more deformed ^{148}Nd, ^{150}Nd and ^{152}Sm isotopes.

In the case of the ^{142}Nd nucleus, the agreement between the scales extracted from the experimental data and those extracted from the SSRPA predictions is particularly good for the Class I region. For Class II scales, there is reasonable agreement between experiment and theory but little to no agreement for Class III scales. A similar trend is seen in the case of the ^{144}Nd nucleus.

In both the ^{146}Nd and ^{148}Nd cases, reasonable agreement between the Class I and Class II scales extracted for experiment and theory is seen. Contrary to what was seen for the more spherical ^{142}Nd and ^{144}Nd nuclei, there is increased agreement between experiment and theory for the scales extracted in the Class III region. For the deformed ^{150}Nd and ^{152}Sm, however, a similar trend to the spherical nuclei is seen whereby the agreement between experiment and theory for Class I and II scales is reasonable and that for the Class III scales is poor. A more detailed discussion of the comparison between the scales extracted for the ^{150}Nd and ^{152}Sm isotopes is provided in Section 4.3.2.

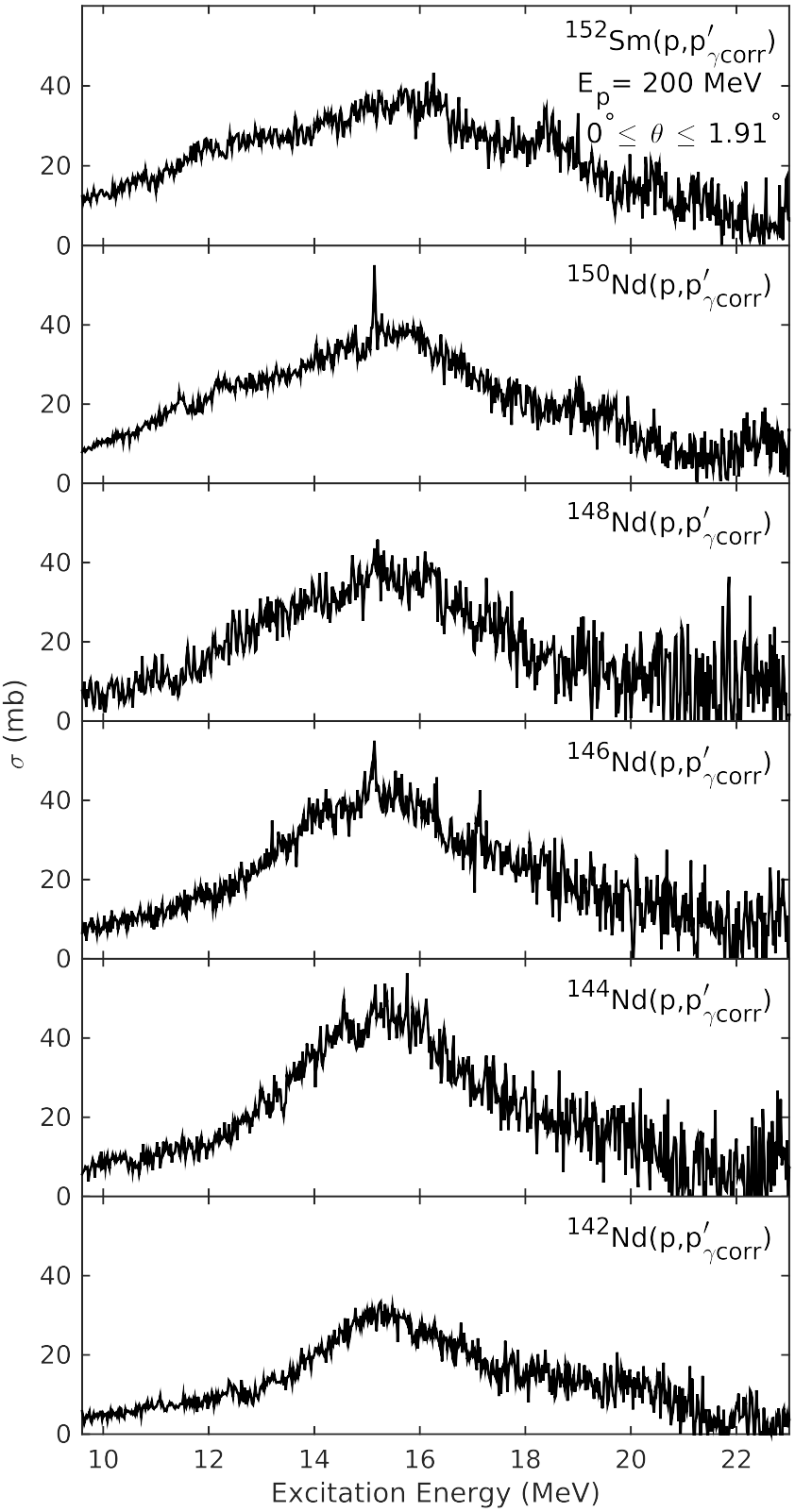


Figure 4.16: Overview of the cross sections obtained for ^{142,144,146,148,150}Nd(p,p′$_{\gamma corr}$) and ^{152}Sm(p,p′$_{\gamma corr}$) with $E_p = 200$ MeV.

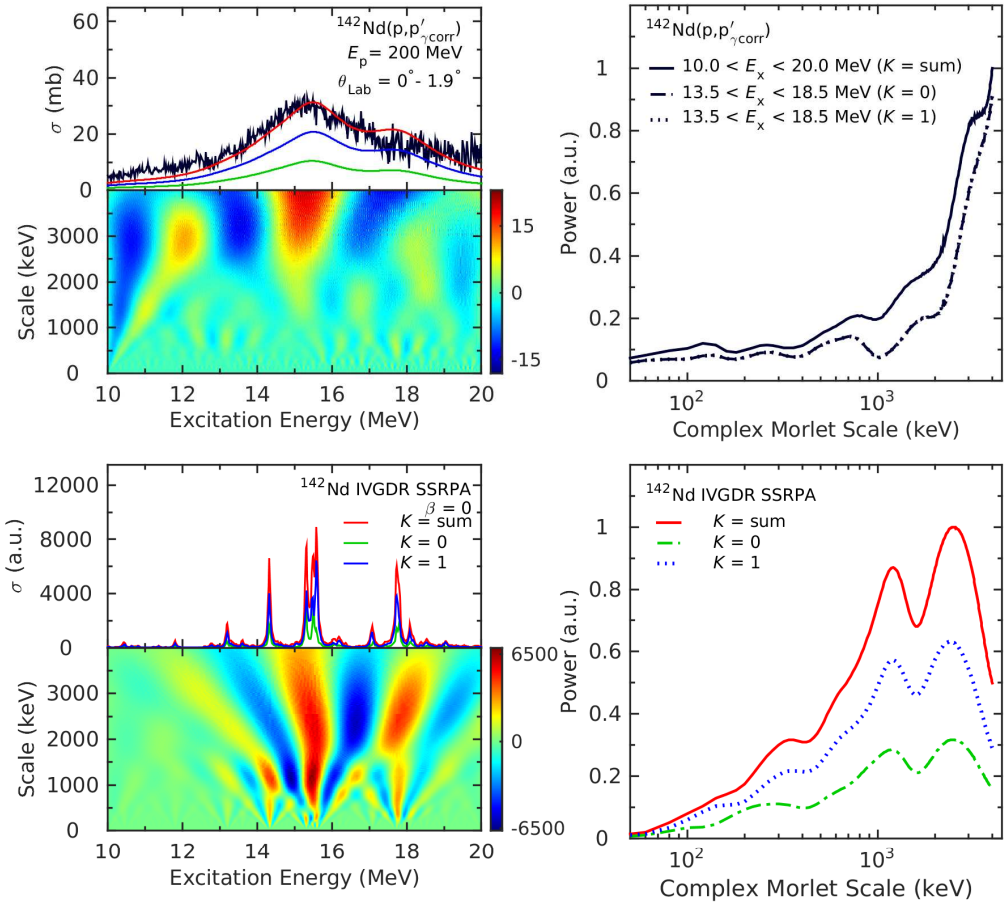


Figure 4.17: A complete overview of wavelet analysis and power spectra results for the experimental and SSRPA cases for ^{142}Nd.

Table 4.2: A comparison between the experimental and SSRPA Complex Morlet scales extracted for ^{142}Nd. Bold print indicates the presence of a clearly identifiable scale.

^{142}**Nd**	**Region**	**Class I**				**Class II**			**Class III**			
K	E_x	$\Delta E \leq 300$				$300 < \Delta E < 1000$			$1000 \leq \Delta E \leq 4000$			
	(MeV)	(keV)				(keV)			(keV)			
sum	10.0 - 20.0	Expt.	80	**120**	260		540	**820**	1560			**3200**
		SSRPA		140		**360**	620		**1200**		**2500**	
0	13.5 - 18.5	Expt.	80	140	**260**		540	**720**		**1900**		
		SSRPA	100		**280**		600		**1180**		**2480**	
1	13.5 - 18.5	Expt.	80	140	**260**		540	**720**		**1900**		
		SSRPA		**140**		**340**	640		**1200**		**2400**	

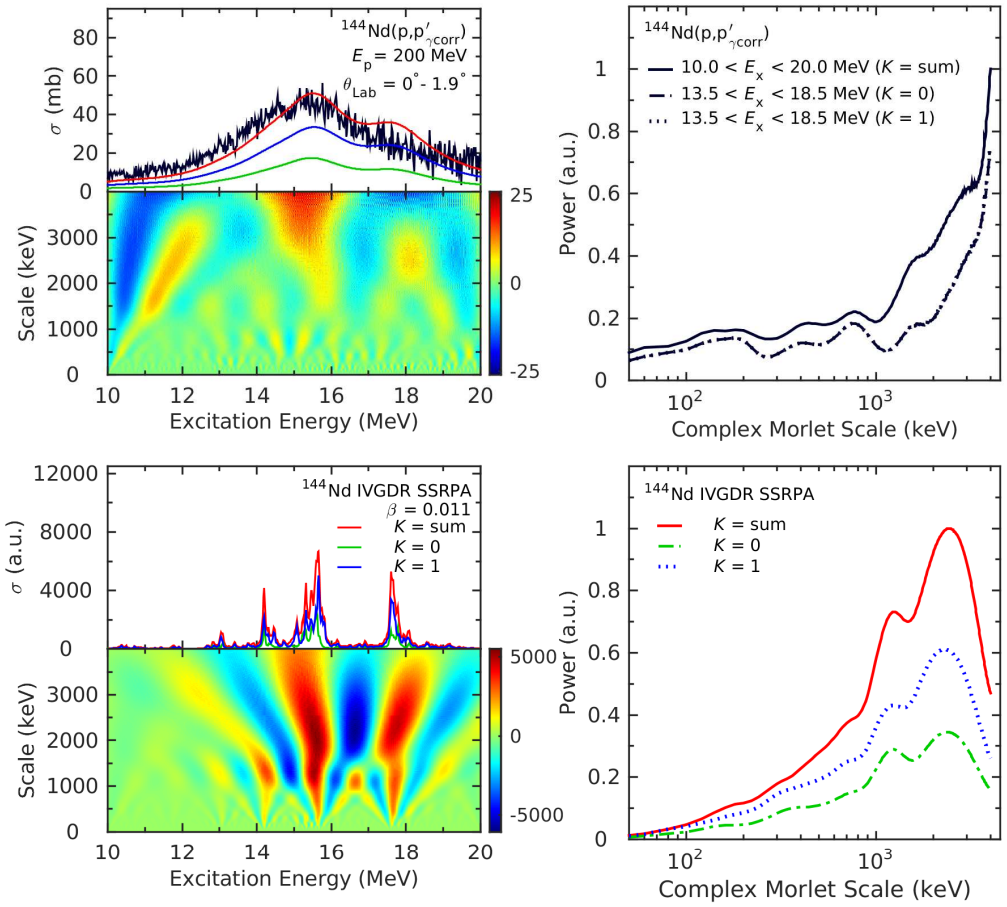


Figure 4.18: A complete overview of wavelet analysis and power spectra results for the experimental and SSRPA cases for ^{144}Nd.

Table 4.3: A comparison between the experimental and SSRPA Complex Morlet scales extracted for ^{144}Nd. Bold print indicates the presence of a clearly identifiable scale.

^{144}**Nd**	**Region**	**Class I**			**Class II**		**Class III**	
K	E_x	$\Delta E \leq 300$			$300 < \Delta E < 1000$		$1000 \leq \Delta E \leq 4000$	
	(MeV)	(keV)			(keV)		(keV)	
sum	10.0 - 20.0	Expt.	60	140 180	**440**	**760**	1520	2860
		SSRPA		180	320	720	**1240**	**2420**
0	13.5 - 18.5	Expt.	80	140 **180**	**420**	**760**	1520	
		SSRPA		160	360	720	**1220**	**2360**
1	13.5 - 18.5	Expt.	80	140 **180**	**420**	**760**	1520	
		SSRPA		180	320	720	**1220**	**2280**

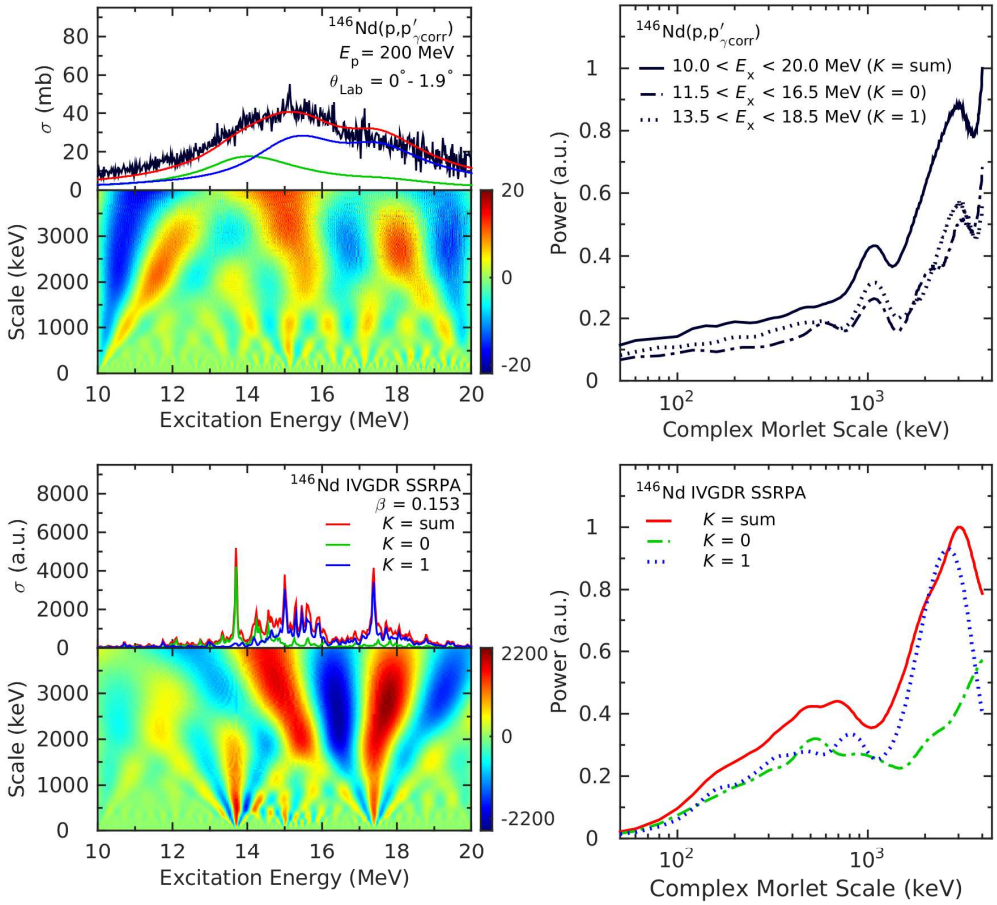


Figure 4.19: A complete overview of wavelet analysis and power spectra results for the experimental and SSRPA cases for ^{146}Nd.

Table 4.4: A comparison between the experimental and SSRPA Complex Morlet scales extracted for ^{146}Nd. Bold print indicates the presence of a clearly identifiable scale.

^{146}Nd	**Region**	**Class I**	**Class II**	**Class III**
K	E_x (MeV)	$\Delta E \leq 300$ (keV)	$300 < \Delta E < 1000$ (keV)	$1000 \leq \Delta E \leq 4000$ (keV)
sum	10.0 - 20.0	Expt. 60 140 200	300 440	**1080** **3020**
		SSRPA 160	500 **680**	2080 **3040**
0	11.5 - 16.5	Expt. 60 120 220	600	**1080** **2220** **3160**
		SSRPA 160	320 **520** **880**	2240
1	13.5 - 18.5	Expt. 80 120 200	**560** **900**	**1080** **3060**
		SSRPA 160	340 480 **820**	**2640**

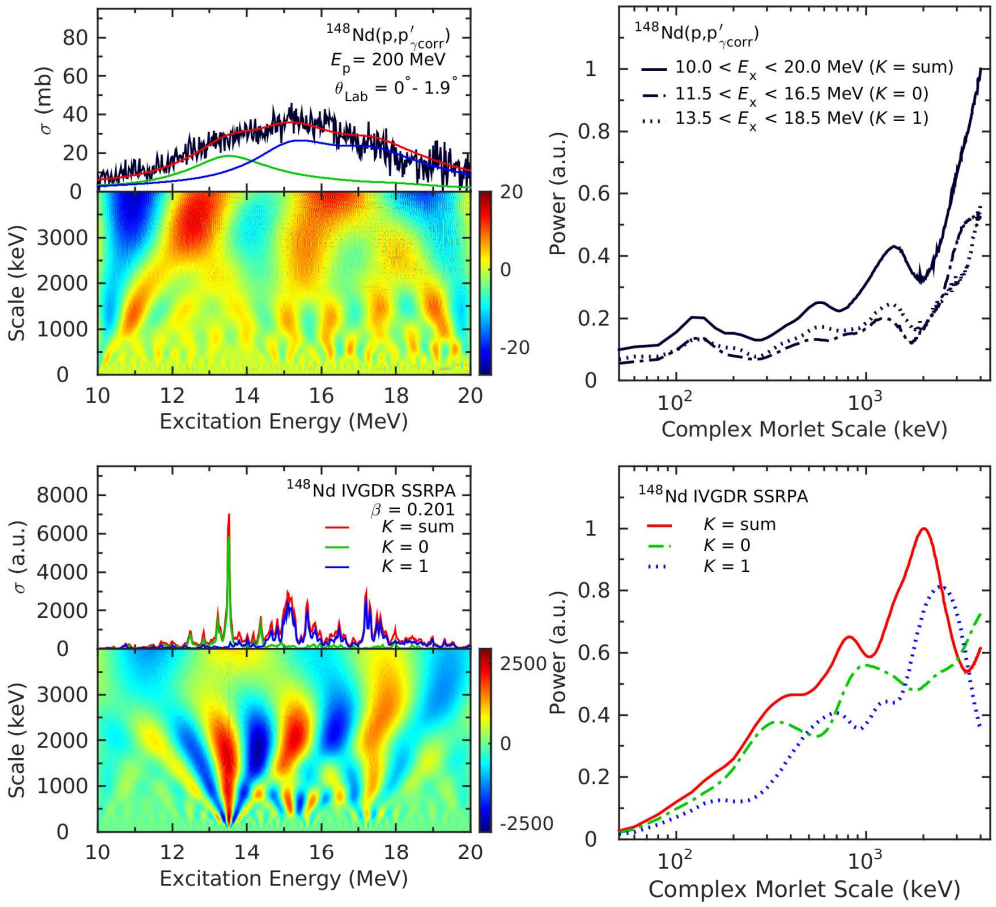


Figure 4.20: A complete overview of wavelet analysis and power spectra results for the experimental and SSRPA cases for ^{148}Nd.

Table 4.5: A comparison between the experimental and SSRPA Complex Morlet scales extracted for ^{148}Nd. Bold print indicates the presence of a clearly identifiable scale.

^{148}Nd	**Region**	**Class I**	**Class II**	**Class III**
K	E_x	$\Delta E < 300$	$300 \leq \Delta E \leq 1000$	$\Delta E \geq 1000$
	(MeV)	(keV)	(keV)	(keV)
sum	10.0 - 20.0	Expt. **120** 200	**580**	**1400**
		SSRPA 160	**360** **820**	1480 **2020**
0	11.5 - 16.5	Expt. **140**	**540** 820	**1220**
		SSRPA	**340** **1000**	2540
1	13.5 - 18.5	Expt. **140** 200	**580**	**1400** 2600
		SSRPA **180**	**700**	1260 **2460**

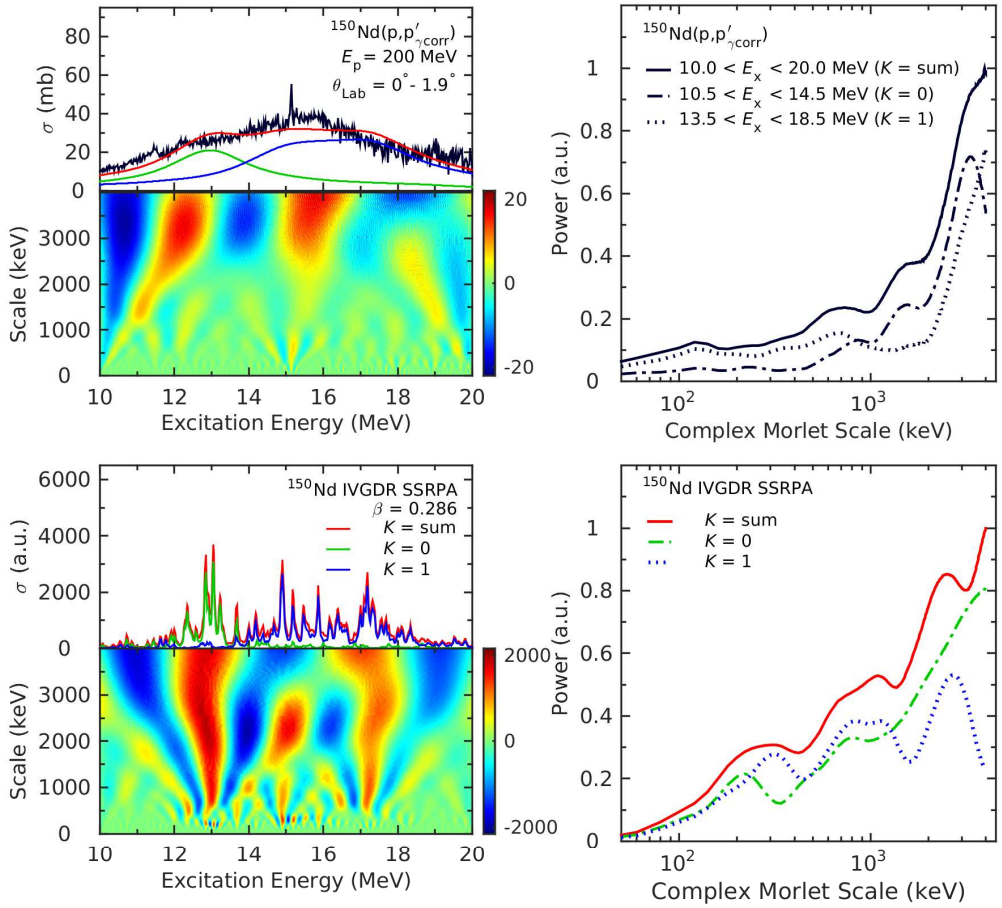


Figure 4.21: A complete overview of wavelet analysis and power spectra results for the experimental and SSRPA cases for ^{150}Nd.

Table 4.6: A comparison between the experimental and SSRPA Complex Morlet scales extracted for ^{150}Nd. Bold print indicates the presence of a clearly identifiable scale.

^{150}Nd K	**Region** E_x (MeV)	**Class I** $\Delta E < 300$ (keV)	**Class II** $300 \leq \Delta E \leq 1000$ (keV)	**Class III** $\Delta E \geq 1000$ (keV)
sum	10.0 - 20.0	Expt. **120** 220	340 **740**	**1580**
		SSRPA 220	680	**1080** **2500**
0	10.5 - 14.5	Expt. 120 240	**860**	**1560** **3320**
		SSRPA **220**	440 **800**	**4000**
1	13.5 - 18.5	Expt. 120	340 **680**	1540
		SSRPA	**320** **840**	1140 **2700**

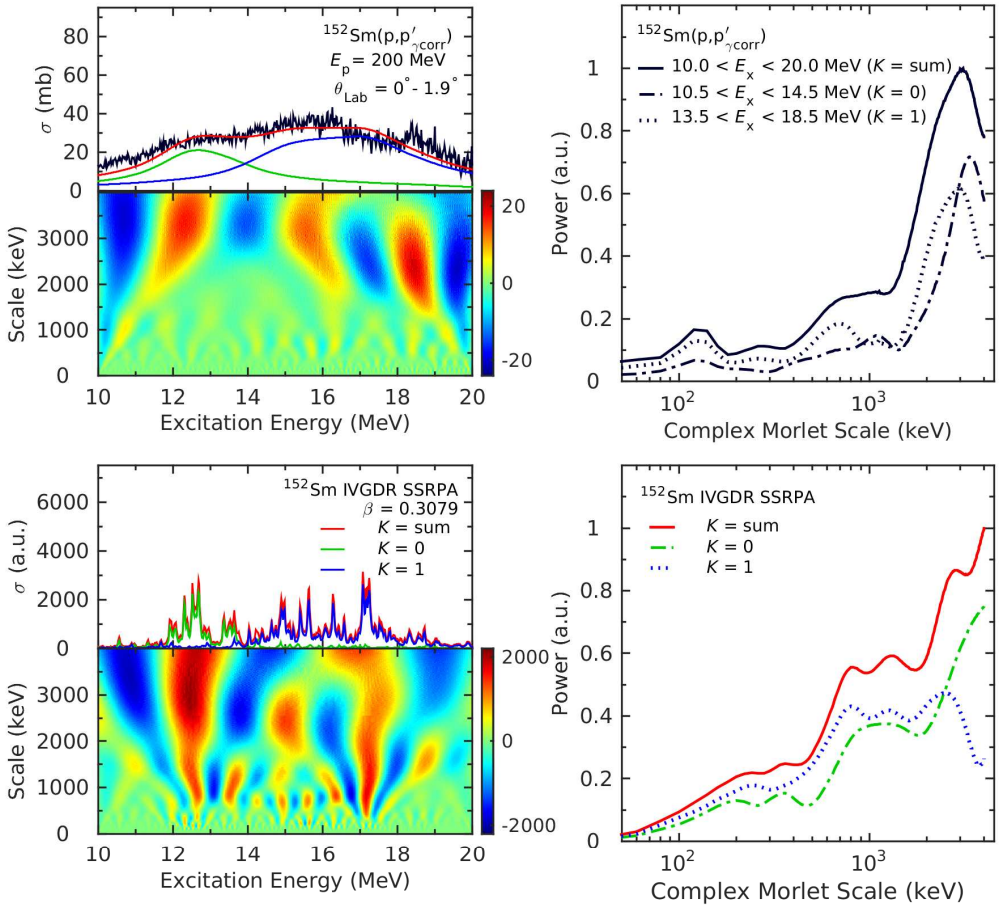


Figure 4.22: A complete overview of wavelet analysis and power spectra results for the experimental and SSRPA cases for ^{152}Sm.

Table 4.7: A comparison between the experimental and SSRPA Complex Morlet scales extracted for ^{152}Sm. Bold print indicates the presence of a clearly identifiable scale.

^{152}**Sm**	**Region**	**Class I**	**Class II**	**Class III**
K	E_x	$\Delta E \leq 300$	$300 < \Delta E < 1000$	$1000 \leq \Delta E \leq 4000$
	(MeV)	(keV)	(keV)	(keV)
sum	10.0 - 20.0	Expt. **120** 140 **280**	**680**	1040 **3100**
		SSRPA 220	**360** **820**	**1300** **2820**
0	10.5 - 14.5	Expt. **120** 140 220	460 680	**1080** **3340**
		SSRPA **200**	**360** 840	1340
1	13.5 - 18.5	Expt. **120** **260**	**700**	1120 **3000**
		SSRPA **240**	**800**	**1240** **2480**

4.3.2 Isotones in the transitional region: ^{150}Nd and ^{152}Sm comparison

The isotopes $^{150}_{60}\mathrm{Nd}_{90}$ and $^{152}_{62}\mathrm{Sm}_{90}$ are isotones in the transitional region as illustrated in Fig. 1.4. A comparison between them could, thus, yield insight into the influence of the proton number, Z, on the fine structure of the IVGDR as a function of nuclear deformation.

Similarities and differences between the experimentally obtained (p,p$'_{\gamma\mathrm{corr}}$) spectra, between the SSRPA predictions and between the experimentally obtained spectra and the corresponding SSRPA predictions can easily be visualised through the use of semblance analysis (see Section 2.6.2 of Chapter 2) which is used here in an exploratory way in the hope of yielding further insight into these comparisons.

Figure 4.23 displays the results of the semblance analysis which was conducted on the experimentally obtained ^{150}Nd(p,p$'_{\gamma\mathrm{corr}}$) and the ^{152}Sm(p,p$'_{\gamma\mathrm{corr}}$) data. In the semblance figure, it can be seen from the red areas that the two sets of data agree for larger scales. A similar result is seen in Fig. 4.24, which displays the semblance analysis results for the SSRPA predictions. A more detailed scales comparison is provided for the experimental spectra in Table 4.8 and for the SSRPA predictions in Table 4.9. Upon closer inspection, there is good agreement for the Class I scales extracted for ^{150}Nd and ^{152}Sm in both the experimental and theoretical cases. There is reasonable agreement for the Class II experimental and theoretical scales. The Class III scales in both the theoretical and experimental cases, however, display a far less consistent pattern and the agreement is generally poor.

The results of the semblance analyses performed on the experimentally obtained (p,p$'_{\gamma\mathrm{corr}}$) spectra and the corresponding SSRPA predictions for the ^{150}Nd and ^{152}Sm isotopes are displayed in Figs. 4.25 and 4.26, respectively. From these figures, it is clear that the results of the semblance analyses between theory and experiment are inconclusive. Although the SSRPA predictions compare well with respect to the broad structure of the (p,p$'_{\gamma\mathrm{corr}}$) spectra (see Figs. 4.17 to 4.22), the semblance analysis results could be indicative of the need for a model calculation which more accurately predicts the experimentally obtained fine structure.

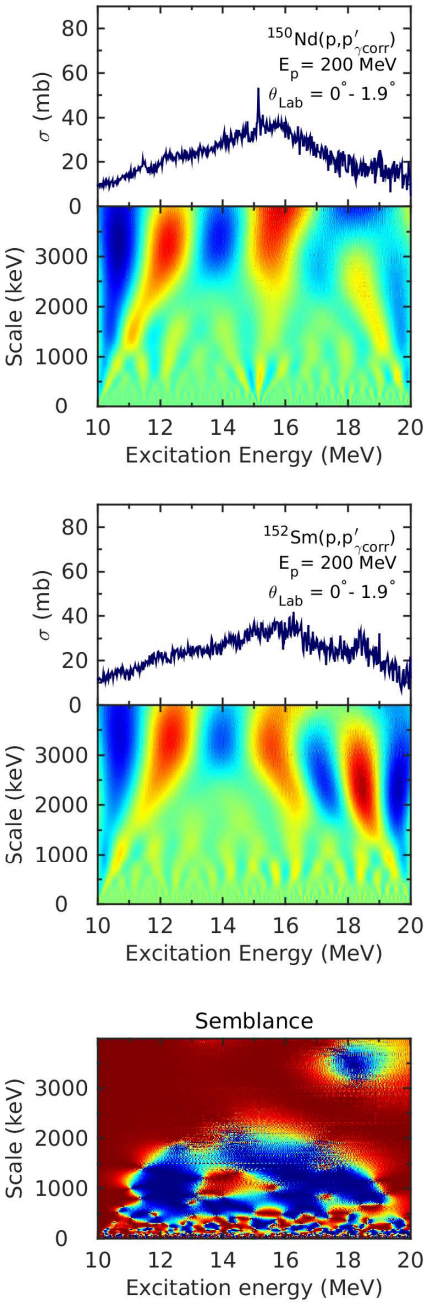


Figure 4.23: The result of the semblance analysis on the experimental ^{150}Nd(p,p$'_{\gamma corr}$) and ^{152}Sm(p,p$'_{\gamma corr}$) spectra.

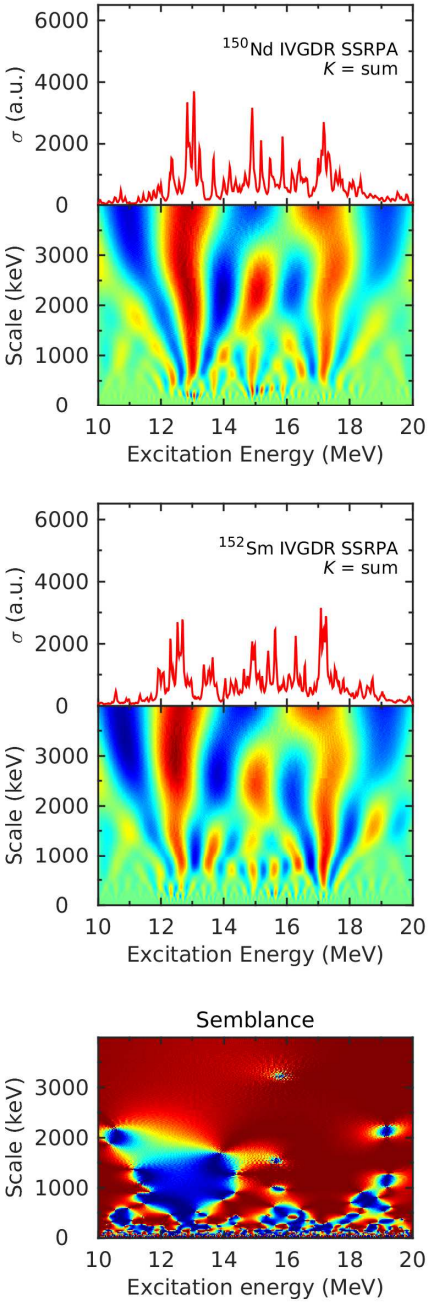


Figure 4.24: The result of the semblance analysis on the theoretical ^{150}Nd and ^{152}Sm SSRPA predictions.

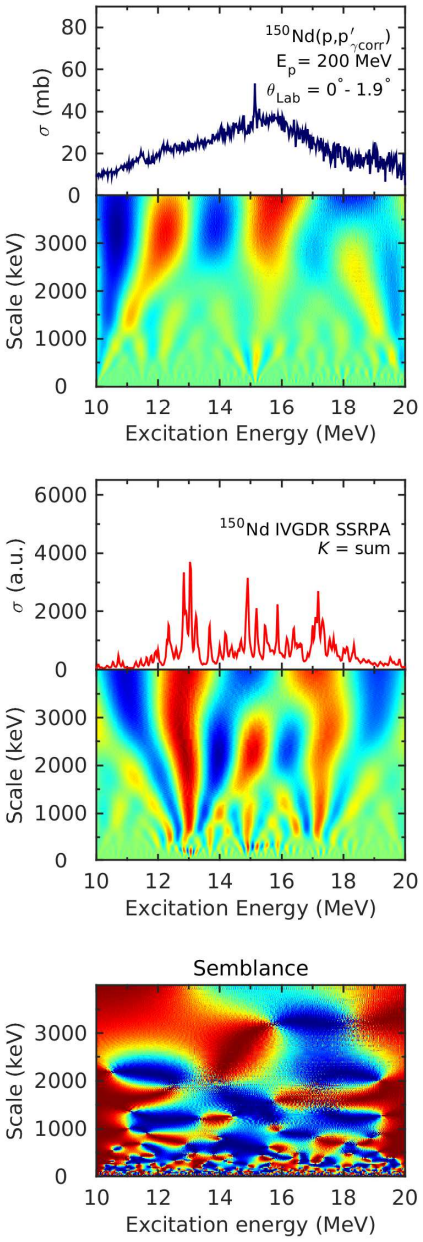


Figure 4.25: The result of the semblance analysis on the experimental ^{150}Nd(p,p$'_{\gamma corr}$) and the associated SSRPA prediction.

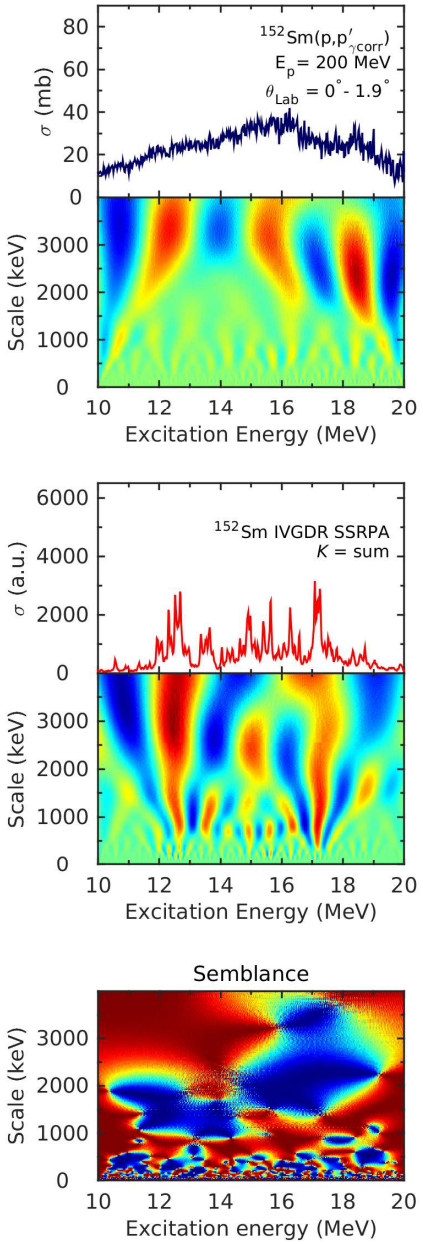


Figure 4.26: The result of the semblance analysis on the experimental ^{152}Sm(p,p$'_{\gamma corr}$) and the associated SSRPA prediction.

Table 4.8: A comparison between the experimental complex Morlet scales extracted for ^{150}Nd(p,p$'_{\gamma corr}$) and ^{152}Sm(p,p$'_{\gamma corr}$). Bold font indicates the presence of a clearly identifiable scale.

K	**Region** E_x (MeV)	**Isotope** (p,p$'_{\gamma corr}$)	**Class I** $\Delta E \leq 300$ (keV)	**Class II** $300 < \Delta E < 1000$ (keV)	**Class III** $1000 \leq \Delta E \leq 4000$ (keV)
sum	10.0 - 20.0	^{150}Nd	**120** 220	340 **740**	**1580**
		^{152}Sm	**120** 140 **280**	**680**	1040 **3100**
0	13.5 - 18.5	^{150}Nd	120 240	**860**	**1560** **3320**
		^{152}Sm	**120** 140 220	460 680	**1080** **3340**
1	13.5 - 18.5	^{150}Nd	**120**	340 **680**	1540
		^{152}Sm	**120** **260**	**700**	1120 **3000**

Table 4.9: A comparison between the complex Morlet scales extracted for ^{150}Nd and ^{152}Sm SSRPA predictions. Bold font indicates the presence of a clearly identifiable scale.

K	**Region** E_x (MeV)	**Isotope** SSRPA	**Class I** $\Delta E \leq 300$ (keV)	**Class II** $300 < \Delta E < 1000$ (keV)	**Class III** $1000 \leq \Delta E \leq 4000$ (keV)
sum	10.0 - 20.0	^{150}Nd	220	680	**1080** **2500**
		^{152}Sm	220	**360** **820**	**1300** **2820**
0	13.5 - 18.5	^{150}Nd	**220**	440 **800**	**4000**
		^{152}Sm	**200**	**360** 840	1340
1	13.5 - 18.5	^{150}Nd		**320** **840**	1140 **2700**
		^{152}Sm	**240**	**800**	**1240** **2480**

4.4 General discussion of results

When considering the (γ,abs) experiments performed by Carlos *et al.* [Car71, Car74], it is important to bear in mind the low energy-resolution of these data. This limits the applicability of the photo-absorption data to broad structure comparisons only. As such, although the (γ,abs) data are capable of illustrating the broadening and eventual splitting of the IVGDR as deformation increases from the nearly spherical ^{142}Nd nucleus to the permanently-deformed ^{150}Nd (see Fig. 1.4), they cannot be used for any fine structure comparisons.

The sequence of the photo-absorption data is typified by the use of a single Lorentzian peak for ^{142}Nd, ^{144}Nd and even for ^{146}Nd. Despite the increasing deformation, the individual $K = 0$ and $K = 1$ components are not yet distinguishable. The splitting of the IVGDR into two components, and thus the need for the use of two Lorentzians only becomes apparent in the case of the ^{148}Nd isotope, which is already reasonably well-deformed. This effect is even more dramatic in the highly deformed ^{150}Nd. Further investigations into a more highly deformed region past ^{150}Nd is not possible since the neodymium isotope chain becomes unstable in the ground state for masses greater than 150.

The new high energy-resolution data presented in this study require sophisticated calculations for the prediction of $B(E1)$ strength. As can be seen in the progression from ^{142}Nd (Fig. 4.17) through to ^{150}Nd (Fig. 4.21), the predicted $B(E1)$ strength function (bottom left panel in each instance) has clear $K = 0$ and $K = 1$ components which make up the total IVGDR strength. As explained in Section 2.3.1.2 of Chapter 2, these K-components correspond to the vibrations along perpendicular axes in the nucleus. In the case of a deformed nucleus, the $K = 0$ component corresponds to the vibrations along the major axis of symmetry of the ellipsoid and the $K = 1$ component corresponds to the vibrations along the minor axes.

Naturally, for close to spherical nuclei, the energies of the $K = 0$ and $K = 1$ components coincide. From the calculational perspective, this is clearly seen for the ^{142}Nd and the ^{144}Nd, where the $K = 0$ component is essentially a factor of 2 smaller than and lies essentially under the $K = 1$ component. Separation of these components becomes apparent for ^{146}Nd as can be seen in Fig. 4.19, noting also that the $K = 0$ component is already starting to increase in strength as can be seen in green in the bottom left panel. This separation and apparent increase in strength of the $K = 0$ contribution was not detected in the (γ,abs) experiment where it was still appropriate to use a single Lorentzian to model the photo-absorption results. In addition, it can be noted that the energy scales extracted from wavelet analysis show different structures in the power spectra for the $K = 0$ and $K = 1$ components (see green and blue components in the bottom right panel of Fig. 4.19, respectively). This is as opposed to essentially identical power spectra for the $K = 0$ and $K = 1$ contributions for the ^{142}Nd and ^{144}Nd cases as can be seen in the bottom

right panels of Figs. 4.17 and 4.18, respectively.

This trend becomes increasingly more significant as deformation increases through to ^{148}Nd and ^{150}Nd. Not only is there a noticeable increase in the separation of the $K = 0$ and $K = 1$ components (as already established by the need for two Lorentzians notably being of different widths to model the (γ,abs) results), but the $K = 0$ component now takes an almost equal amount of the available $B(E1)$ strength and is significantly more compact in its appearance in the lower excitation-energy region. This can be seen in Figs. 4.20 and 4.21. The $K = 0$ and $K = 1$ contributions in the associated power spectra are seen to be dramatically different. Although this predicted increase in strength of the $K = 0$ component was fairly dramatic in the (γ,abs) experiments of Carlos *et al.* [Car71, Car74], it was found to be far less extreme in the present equivalent photo-absorption spectra and in recent photo-neutron experiments [Nyh15, Fil14].

One of the goals of this high energy-resolution investigation of the IVGDR was to determine if corresponding isotones in the neodymium and samarium isotope chains, that is, $^{150}_{60}\mathrm{Nd}_{90}$ and $^{152}_{62}\mathrm{Sm}_{90}$, show any effect with an increase in proton number for the same neutron number. In this regard, a comparison of the bottom right panels of Figs. 4.21 and 4.22 reveals that the corresponding power spectra display very similar structures for the $K = 0$ components. The corresponding power spectra for the $K = 1$ components, however, vary more noticeably. A detailed energy-scales analysis uncovers some minor discrepancies between the isotones (particularly with respect to Class III scales) but overall, the agreement is reasonable. This reasonable agreement is especially true for the Class I and Class II experimental scales as can be seen in Table 4.8.

Chapter 5

Conclusions

High energy-resolution inelastic proton scattering experiments with $E_{\mathrm{p}} = 200$ MeV were performed on ^{142,144,146,148,150}Nd and ^{152}Sm in the excitation-energy region of the IVGDR using the Zero-degree Facility of the K600 magnetic spectrometer of iThemba LABS. The data collected from these high energy-resolution, 45 keV (FWHM) experiments were used to investigate the effect of nuclear deformation on both the broad and fine structure of the IVGDR in the rare-earth region.

A goal of the present study was to extend, for the first time, the IVGDR measurements to high energy-resolution and confirm the K-splitting observed in photo-absorption results obtained by Carlos *et al.* [Car71, Car74]. The applicability of these photo-absorption data to the present study was limited to broad structure comparisons only owing to the low energy-resolution of these data. Following the conversion of the experimentally obtained (p,p′) double-differential cross sections to equivalent photo-absorption cross sections i.e. (p,p$'_{\gamma\mathrm{corr}}$) cross sections, comparisons could be made to the existing photo-absorption spectra. A general broadening of the IVGDR with increasing neutron number as reported by Carlos *et al.* [Car71] was confirmed by the present (p,p$'_{\gamma\mathrm{corr}}$) spectra and a good correspondence between the (p,p$'_{\gamma\mathrm{corr}}$) and (γ,abs) results with respect to the shape of the IVGDR was seen for ^{142}Nd, ^{144}Nd, ^{146}Nd and ^{148}Nd. The resonances for the more deformed ^{150}Nd and ^{152}Sm, although significantly broader than the resonances for the less deformed nuclei, lacked the expected double-peaked structure, which contradicts the findings of Carlos *et al.* [Car71, Car74].

The strength of the $K = 0$ component in both the ^{150}Nd (p,p$'_{\gamma\text{corr}}$) and ^{152}Sm (p,p$'_{\gamma\text{corr}}$) spectra was seen to be significantly reduced compared to the (γ,abs) data. This is particularly interesting since these results compare very well with the findings of recent photo-neutron experiments by Filipescu *et al.* [Fil14] and Nyhus *et al.* [Nyh15]. A comparison of the parametrisations obtained in this study with those released by Carlos *et al.* [Car71, Car74] indicate that a 20 % reduction in the parameter describing the strength of the $K = 0$ component was necessary for both the ^{150}Nd and ^{152}Sm isotopes.

Techniques based on the continuous wavelet transform were implemented in order to perform a fine structure analysis on the high energy-resolution (p,p$'_{\gamma\text{corr}}$) data. Characteristic energy scales were extracted using the complex Morlet mother-wavelet and were compared to those extracted for the theoretically predicted $B(E1)$ strength functions. A global phenomenon was confirmed in the present experimentally obtained data since fine structure was visible in all of the equivalent photo-absorption cross sections, thus allowing for stringent model tests. The comparison between the energy scales obtained for the experimental data and those obtained for the SSRPA predictions showed particularly good agreement for Class I and Class II scales. Note that Class I contains all scales below 300 keV and Class II containes those between 300 keV and 1000 keV. The agreement for Class III scales, which contains all scales between 1000 keV and 4000 keV, was particularly poor for all isotopes with the exception of ^{146}Nd and ^{148}Nd.

It is important to note that the SLy6 Skyrme interaction was selected for use in the SSRPA predictions on the basis that it most accurately modelled the photo-absorption data obtained by Carlos *et al.* [Car71, Car74]. As a result of the most recent (p,p$'_{\gamma\text{corr}}$) and (γ,n) data, which indicate significantly reduced $K = 0$ strength for the deformed isotopes, it might be prudent to consider an adjustment in the chosen theoretical model interaction.

A comparison of corresponding isotones in the neodymium and samarium isotope chains, namely $^{150}_{60}\text{Nd}_{90}$ and $^{152}_{62}\text{Sm}_{90}$, yielded no obvious discrepancies in the shape of the IVGDR on a broad structural level. With regards to a fine structure comparison, minor differences were observed for Class III scales whereas for Class I and Class II experimental scales, the agreement was reasonable. It can, therefore, be concluded that the change in proton number

between these closely associated isotope chains has little to do with the excitation of the IVGDR. With regard to further experimental investigation, the present study could be extended by undertaking a series of complementary measurements on the other members of the even-even samarium isotope chain.

References

[Aib03] H. Aiba, M. Matsuo, S. Nishizaki, and T Suzuki. In: *Phys. Rev. C* 68 (2003), p. 054316.

[Aib99] H. Aiba and M. Matsuo. In: *Phys. Rev. C* 60 (1999), p. 034307.

[Ang12] C. T. Angell, S. L. Hammond, H. J. Karwowski, J. H. Kelley, M. Krticka, E. Kwan, A. Makinaga, and G. Rusev. In: *Phys. Rev. C* 86 (2012), p. 051302.

[Ben03] M. Bender, P. -H. Heenen, and P. -G. Reinhard. "Self-consistent mean-field models for nuclear structure". In: *Rev. Mod. Phys.* 75 (2003), pp. 121–180.

[Ben84] R. Bengtsson, P. Möller, J. R. Nix, and J. -Y. Zhang. In: *Phys. Scr.* 29 (1984), pp. 402–430.

[Ber09] C.A. Bertulani. 2009. arXiv: `0908.4307 [nucl-th]`.

[Ber75] B. Berman and S. Fultz. In: *Rev. Mod. Phys.* 47 (1975), pp. 713–761.

[Ber77] W. Bertozzi, M. V. Hynes, C. P. Sargent, C. Creswell, P. C. Dunn, A. Hirsch, M. Leitch, B. Norum, F. N. Rad, and T. Sasanuma. In: *Nucl. Instruments Methods* 141 (1977), pp. 457–476.

[Ber81] F.E. Bertrand. In: *Nucl. Phys. A* 354 (1981).

[Ber87] B. L. Berman, R. E. Pywell, S. S. Dietrich, M. N. Thompson, K. G. McNeill, and J. W. Jury. In: *Phys. Rev. C* 36 (1987), pp. 1286–1292.

[Ber88] C. Bertulani and G. Baur. In: *Phys. Rep.* 163 (1988), pp. 299–408.

[Ber93] C. Bertulani and A. Nathan. In: *Nucl. Phys. A* 554 (1993), pp. 158–172.

[Bli91] R. J. Blin-Stoyle. *Nuclear and Particle Physics*. London: Chapman and Hall, 1991.

[Blo71] H. G. Blosser, G. M. Crawley, R. Deforest, E. Kashy, and B. H. Wildenthal. In: *Nucl. Instrum. Methods* 91 (1971), pp. 61–65.

[Bot37] W. Bothe and W. Z. Genther. In: *Phys.* 106 (1937), p. 236.

[Bro83] K.L. Brown, F. Rothacker, D. C. Carey, and Ch. Iselin. *TRANSPORT A computer program for designing charged particle beam transport systems*. CERN-80-04. May 1983.

[Cap09] R. Capote, M. Herman, P. Oblozinsky, P. G. Young, S. Goriely, T. Belgya, A. V. Ignatyuk, A. J. Koning, S. Hilaire, V. A. Plujko, M. Avrigeanu, O. Bersillon, M. B. Chadwick, T. Fukahori, Z. Ge, Y. Han, S. Kailas, J. Kopecky, V. M. Maslov, G. Reffo, M. Sin, E. Sh. Soukhovitskii, and P. Talou. In: *Nucl. Data Sheets* 110 (2009), pp. 3107–3214. URL: `www-nds.iaea.org/RIPL-3/`.

[Car71] P. Carlos, H. Beil, R. Bergere, A. Lepretre, and A. Veyssiere. In: *Nucl. Phys. A* 172 (1971), pp. 437–448.

[Car74] P. Carlos, H. Beil, R. Bergere, A. Lepretre, A. De Miniac, and A. Veyssiere. In: *Nucl. Phys. A* 225 (1974), pp. 171–188.

[Cli86] D. Cline. In: *Ann. Rev. Nucl. Part. Sci.* 36 (1986), pp. 683–716.

[Coh59] B. L. Cohen. In: *Rev. Sci. Instrum.* 30 (1959), p. 415.

[Coo08] G. R. J. Cooper and D. R. Cowan. In: *Comput. Geosci.* 34 (2008), pp. 95–102.

[Dro91] S. Drozdz, S. Nishizaki, J. Speth, and J. Wambach. In: *Phys. Rep.* 197 (1991), pp. 1–65.

[Eji99] H. Ejiri and H. Toki, eds. *Nucleon-hadron Many-body Systems: From Hadron-meson to Quark-lepton Nuclear Physics*. Oxford Studies in Nuclear Physics. Oxford: Oxford University Press, 1999.

[End98] P.M. Endt. In: *Nucl. Phys. A* (1998), pp. 1–220.

[Eng81] H.A. Enge. In: *Nucl. Instrum. Methods* 187 (1981), pp. 1–11.

[Fil14] D. M. Filipescu, I. Gheorghe, H. Utsunomiya, S. Goriely, T. Renstrø m, H. -T. Nyhus, O. Tesileanu, T. Glodariu, T. Shima, K. Takahisa, S. Miyamoto, Y. -W. Lui, S. Hilaire, S. Péru, M. Martini, and A. J. Koning. In: *Phys. Rev. C* 90 (2014), p. 064616.

[Fir07] R. B. Firestone. In: *Nucl. Data Sheets* 108.11 (2007), pp. 2319–2392.

[Fuj01] H. Fujita, G. P. A. Berg, Y. Fujita, K. Hatanaka, T. Noro, E. J. Stephenson, C. C. Foster, H. Sakaguchi, M. Itoh, T. Taki, K. Tamura, and H. Ueno. In: *Nucl. Instrum. Meth. A* 469 (2001), pp. 55–62.

[Fuj02] H. Fujita, Y. Fujita, G. P. A. Berg, A. D. Bacher, C. C. Foster, K. Hara, K. Hatanaka, T. Kawabata, T. Noro, H. Sakaguchi, Y. Shimbara, T. Shinada, E. J. Stephenson, H. Ueno, and M. Yosoi. In: *Nucl. Instrum. Meth. A* 484 (2002), pp. 17–26. ISSN: 01689002.

[Fuj97] Y. Fujita, K. Hatanaka, G. P. A. Berg, K. Hosono, N. Matsuoka, S. Morinobu, T. Noro, M. Sato, K. Tamura, and H. Ueno. In: *Nucl. Instrum. Meth. B* 126.96 (1997), pp. 274–278.

[Goe82] K. Goeke and J. Speth. "Theory of Giant Resonances". In: *Ann. Rev. of Nucl. Part. Sci.* 32 (1982), pp. 65–115.

[Gra95] A. Graps. In: *IEEE Comput. Sci. Eng.* 2 (1995).

[Ham12] I. Hamamoto and B. Mottelson. In: 7 (2012), p. 10693.

[Har01] M. N. Harakeh and A. Van der Woude. *Giant resonances: Fundamental High-Frequency Modes of Nuclear Excitation.* Oxford Studies in Nuclear Physics. Oxford: Oxford University Press, 2001.

[Har07] K. Y. Hara, H. Harada, F. Kitatani, S. Goko, S. Hohara, T. Kaihori, A. Makinaga, H. Utsunomiya, H. Toyokawa, and K. Yamada. In: *J. Nucl. Sci. Technol.* 44 (2007), p. 938.

[Hin74] F. Hinterberger. In: *Nucl. Instrum. Methods* 119 (1974), pp. 43–49.

[Ish11] B. S. Ishkhanov and S. Yu Troshchiev. In: *Moscow University Physics Bulletin* 66 (2011), pp. 325–337.

[Jin14] M. Jingo. "Fine structure of the Isovector Giant Dipole Resonance : A survey with the (p,p′) reaction at zero degrees". PhD. University of the Witwatersrand, 2014.

[Kal06] Y. Kalmykov, T. Adachi, G. P. A. Berg, H. Fujita, K. Fujita, Y. Fujita, K. Hatanaka, J. Kamiya, K. Nakanishi, P. von Neumann-Cosel, V. Yu. Ponomarev, A. Richter, N. Sakamoto, Y. Sakemi, A. Shevchenko, Y. Shimbara, Y. Shimizu, F. D. Smit, T. Wakasa, J. Wambach, and M. Yosoi. In: *Phys. Rev. Lett.* 96 (2006), p. 012502.

[Kap15] I. M. Kapitonov. In: *Bull. Russ. Acad. Sci. Phys.* 79 (2015), pp. 526–531.

[Khe11] N. Y. Kheswa, P. Papka, C. A. Pineda-Vargas, and R. T. Newman. In: *Nucl. Instrum. Meth. A* 655 (2011). Proceedings of the 25th World Conference of the International Nuclear Target Development Society, pp. 85–87.

[Khe15] N. Y. Kheswa. Private Communication. 2015.

[Kle08] W. Kleinig, V. O. Nesterenko, J. Kvasil, P.-G. Reinhard, and P. Vesely. In: *Phys. Rev. C* 78 (2008), p. 044313.

[Kra88] K. S. Krane. *Introductory Nuclear Physics*. Canada: John Wiley and Sons, Inc, 1988.

[Kru14] A. Krugmann. "Off-Yrast low-spin structure of deformed nuclei at mass number A≈150". PhD. TU Darmstadt, 2014.

[Kur14] C. O. Kureba. "Fine structure of the Isoscalar Giant Quadrupole Resonance and 2^+ level densities in spherical to deformed nuclei across the isotope chain ^{142,144,146,148,150}Nd using the (p,p′) reaction". PhD. University of the Witwatersrand, 2014.

[Lac00] D. Lacroix, A. Mai, P. von Neumann-Cosel, A. Richter, and J. Wambach. In: *Phys. Lett. B* 479 (2000), pp. 15–20.

[Lac99] D. Lacroix and P. Chomaz. In: *Phys. Rev. C* 60 (1999), pp. 1–14.

[Liv66] D. L. Livesey. *Atomic and Nuclear Physics*. Massachusetts: Blaisdell Publishing Company, 1966.

[Mar70] P. Marmier and E. Sheldon. *Physics of Nuclei and Particles Volume II*. New York: Academic Press Inc., 1970.

[Mar83] S. A. Martin, A. Hardt, J. Meissburger, G. P. A. Berg, U. Hacker, W. Hürlimann, J. G. M. Römer, T. Sagefka, A. Retz, O. W. B. Schult, K. L. Brown, and K. Halbach. In: *Nucl. Instrum. Methods* 214 (1983), pp. 281–303.

[Mas06] V. M. Masur and L. M. Mel'nikova. In: *Phys. Part. Nuclei* 37 (2006), pp. 923–940.

[Mye77] W. Myers, W. J. Swiatecki, T. Kodama, L. J. El-Jaick, and E. R. Hilf. In: *Phys. Rev. C* 15 (1977).

[Nai10] C. Nair, A. R. Junghans, M. Erhard, D. Bemmerer, R. Beyer, E. Grosse, K. Kosev, M. Marta, G. Rusev, K. D. Schilling, R. Schwengner, and A. Wagner. "Dipole strength in ^{144}Sm studied via (γ, n), (γ, p), and (γ, α) reactions". In: *Phys. Rev. C* 81 (2010), p. 055806.

[Nes02] V. O. Nesterenko, J. Kvasil, and P. -G. Reinhard. In: *Phys. Rev. C* 66 (2002), p. 044307.

[Nes06] V. O. Nesterenko, W. Kleinig, J. Kvasil, P. Vesely, P. -G. Reinhard, and D. S. Dolci. In: *Phys. Rev. C* 74 (2006), p. 064306.

[Nes07] V. O. Nesterenko, W. Kleinig, J. Kvasil, P. Vesely, and P. -G. Reinhard. In: (2007). arXiv: `0711.1090`.

[Nes15] V. O. Nesterenko. Private Communication. 2015.

[Nes16] V. O. Nesterenko. Private Communication. 2016.

[Neu15] P. von Neumann-Cosel. Private Communication. 2015.

[Nev01] R. Neveling. "Nuclear medium effects on analyzing power investigated with a proton knockout reaction". PhD. University of Stellenbosch, 2001.

[Nev11a] R. Neveling, H. Fujita, F. D. Smit, T. Adachi, G. P. A. Berg, E. Z. Buthelezi, J. Carter, J. L. Conradie, M. Couder, R. W. Fearick, S. V. Förtsch, D. T. Fourie, Y. Fujita, J. Görres, K. Hatanaka, M. Jingo, A. M. Krumbholz, C. O. Kureba, J. P. Mira, S. H. T. Murray, P. von Neumann-Cosel, S. O'Brien, P. Papka, I. Poltoratska, A. Richter, E. Sideras-Haddad, J. A. Swartz, A. Tamii, I. T. Usman, and J. J. van Zyl. In: *Nucl. Instrum. Meth. A* 654 (2011), pp. 29–39.

[Nev11b] R. Neveling, H. Fujita, F. D. Smit, T. Adachi, G. P. A. Berg, E. Z. Buthelezi, J. Carter, J. L. Conradie, M. Couder, R. W. Fearick, S. V. Förtsch, D. Fourie, Y. Fujita, J. Görres, K. Hatanaka, A. M. Heilmann, J. P. Mira, S. H. T. Murray, P. Von Neumann-Cosel, S. O'Brien, P. Papka, I. Poltoratska, A. Richter, E. Sideras-Haddad, J. A. Swartz, A. Tamii, I. T. Usman, and J. J. Van Zyl. In: *J. Phys. Conference Series* 312 (2011), p. 052016.

[Nev14] R. Neveling, F. D. Smit, H. Fujita, and R. T. Newman. *Guide to the K600 magnetic spectrometer*. unpublished. 2014.

[Nev15] R. Neveling. Private Communication. 2015.

[Nyh15] H. -T. Nyhus, T. Renstrø m, H. Utsunomiya, S. Goriely, D. M. Filipescu, I. Gheorghe, O. Tesileanu, T. Glodariu, T. Shima, K. Takahisa, S. Miyamoto, Y. -W. Lui, S. Hilaire, S. Péru, M. Martini, L. Siess, and A. J. Koning. In: *Phys. Rev. C* 91 (2015), p. 015808.

[Opr12] C. Oprea, A. Oprea, and A. Mihul. In: *Phys. Procedia* 31 (2012), pp. 178–184.

[Pol11] I. Poltoratska. PhD. T. U. Darmstadt, 2011.

[Pon15] V. -Yu. Ponomarev. Private Communication. 2015.

[Ric05] A. Richter. In: *Prog. Part. Nucl. Phys.* 55 (2005), pp. 387–396.

[Rit97] S. Ritt and P. A. Amaudruz. In: *Proc. 10th IEEE Real Time Conf.* 1997, pp. 309–312.

[She04] A. Shevchenko, J. Carter, R. W. Fearick, S. V. Förtsch, H. Fujita, Y. Fujita, Y. Kalmykov, D. Lacroix, J. J. Lawrie, P. von Neumann-Cosel, R. Neveling, V. Yu. Ponomarev, A. Richter, E. Sideras-Haddad, F. D. Smit, and J. Wambach. In: *Phys. Rev. Lett.* 93 (2004), p. 122501.

[She05] A. Shevchenko. "Fine Structure of the Isoscalar Giant Quadrupole Resonance from High-Resolution Inelastic Proton Scattering Experiments". PhD. T. U. Darmstadt, 2005.

[She08] A. Shevchenko, J. Carter, G. R. J. Cooper, R. W. Fearick, Y. Kalmykov, P. von Neumann-Cosel, V. Yu. Ponomarev, A. Richter, I. Usman, and J. Wambach. In: *Phys. Rev. C* 77 (2008), p. 024302.

[She09] A. Shevchenko, O. Burda, J. Carter, G. Cooper, R. Fearick, S. Förtsch, H. Fujita, Y. Fujita, Y. Kalmykov, D. Lacroix, J. Lawrie, P. von Neumann-Cosel, R. Neveling, V. Ponomarev, A. Richter, E. Sideras-Haddad, F. Smit, and J. Wambach. In: *Phys. Rev. C* 79 (2009), p. 044305.

[Sno86] K. Snover. In: *Ann. Rev. Nucl. Part. Sci.* 36 (1986), pp. 545–603.

[Spe81] J. Speth and A. van der Woude. In: *Rep. Prog. Phys.* 44 (1981), p. 719.

[Tam09] A. Tamii, Y. Fujita, H. Matsubara, T. Adachi, J. Carter, M. Dozono, H. Fujita, K. Fujita, H. Hashimoto, K. Hatanaka, T. Itahashi, M. Itoh, T. Kawabata, K. Nakanishi, S. Ninomiya, A. B. Perez-Cerdan, L. Popescu, B. Rubio, T. Saito, H. Sakaguchi, Y. Sakemi, Y. Sasamoto, Y. Shimbara, Y. Shimizu, F. D. Smit, Y. Tameshige, M. Yosoi, and J. Zenhiro. In: *Nucl. Instrum. Meth. A* 605 (2009), pp. 326–338.

[Tam15] A. Tamii. Private Communication. 2015.

[Tor98] C. Torrence and G. P. Compo. In: *Bull. Am. Meteorol. Soc.* 79 (1998), pp. 61–78.

[Usm07] I.T. Usman. *Elucidating the damping mechanisms of nuclear giant resonances by high energy-resolution measurements of the isoscalar quadrupole and isovector dipole modes.* Unpublished. PhD Research Proposal. 2007.

[Usm09] I. T. Usman. "Fragmentation of the Isoscalar Giant Quadrupole Resonance in low mass $12 \leq A \leq 40$ nuclei and 2^+ level density in ^{40}Ca from high energy-resolution (p,p′) scattering at 200 MeV". PhD. University of the Witwatersrand, 2009.

[Usm11a] I. Usman, Z. Buthelezi, J. Carter, G. R. J. Cooper, R. W. Fearick, H. Förtsch S. V. and Fujita, Y. Fujita, Y. Kalmykov, P. von Neumann-Cosel, R. Neveling, P. Papakonstantinou, A. Richter, R. Roth, A. Shevchenko, E. Sideras-Haddad, and F. D. Smit. In: *Phys. Lett. B* 698 (2011), pp. 191–195.

[Usm11b] I. Usman, Z. Buthelezi, J. Carter, G. R. J. Cooper, R. W. Fearick, S. V. Förtsch, H. Fujita, Y. Kalmykov, P. von Neumann-Cosel, R. Neveling, I. Poltoratska, A. Richter, A. Shevchenko, E. Sideras-Haddad, F. D. Smit, and J. Wambach. In: *Phys. Rev. C* 84 (2011), p. 054322.

[Uts15] H. Utsunomiya. Private Communication. 2015.

[Wak02] T. Wakasa, K. Hatanaka, Y. Fujita, G. P. A Berg, H. Fujimura, H. Fujita, M. Itoh, J. Kamiya, T. Kawabata, K. Nagayama, T. Noro, H. Sakaguchi, Y. Shimbara, H. Takeda, K. Tamura, H. Ueno, M. Uchida, M. Uraki, and M. Yosoi. In: *Nucl. Instrum. Meth. A* 482 (2002), pp. 79–93.

[Whe14] C. Wheldon. *Derivations for two-body kinematics (both relativistic and non-relativistic)*. 2014.

[Win79] A. Winther and K. Alder. In: *Nucl. Phys. A* 319 (1979), pp. 518–532.

[Wou91] A. van der Woude. "The Electric Giant Resonances". In: *Electric and Magnetic Giant Resonances in Nuclei*. Ed. by J. Speth. Vol. 7. International Review of Nuclear Physics. World Scientific, 1991, pp. 99–232.

Appendix A

Matching the beamline and spectrometer

At any position in the system, an arbitrary charged particle is represented by a vector $\vec{X}$ [Bro83], which is given by:

$$\vec{X} = \begin{bmatrix} x \\ \theta \\ y \\ \phi \\ l \\ \delta \end{bmatrix} \quad , \tag{A.1}$$

where

x = the horizontal displacement of the arbitrary ray with respect to the assumed central ray,
θ = the angle this ray makes in the horizontal plane with respect to the assumed central ray,
y = the vertical displacement of the ray with respect to the assumed central ray,
ϕ = the vertical angle of the ray with respect to the assumed central ray,
l = the path length difference between the arbitrary ray and the central ray and
$\delta = \Delta p/p$ is the fractional momentum deviation of the ray from the assumed central ray.

Figure A.1 illustrates schematically the relationship between an incident particle ray 1 and an outgoing particle ray 2 relative to the beam and the

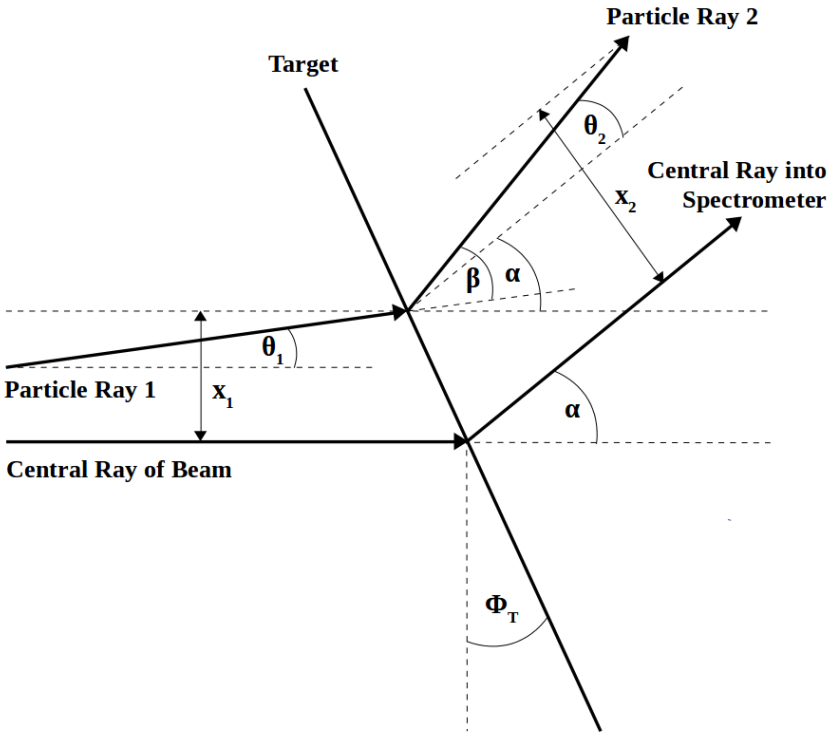


Figure A.1: A schematic representation of the relationship between the incident particle ray 1 and the outgoing particle ray 2 relative to the central ray in the beamline and the spectrometer.

spectrometer. With reference to this figure, a summary of the ion-optical considerations as discussed in Refs. [Fuj97, Fuj02, Mar83] is given below.

At the source point, it is assumed that a particle has horizontal coordinates $\vec{x_0} = (x_0, \theta_0, \delta_0)$. It is then transformed down the beamline by the reduced, horizontal 3×3 matrix $\mathbf{B} = (b_{\mu\nu})$ where $\mu, \nu = 1, 2, 6$. Note that the suffixes 1, 2 and 6 refer to x, θ and δ respectively as defined in Eq. (A.1). At the target in the scattering chamber, the coordinates of the particle are given by

$\vec{x_1} = (x_1, \theta_1, \delta_1)$ where

$$\begin{aligned} \vec{x_1} &= \mathbf{B}\vec{x_0} \\ &= \begin{pmatrix} b_{11} & b_{12} & b_{16} \\ b_{21} & b_{22} & b_{26} \\ 0 & 0 & 1 \end{pmatrix} \begin{pmatrix} x_0 \\ \theta_0 \\ \delta_0 \end{pmatrix} \\ &= \begin{pmatrix} b_{11}x_0 + b_{12}\theta_0 + b_{16}\delta_0 \\ b_{12}x_0 + b_{22}\theta_0 + b_{26}\delta_0 \\ \delta_0 \end{pmatrix} \\ &= \begin{pmatrix} x_1 \\ \theta_1 \\ \delta_1 \end{pmatrix} \quad . \end{aligned} \tag{A.2}$$

Note that $\delta_0 = \delta_1$ since the beam energy has not changed and so matrix elements $b_{61} = b_{62} = 0$ and $b_{66} = 1$. The critical transformation, however, is that of $\vec{x_1}$ to $\vec{x_2}$ at the target such that:

$$\begin{aligned} \vec{x_2} &= \begin{pmatrix} x_2 \\ \theta_2 \\ \delta_2 \end{pmatrix} \\ &= \begin{pmatrix} Tx_1 \\ \theta_2 \\ \delta_2 \end{pmatrix} \quad , \end{aligned} \tag{A.3}$$

where the target function T is given by

$$T = \cos(\alpha - \Phi_{\mathrm{T}})/\cos(\Phi_{\mathrm{T}}) \tag{A.4}$$

with α being the nominal scattering angle in the laboratory frame and Φ_{T} being the inclination angle of the target as illustrated in Fig. A.1.

For a particle with incident angle θ_1 that is scattered by a target with an angle θ_2 relative to the scattering angle α, the absolute scattering angle is given by

$$\beta = \alpha + \theta_2 - \theta_1 \tag{A.5}$$

and thus the effective scattering angle, that is, how much the scattering angle differs from the nominal scattering angle, is given by

$$\begin{aligned} \Theta &= \theta_2 - \theta_1 \\ \Rightarrow \theta_2 &= \theta_1 + \Theta \quad . \end{aligned} \tag{A.6}$$

The relationship between δ_1 and δ_2 is

$$\begin{aligned} \delta_2 &= K\left(\theta_2 - \theta_1\right) + C\delta_1 \\ &= K\Theta + C\delta_1 \\ &= K\Theta + C\delta_0 \quad , \end{aligned} \tag{A.7}$$

where K is the kinematic factor and C is the relative momentum ratio, which are defined by

$$K = \left(\frac{1}{p_{out}}\right)\left(\frac{\partial p_{out}}{\partial \alpha}\right) \tag{A.8}$$

$$C = \left(\frac{p_{in}}{p_{out}}\right)\left(\frac{\partial p_{out}}{\partial p_{in}}\right) \quad . \tag{A.9}$$

Here, K is zero at $\alpha = 0°$ and less than zero for larger angles, and C is unity for elastic scattering [Fuj02, Fuj97].

Substituting Eqs. (A.5) and (A.7) into Eq. (A.3) gives:

$$\begin{aligned} \vec{x_2} &= \begin{pmatrix} Tx_1 \\ \theta_1 + \Theta \\ K\Theta + C\delta_0 \end{pmatrix} \\ &= \begin{pmatrix} b_{11}Tx_0 + b_{12}T\theta_0 + b_{16}T\delta_0 \\ b_{21}x_0 + b_{22}T\theta_0 + b_{26}T\delta_0 + \Theta \\ K\Theta + C\delta_0 \end{pmatrix} \quad . \end{aligned} \tag{A.10}$$

The coordinates are then further transformed from behind the target to the detector plane by the spectrometer matrix $\mathbf{S} = (s_{\mu\nu})$. The total transformation of the particle from extraction to the detector plane can thus be represented in the following way [Mar83]:

$$\mathbf{B}\begin{pmatrix} x_0 \\ \theta_0 \\ \delta_0 \end{pmatrix} \rightarrow \begin{pmatrix} x_1 \\ \theta_1 \\ \delta_0 \end{pmatrix} \rightarrow \mathbf{T} \rightarrow \begin{pmatrix} x_2 \\ \theta_2 \\ \delta_2 \end{pmatrix} \qquad \mathbf{S} = \begin{pmatrix} x_{\mathrm{fp}} \\ \theta_{\mathrm{fp}} \\ \delta_{\mathrm{fp}} \end{pmatrix} \quad .$$

source point	in front of target	target transformation	in K600 focal plane

The result of the above described transformations is the following set of equations [Fuj02, Fuj97, Mar83]:

$$\begin{aligned} \vec{x_{\mathrm{fp}}} &= \mathbf{S}\vec{x_2} \\ &= \begin{pmatrix} s_{11} & s_{12} & s_{16} \\ s_{21} & s_{22} & s_{26} \\ s_{61} & s_{62} & s_{66} \end{pmatrix} \begin{pmatrix} b_{11}Tx_0 + b_{12}T\theta_0 + b_{16}T\delta_0 \\ b_{21}x_0 + b_{22}T\theta_0 + b_{26}T\delta_0 + \Theta \\ K\Theta + C\delta_0 \end{pmatrix} \end{aligned}$$

but since the beam energy remains unchanged, $s_{61} = s_{62} = 0$ and $s_{66} = 1$ which means

$$\begin{aligned} x_{\mathrm{fp}} = \; & x_0 \; (s_{11}b_{11}T + s_{12}b_{21}) \\ & + \; \theta_0 \, (s_{11}b_{12}T + s_{12}b_{22}) \\ & + \; \delta_0 \, (s_{11}b_{16}T + s_{12}b_{26} + s_{16}C) \\ & + \; \Theta \, (s_{12} + s_{16}K) \end{aligned} \tag{A.11}$$

$$\begin{aligned} \theta_{\mathrm{fp}} = \; & x_0 \; (s_{21}b_{11}T + s_{22}b_{21}) \\ & + \; \theta_0 \, (s_{21}b_{12}T + s_{22}b_{22}) \\ & + \; \delta_0 \, (s_{21}b_{16}T + s_{22}b_{26} + s_{26}C) \\ & + \; \Theta \, (s_{22} + s_{26}K) \end{aligned} \tag{A.12}$$

and

$$\delta_{\mathrm{fp}} = \delta_2 = K\Theta + C\delta_0 \quad . \tag{A.13}$$